Characterization of the Atmospheric Chemistry in the Southern San Joaquin Valley

Final Report

Contract 08-316

Prepared for:
The California Environmental Protection Agency
and
The California Air Resources Board

Principal Investigators:

Ronald C. Cohen

Professor, Department of Chemistry and
Department of Earth and Planetary Science
University of California, Berkeley

and

Allen H. Goldstein

Professor, Department of Environmental Science, Management and Policy
University of California, Berkeley

May 15, 2013

Acknowledgements

We acknowledge John Karlik, Rick Ramirez, and the entire staff at the University of California Extension in Kern County, without whom we could not have successfully completed the California Research at the Nexus of Air Quality and Climate Change Project in the San Joaquin Valley (hereafter CalNex-SJV). We also thank our collaborators Tad Kleindienst, Jennifer Murphy, John Offenberg, Xinrong Ren, Lynn Russell, Scott Scheller, Jason Surratt, Mark Zondlo, and their students.

Disclaimer

This report was prepared as one of the project deliverables associated with contract number 08-316 with the California Air Resources Board. The statements and conclusions in this report are those of the authors from the University of California, Berkeley, and our colleagues at Pennsylvania State University, the University of Wisconsin-Madison, the University of Washington, and the California Institute of Technology, and not necessarily those of the California Air Resources Board. The mention of commercial products, their sources, or their use in connection with the material reported herein is not to be construed as actual or implied endorsement of such products.

Table of Contents

List of Figures v

List of Tables ix

Abstract x

Executive Summary xi

1. Introduction 1

2. Summary of CalNex-SJV Measurements by Contractors, Sub-Contractors, and Researchers Who Participated with Other Funding 5

2.1. Cohen (UCB) 7

2.2. Goldstein (UCB) 8

2.3. Brune (PSU) 15

2.4. Keutsch (UW-M) 19

2.5. Thornton (UW) 20

2.6. Wennberg (CIT) 23

3. Data Analyses 28

3.1. On the observed response of ozone to NO_x and VOC reactivity reductions in San Joaquin Valley California 1995–present 28

3.2. Evidence for NO_x control over nighttime SOA formation 55

3.3. Elucidating secondary organic aerosol from diesel and gasoline vehicles through detailed characterization of organic carbon emissions 70

3.4. Evidence for emissions from petroleum operations in California's San Joaquin Valley 126

4. Anticipated Analytical Research after this Contract 143

4.1. The coupling of VOC reactivity, temperature, nitrogen oxides, and O_3 production (Cohen, UCB) 143

4.2. Comparing the VOC sources in the San Joaquin and South Coast Air Basins (Goldstein, UCB) 149

4.3. Improving our understanding of HO_x mechanisms (Brune, PSU) 152

4.4. Small-oxygenated VOCs, VOC sources, O_3, and aerosol formation (Keutsch, UW-M) 153

4.5. Peroxy nitrate chemistry in the SJVAB (Thornton, UW) 154

4.6. Impacts of organic and nitric acids (Wennberg, CIT) 155

5. Publications and Presentations by Investigators Receiving Funding 156

6. Conclusions and Recommendations 161

7. References 162

8. Glossary of Abbreviations 168

List of Figures

Figure 1.1	Location of the CalNex-SJV site southeast of the urban core of Bakersfield	3
Figure 2.1	Diurnal averages of temperature, relative humidity, wind speed, and wind direction during CalNex-SJV	6
Figure 2.2	CalNex-SJV wind roses	7
Figure 2.3	Observed ozone for the CalNex-SJV study period compared to historical data	15
Figure 2.4	Diurnal averages of measured and modeled OH and HO_2 separated by temperature	17
Figure 2.5	Diurnal averages of the measured OH reactivity and the OH reactivity calculated as the sum of all modeled species	18
Figure 2.6	Measured OH loss, OH production by HO_2 +NO, and NO	19
Figure 2.7	Time series of UW PAN and PPN measurements and the PPN/PAN ratio	21
Figure 2.8	Hourly mean values of PAN and PPN mixing ratios and the PPN/PAN ratio	22
Figure 2.9	Comparison of UW and UCB measurements of peroxy nitrates	23
Figure 2.10	Time series and diurnal means of inorganic and organic acids measured during CalNex-SJV	24
Figure 2.11	Correlation between acetic and formic acid	25
Figure 2.12	Gas phase CIT CIMS HNO_3 + particle phase NO_3^- shown versus UCB HNO_3 measurement (gas + particle)	26
Figure 2.13	HCN vs. CO	27
Figure 3.1.1	Schematic of the chemistry of photochemical O_3 production	30
Figure 3.1.2	The instantaneous ozone production rate as a function of NO_x	31
Figure 3.1.3	Map and satellite OMI NO_2 imagery of the San Joaquin Valley, CA	34
Figure 3.1.4	Southern SJV 8-hour O_3 CA standard exceedance probability vs. NO_2* with temperature	35
Figure 3.1.5	Southern SJV 8-hour O_3 CA standard exceedance probability vs. year with temperature	36
Figure 3.1.6	Southern SJV 8-hour O_3 CA standard exceedance probability vs. NO_2* tethering weekdays and weekends	38
Figure 3.1.7	Central SJV 8-hour O_3 CA standard exceedance probability vs. year with temperature	40

Figure 3.1.8	Central SJV 8-hour O_3 CA standard exceedance probability vs. NO_2* tethering weekdays and weekends	40
Figure 3.1.9	Northern SJV 8-hour O_3 CA standard exceedance probability vs. year with temperature	41
Figure 3.1.10	Northern SJV 8-hour O_3 CA standard exceedance probability vs. NO_2* tethering weekdays and weekends	42
Figure 3.2.1	Diurnal trends in pΣAN, OA, pΣAN/OA, and NO_3 production rate	56
Figure 3.2.2	Observations of trends in nighttime production of pΣAN with NO_3 production rate	58
Figure 3.2.3	Simulation of multigenerational SOA formation from the reaction of NO_3 with limonene as a function of NO_2 and limonene	59
Figure 3.2.4	Map of typical transport of air upwind of the CalNex-SJV site	60
Figure 3.2.5	Diurnal averages of temperature, relative humidity, ozone, and NO_2 at CalNex-SJV	61
Figure 3.2.6	Calculated average NO_3 reactivity for each night during CalNex-SJV	65
Figure 3.2.7	Schematic of kinetics model for Rollins et al. (2012)	66
Figure 3.3.1	Distributions of chemical classes for diesel and gasoline as shown via gas chromatography/mass spectrometry	89
Figure 3.3.2	Distribution of mass and SOA formation potential in diesel and gasoline fuel and non-tailpipe gasoline emissions	90
Figure 3.3.3	Demonstration of compositional consistency between gasoline and diesel fuel to gasoline and diesel exhaust at Bakersfield and the Caldecott tunnel	91
Figure 3.3.4	Verification of model perfomance at CalNex-Bakersfield by comparing predicted compound concentrations with observations of independent compounds	92
Figure 3.3.5	Verification of model perfomance at the Caldecott tunnel by comparing predicted compound concentrations with observations of independent compounds	93
Figure 3.3.6	Internal model diagnotics for CalNex-Bakersfield site	94
Figure 3.3.7	Internal model diagnotics for the Caldecott tunnel site	94
Figure 3.3.8	Distibutions of SOA yield uncertainties from each gas and diesel source	95
Figure 3.3.9	Percent contribution of gasoline and diesel exhaust to SOA over 0-50% diesel fuel use	96
Figure 3.3.10	Volatility basis set distribution of diesel fuel broken down by chemical class	97

Figure 3.3.11	Comparisons of organic aerosol vs. carbon monoxide for vehicular OA and total OA, and the diurnal pattern of ΔOA/ΔCO ratios	98
Figure 3.3.12	Weekday/weekend diurnal profiles of of diesel exhaust, gasoline exhaust, and non-tailpipe gasoline source contributions, and the ratio of diesel to gasoline exhaust at Bakersfield	99
Figure 3.3.13	Overall, weekday, and weekend diurnal patterns for total and vehicular organic aerosol, and their respective ΔOA/ΔCO ratios at Bakersfield, CA	100
Figure 3.3.14	Weekday/weekend behavior of ΔOA/ΔCO ratios in Los Angeles, CA	101
Figure 3.3.15	Observed organic aerosol vs. carbon monoxide at Bakersfield, CA with contributions for major non-vehicular sources as determined by factor analysis of AMS data	102
Figure 3.3.16	Percent contribution of diesel exhaust to gas-phase organic carbon and SOA versus percent diesel fuel use	103
Figure 3.3.17	Vehicular organic aerosol vs. carbon monoxide at Bakersfield, CA with weekday/weekend and day/night differences shown	104
Figure 3.4.1	6 and 12 hour statistical footprints determined using Flexpart meteorological data for the Bakersfield ground site averaged across the entire CalNex campaign	136
Figure 3.4.2	Observations of ethane vs. propane using canister measurements at Bakersfield	137
Figure 3.4.3	The average unexplained concentration of each compound and the percentage of unexplained mass out of total observations shown with examples of exceedances of observed over predicted values	137
Figure 3.4.4	Comparison of methylcyclohexane and isooctane at the Bakersfield ground site	138
Figure 3.4.5	Average diurnal pattern for the petroleum gas source contribution	138
Figure 3.4.6	The sum of unexplained compounds vs. the petroleum gas source	139
Figure 3.4.7	The diurnal average of the ratio of petroleum gas to the sum of motor vehicle emissions	139
Figure 3.4.8	Maps of southern part of the San Joaquin Valley with the location of oil and gas wells, the spatial distribution of petroleum gas emissions determined using statistical footprint analysis, and aircraft canister measurements of propane	140
Figure 3.4.9	Observations of methane vs. the petroleum gas source	141
Figure 3.4.10	Observations of methane vs. non-vehicular ethanol	141
Figure 4.1.1.	Daily average speciated reactivity calculated from measured VOCs vs. the max 1-h average temperature	143

Figure 4.1.2	Daily average ozone production vs. NO_x and HO_x chain termination vs. daily max. temperature	144
Figure 4.1.3	Mixing ratio (ppb) vs. OH reaction rate	145
Figure 4.1.4	Daily average calculated PO_3 vs. $PRONO_2$ and O_x vs. sum of alkyl nitrates	145
Figure 4.1.5	PO_3 vs. $PRONO_2$ recalculated	146
Figure 4.1.6	Modeled ozone production vs. NO_x	147
Figure 4.2.1	Comparison of emissions ratios for prominent gasoline-related VOCs	149
Figure 4.2.2	Comparison of VOC abundances, expressed as geometric means, at the CalNex-SJV and CalNex-LA sites	150
Figure 4.2.3	Diurnal cycles of anthropogenic contributions to gas-phase organic carbon (from motor vehicles) with the sum of biogenic compounds observed	151

List of Tables

Table 2.1	Overview of Measurements at Site	5
Table 2.2	VOCs measured during CalNex-SJV	11
Table 3.2.1	Reaction rates used in the calculation of NO_3 gas phase sinks	63
Table 3.3.1	Distribution of mass and SOA potential by chemical class for diesel exhaust, gasoline exhaust, and non-tailpipe gasoline	105
Table 3.3.2	Sales of on-road gasoline and diesel fuel in California and its counties	106
Table 3.3.3	Chemical class distribution of gasoline and diesel sources by total mass	106
Table 3.3.4	Summary of compounds used in source receptor modeling at Bakersfield	107
Table 3.3.5	Summary of compounds used in source receptor modeling at the Caldecott tunnel	107
Table 3.3.6	Mass and chemical class distribution of diesel fuel	108
Table 3.3.7	Mass and chemical class distribution of liquid gasoline	109
Table 3.3.8	Mass and chemical class distribution of non-tailpipe gasoline	110
Table 3.3.9	Average high-NO_x SOA yields with uncertainties constructed from scenarios and Monte Carlo analysis	111
Table 3.3.10	Compound specific liquid gasoline speciation for California in Summer 2010	112
Table 3.3.11	Compound specific diesel fuel speciation for California in Summer 2010	119
Table 3.3.12	Compound specific non-tailpipe gasoline speciation for California in Summer 2010	122
Table 3.4.1	Unrefined natural gas profile for thermogenic wet wells in the San Joaquin Valley from U.S.G.S. samples	131
Table 3.4.2	Interquartile ranges and MIRs for alkanes	133
Table 3.4.3	Quartiles for ambient concentrations from major petroleum-based sources measured at the Bakersfield site	135

Characterization of the Atmospheric Chemistry in the Southern San Joaquin Valley

Abstract

While air quality in the San Joaquin Valley Air Basin (SJVAB) was never as poor as it was in the South Coast Air Basin (SOCAB), reductions in ozone (O_3) and particulate matter (PM2.5) in the SJVAB have been slow compared to those in the SoCAB. These different responses in ambient air quality to similar regulatory control strategies are likely a result of different atmospheric chemistry regimes occurring in the two air basins. To improve our understanding of the chemistry in the southern SJV, and thus assess one part of the comparative question, we organized a field site in Bakersfield, CA. Here we measured a wide suite of organic molecules (hydrocarbons, oxygenates, peroxides, organic acids, aldehydes; including primary emissions and secondary oxidation products), nitrogen oxides (NO, NO_2, total and speciated peroxynitrates, total organic nitrates ($RONO_2$), HNO_3), hydrogen oxides (OH, HO_2), O_3, CO, CO_2, H_2O, and meteorological parameters during CalNex 2010. We also measured aerosol organic nitrate, ozone production rates, and total OH loss rates. Collaborators at the site measured a wide suite of additional gas and aerosol properties. The data are posted in a publically accessible website: https://bspace.berkeley.edu/portal. The measurements were made from May 18–June 29, 2010 providing a statistical sampling of atmospheric variation in response to fluctuations in winds and temperature and to systematic variations in emissions with day-of-week and time-of-day. The observations form the basis for analyses aimed at understanding the photochemistry controlling ozone and PM2.5 production in the study region. Here we describe the measurements made under this contract and briefly list the additional observations at the site. We then present several analyses of these and earlier measurements. These analyses indicate that volatile organic compound (VOC) controls have been effective in all areas of the SJV at moderate temperatures and in the central and northern locations of the SJV at high temperatures and in central and northern locations but they have been minimally effective at high temperatures in the southern SJV. Controls on oxides of nitrogen (NO_x) have recently become effective at reducing the frequency of high ozone days in some cases in the SJV and they are poised to be even more effective in the future. The observations also provide insight into the sources of VOCs and the extent to which those sources might be controllable. In this work, we present assessments of several prominent sources in the SJV, which include motor vehicles and petroleum operations, and include their potential to produce secondary pollutants. Observations of aerosol supported by this contract were limited. Those observations we did make show that nitrate radical (NO_3) chemistry is an important source of aerosol growth at night. Further, in combination with aerosol mass spectrometry (AMS) these observations demonstrate that about 20% of the individual molecules in secondary organic aerosol (SOA) are chemicals of the form $RONO_2$. Additional results will no doubt emerge with further analyses that are ongoing with continuing support from other funding sources.

Characterization of the Atmospheric Chemistry in the Southern San Joaquin Valley

Executive Summary

We established and coordinated the CalNex-SJV site, where a chemically comprehensive, state-of-the-art suite of observations were obtained from May 18–June 29, 2010. Some of these measurements were directly funded by this contract and others were able to take advantage of infrastructure funded by this contract (the setup of a walk-up tower, electrical hook-ups, office space, etc.). The measurements have been archived at a publically available site: https://bspace.berkeley.edu/portal. The measurements supported by this contract included: NO, NO_2, total peroxy nitrates (ΣRO_2NO_2), total alkyl nitrates ($\Sigma RONO_2$), HNO_3, and aerosol phase organic nitrates (Cohen, UCB); more than 100 speciated VOCs, CO_2, CO, O_3, N_2O, and meteorological parameters (Goldstein, UCB); OH, HO_2, and total OH reactivity (Brune, PSU); formaldehyde (CH_2O), glyoxal, and larger α-dicarbonyls (Keutsch, UW-Madison); PAN and PPN (Thornton, UW); and H_2O_2, HNO_3, HCN, acetic acid, and formic acid (Wennberg, CIT). Additional measurements contributed to the archive include: gas phase NH_3, HCl, HNO_3, SO_2 and their ion analogs ammonium, chloride, nitrate, nitrite, and sulfate (Murphy, U Toronto); HONO concentrations and REA fluxes (Ren, U Miami); PM1 mass concentrations of alkane, carboxylic acid, alcohol, amine, organonitrate, and non-acid carbonyl organic species, size distribution of submicron particles, and PM1 mass concentrations of organic, nitrate, sulfate, ammonium, and non-NaCl chloride aerosol (Russell, UCSD); isoprene and monoterpene-derived organosulphate aerosols (Surratt, UNC); and EC/OC composition (Scheller, CARB).

Analysis and interpretation of the measurements is ongoing; however, some clear ideas have emerged from the initial round of planned analyses of the CalNex and earlier data. These include:

- It has been hypothesized that the VOCs that contribute to violations of the 8-hour CA ozone standard on the hottest days (daily T_{max} >34°C) in the southern San Joaquin Valley have not been reduced over the last 15 years. The NO_x reductions that have occurred over this time period have brought the region from a position of VOC-limited chemistry to one of NO_x-limited chemistry and additional NO_x reductions will be immediately effective. These temperatures were not significantly sampled during the CalNex-SJV intensive period.
- At a moderate-range of temperatures (daily T_{max} is 28–33°C), which occur frequently in the southern, central and northern SJV, and during the CalNex campaign, both VOC and NO_x reductions over the last 15 years have contributed to reductions in the frequency of days exceeding the CA 8-hour ozone standard.
- At low temperatures, the VOCs that dominate ozone production at the CalNex-SJV site are identified. This identified fraction decreases with temperature, suggesting that oxygenates, for which current analytical methods are poor, are increasingly important as temperature increases. We also observe very low effective $RONO_2$ yields compared to other cities, an indication that smaller molecules are important. These facts are consistent with the analysis of ozone

trends and the conclusion that the control of some VOC compounds associated with high temperatures has not been effective in the Bakersfield region of the last decade. While this idea is consistent with an emerging hypothesis that evaporative emissions from fermenting animal feed are an important source of reactive VOC (e.g. organic acids and small alcohols) in the SJV, much research remains to be done to identify the source of the unidentified VOC reactivity.

- Secondary organic aerosol (SOA) in the SJV has multiple sources. One set of CalNex-SJV measurements quantifies the contribution of $RONO_2$ molecules, finding that these are approximately 15–20% of the mass and that NO_3 radical chemistry at night is responsible for much of the nighttime growth in SOA.
- Emissions from gasoline and diesel vehicles are prominant anthropogenic sources of reactive gas-phase organic carbon and key precursors to SOA in the SJV. We characterize the chemical composition, mass distribution, and organic aerosol formation potential of emissions from gasoline and diesel vehicles, and find both sources are important; but, depending on a region's fuel usage, diesel is responsible for 65-90% of vehicular-derived SOA.
- Petroleum operations are prominent in the southern SJV and we present evidence of a large source of paraffinic hydrocarbons associated with unrefined petroleum gas. Methane emissions associated with the petroleum gas were not significant, consistent with emissions from condensate storage tanks containing the non-methane liquids, which have been separated from the associated gas. The abundance of non-methane hydrocarbons in Bakersfield from this source ranges from 30 to 150% with an average of 82 ± 74% of motor vehicle emissions by carbon mass, but is less reactive.

Characterization of the Atmospheric Chemistry in the Southern San Joaquin Valley

1. Introduction

A wide suite of volatile organic compounds (VOCs) reacts in the atmosphere with nitrogen oxides (NO_x = NO + NO_2) and sunlight, leading to the formation of ozone (O_3) and secondary organic aerosols (SOA). Reducing anthropogenic VOC and/or NO_x emissions has been the main method of controlling ozone in the United States over the past several decades (National Research Council, 1991). In the South Coast Air Basin, control of anthropogenic VOCs from automobiles and industrial processes has proven effective at reducing the frequency of ozone exceedances over the past three decades, indicating that VOCs were the limiting factor in ozone production in this region (e.g. Milford et al., 1989; Martien and Harley, 2006). In regions with high emissions of biogenic VOCs, NO_x control has been more efficient at reducing ozone (Trainer et al., 1987; Sillman et al., 1990; Cardelino and Chameides, 1990; Sillman et al., 1997; Han et al., 2005; LaFranchi et al. 2011). In Central California, differences between weekday and weekend ozone concentrations indicate that ozone production in urban regions are NO_x-saturated (VOC-limited) while more remote areas such as the Southern SJVAB and the Sierra Nevada are more NO_x-sensitive (Blanchard and Fairley, 2001; Marr and Harley, 2002; Murphy et al., 2006; Murphy et al., 2007). There is also a debate over how much NO_x reductions are enhancing or impeding the effectiveness of controls for reducing ozone (Fraas and Lutter, 2011), for example in the South Coast Air Basin.

Assessments of VOC reactivity in Central California using a photochemical air quality model, the Community Multi-scale Air Quality model (CMAQ), and available ground-based measurements to evaluate the contribution of different types of VOCs to the photochemical activity by Steiner et al. (2008) found that current models predict total OH reactivity (VOCR) to within 25–40% at urban, suburban, and rural sites in the Sacramento region. However, in the urban area of Fresno, the model predicted NO_x and VOCR that were lower than observations by a factor of 2–3. Furthermore, modeled concentrations of biogenic hydrocarbons and aldehydes were poorly characterized by existing measurements in the San Joaquin Valley Air Basin (SJVAB), thus making observational evaluation of the modeling results highly uncertain. According to the model, 30–50% of the urban VOCR in Central California is due to aldehydes and other oxygenated species. This total is nearly equivalent to the anthropogenic VOCR in the region. In rural vegetated regions, biogenic and aldehyde reactivity dominates. Based on this analysis and on analyses of day-of-week variation in O_3, we hypothesized in our project proposal that:

> *The San Joaquin Valley of California is a region where secondary pollutants will respond weakly or not at all to continued anthropogenic VOC controls while NO_x controls will be effective.*

If this hypothesis is correct and NO_x controls are implemented, we expect improvements first in outlying regions followed by improvement in the city centers.

To evaluate this hypothesis we established a field site SE of Bakersfield, CA (Figure 1.1) as part of the CalNex (California at the Nexus of Air Quality and Climate Change) experiment. The site, designated CalNex-SJV, included measurements of a comprehensive suite of radicals (NO, NO_2,

OH, and HO_2), their precursors (O_3, CH_2O, gyloxal, and HONO) and radical sinks (H_2O_2, PAN, PPN, total peroxy nitrates (ΣRO_2NO_2), total alkyl nitrates ($\Sigma RONO_2$), and HNO_3) along with organics emitted directly by anthropogenic and biogenic processes, the total reactivity of OH toward the local organic mixture, organic species that are unique markers of oxidation of specific individual precursors, and a number of aerosol properties (many of these were not funded by this contract). This collection of observations enables tests of our understanding of ozone and secondary organic aerosol chemistry at a level of detail never before achieved in the SJV. The measurements were made over a 6-week period, providing a statistical sampling of atmospheric variation in response to fluctuations in winds, temperature, and to systematic variations in emissions with day-of-week and time-of-day.

.

Figure 1.1. *Photographs of:* ***top)*** *monitoring platform,* ***middle)*** *local setting, and* ***bottom)*** *regional setting of the CalNex-SJV site located southeast of the urban core of Bakersfield. The site is marked by a yellow pin in the middle panel and by a red triangle in the bottom panel.*

Our measurements provided data to address the following specific questions regarding chemical evolution of O_3 and PM2.5 in the SJVAB. Several of the questions are addressed in this report and others are ongoing with other funding.

- How well do we understand the sources of NO_x and VOC in the SJVAB?
- How well do we understand the coupling of HO_x, NO_x, O_3, and VOC photochemistry under the conditions of VOC reactivity typical of the SJVAB?
- What happens to NO_x and VOC oxidation products at night? In the nocturnal boundary layer? In the residual layer? How does this chemistry affect NO_x, VOC, O_3, and aerosol production at night and on the following day?
- What factors affect the time scales for production and removal of 1st, 2nd, 3rd, etc. generation products of VOC and NO_x oxidation?
- How do these VOC reactions impact the photochemical production and loss of ozone, OH, NO_y species, and aerosols?

In cooperation with other CalNex investigators, broad questions that can be addressed include those identified by the ARB and NOAA in the CalNex-2010 planning documents:

- Are there significant differences in precursors or ozone formation chemistry between the San Joaquin Valley and South Coast Air Basin?
- Will precursor differences between the San Joaquin Valley and the South Coast Air Basin lead to different chemical transformation processes and different responses to emissions reductions?
- What is the importance of natural emissions to the ozone formation process? Are there regional differences in the formation rates and efficiency for particulate matter as well?

The primary emphasis of this project was on obtaining and making available to the entire atmospheric science community a suite of observations that can be used to test a range of hypotheses outlined here, along with hypotheses that might be developed in the future. We note that the most significant atmospheric science results usually take more than 2 years after a major field experiment to fully incubate and develop into manuscripts. All the members of this team are fully committed to seeking continued support (from a range of funding agencies) for completing analysis of the CalNex-2010 observations. The measurements we have reported are publically available and we encourage anyone interested to make use of the data to investigate science questions that interest them. At this stage of analysis we describe our preliminary findings from the investigations conducted under this contract.

The main elements of our contract were spread over 11 tasks but can be summarized as follows:

1. To coordinate site preparations, to make observations of a variety of gases and aerosol properties, and to report the observations to a public archive,
2. To summarize key findings of the observations and to publish at least one scientific paper, and
3. To report on our efforts to ARB and to work within the larger CalNex context to integrate our findings with those of other field sites/investigators.

In section 2 of this report we describe results from the first set of tasks, providing a brief overview of the field site and measurements. All researchers receiving funding under this contract, as well as our collaborators, have completed and submitted their final datasets to the CalNex-SJV archive. In section 3, we summarize some of the key findings, including four subsections that are manuscripts that will be published or submitted before this report is approved. In section 4 we describe preliminary findings from analyses that are still ongoing. In both sections 3 and 4 we indicate with keywords which of the specific questions listed above are addressed in the text. In section 5 we present a report summary with our recommendations. Our reporting to ARB and other CalNex investigators includes this document, as well as numerous presentations at meetings organized by ARB and at the 2010 and 2011 AGU meetings (among others).

2. Summary of CalNex-SJV Measurements by Contractors, Sub-Contractors, and Researchers Who Participated with Other Funding

Table 2.1: *Overview of Measurements at the CalNex-SJV Site*

Measurement	Technique/ Instrumentation	Lab/Group	Height
NO_2, ΣRO_2NO_2, $\Sigma RONO_2$, and HNO_3	TD-LIF	Cohen	18 m
Aerosol phase organic nitrates (pΣANs)	TD-LIF	Cohen	18 m
NO	chemiluminescence	Cohen	18 m
VOCs	GC/MS-FID	Goldstein	18 m
CO_2, CO, N_2O, CH_4	IR spectroscopy, cavity output spectroscopy	Goldstein	18 m
Ozone	UV spectroscopy	Goldstein	18 m
Meteorological parameters (wind, temperature, radiation)	wind vane, thermocouple, photosynthetically active radiation sensor	Goldstein	18 m
OH, HO_2, OH reactivity	laser induced fluorescence	Brune	18 m
Formaldehyde, glyoxal, and larger α-dicarbonyls	laser induced fluorescence & phosphorescence	Keutsch	18 m
Acyl peroxy nitrates	TD-CIMS	Thornton	4 m
H_2O_2, HNO_3, acetic acid, formic acid, and HCN	CIT-CIMS	Wennberg	18 m
EC/OC	Sunset Analyzer	ARB	4 m
NH_3, NH_4^+, HCl, Cl^-, HNO_3, NO_3^-, NO_2^{2-}, SO_2, SO_4^{2+}	ambient ion monitor-ion chromatography	Murphy	4 m
HONO	long path absorption photometry	Ren	16 m
Alkane, carboxylic acid, alcohol, amine, organonitrate, and non-acid carbonyl PM1 mass	Fourier transform-infrared spectroscopy (of filter samples)	Russell	4 m

concentrations			
submicron particle size distribution	scanning mobility particle sizer	Russell	4 m
organic, nitrate, sulfate, ammonium, and non-NaCl chloride PM1 mass concentration	aerosol mass spectrometry	Russell	4 m
isoprene and monoterpene-derived organosulphate aerosols	electrospray ionization-mass spectrometry (of filter samples)	Surratt	2 m

Site description: These measurements were performed at the Bakersfield supersite, a site approximately 6 km southeast of the Bakersfield city center at the southern end of the San Joaquin Valley in California. A map of the area near the measurement site is shown in Figure 1.1. We show the diurnal profiles of temperature, relative humidity, wind speed, and wind direction in Figure 2.1. Summaries of the wind directions and speeds during daytime (10:00-19:00 PST) and nighttime (22:00-08:00 PST) hours are shown in Figure 2.2. Time periods were chosen to capture the consistent daytime conditions and avoid the transition period at sunset. Daytime winds are dominated by northwesterly up-valley flows. Nighttime flows are substantially more variable with relatively fast up-valley northwesterly winds and occasional downslope flows from the south and west. These downslope flows were only observed at the site at night and would, many times, occur once or twice a night with very slow wind speeds. This resulted in intermittent nighttime maxima of locally emitted compounds building up in the nocturnal boundary layer and frequent dilution to daytime minima by fast winds from the northwest.

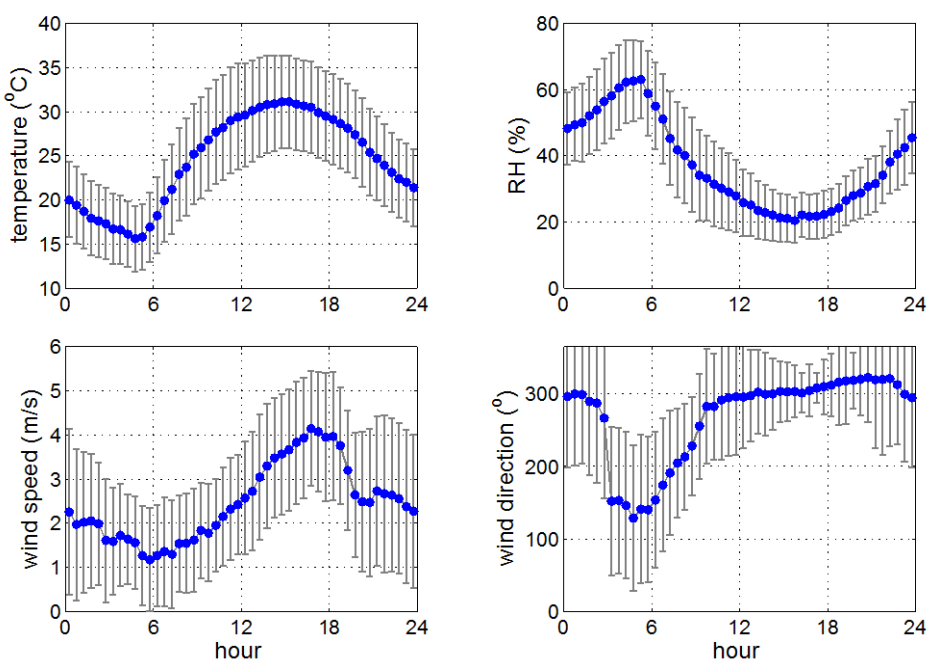

Figure 2.1. *Diurnal means of temperature* ***(above left)****, relative humidity* ***(above left)****, wind speed* ***(below left)****, and wind direction* ***(below right)*** *for the CalNex-SJV experiment (May 15–June 30). The vertical lines are 1σ from the mean.*

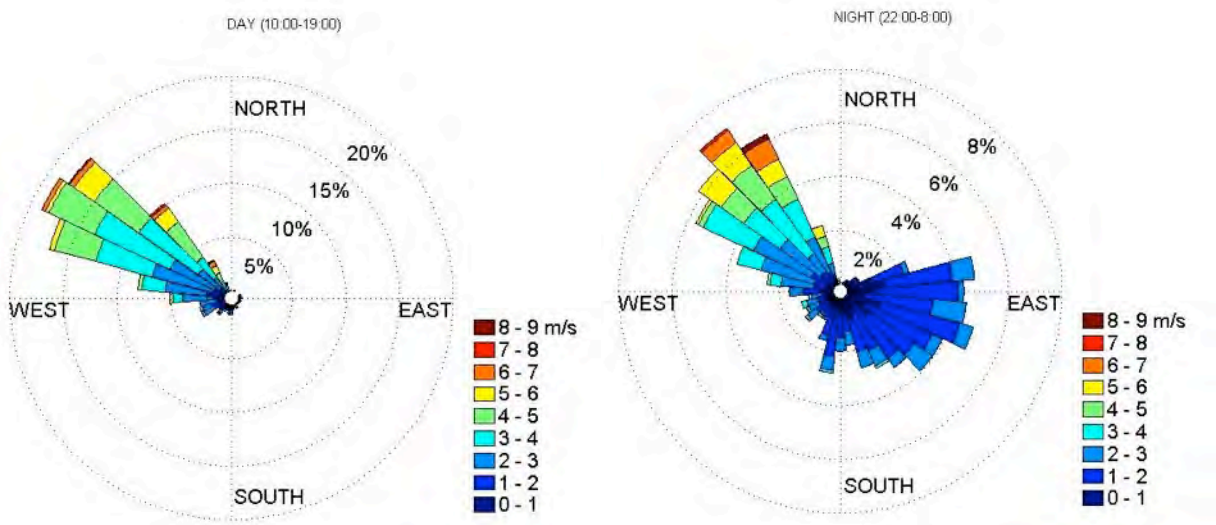

Figure 2.2. *Wind roses at the CalNex-SJV site for all days (10:00-19:00 PST) and nights (22:00-8:00 PST).*

2.1. Cohen (UC-Berkeley)

NO_2, ΣRO_2NO_2, $\Sigma RONO_2$, and HNO_3: UC-Berkeley collected thermal dissociation laser induced fluorescence (TD-LIF) measurements of NO_2, total peroxy nitrates (ΣPNs), total alkyl nitrates (ΣANs), and nitric acid (HNO_3). The TD-LIF operating principle is as follows: NO_2 is detected by laser-induced fluorescence (LIF) (Thornton et al., 2000). A tunable dye laser is pumped by a Q-switched, frequency doubled Nd^{3+}:YAG laser. The narrow band dye laser is etalon-tuned to a specific 585 nm rovibronic feature of NO_2, alternating between this feature and the weaker continuum absorption. The beam is split and twice directed sequentially through 4 multi-pass white cells. The resulting red-shifted photons are imaged onto a PMT and collected using time-gated counting. The LIF technique is spectroscopically specific and accurate (± 5%).

ΣPNs, ΣANs, and HNO_3 are detected by thermal dissociation (TD) coupled to LIF (Day et al., 2002). Dissociation of labile NO_y species into NO_2 and a companion radical occurs at characteristic temperatures due to differing N—O bond strengths. Air is pulled through heated quartz tube ovens followed by Perfluoroalkoxy (PFA) sampling lines before reaching the NO_2 detection cell. An ambient channel detects only NO_2, a second channel (180°C) measures NO_2 + ΣPNs, a third channel (350°C) measures NO_2 + ΣPNs + ΣANs, and a fourth measures NO_2 + ΣPNs + ΣANs + HNO_3. Mixing ratios of each species are determined as the difference between adjacent temperature channels. The uncertainty in these species is 15%. The instrument is calibrated hourly in the field with an NO_2 reference standard added to the system at the inlet. This is a multi-point calibration with the following mixing ratios added in this sequence: 0 ppb, 20 ppb, 5 ppb, and 10 ppb. The full dataset is complete and available on the CalNex-SJV archive.

Aerosol phase organic nitrates (pΣAN): pΣAN measurements were made by TD-LIF. This instrument functions identically to the above-described TD-LIF with two exceptions: the excitation light source is a solid-state, continuous wave laser system at a 408 nm and, more

importantly, that the pΣAN channel is fitted with an activated carbon denuder to remove gas phase NO_y prior to sampling with a PM2.5 cyclone at the inlet upstream of the denuder to reject larger particles (Rollins et al, 2010). This system is calibrated in the same way, and also hourly, as the above TD-LIF. The pΣAN channel specifically is calibrated with an NO_2 reference bypassing the denuder and every few days, the NO_2 reference is added through the denuder to confirm gas-phase NO_2 is quantitatively removed. The uncertainty in pΣANs is 10%. These data are available on the CalNex-SJV archive.

NO: Nitric oxide (NO) was measured with a custom-made two-channel chemiluminescence instrument based on the standard O_3 chemiluminescence method (Drummond et al., 1985). This measurement works by combining sampled air with excess O_3 to chemically convert ambient NO to excited-state NO_2 that then fluoresces. The emitted red shifted photons are counted with a PMT. This instrument was calibrated every hour in the field with an NO reference standard. These calibrations were multi-point, added mixing ratios were in the range 2.25–6.7 ppb, and calibrations were always preceeded with flow of zero air. The accuracy is ± 5%. These data are available on the CalNex-SJV archive. For more information see Min et al. (2013).

2.2. Goldstein (UC-Berkeley)

VOC Measurements: Chemical speciation of VOCs was achieved using a gas chromatograph (Hewlett Packard 5890 Series II) that was equipped with a quadrapole mass selective detector (MSD) (Hewlett Packard 5971) and a flame ionization detector (GC/MS-FID). The instrument was operated *in situ* with a custom system that automated sample collection and analysis. Ambient samples were collected for the first 30 minutes of every hour via an inlet located at the top of the 18-m tower. Measurements of VOCs were made at this height to be colocated with other gas-phase measurements on the tower. To prevent line losses and accurately preserve gas-phase VOCs in the ambient sample, ozone and particulate matter were removed at the inlet using 47 mm glass fiber filters (Pall, type A/E) that were coated in sodium thiosulfate according to the method vetted by Pollmann et al. (2005). After ozone and particulate removal, the sample traveled at ~1 L min^{-1} through a ¼" Silcosteel line that was insulated and heated to >80°C. The sample line went down the 20 m tower to the trailer adjacent to the base of the tower. Once in the instrument trailer the sample proceeded to a preconcentration system, where two separate channels sub-sampled off the main flow each at ~20 mL min^{-1}. Ozone removal was confirmed by measuring the remainder of the main flow with a spectroscopic ozone analyzer (Dasibi model 1008-AH).

The instrument was equipped with two independent measurement channels sampling from the same inlet line. Channel 1 was focused on measuring a broad range of VOC including those with lower volatilities (ranging from isopentane to tetradecane). Channel 2 measured low-molecular weight compounds that are more volatile (e.g. propene–isopentane). Prior to subsampling from the inlet line for the two channels, an internal standard (n-octane, 5.0 ppm) was constantly added to the sample flow at 2mL/min, such that after the dynamic dilution its concentration was ~2 ppb. The internal standard was used to correct for any drift in the sensitivity of the mass selective detector and to confirm overall instrument analytical stability. The entire sampling line and all other elements of the sampling/preconcentration system that pertain to Channel 1 were constructed with passivated steel or other highly inert materials that were heated to constant

temperatures at or above 80°C using resistive heaters. This was done to minimize losses of any VOC due to adsorption, absorption, or condensation, especially for compounds with lower volatility. Prior to the beginning of the measurement period, the heated inlet was allowed to condition for several days.

The Channel 2 sub-sample was run through a custom-made water trap to remove water that would have otherwise adsorbed onto the Channel 2 adsorbent trap. This was accomplished by passing the Channel 2 Teflon sample line through an aluminum block that was cooled to 0°C and routinely heated and purged when sample was not being collected.

The samples in both channels were concentrated on custom-made multilayer adsorbent traps via a system of three 12-port rotary valves (Valco, Valcon E) to facilitate the automation of sampling and injection. The adsorbent traps were constructed out of 1/8" Sulfinert steel tubing and contained the following sequence of adsorbents held in place by glass wool on each end. Channel 1: 60 mg glass beads (Alltech, 60/80 mesh, DCMS-treated), 20 mg Tenax TA (Supelco, 60/80 mesh), 30 mg Carbopak B (Supelco, 60/80 mesh), and 40 mg Carbopak X (Supelco, 60/80 mesh). Channel 2: 60 mg glass beads, 30 mg Carbopak B, 40 mg Carbopak X, and 40 mg Carboxen 1000 (Supelco, 60/80 mesh). During sample collection the adsorbent traps were thermoelectrically cooled to a constant 15°C and 5°C for Channels 1 and 2, respectively. Following the preconcentration of ~1 L samples on each adsorbent trap, the analytes were thermally desorbed at 320°C with a reverse flow of helium and injected directly onto their respective capillary columns where chromatographic separation was assisted by a ramped temperature program in the GC oven. The effluent from the traps was injected onto a DB-624 (60 m × 0.32 mm × 1.8 μm) and a HP-Plot-Q (30 m × 0.32 mm × 20.0 μm) for Channels 1 and 2, respectively.

All flows were measured and controlled using mass-flow controllers (MKS Instruments), and system temperatures were monitored using T-type thermocouples (Thermo Scientific). All system data were recorded on a data-logging system (Campbell-Scientific).

The instrument was calibrated for more than 100 individual VOCs using a combination of standard gas mixtures and liquid standards. Three gas standard cylinders with ppm-level concentrations (Apel-Riemer, Scotty Gas) were dynamically diluted into a ~1 L min^{-1} flow of pure air supplied from a zero air generator (Aadco Inc.) to get ppt- to ppb-level concentrations. Using standards introduced at the inlet, most measured compounds were determined did not have any significant sampling line losses. Measured compounds with lower voilatilities were calibrated vis the liquid standards introduced into the system at the top of the tower to account for any losses in the sample line or preconcentration system. Multi-point calibrations were run at the beginning and end of the measurement campaign, and daily single-point standards were run to verify the calibrations. Pure air from the zero air generator was also used to run daily blank runs to account for any artifacts or biases in the system. For identified compounds without standards, their response factors on the MSD were determined by multiplying the fraction of the quantifying ion in a representative mass spectrum by the total ion response factor calculated from known compounds of similar chemical classes. This method, while approximate, provides concentration data with a reasonable amount of uncertainty when standards are not available for relatively stable hydrocarbons.

We quantified hourly concentrations for ~200 VOCs at CalNex-SJV from May 22nd through June 28th, 2010. The abundances of the VOCs are summarized in Table 2.1. We reported hourly data averaged over the first half of the hour for linear alkanes, branched alkanes, cyclic alkanes, alkenes, aromatics, polycyclic aromatic hydrocarbons (PAHs), terpenoids, halogenated compounds, species containing sulfur, oxygenates, and alcohols. Numerous species reported here represent the first ever-reported ambient measurements, and some others have only been reported in a very limited number of studies. This includes compounds in the intermediate-volatility range (IVOCs), such as the methylnaphthalenes and dimethylnaphthalenes. Some of the VOCs are reported together as groups because it was infeasible to accurately separate them on the chromatographic column used while measuring such a wide range of compounds. For most VOCs, abundances were within the ranges reported for other urban field studies in the U.S. (e.g. Millet et al., 2005; Heald, et al., 2008). A comparison to the CalNex-Los Angeles site is in the following section. The full dataset has been made available to the CalNex science team through the CalNex-SJV archive.

Table 2.2. *VOCs Measured at the CalNex-SJV site between 5/22 and 6/28/10. Listed are VOCs and abundances for ~200 compounds in 170 entries.*

Compound	Concentration Quartiles (pptv) 25%	50%	75%
Straight-chain Alkanes			
propane	1100	2100	5600
n-butane	230	480	1700
n-pentane	220	360	890
n-hexane	52	94	260
n-heptane	34	57	140
n-nonane	5.6	11	23
n-decane	6.3	11	21
n-undecane	5.8	10	20
n-dodecane	3.6	6.0	12
n-tridecane	3.8	6.2	14
n-tetradecane	3.0	4.9	10
Branched Alkanes			
iso-pentane	450	770	1900
2,2-dimethylbutane	28	43	77
2-methylpentane & 2,3-dimethylbutane	120	200	500
3-methylpentane	50	90	250
2,2 & 2,4-dimethylpentane	14	24	55
3-3-dimethylpentane	4.0	7.7	17
2,3-dimethylpentane	20	37	93
2-methylhexane	23	39	90
3-methylhexane	28	49	120
2,2-dimethylhexane	1.0	2.0	4.0
2,5-dimethylhexane	6.2	12	36
2,4-dimethylhexane	7.4	13	32
2,2,3-trimethylpentane	2.7	5.8	12
iso-octane	39	65	120
2,3,4-trimethylpentane & ctc-1,2,3-trimethylcyclopentane	32	62	160
2,3,3-trimethylpentane & 2,3-dimethylhexane	11	19	33
2-methylheptane	10	19	49
4-methylheptane	4.3	9.0	21
3-methylheptane	9.3	18	44
2,2,5-trimethylhexane	5.4	9.1	16
2,6-dimethylheptane	5.4	12	31
3,5-dimetylheptane	2.2	4.1	10
2,3-dimethylheptane	0.9	1.6	4.7
2 & 4-methyloctane	2.9	5.5	13
3-methyloctane & 4-ethylheptane	3.1	5.7	13
2,2,5-trimethylheptane	0.7	1.0	1.7
2,2,4-trimethylheptane	0.8	1.4	2.6
unidentified C10 branched alkanes (5 isomers)	3.0	5.3	12
2,6-dimethyloctane	0.7	1.3	3.2
2 & 3 & 4-methylnonane & 3 & 4-ethyloctane & 2,3-dimetyloctane	6.9	12	25
unidentified C11 branched alkanes (3 isomers)	0.7	1.3	2.6
unidentified C11 branched alkanes (10 isomers)	5.4	9.3	18
unidentified dimethylundecane isomer #1	0.8	1.4	3.3

unidentified dimethylundecane isomer #2	0.8	1.2	2.6
unidentified C13 branched alkanes (2 isomers)	2.3	3.6	5.8
unidentified C14 branched alkanes (6 isomers)	4.4	6.5	11
unidentified C16 branched alkane	1.3	1.9	3.1
Cycloalkanes			
cyclopentane	37	64	160
methylcyclopentane	57	100	320
cis-1,3-dimethylcyclopentane	15	30	100
trans-1,3-dimethylcyclopentane	16	42	180
ethylcyclopentane	7.9	15	44
ctc-1,2,4-trimethylcyclopentane	5.4	14	52
ctt-1,2,4-trimethylcyclopentane	1.7	3.8	16
unidentified-methyl-ethylcyclopentane	0.7	1.8	4.3
iso-propylcyclopentane	1.1	2.3	5.9
n-propylcyclopentane	2.1	3.9	10
cyclohexane	28	54	150
methylcyclohexane	20	40	150
cis-1,3 & 1,1-dimethylcyclohexane	4.6	10	38
trans-1,2-dimethylcyclohexane	4.6	11	42
trans-1,3-dimethylcyclohexane	2.9	6.1	18
cis-1,2-dimethylcyclohexane	1.9	3.4	9.8
ethylcyclohexane	4.8	9.9	32
ccc-1,3,5-trimethylcyclohexane	1.0	2.2	6.6
1,1,3-trimethylcyclohexane	2.0	5.3	20
1,1,4-trimethylcyclohexane	1.1	2.8	8.8
ctt-1,2,4 & cct-135-trimethylcyclohexane	0.7	1.7	3.9
ctc-1,2,4-trimethylcyclohexane	1.2	2.9	9.6
1,1,2-trimethylcyclohexane & isobutylcyclopentane	0.7	1.2	2.0
unidentified methylethylcyclohexane isomer #1	0.8	1.6	4.5
unidentified methylethylcyclohexane isomer #2	0.7	1.4	3.7
iso-propylcyclohexane	0.9	2.0	5.2
n-propylcyclohexane	2.9	5.6	16
unidentified C10 cyclohexane	2.5	4.8	7.8
unidentified C10 cyclohexanes	0.7	1.2	2.7
unidentified C9 cycloalkane	1.7	4.6	16
Alkenes			
propene	90	160	330
1-butene & isobutene	40	60	100
trans-2-butene	7.9	11	16
cis-2-butene	10	14	22
1-pentene	14	18	28
cis-2-pentene	12	19	31
1-hexene	14	22	35
2-methyl-2-pentene & cis-3-methyl-2-pentene	1.0	1.4	2.2
1-methylcyclopentene	4.5	7.1	13
unidentified C7 cyclopentenes (2 isomers)	0.7	1.2	2.3
1-methylcyclohexene	0.6	0.9	1.4
unidentified C9 cycloalkene	1.6	3.5	11
Aromatics			

toluene	120	220	440
ethyl-benzene	17	32	59
m & p-xylene	52	100	210
o-xylene	20	36	72
cumene	1.4	2.5	5.8
n-propyl-benzene	3.7	6.7	14
1,2,3-trimethyl-benzene	4.4	8.9	24
1,3,5-trimethyl-benzene	5.7	13	29
1,2,4-trimethyl-benzene	16	31	73
1-ethyl-3-methyl-benzene & 1-ethyl-4-methyl-benzene	14	28	62
1-ethyl-2-methyl-benzene	3.9	7.4	16
1-methylethenyl-benzene	0.5	0.5	0.7
1-ethenyl-2 [or 3]-methyl-benzene	0.5	0.6	0.8
iso-butyl-benzene	0.6	0.9	1.5
n-butyl-benzene	0.6	1.1	2.1
m-cymene	0.6	0.9	1.6
p-cymene	1.9	3.5	10
m-diethyl-benzene	1.4	2.2	4.0
p-diethyl-benzene	3.3	6.7	17
o-diethyl-benzene	0.6	0.8	1.2
1-methyl-3-n-propyl-benzene	2.9	5.6	10
1-methyl-2-n-propyl-benzene	0.7	1.2	2.5
indan	1.1	2.1	4.6
indene	0.5	0.6	0.9
1,4-dimethyl-2-ethyl-benzene	0.9	1.9	4.3
1,3-dimethyl-4-ethyl-benzene	0.9	1.9	4.4
1,2-dimethyl-4-ethyl-benzene	0.8	1.6	3.4
1,3-dimethyl-2-ethyl-benzene	0.6	0.9	1.4
1,2-dimethyl-3-ethyl-benzene	0.7	1.2	1.9
trans-2-butenyl-benzene	1.4	2.7	4.6
1,2,4-5-tetramethyl-benzene	0.7	1.3	2.5
1,2,3,5-tetramethyl-benzene	0.8	1.6	3.3
1,2,3,4-tetramethyl-benzene	0.7	1.5	3.0
1-methyl-indan	0.6	1.1	1.9
2-methyl-indan	0.7	1.4	2.8
unidentified C11 aromatics (5 isomers)	0.9	1.8	2.9
Polycyclic Aromatic Hydrocarbons (PAHs)			
naphthalene	1.1	2.3	5.4
1-methylnaphthalene	0.6	1.4	2.9
2-methylnaphthalene	0.6	1.6	3.8
dimethylnaphthalenes (sum of isomers)	1.2	2.4	4.4
Oxygenates and Alcohols			
methacrolien	40	61	100
methanol	9500	16000	26000
ethanol	4100	7600	15000
isopropyl alcohol	59	94	180
acetone	580	880	1600
methyl ethyl ketone	69	130	270
methyl isobutyl ketone	5.1	7.8	15

methyl n-butyl ketone	5.1	7.8	13
propanal	18	25	40
butanal	7.0	9.8	14
pentanal	19	28	45
hexanal	32	52	85
heptanal	23	36	51
nonanal	28	42	64
phenol	18	24	40
acetophenone	4.3	6.8	9.4
Terpenoids (Biogenic Compounds)			
isoprene	33	57	95
alpha-pinene	10	18	32
d-limonene	6.6	11	22
nopinone	2.2	4.0	8.2
alpha-thujene	1.4	2.0	3.5
camphene	2.1	3.1	5.8
sabinene	1.4	2.6	5.2
beta-myrcene	2.2	4.6	17
beta-pinene	1.1	1.8	3.3
d3-carene	5.1	7.9	14
trans-beta-ocimene	0.8	1.4	3.4
gamma-terpinene	0.5	0.9	1.5
Halogenated Species			
chloroform	42	48	60
tetrachloroethylene	6.9	9.4	15
1,1-dichloroethene	6.4	8.1	10
cis-1,2-dichloroethylene	5.1	9.0	13
1,2-dichloroethane	44	53	66
trichloroethylene	2.5	3.7	6.2
1,2-dichloropropane	5.2	7.2	11
trans-1,3-dichloropropene	3.4	5.3	9.2
cis-1,3-dichloropropene	3.9	6.7	10
1,3-dichlorobenzene	1.8	2.8	4.6
para-chlorobenzotrifluoride	2.8	4.8	8.2
Sulfur-containing Species			
carbon disulfide	18	28	42
Ethanethiol	11	19	57

O_3 and other greenhouse gases: Ozone was measured with a UV ozone monitor (1008 DASIBI Environmental). Carbon monoxide (CO) was measured via gas filter correlation infrared spectroscopy (Teledyne Inc.) and also by off-axis integrated cavity output spectroscopy (Los Gatos Research, N_2O/CO Analyzer). Carbon dioxide (CO_2) was measured via integrated cavity output spectroscopy (Los Gatos Research, Fast Greenhouse Gas Analyzer). In addition to the CO and CO_2 measurements contracted, we also measured methane (CH_4) and nitrous oxide (N_2O) (Los Gatos Research, Fast Greenhouse Gas Analyzer and N_2O/CO Analyzer, respectively). All data have been made available through the online site at 1- and 30-minute measurement intervals. Air for these measurements was sampled at the top of the 18 m tower through Teflon inlets that each contained a Teflon filter (PFA holder, PTFE membrane, pore size 2μm) to

remove particulate matter from the gas stream. Air was sampled at 18 m to be coincident with most other gas-phase measurements made on the CalNex-SJV tower. The filters were replaced weekly to avoid contamination or flow problems. All measurements were made in trailers at ground level and sample lines were constructed of Teflon.

O_3 observations during the CalNex-SJV study period (May 18–June 29, 2010) were slightly lower on average than recent years due to mild weather early in the campaign, but concentrations still exceeded the California 70 ppb 8-hour standard several times throughout the study period (Figure 2.3).

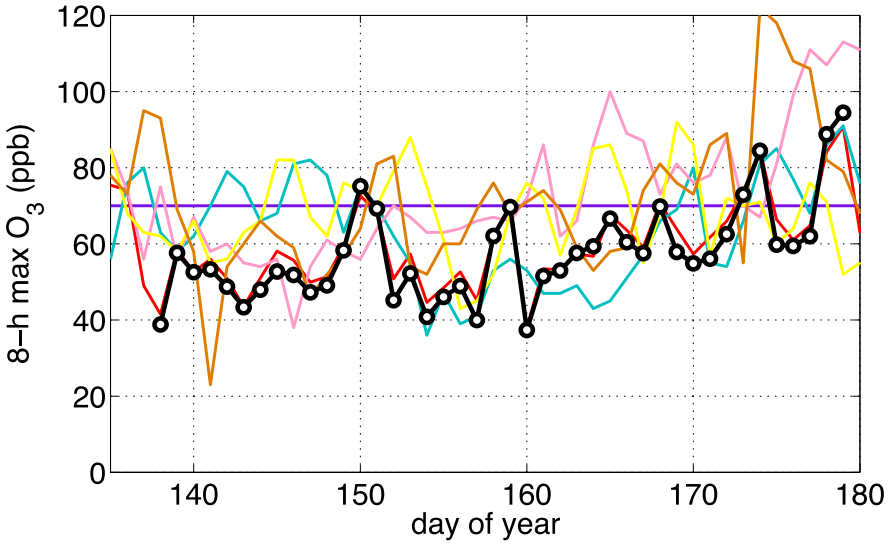

Figure 2.3. *Observed daily 8-hr ozone maxima for the CalNex-SJV study period compared to historical data from the Edison monitoring station for 2006 (orange), 2007 (yellow), 2008 (pink), 2009 (turquoise), and 2010 (red). We note that there were many forest fires in 2008. The purple line is the California 8-hr standard of 70.4 ppb and the daily 8-hr O_3 maxima at the CalNex site in 2010 are shown in black. The ozone concentrations at the CalNex and Edison sites tracked each other closely during 2010.*

Meteorological parameters: The measured environmental variables included windspeed and direction (R.M. Young model 5305), photosynthetically active radiation (Li-Cor Inc.), barometric pressure (Campbell Scientific Inc. CS105), air temperature and relative humidity (Vaisala Inc.). These data were measured at the top of the 18 m tower and recorded using dataloggers (CR10x and CR5000, Campbell Scientific Inc.). All data have been reported at both 1 min and 30 min intervals.

2.3. Brune (Penn State)

Hydroxyl (OH), hydroperoxyl (HO_2), and OH reactivity: OH, HO_2, and OH reactivity were measured by the Penn State research group during CALNEX. Measurements were recorded for approximately 70% of the time between 16 May and 29 June and have been reported to the CalNex-SJV archive. These measurements are described in detail in elsewhere (Kovacs et al.,

2001; Ren et al., 2003a; Faloona et al., 2004; Martinez et al., 2004; Ren et al., 2004; Kang et al., 2007) and are described as they were specifically made during CalNex here.

GTHOS: The Ground-based Tropospheric Hydrogen Oxides Sensor GTHOS uses laser-induced fluorescence (LIF) to measure OH and HO_2 simultaneously. The instrument consists of three parts: a detection system, which is mounted on top of the scaffolding tower; and the electronics and laser, which reside in a trailer at the base of the tower; and a vacuum pumping system that resides at the base of the tower. The detection system is connected to the ground-based systems with electronic cables, optical fibers, and a vacuum hose.

OH is both excited and detected with the $A^2\Sigma^+$ (v'=0) $\rightarrow$ $X^2\Pi$ (v"=0) transition near 308 nm. HO_2 is reacted with reagent NO to form OH and is then detected with LIF. The laser is tuned on and off the OH wavelength to determine the fluorescence and background signals. The sampled air stream is pulled by a vacuum pump through a small inlet, down a sampling tube, and into two low-pressure detection cells - the first for OH and the second for HO_2. Detection occurs in each cell at the intersection of the airflow, the laser beam, and the detector field-of-view. ATHOS is absolutely calibrated in the laboratory and during the mission, as given in the table below. OH is be detected a second way with the periodic addition of perfluoropropene to remove all the OH while leaving a background signal unchanged. Tests have shown that this second method gives the true OH.

OH reactivity measurement: The OH reactivity is the sum of the product of the concentrations of all atmospheric constituents that react with OH and their reaction rate coefficients. It is measured directly by pulling the ambient air at a known velocity through a cylinder. An OH detection system, similar to the one used in ATHOS, protrudes into the cylinder near its end. A few pptv of OH is added to the ambient air through a probe that moves along the cylinder's axis. As the probe is pulled back, the reaction distance and time increases and the OH decreases as it reacts. The slope of the logarithm of OH versus time gives the OH reactivity (s^{-1}).

GTHOS and OH Reactivity Measurement Characteristics			
measurement	minimum integration time	limit-of-detection	accuracy (2σ. 1 minute)
OH	20 s	0.01 pptv	± 32 %
HO_2	0.2 s to 20 s	0.1 pptv	± 32 %
OH reactivity	20 s	about < 1 s^{-1}	about ± 15 %

Measurement analysis: The OH and HO_2 measurements have been compared to a photochemical box model that is constrained by the other measurements. Generally the measured OH and HO_2 are significantly less than the modeled OH and HO_2. On the other hand, the measured OH reactivity is much greater than the OH calculated from the measurements of chemicals that react with OH. The reason for these differences is not clear, but we are reviewing our calibrations for CalNex to make sure that they are consistent with calibrations from other studies and that the instruments were operating normally.

For the analysis, the comparison of modeled and measured OH, HO_2, and OH reactivity were separated into two distinct periods: a cool period (May 24–May 30, 2010) and a warm period (June 16–June 24, 2010) (Figure 2.4). During the cool period, the measured OH and HO_2 are

much lower than the modelled values for the area. During the warm period, the measured OH and HO_2 values increased, but are still far lower than the modelled values for the region and time of year. While the measured and modelled HO_2 agree within the uncertainties of the measurement and model, the modelled OH is significantly greater than measured, a factor of three in the warm period.

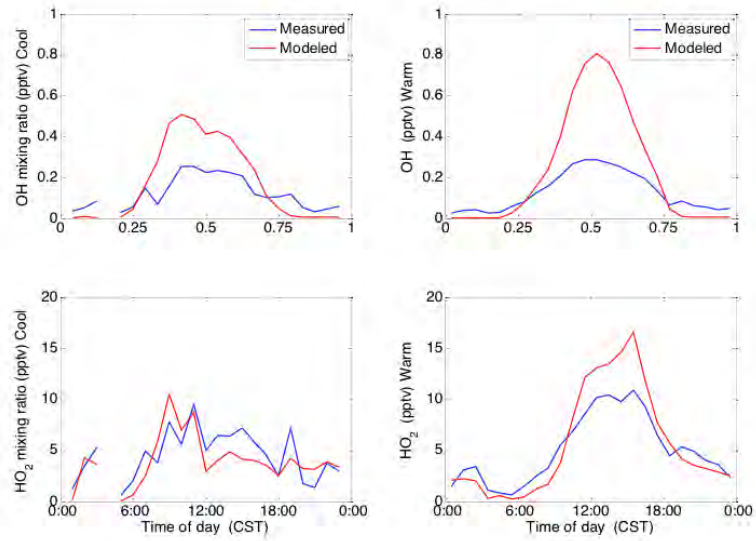

Figure 2.4. *Diurnal averages of measured* ***(blue lines)*** *and modeled* ***(red lines)*** *OH and HO_2 during a cool period (May 24–May 30, 2010), on the left, and a warm period (June 16–June 24, 2010), on the right. Modeled and measured values are averaged over all days in each period for each hour of the day (PST).*

Measured OH being much smaller than modelled OH is not what is typically seen with our instrument. In Nashville (Martinez et al., 2003), Houston, New York City (Ren et al., 2003b; Ren et al., 2003c; Ren et al., 2006), and Mexico City (Shirley et al., 2006), measured median midday OH and HO_2 were typically 1.3-1.5 times larger than modelled values. One significant difference between the CalNex-SJV site and the other sites is the amount of local sources of NO. In CalNex, NO spikes from vehicles are frequent all during the day, while at the other sites the midday NO was typically low with fewer spikes. Since the NO data were averaged into 10-minute bins for the model, this averaging of spikes could be affecting the comparison with the measured OH and HO_2. We will investigate this possibility with model runs for which NO spikes have been considered.

The measured OH reactivity can be compared to the OH reactivity calculated from the sum of all the measured species that react with OH and from the sum of all the modelled species that react with OH (Figure 2.5). The measured OH reactivity during the cool period was ~5 s^{-1} at midday and 15–25 s^{-1} at night (Figure 2.5 top panel). During the warm period, the measured OH reactivity values were ~10 s^{-1} at midday and 20–25 s^{-1} at night (Figure 2.5 bottom panel). In the cool period, the measured OH reactivity agrees well with that calculated from observed chemical and modelled species during midday. In the warm period the OH reactivity is twice that calculated from observed VOC, NO_x, and other species during midday. At night, the measured and calculated OH reactivity agree for the warm period, but for the cool period the calculated value is much greater than the measured OH reactivity at night. Further, the calculated OH reactivity is greater than the measured OH reactivity at morning rush hour. These latter two are

consistent with an effect of NO_x plumes, or high NO_x, on the observations that is not fully understood. In general, the agreement between measured OH reactivity and that calculated from measurements is not as good as has been observed in other U.S. cities (Kovacs et al., 2003).

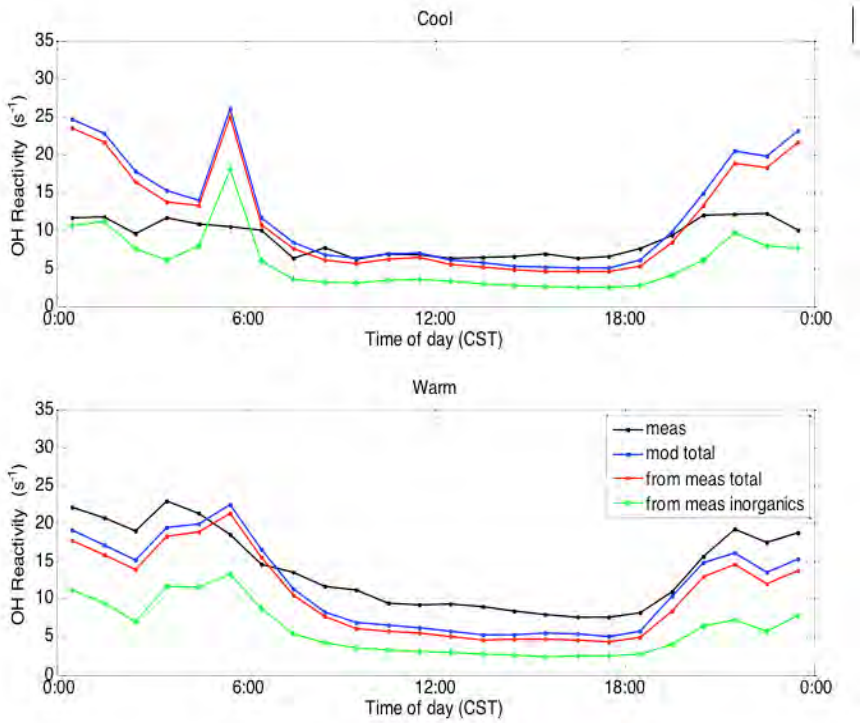

Figure 2.5. *Diurnal average of the measured* ***(black lines)*** *OH reactivity (s^{-1}) and the calculated OH reactivity from the sum of all the modelled species that react with OH* ***(blue lines)*** *during the cool period (May 24–May 30, 2010), on the top, and warm period (June 16–June 24, 2010), on the bottom. Additionally, the red lines show the OH reactivity calculated from the measured species that react with OH and the green lines show the OH reactivity calculated from the inorganics that react with OH. CST stands for California standard time.*

OH should be in steady state so that the OH production rate equals the OH loss rate. The OH loss rate is the product of [OH] and the OH reactivity and thus is measured. The OH production comes from primary sources and from the recycling of $HO_2 + NO \rightarrow OH + NO_2$. Measured OH loss and measured OH production from $HO_2 + NO$ is illustrated for one day (Figure 2.6). For some time periods, OH production and loss are equal, but at other times, the two are not in balance. At night, OH loss appears to exceed OH production, suggesting that some sources are missing. However, OH production is greater than OH loss when NO is high. This imbalance, which has been seen at other sites, is difficult to understand, since the OH source must be at minimum the cycling through HO_2. Thus, this imbalance suggests that the NO_2 + OH correction applied to the OH reactivity data may not be sufficient and will be rechecked.

The high variability of NO and NO_2 during CalNex-SJV provided a challenge for comparing measured and modelled OH, HO_2, and OH reactivity. However, it also provides an opportunity to examine the dependence of the model and the measurements to this high variability. Examining these interactions will be a focus of our on-going research.

The initial analysis has raised several issues that require more investigative work. The first is the large discrepancy between the measured and modeled OH. It is likely that this large discrepancy is due to the frequent NO spikes that were averaged in the model. This possible cause of the difference will be investigated by removing the measurements for NO spikes from the data before averaging. The second issue is the surprising disagreement between the measured and calculated OH reactivity, a disagreement that has not been seen in other cities. A comparison of the OH production rate and OH loss rate as a function of NO suggests that the NO correction being used for the OH reactivity measurement is incorrect. This correction is necessary because the reaction of HO_2 + NO to produce OH and NO_2 recycles HO_x to OH and thus affects the measured OH decay in the OH reactivity instrument. Once the correction has been tested and improved, a new version of the OH reactivity data will be generated and submitted to the archive.

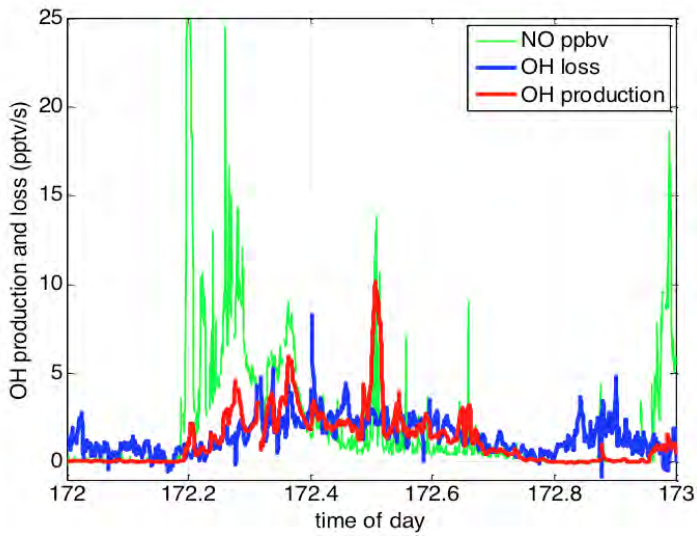

Figure 2.6. *Measured OH loss* ***(red line)*** *and OH production by HO_2 +NO only* ***(blue line)*** *in ppbv hr^{-1}, and NO (green line) on June 21, 2010.*

2.4. Keutsch (University of Wisconsin-Madison)

Formaldehyde, glyoxal, and larger α-dicarbonyls: The Keutsch team prepared the instruments for measurement of formaldehyde (CH_2O), glyoxal (CHOCHO), and larger α-dicarbonyls, conducted extensive calibrations of instruments prior to the CalNex-SJV campaign, and conducted tests for interferences prior to and during the CalNex-SJV campaign. Calibrations were conducted every six days during the CalNex-SJV campaign as well as after. Calibration factors for both instruments were constant across the entire campaign. The Keutsch team participated in science planning discussion based on our experience from previous ground-based experiments, including BEARPEX, CA. We also participated in the CalNex Science meeting in May 2011 in Sacramento, CA.

The final data set is complete and has been submitted to the data archive. Both instruments have similar operating principals: Ambient air is drawn into the measurement cell through PFA (formaldehyde) or PTFE (glyoxal) inlets at a high flow rate (30 and 10 standard liters per minute

for glyoxal and formaldehyde, respectively). The measurement cell is maintained at a constant pressure of 100 Torr and exposed to laser radiation that is tuned between wavelengths of a strong and weak absorption feature. As other molecules in this wavelength range do not have structured absorptions, the method is selective to glyoxal/formaldehyde. The excited molecules luminesce with a characteric lifetime and wavelength. Use of band-pass filters and time-gated detection further improves the selectivity and detection limit as broadband emission and background counts are minimized. The sensitity of the instrument to glyoxal/formaldehyde, i.e., the detected signal per ppt, is determined via calibrations with a gas standard taking the incident laser power into account. This calibration factor is used to convert the laser power-normalized difference in luminescence counts between the high and low absorption wavelength into mixing ratios. Both instruments are highly selective with no known interferences and have low detection limits (3σ) of better than 15 ppt in one minute for glyoxal and 50 ppt in one minute for formaldehyde. For additional instrumental details see Hottle et al. (2009) and Huisman et al. (2008) for formaldehyde measurements by laser induced fluorescence and glyoxal measurements by laser induced phosphorescence, respectively.

2.5. Thornton (University of Washington)

Acyl peroxy nitrates (UW-APN): The University of Washington successfully met the goals set out in the original proposal to ARB. We made nearly continuous speciated acyl peroxy nitrate concentration measurements at the Bakersfield, CA site from May 19–June 22, 2010. Measurements were conducted outside of these dates as well, but after quality control processing of the data, we determined they were not suitable for consideration. Sara Harrold, a graduate student in the Department of Atmospheric Sciences at the University of Washington led the deployment and operation of the Thermal Dissociation Chemical Ionization Mass Spectrometer (TD-CIMS) used to measure acyl peroxy nitrates concentrations. Ambient air was continuously drawn from the top of the 18-m tall scaffolding through 1 cm OD Teflon tubing at approximately 20 standard liters per minute by means of an auxiliary diaphragm pump. Approximately 10% of this flow was sampled through a critical orifice at the inlet of the TD-CIMS into a 20 cm length of 1.5 cm OD PFA tube heated to 180°C to thermally decompose peroxy acyl nitrates into their corresponding acyl peroxy radicals ($RC(O)O_2$) and nitrogen dioxide. The peroxy radicals were then detected by iodide chemical ionization, which converts acyl peroxy radicals to carboxylate anions ($RC(O)O^-$); these ions are then mass selected and counted with a quadrupole mass spectrometer. Online calibrations were performed using with C-12 and C-13 labeled PAN synthesized continuously, and instrument zeros were determined every 30 minutes by adding sufficient nitric oxide to the heated inlet for titration of the acyl peroxy radicals prior to ionization.

We have posted quality controlled 30-minute average data for peroxy acetyl nitrate (PAN) and propionyl peroxy nitrate (PPN) to the data archive. We note in our data files that faster time resolution data and methyl peroxy acetyl nitrate (MPAN) concentration estimates are available upon request. The configuration of the instrument during the CalNex-SJV intensive was slightly different than previous deployments, leading to higher uncertainty regarding the calibration to MPAN, which could not be tested in the field. As such, we are more cautious about the viability of this particular measurement. That said, the large data set available in PAN and PPN will allow several interesting questions to be addressed in that PPN is derived primarily from the *in situ*

atmospheric oxidation of anthropogenic hydrocarbons while PAN is derived from the oxidation of both anthropogenic and biogenic hydrocarbons. In particular, these characteristics allow for testing for the influence of anthropogenic VOC on ozone formation and nitrate formation and for whether regional scale air quality models adequately capture the oxidation of biogenic VOC to important intermediates such as the peroxy acetyl radical. We note that this data has already been compared against results from a regional air quality modeling study (Cai et al., 2011).

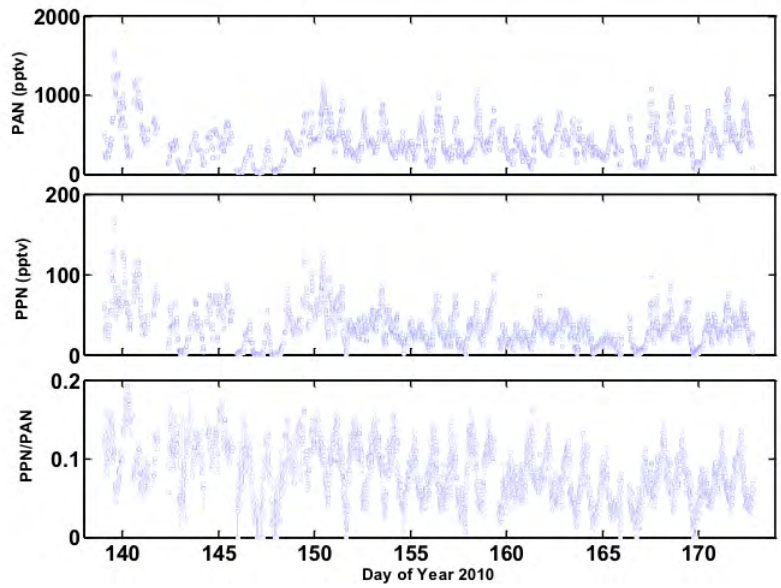

Figure 2.7. *Time series of UW PAN* ***(top)*** *and PPN* ***(middle)*** *measurements during the CalNex-SJV intensive in Bakersfield. Also included is the PPN/PAN ratio* ***(bottom)****.*

Consistent with this site being near an urban area with exposure to pollution sources, PAN concentrations routinely exceeded 1 ppbv throughout the measurement period (Figure 2.7). The maximum PAN mixing ratio reached was 1500 pptv and the mean over the entire period was 400 pptv. During June and July, 2009 we measured a mean PAN mixing ratio of 300 pptv and a maximum of 1600 pptv in the Sierra Nevada foothills, 75 km downwind of Sacramento (Blodgett Forest). These are remarkably similar concentrations for being in such different environments. The maximum PPN mixing ratio at the Bakersfield site was 170 pptv, with a mean of 30 pptv; while at Blodgett Forest a similar maximum PPN was detected while the mean was 20 pptv. While similar in absolute magnitude between these two locations, the detailed relationships between PAN and PPN were quite different. PAN and PPN at the Bakersfield site both displayed a diel pattern typical of photochemical products, with maxima during the day and minima at night, which is pronounced even in the full time series. PAN and PPN were broadly correlated over the entire time series as expected in that they both require VOC oxidation in the presence of NO_x, but their relationship varied reproducibly on an hourly timescale most likely reflecting the differences in VOC precursors. For example, the ratio of PPN to PAN exhibits a diel cycle, reaching a minimum in late afternoon, and a maximum during the night. Synoptic variation in air mass origin is also evident over the month long measurement period, bringing at times air with very low PAN and PPN mixing ratios characteristic of the remote Pacific Ocean. There appears to be a general trend over the course of the measurement period of increasing influence from biogenic hydrocarbons in that the PPN/PAN ratio decreases on average over this

time from ~0.15 to 0.09. In contrast, at Blodgett Forest, the PPN/PAN ratio lacked as pronounced diel cycle and the mean and maximum PPN/PAN ratios were both significantly lower than at Bakersfield, consistent with a greater biogenic contribution to VOC reactivity on average upwind of Blodgett Forest.

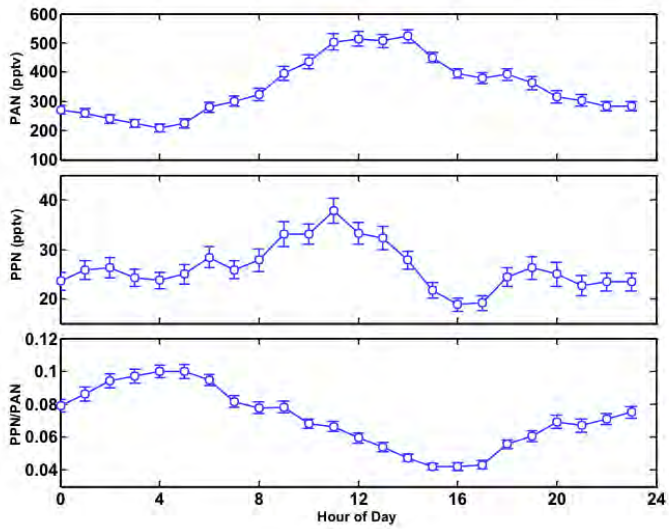

Figure 2.8. *Hourly mean values of PAN* ***(top)*** *and PPN* ***(middle)*** *mixing ratios, and the PPN/PAN ratio* ***(bottom)*** *during the CalNex-SJV intensive in Bakersfield, CA.*

The mean diel cycles of PAN, PPN, and the ratio of PPN/PAN also appear consistent with expectations (Figure 2.8). PAN shows a minimum in the early morning hours and a pronounced daily maximum peaking between 10am and 2pm local time. PPN peaks late in the morning, around 11am and then falls sharply through the afternoon, reaching a minimum on average around 4pm local time. A secondary maximum is reached between 6 and 8pm. This behavior would seem well-aligned with a photochemical product of alkane oxidation with morning and afternoon rush hours contributing the necessary precursors. As a result of these contrasting behaviors, the PPN/PAN ratio maximizes in the early morning hours and reaches a minimum in late afternoon. The implication being that for a substantial portion of the morning, alkanes contribute significantly to OH reactivity, while in the late afternoon, oxidation of biogenic VOC or at least hydrocarbons that when oxidized do not lead to propionyl peroxy radicals, are more important. Interestingly, these behaviors are somewhat different than those observed at Blodgett Forest, for which most of the daytime, biogenic VOC were the dominant source of acyl peroxy nitrate precursors. These aspects deserve further investigation.

An additional goal of the UW APN measurements was to provide speciation for context and assessment of the UC-Berkeley sum total peroxy nitrate measurements (PNs). There was generally good correlation between the sum of PAN and PPN, and the total PNs with a correlation coefficient of 0.73 (Figure 2.9 left). On average the PNs measurement was greater than the sum of PAN and PPN suggesting a significant contribution of peroxy nitrates other than PAN and PPN, which could include MPAN, HO_2NO_2, $CH_3O_2NO_2$, hydroxy peroxy acetyl nitrate (HPAN), etc. The bias between the sum of PAN and PPN with the total PNs measurement exhibits a weak negative correlation with temperature and a weak positive correlation with NO_2.

The poor correlation of the difference with other constituents or environmental parameters makes it difficult to attribute the source of this bias to any particular peroxy nitrate. A higher quality MPAN measurement would possibly help explain some of the bias, but at Blodgett Forest, strongly impacted by isoprene oxidation products, MPAN rarely exceeded 15% of PAN concentrations. This is a larger discrepancy than is usually observed between speciated peroxy nitrates and ΣPNs measured by TD-LIF, where these measurements frequently agree to within 10% (Wooldridge et al., 2011). An analysis of the diurnal profiles of the UW CIMS speciated peroxy nitrates and ΣPNs shows that in the afternoon and evening the two observations are nearly equal (Figure 2.9 right) and that ΣPNs see larger mixing ratios in the morning and at noontime. At this time we do not understand the source of the observed difference. We are confident ΣANs and HNO_3 are not measured in the ΣPNs channel.

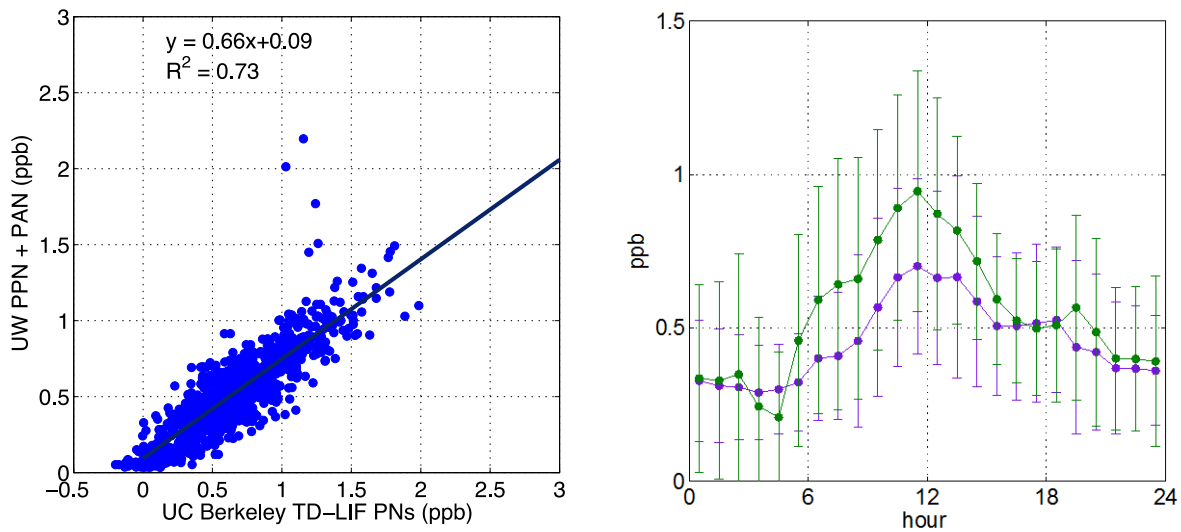

Figure 2.9. *Comparison of UW and UC-Berkeley measurements of peroxy nitrates.* ***Left:*** *The sum of PAN and PPN mixing ratios measured by UW is plotted versus the total peroxy nitrate mixing ratio measured by UC Berkeley.* ***Right:*** *Diurnal profiles of ΣPNs* ***(green)*** *and the sum of PAN and PPN* ***(purple)****.*

2.6. Wennberg (California Institute of Technology)

H_2O_2, HNO_3, acetic acid, formic acid, and HCN: The CIT-CIMS instruments (Crounse et al., 2006) provided data for hydrogen peroxide (H_2O_2), nitric acid (HNO_3), acetic acid, formic acid, and hydrogen cyanide (HCN) for CalNex-SJV. The CIT-CIMs uses the following ion chemistry: $CF_3O^- + HA \rightarrow HF \cdot A^-$ or $CF_3O^- + HB \rightarrow CF_3O^- \cdot HB$, where HA and HB are the target analytes. The product ion (either $HF \cdot A^-$ or $CF_3O^- \cdot HB$) for a given analyte depends on the acidity (or fluoride affinity) of the analyte. This instrument has been used at ground-based field locations in urban and rural environments and was operated in the same way as during the BEARPEX project in 2009 (e.g., Beaver et al., 2012). Calibrations were conducted every hour and performed by standard addition of analytes derived from permeation tubes. Measurements are reported as 0.5 s integration periods every 10 to 15 s, depending on the number of species that are being monitored. Detection limits are determined by instrument background level and

sensitivity are ~20-50 pptv for most species monitored. Data are corrected for sensitivity changes due to variations in water vapor. The data posted to the archive span the dates May 21–June 28, 2010 and are shown in Figure 2.10 for the acids, with minor gaps in data coverage due to instrument downtime or inclement weather. The CIT-CIMS instrument team contributed to science planning discussions for the CalNex-SJV site.

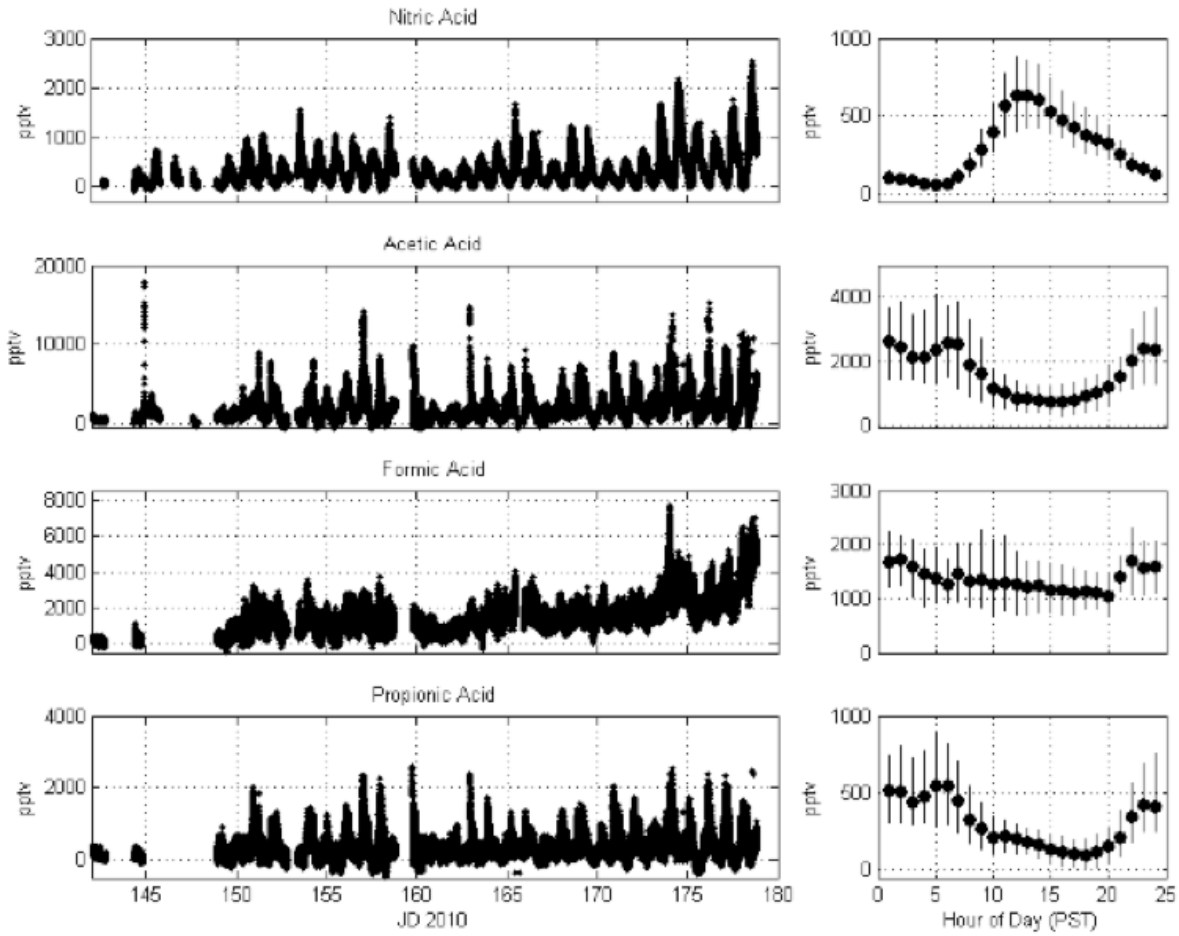

Figure 2.10. *Time series and diurnal means of inorganic and organic acids measured during CalNex-SJV in Bakersfield, CA (JD 145 is May 25). The diurnal profiles are shown as the campaign median with the inter-quartile ranges.*

Observations of acetic and formic acids indicate a substantial source of these organic acids in the San Joaquin Valley, most likely from agriculture (Ngwabie et al., 2008; Alanis et al., 2010). The measured concentrations of these acids are the highest ever measured by the Caltech group. The highest acetic acid mixing ratios occurred when the wind was coming from the south, usually at night. Figure 2.11 displays how the relationship between acetic acid and formic acid changes from daytime to nighttime. At night, the correlation between the two species is variable. During the day, however, the acetic acid mixing ratios are lower and highly correlated with formic acid, suggesting a common daytime source for the two acids. CO_2 can be used as a marker for depth of the nighttime boundary layer (e.g., Newman et al., 2013), and it correlates well with the nighttime acetic acid mixing ratio.

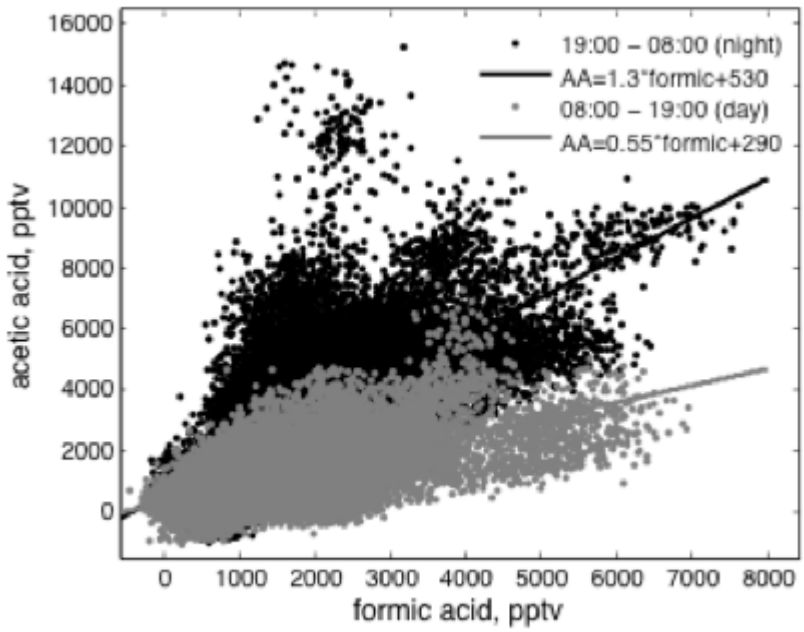

Figure 2.11. *Acetic (AA) and formic acid (FA) are shown during the hours of 19:00–08:00* ***(black)*** *and 08:00–19:00* ***(gray)****.*

The CIT-CIMS measurement of HNO_3 enables the study of the ammonia-nitric acid-ammonium nitrate system in the SJV, one of the key goals of the measurement campaign. Figure 2.12 shows good agreement between the UC-Berkeley HNO_3 (gas + particle) measurement and the sum of the CIT-CIMS HNO_3 (gas) and the University of Toronto NO_3^- (particle) measurements (J. Murphy). The CIT-CIMS and U. Toronto measurements of gas phase HNO_3 correlate well but with a slope of 0.4 (not shown). The disagreement may reflect the different sampling heights and a vertical gradient in HNO_3: the CIT-CIMS sampled at 18 m and the U. Toronto IC sampled at 4 m (the 18 m height was for gas-phase sampling and the 4 m height was for aerosol sampling). Understanding these measurements is a goal of this work. Analysis is in progress but not yet completed.

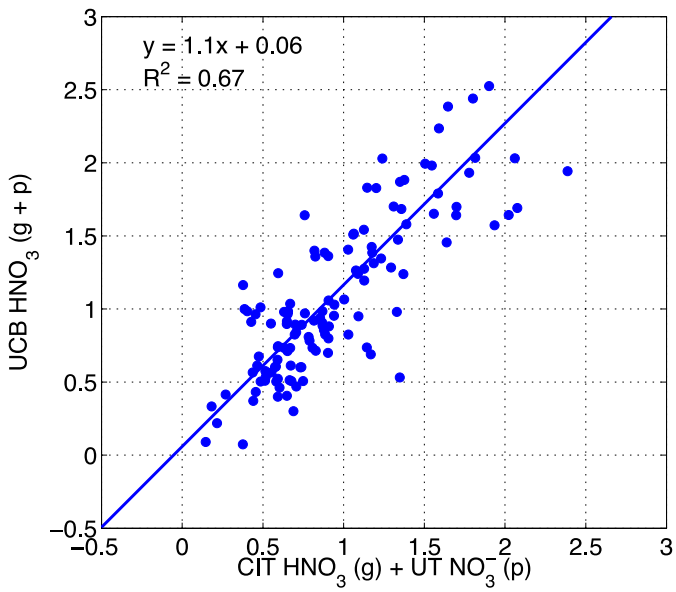

Figure 2.12. *UCB HNO_3 measurement (gas + particle) shown versus gas phase (CIT CIMS)+ particle phase (UT IC) HNO_3 measurements (9 AM–7PM).*

The CIT-CIMS HCN data allow the evaluation of the biomass burning contribution to the chemistry at the site, particularly in conjunction with the burn authorization information provided by the San Joaquin Valley Air Pollution Control District. Figure 2.13 shows the relationship between the CIT-CIMS HCN data (averaged to 1 minute) and the LGR CO data. The green solid line indicates a fit to the data, and the blue (dash) and red (dash-dot) lines utilize enhancement ratios from Mexico City data for anthropogenic and biomass burning sources, respectively (Yokelson et al., 2007; Crounse et al., 2009). The data suggest biomass burning is an important source in the SJV.

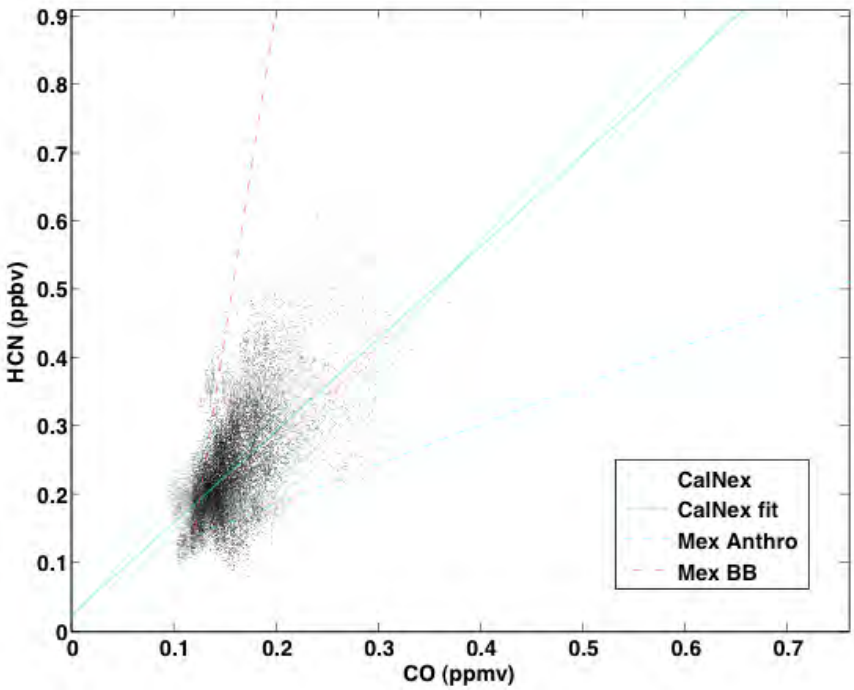

Figure 2.13. *HCN versus CO concentration plot (both 1-minute averages). Fit to data* ***(green solid line)*** *is also shown. Trends using enhancement ratios for anthropogenic* ***(blue dash)*** *and biomass burning* ***(red dash-dot)*** *from Mexico City are also shown.*

3. Data Analyses

3.1. On the observed response of ozone to NO_x and VOC reactivity reductions in San Joaquin Valley California 1995–present

Reproduced from: S. E. Pusede and R. C. Cohen (2012) On the observed response of ozone to NO_x and VOC reductions in San Joaquin Valley California 1995–present, Atmos. Chem. Phys., 12, 8323-8339.

CalNex study topics addressed: *sources of NO_x and VOC, HO_x photochemistry, role of VOCs, SJVAB vs. SoCAB O_3 precursors.*

Abstract: We describe the effects of nitrogen oxide (NO_x) and organic reactivity reductions on the frequency of high ozone days in California's San Joaquin Valley. We use sixteen years of observations of ozone, nitrogen oxides, and temperature at sites upwind, within, and downwind of three cities to assess the probability of exceeding the California 8-hour average ozone standard of 70.4 ppb at each location. The comprehensive data records in the region and the steep decreases in emissions over the last decade are sufficient to constrain the relative import of NO_x and organic reactivity reductions on the frequency of violations. We show that high ozone has a large component that is due to local production, as the probability of exceeding the state standard is lowest for each city at the upwind site, increases in the city center, is highest at downwind locations, and then decreases at the receptor city to the south. We see that reductions in organic reactivity have been very effective in the central and northern regions of the San Joaquin but less so in the southern portion of the Valley. We find evidence for two distinct categories of reactivity sources: one source that has decreased and dominates at moderate temperatures, and a second source that dominates at high temperatures, particularly in the southern San Joaquin, and has not changed over the last twelve years. We show that NO_x reductions are already effective or are poised to become so in the southern and central Valley, where violations are most frequent, as conditions in these regions have or are transitioning to NO_x-limited chemistry when temperatures are hottest and high ozone most probable.

3.1.1. Introduction

Ozone formation is a nonlinear function of nitrogen oxides (NO_x) and the reactivity of gas phase organic molecules and consequently, reductions in the emissions of these precursors can decrease, increase, or leave unchanged the rate of ozone production. Emissions control policies aimed at improving ozone (O_3) air quality therefore require sufficient information on how the chemical system at a given location will respond to reductions in precursor concentrations. Over the last decade there have been dramatic reductions in NO_x concentrations across North America and Europe (e.g., Richter et al., 2005; Kim et al., 2006; Stavrakou et al., 2008; van der A et al., 2008; Kim et al., 2009; Konovalov et al., 2010; Russell et al., 2010; Russell et al., 2012). At many locations there are reports of decreases in organic emissions (e.g., Environmental Protection Agency, 2003; Parrish, 2006; Bishop and Stedman, 2008; Monks et al., 2009; Wilson et al., 2012) but changes to the total organic reactivity are not well documented. These precursor changes are predicted to have substantially affected the photochemical ozone production rate and thus the probability of exceeding health-based standards. Reports of improved air quality are

mixed and there has been little success in attributing quantitative measures of changes in ozone concentrations to the reductions of specific emissions.

A variety of observational and modeling approaches have been used to evaluate ozone's sensitivity to NO_x and organic reactivity. These include analyses of ratios of peroxides to nitric acid (e.g., Sillman et al. 1995; Sillman et al., 1997), relationships between measured nitrogen oxides and organic molecules (e.g., Kleinman et al., 2000; Trainer et al., 2000; Martin et al., 2004; Kleinman et al., 2005; Stephens et al., 2008; Pollack et al., 2012), rates of ozone production derived from observed reactant concentrations (e.g., Thornton, et al., 2002; Martinez et al., 2003; Ren et al., 2003), and, very recently, the direct measurement of the instantaneous ozone formation rate (Cazorla and Brune, 2010; Cazorla et al., 2012). These methods each work to constrain the chemistry of ozone production at the specific local NO_x and organic reactivity. Predictions of the effects of emissions reductions are usually based on models that hindcast a small subset of historical high ozone episodes. These studies typically implement a given percentage reduction in NO_x and/or organic emissions and calculate whether O_3 would have indeed been reduced during that episode. However, the short-time and/or limited-spatial scales of these measurement and modeling analyses make it difficult to assess the accuracy of the predictions. For example, we know of no case where a quantitative prediction of the reduction in the number of annual violations of a health-based standard was made in advance of a policy and then explicitly verified with observations after the fact.

Growth in the observational database and the increase in computational power have made it possible to think about ozone statistics over wide regions of space and over long periods of time instead of focusing on individual episodes. For example, Gilliland et al. (2008) examined models and observations before and after implementation of controls on the electric generating utilities in the eastern U.S. and used the ensemble to suggest that air quality models underestimated the benefits of the NO_x reductions. In this paper, we describe changes in the frequency of high ozone days and show that the existing routine observations of O_3, nitrogen oxides, and temperature can provide direct insight into the probabilistic response of ozone to emission reductions. We develop our methodology using the example of California's San Joaquin Valley (SJV), a region competing with the Los Angeles basin for the most frequent number of high ozone days in the U.S. (American Lung Association, 2011) and where ambient O_3 concentrations persistently violate health-based air quality standards (Cox et al., 2009) despite sustained scientific attention (Venkatram et al., 1994; Andreani-Aksoyoglu et al., 2001; Marr et al., 2002a; Marr et al., 2002b; Steiner et al., 2006; Steiner et al., 2008; Lin et al., 2008; Howard et al., 2008; Howard et al., 2010a; Howard et al., 2010b; Hu et al., 2012) and regulatory efforts at both the local (e.g., San Joaquin Valley Air Pollution Control District, 2007) and state level (California Air Resources Board, 2011). We use the results from our statistical approach to make policy-relevant conclusions about how the frequency of high O_3 in the SJV will respond to future NO_x and organic reactivity emissions reductions. We note that the data to support this type of analysis are available at many locations in North America and Europe.

3.1.2. Conceptual framework

3.1.2.1. Ozone production

Photochemical ozone production results from a pair of catalytic cycles initiated by creation of odd-hydrogen (OH or HO_2) or organic peroxy radicals (RO_2), collectively referred to as HO_x

($HO_x \equiv OH + HO_2 + RO_2$) (Fig. 3.1.1). Entering the HO_x cycle, a generic organic molecule is oxidized by OH, forming RO_2, then HO_2, and subsequently regenerating OH (Fig. 3.1.1a). This cycle drives the oxidation of NO to NO_2 twice (Fig. 3.1.1b). The photolysis of NO_2 is rapid and the product oxygen atom combines with O_2 to yield O_3. During the daytime, HO_x chain lengths are long enough that the ratio of HO_2 to RO_2 is near one.

Figure 3.1.1. *Schematic of photochemical production of two new O_3 molecules from the oxidation of one generic organic molecule at the overlap of the HO_x* ***(a)*** *and NO_x* ***(b)*** *catalytic cycles. Only the NO_x termination channels are shown. HO_x chain terminations are reactions among peroxy radicals and OH.*

Fig. 3.1.2 shows the nonlinear dependence of the instantaneous rate of O_3 production (PO_3) on NO_x (NO_2 + NO) and the organic reactivity (VOCR). Moving left to right, i.e., from a scenario of remote continental to urban photochemistry, PO_3 grows steeply with increasing NO_x abundance, reaches a peak, and then decreases with continued NO_x increases. This initial rise results from NO_x's role as modulator of the ($HO_2 + RO_2$) to OH ratio. At low NO_x, adding NO enhances OH via reactions between NO and HO_2 or RO_2, and thereby the oxidation rate of organic molecules (NO_x-limited chemistry). Because OH is typically 100 times less abundant than HO_2 or RO_2, this has little effect on the comparatively large $HO_2 + RO_2$ reservoir. At high NO_x, OH reacts with NO_2 to form nitric acid reducing the HO_x radical pool (NO_x-suppressed chemistry). In the intermediate regime, reactions forming alkyl and peroxy nitrates are important to the absolute rate but do not strongly affect the shape of the curves (Farmer et al., 2011).

Participating organic molecules are commonly referred to as volatile organic compounds (VOCs) distinguishing them from low vapor pressure species that are instead more likely to condense onto aerosol surfaces. The impact of any individual VOC to ozone production depends mainly on its reaction rate with OH (except for a small subset of VOCs that are photolabile); rapidly reacting molecules such as alkenes and aldehydes are disproportionally important compared to less reactive alkanes, acids, and ketones. The rate at which the sum of all VOCs reacts with OH is defined as the VOC reactivity (VOCR). This is a condensed parameter summarizing the integrated effects of the local VOC mixture. In Fig. 3.1.2, we show PO_3 calculated with three different VOCRs: a base case, twice the base VOCR, and three times the base VOCR. Note that

at the left of Fig. 3.1.2 (low NO_x), the VOCR has no effect on the rate of O_3 production, while at the right, PO_3 increases with VOCR almost linearly (VOC-limited chemistry).

Just as decreases in VOCR decrease PO_3, so will reductions in the rate of HO_x production (PHO_x), as a shrinking HO_x pool will slow VOC oxidation rates (not shown). PO_3 scales nearly linearly with PHO_x, its response smaller at low NO_x than high. Net sources of HO_x include the photolysis of O_3, formaldehyde and other aldehydes, nitrous acid, and nitryl chloride, reactions between O_3 and alkenes, and organic radical reactions that amplify rather than merely propagate OH and HO_2. PHO_x and VOCR are linked. For example, formaldehyde is both a primary anthropogenic emission and is an oxidation product of virtually every gas phase organic molecule. Formaldehyde is also reactive with OH and, after oxidation, enters the HO_x cycle at HO_2 formation directly. Emissions reductions targeting formaldehyde and/or any of its precursors will have the combined effect of simultaneously reducing PHO_x and VOCR. In addition, VOC emission controls that improve O_3 air quality will also decrease PHO_x. The photolysis of O_3 is the single largest HO_x source in many locations and lower O_3 concentrations impact PHO_x in a positive feedback resulting in further decreased ozone production rates. That said, in the SJV the average Valley-wide summertime (June–August) 8-hour O_3 has varied by less than 16 ppb in the last twelve years (it was 70.2 ppb in 1999 and 66.4 ppb in 2010). In the analysis that follows, we make no attempt to tease apart the effects of PHO_x from those of VOCR as data do not exist with which to do this; we acknowledge that our "VOCR" likely includes a component due to changes in HO_x sources.

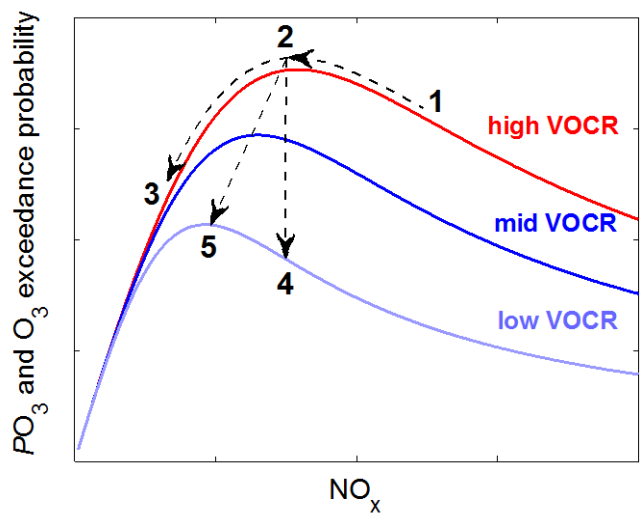

Figure 3.1.2. *The instantaneous ozone production rate (PO_3) and, by analogy the ozone exceedance probability, as a function of NO_x is shown for three categories of organic reactivity (VOCR): high* ***(red)****, mid* ***(blue)****, and low* ***(violet)****. The mid- and high-VOCR curves correspond to scaling the base VOCR by 2 and 3, respectively. If temperature serves as an adequate proxy for VOCR then the three curves will also describe high-* ***(red)****, moderate-* ***(blue)****, and low-* ***(violet)*** *temperature regimes.*

We illustrate the change in ozone production in response to three scenarios of NO_x and/or VOCR reductions with dashed lines in Fig. 3.1.2:

Scenario ***A*** *decreases NO_x at constant VOCR* ***(1 → 2 → 3)***. NO_x reductions initially increase PO_3 at high NO_x **(1 → 2)** followed by a decrease in PO_3 at low NO_x **(2 → 3)**. This scenario

occurs on weekends in locations where dramatic reductions in diesel truck traffic result in lower NO_x emissions alongside small changes in VOCR.

*Scenario **B** decreases VOCR at constant NO_x **(2 → 4)***. VOC reductions have the effect of proportionally reducing PO_3 at high NO_x and of negligibly changing PO_3 at low NO_x. This scenario occurs in regions where NO_x emissions are constant and VOC emissions are exponential with temperature. One such example is in forested regions downwind of cities where VOCR is largely biogenic and higher at hotter temperatures (e.g., LaFranchi et al., 2011).

*Scenario **C** reduces NO_x and VOCR simultaneously **(2 → 5)***. This transition is typical of what has occurred over the last decade in cities where vehicular emissions dominate both NO_x and VOCR.

3.1.2.2. Ozone production, O_3 concentration, and the frequency of high O_3 days

The atmospheric O_3 concentration is a function of the time-integrated effects of PO_3, chemical and depositional loss, and mixing. All of these terms vary and often co-vary. Over the time interval of our study, we expect no significant changes in the chemical or depositional loss terms or in the frequency of stagnation in the SJV. Trends in the mean, median, and width of the distribution of ozone concentrations—observed to be Gaussian in our dataset—are thus dominated by the statistics of changes in PO_3. Moreover, O_3 exceedances varying in the nonlinear manner shown in Fig. 3.1.2, as we will show they do, bolster the notion that production is the principal term changing over time. To make the association between the O_3 concentration and the frequency of high ozone days, we take advantage of the statistical properties of normal distributions. Specifically that the cumulative probability of the portion of a normal distribution above a particular threshold varies linearly with shifts in the mean (assuming the width is constant) so long as the threshold is within one standard deviation of the mean, or between approximately 15% and 85%. On this basis, we hypothesize that the curves representing PO_3 in Fig. 3.1.2 also describe the statistics of high ozone days and use this conceptual framework, which in our analysis we support empirically, to interpret observed changes in the probability of high ozone defined as the fraction of days exceeding the 8-hour O_3 California Ambient Air Quality Standard (CAAQS) of 70 ppb (>70.4 ppb).

3.1.2.3. NO_x

NO_x abundances across California have fallen at near constant rates over the last decade; this is consistent with our understanding of trends in emissions (Cox et al., 2009; Millstein and Harley, 2010; Dallmann and Harley, 2010) and supported by surface measurements (Ban-Weiss et al., 2008; Lafranchi et al., 2011; Parrish et al., 2011) and space-based observations (Kim et al., 2009; Russell et al., 2010, Russell et al., 2012). These NO_x decreases have led to striking improvements in ozone air quality in the Sacramento Valley (Lafranchi et al., 2011) but less so in the Los Angeles basin, where chemistry remains NO_x-suppressed and the dramatic improvements of the 1980s and 1990s have slowed (e.g., Pollack et al., 2012). In the SJV, both satellite NO_2 and the ground-based nitrogen oxide data records indicate steady decreases of approximately 5% per year Valley wide (Russell et al., 2010; Russell et al., 2012).

In addition to long-term reductions, NO_x concentrations have a well known day-of-week dependence. In the SJV, NO_x is typically 30–50% lower on weekends than weekdays, a phenomenon largely due to reduced weekend heavy-duty diesel truck traffic (e.g., Marr et al.,

2002b; Millstein and Harley, 2010). Meteorological and chemical conditions, such as VOCR, are far less day-of-week dependent than are changes in NO_x and, as a result, comparison of weekdays to weekends is an effective and widely used tool to study the NO_x dependence of O_3 formation (e.g., Murphy et al., 2006; Murphy et al., 2007; Stephens et al. 2009; LaFranchi et al., 2011; Pollack et al., 2012).

In this work, we consider both annual and day-of-week NO_x trends comparing curves describing weekday and weekend O_3 CAAQS exceedance probabilities over the past sixteen years. We note that the NO_2 data presented here are obtained by chemiluminescence coupled with a heated molybdenum catalyst, a technique with a known positive interference from the higher oxides of nitrogen (alkyl and peroxy nitrates and nitric acid). We refer to measured "NO_2" as NO_2* hereafter (a more detailed description of all measurements is found in the Appendix). To a reasonable approximation NO_2 is a constant fraction of NO_2* at a given location at a given time of day (Dunlea et al., 2007).

3.1.2.4. VOCR and temperature

Tailpipe emissions from vehicles are only weakly temperature dependent, for example due to the increase in fuel consumption for air conditioning on hot days. By contrast, biogenic VOCs from forests (e.g. Guenther et al., 1993; Schade and Goldstein, 2001) and agriculture (e.g., Ormeño et al., 2010) are emitted as an exponential function of temperature until, for certain species, inhibited by extreme heat. Vapor pressures rise exponentially with temperature and so evaporative emissions, such as from fuels and farm residues, are also strongly temperature dependent (Rubin et al., 2006). Temperature also influences the rates of reaction of organic molecules with OH and of radical cycling, but this effect is much smaller than that due to the increase in VOC abundance (Steiner et al., 2006).

There is evidence for decreases in both the concentrations (Harley et al., 2006) and emissions (Cox et al., 2009) of some VOCs in the SJV over the last twenty years; observations in many locations indicate VOCs and NO_x emissions from passenger vehicles have decreased in tandem (e.g., Parrish et al., 2002; Parrish, 2006). However, how or if these reductions have broadly translated to decreases to total reactivity is not known as measurements not necessarily including VOCR's major components. Observations of VOCR are not generally available because techniques for direct measurement have only recently been developed (Kovacs et al., 2001; Sadanaga et al., 2004a; Sinha et al., 2008; Ingham et al., 2009). The use of these techniques is still limited to large-scale field experiments and at most sites observations of individual VOCs do not add up to the total VOCR measured (e.g., Kovacs et al., 2003; Di Carlo et al., 2004; Sinha et al., 2008; Ingham et al., 2009; Lou et al., 2010; Sinha et al., 2010). In the SJV, we show temperature is a useful surrogate for VOCR insofar as we recreate distinct curves analogous to Fig. 3.1.2 by organizing observations by temperature (details to follow).

Meteorological conditions conducive to high ozone, including stagnation events and clear skies, correlate with increasing temperature. We group data into two temperature regimes, high (34–45°C) and moderate (28–33°C); we find these ranges are sufficiently distinct to identify differences in production of ozone (see below) while still maintaining sufficient statistics to characterize the ensemble of ozone at each site. We note that in the SJV, boundary layer dynamics are strongly influenced by mountain valley flow and as a result we do not expect meteorological factors (e.g. wind speeds) that are particularly different between high and moderate temperatures.

3.1.3. The San Joaquin Valley

The SJV is characterized by regular airflow from north to south during ozone season (~May–October) with background O_3 well mixed Valley-wide (Zhong et al., 2004). Here we divide the SJV (Fig. 3.1.3a) into three distinct urban photochemical plumes each captured by California Air Resources Board (CARB) monitoring stations and refer to these three regions as *Southern SJV* (Fig. 3.1.3b), *Central SJV* (Fig. 3.1.3c), and *Northern SJV* (Fig. 3.1.3d). Within each plume we identify an upwind, city center, and downwind location all along the axis of air movement (nine locations total). We see the lowest exceedance probabilities at upwind sites (Figs. 3.1.4–3.1.10 panels a), increased probabilities across the city center (Figs. 3.1.4–3.1.10 panels b), and the highest probabilities at locations downwind (Figs. 3.1.4–3.1.10 panels c). At the upwind site of the adjacent study regions to the south, the likelihood of a violation is again at a minimum. This is evidence for the production of ozone within each transect (details in Sect. 3.1.4.4).

The bottom panels in Fig. 3.1.3 show NO_2 observations from the Ozone Monitoring Instrument (OMI) averaged for weekdays in June–August in 2007–2010 using the Berkeley High-Resolution (BEHR) product (Russell et al., 2011). The OMI images highlight three separate NO_2 plumes in our three study areas and point to the local nature of NO_x emissions (and presumably some component of VOCR) in the SJV. In what follows, we discuss each region in turn, starting in the south and moving north.

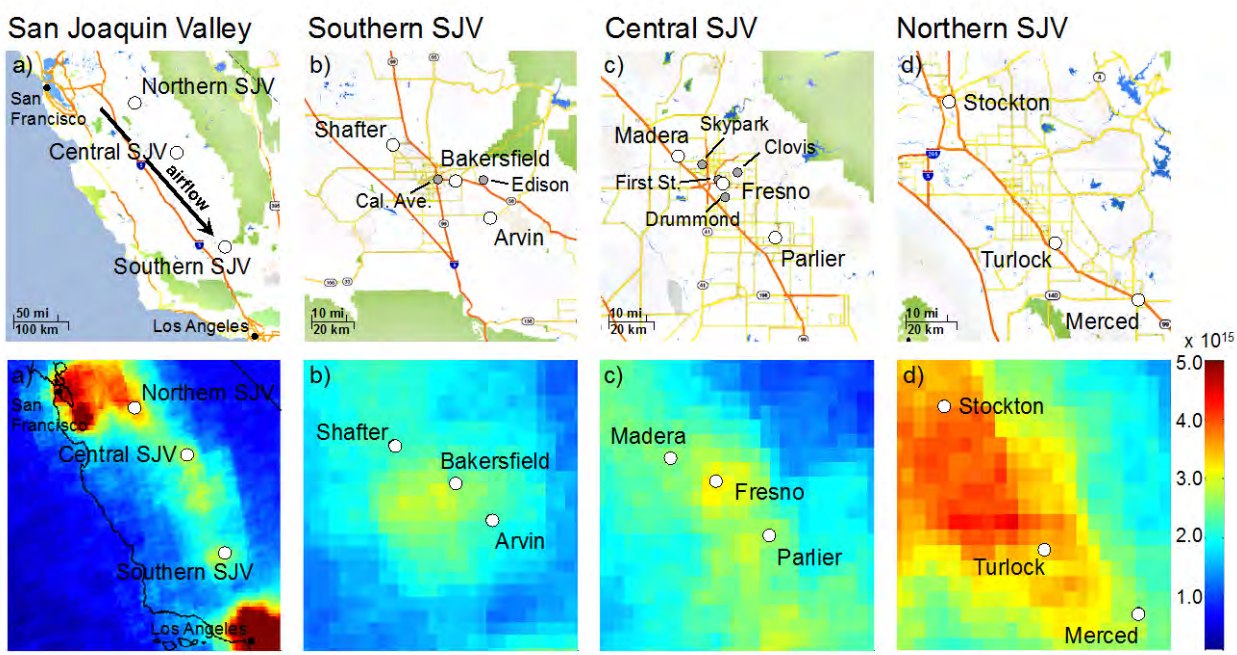

Figure 3.1.3. *Map of the California San Joaquin Valley (SJV)* ***(a top)*** *and details of each region for this study: Southern SJV* ***(b top)****, Central SJV* ***(c top)****, and Northern SJV* ***(d top)****. CARB 8-hour maximum average O_3 and NO_2* data are used from thirteen CARB sites: Shafter (upwind), Bakersfield, and Arvin (downwind)* ***(white circles)****, where Bakersfield is the median of the California Avenue and Edison stations* ***(grey circles)****; Madera (upwind), Fresno, and Parlier (downwind)* ***(white circles)****, where Fresno is the median of the Skypark, First Street, Drummond, and Clovis stations* ***(grey circles)****; Stockton (upwind), Turlock, and Merced (downwind)* ***(white circles)****. OMI NO_2 columns (molecules cm^{-2}) are shown over the same regions. These images are June–August weekday averages from 2007–2010 for the California San Joaquin Valley* ***(a bottom)****, Southern SJV* ***(b bottom)****, Central SJV* ***(c bottom)****, and Northern SJV* ***(d bottom)****.*

3.1.4. Results

3.1.4.1. Southern San Joaquin Valley

In Fig. 3.1.4 we show the Southern SJV 8-hour O_3 CAAQS exceedance probability vs. NO_2* and in Fig. 3.1.5 we show the trend in this probability vs. year (year increases right to left analogous to NO_2* concentration). The red symbols are statistics for high temperatures (34–45°C) and the blue for moderate temperatures (28–33°C). Solid symbols are weekdays (Tuesday–Friday) and open diamonds are weekends (Saturday–Sunday). Mondays and Saturdays are considered transition days as they are influenced by carryover from the previous day. We omit Mondays for this reason but retain Saturdays to improve statistics for weekends. Uncertainties in exceedance probabilities are treated as counting errors and computed as $0.5(N)^{1/2}/N$, where N is the total number of days in that bin. Uncertainties are typically less than ±0.09 (1σ) for weekdays and ±0.12 (1σ) for weekends. Uncertainties in the four-year median probabilities are less than ±0.04 (1σ) for weekdays and ±0.06 (1σ) for weekends.

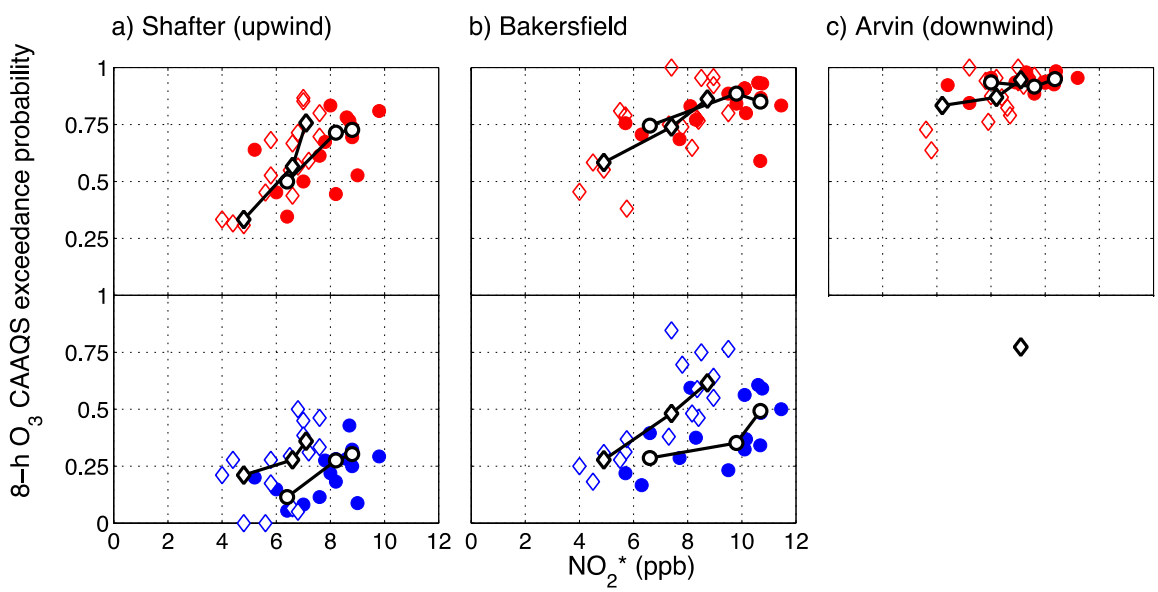

Figure 3.1.4. Southern SJV, Shafter **(a)**, Bakersfield **(b)**, and Arvin **(c)**, exceedance probabilities vs. NO_2* at high (34–45°C) and moderate (28–33°C) temperatures in **red** and **blue**, respectively. Data from weekdays **(closed circles)** and weekends **(open diamonds)** are shown as separate symbols. NO_2* are averages (10 am–2 pm local time) of hourly data at each site. Uncertainties are typically less than ±0.09 (1σ) for weekdays and less than ±0.12 (1σ) for weekends. NO_2* data are reported by CARB to be accurate to at least 15%. Black lines connect the median percentage of violations at every 5th NO_2* data point. Over the past sixteen years, the average annual number of days per year (rounded up) in the Southern SJV with a maximum temperature in the high-temperature range is 66 and the average number in the moderate-temperature range is 72.

At high temperatures, the probability of an ozone violation at the upwind site, Shafter, decreased from 80% on weekdays when NO_2* was 9.8 ppb in 1996 to 30% on weekends in 2010 when NO_2* was 4.6 ppb (Fig. 3.1.4a). In Bakersfield, the exceedance probability fell from greater than 90% on weekdays at 10.7 ppb NO_2* to 75% on weekdays at 5.7 ppb NO_2* and 50% on

weekends at 4.0 ppb NO_2* in 2010 (Fig. 3.1.4b). Downwind in Arvin, the probability held constant and near unity on weekdays despite an NO_2* decrease from 9.2 to 4.4 ppb over the window of the measurements; in the last two years it fell to 60–70% on weekends at ~3.7 ppb NO_2* (Fig. 3.1.4c).[1]

A key observation from Figs. 3.1.4b and 3.1.4c is that the probability of an exceedance on weekends, when NO_x is 30–50% lower within a given year, is essentially identical to the weekday probability years later when the same NO_x decrease is achieved. This can only occur if VOCR remained constant over that same interval (Scenario **A**). From the shape of the curves in Fig. 3.1.4a, we infer that PO_3 in Shafter is presently NO_x-limited (to the left of peak production). In Bakersfield, the exceedance probability is NO_x-limited on weekends and appears to have recently transitioned to NO_x-limited chemistry on weekdays at NO_2* less than ~9 ppb. In Arvin, while the weekday probability of exceeding the state ozone standard has been at or near unity for the last sixteen years, we do observe a small decrease in the probability of high ozone on weekends at NO_2* less than ~4 ppb. We interpret the shape of these curves to indicate that we are at or near the peak of ozone production as a function of NO_x in Bakersfield and Arvin. Consequently, reductions in the frequency of ozone exceedances have been slow to accrue despite a more than two-fold decrease in NO_2*.

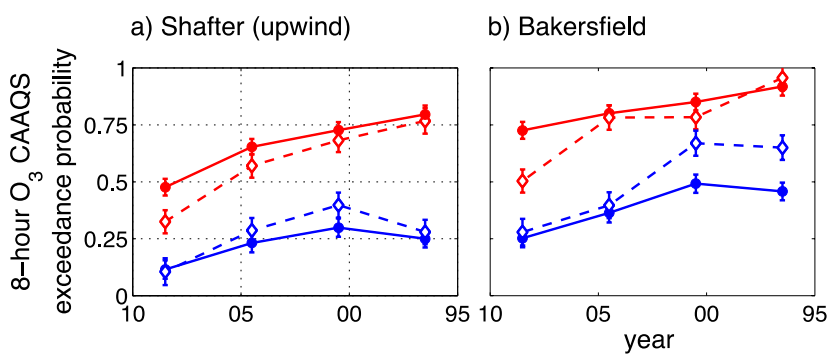

Figure 3.1.5. *Four-year median exceedance probabilities of the 8-hour O_3 CAAQS vs. year (increasing right to left) in the Southern SJV: Shafter* ***(a)****, Bakersfield* ***(b)****, and Arvin* ***(c)****. Data are shown for two temperature regimes: high (34–45°C) and moderate (28–33°C) in* ***red*** *and* ***blue****, respectively and divided into weekdays* ***(closed circles)*** *and weekends* ***(open diamonds)****. The exceedance probabilities are shown for 1995–1998, 1999–2002, 2003–2006, and 2007–2010. Error bars are uncertainties in the four-year median exceedance probabilities, are calculated as counting errors, and are typically less than ±0.04 (1σ) for weekdays and ±0.06 (1σ) for weekends. The average number of days per year over the past sixteen years for both temperature regimes is 66 (high) and 72 (moderate).*

We estimate the effects of future NO_x reductions from weekend observations (Fig. 3.1.5). Regionally, over the past four years, exceedances are less likely on weekends than weekdays at high temperatures (20% in Shafter, 25% in Bakersfield, and 20% in Arvin), indicating that at each point along the Southern SJV transect at these temperatures the frequency of exceedances has indeed crossed the peak in probability and is now in a regime of NO_x-limited chemistry on weekends. Although NO_x decreases substantially larger than those occurring on weekends are

[1] Titration of O_3 by NO can affect the frequency of violations even when the odd oxygen, O_x ($O_x \equiv O_3 + NO_2$), is constant. We checked our results using O_x instead of O_3 and found no significant differences.

required to eliminate violations, those reductions that do occur will be immediately effective on weekdays and even more so on weekends.

At moderate temperatures, although NO_2* is unchanged, the observed exceedance probabilities are lower than at high temperatures. This is evidence that temperature is a proxy for VOCR (Figs. 3.1.4 and 3.1.5). A second piece of evidence is that the weekday and weekend curves vs. NO_2* do not overlap in this temperature regime (Fig. 3.1.4). Rather, we see a different functional dependence in the probability of violations by day of week. When weekday NO_2* matches the weekend value of several years earlier the probability of violations is noticeably lower. This implies that annual NO_x reductions are attended by year-to-year changes in VOCR (Scenario **C**) at moderate temperatures. As shown in Fig. 3.1.5, exceedances were much more frequent on weekends than weekdays for 1995–1998 and 1999–2002, placing regional ozone chemistry to the right of peak PO_3 (NO_x-suppressed). At all three locations in the last four years, the probability of a high ozone day is almost identical on weekdays and weekends, indicating that at moderate temperatures Southern SJV ozone chemistry is near the peak, where the derivative with respect to NO_x at the current VOCR is small.

Another perspective on the impact of NO_x and VOCR reductions is shown in Fig. 3.1.6. Here, four-year median exceedance probabilities are shown as a function of NO_2* with lines tethering weekday (solid circles) and weekend (open diamonds) conjugates. For each measurement point shown, because day-of-week variability in VOCR and meteorology is small, the weekday-weekend pair describes the NO_x dependence along a single PO_3 curve. For visual aid, we have included a set of dashed lines as a qualitative description of the PO_3 curves corresponding to the data, which were created with the same equations (with tuned parameters) used to draw the curves in Fig. 3.1.2. If inter-annual decreases in NO_x have occurred without simultaneous changes in VOCR, as in Scenario **A**, consecutive yearly weekday-weekend pairs would trace a single curve. This is what we observe at high temperatures at Bakersfield and Arvin. If VOCR changes occurred in concert with NO_x reductions, as in Scenario **C**, the weekday-weekend pairs will each lie on separate curves. This is what we observe at moderate temperatures. We also see in Fig. 3.1.6 that the relationship between high- and moderate-temperature curves is consistent with overall lower VOCR at moderate-temperatures. We observe a shift of peak ozone production to lower rates and that the peak occurs at lower NO_x concentrations.

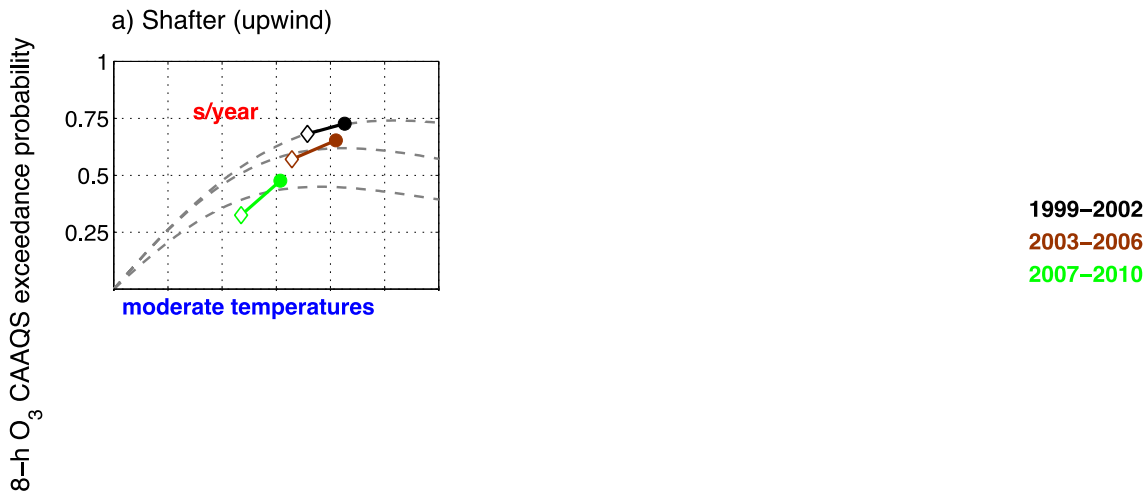

Figure 3.1.6. *Southern SJV four-year median 8-hour O_3 CAAQS exceedance probabilities vs. NO_2* tethering weekday* ***(circles)*** *and weekend* ***(diamonds)*** *conjugates for 1999–2002* ***(black)****, 2003–2006* ***(brown)****, and 2007–2010* ***(green)****. Data are shown separated by high-* ***(top)*** *and moderate-* ***(bottom)*** *temperature regimes for Shafter* ***(a)****, Bakersfield* ***(b)****, and Arvin* ***(c)****. Uncertainties in the probability of violations (by counting statistics) are typically less than ±0.04 (1σ) for weekdays and ±0.06 (1σ) for weekends. Curves* ***(dashed grey lines)*** *are included for visual aid and are not meant to be quantitative; the lines were generated with an analytical model where only VOCR was tuned and PO_3 was then scaled to fit.*

When temperatures are highest, Fig. 3.1.6 reinforces the conclusions drawn from Fig. 3.1.4 that VOCR in Bakersfield and Arvin has been almost constant over the last twelve years, as subsequent weekday-weekend pairs each trace the same curve. Decreases in the frequency of violations are recent and appear to be solely a result of sustained NO_x reductions. In contrast in Shafter, VOCR reductions appear to have influenced the trends over time. At high temperatures, throughout the metropolitan region spanned by these three sites, conditions have transitioned to NO_x-limited chemistry on weekends as depicted by the steep positive slopes of the most recent conjugates (green).

With the near unity exceedance probabilities observed in Arvin, it is possible that the O_3 concentration did actually decrease but that the normal distribution did not shift sufficiently to move any of the population below the threshold of 70.4 ppb. If this is the case then the VOCR may have also decreased. To check our conclusion in the Southern SJV, we use exceedance thresholds of 80.4 and 90.4 ppb, where the probability of exceeding these higher standards is low enough (with maximum values of 83% and 63%, respectively) that we expect a linear response in violations to changes in PO_3. In Shafter, we find no difference in the slopes and in the NO_2* and VOCR relationships depicted in Fig. 3.1.6 for either the 80.4 or 90.4 ppb standard. In Bakersfield, the shape of the curves for the 90.4 ppb standard is the same as for the 70.4 ppb; however, we find some evidence for VOCR decreases using the 80.4 ppb standard. We attribute this behavior to Bakersfield's transitional location within the plume between upwind Shafter and downwind Arvin. In Arvin (perhaps most importantly) the slopes of the three weekend-weekday

conjugates and the chemical conditions they describe are unchanged; using either the 80.4 or 90.4 ppb standard, we find no evidence for VOCR reductions.

In contrast to the high temperature observations, at moderate temperatures the O_3 exceedance probability has been largely NO_x-suppressed over the past twelve years. In Shafter and Bakersfield, ozone production has remained NO_x-suppressed since 1999 (negative slopes) with PO_3 nearing the peak (small slopes) in the last eight years (Figs. 3.1.6a and 3.1.6b). In Arvin, early in the data record the sign of the slope fluctuated at constant NO_x; if the NO_x level corresponds to peak ozone production then the slope is more sensitive to changes in VOCR. In 2007–2010, the slope is near zero and ozone chemistry close to peak production. Although it appears from Fig. 3.1.4 that at moderate temperatures the percentage of violations has fallen because of decreasing NO_2*, Fig. 3.1.6 shows that VOCR reductions are the primary cause of the smaller observed exceedance probabilities at moderate temperatures. This situation is best described by Scenario **C**, where VOCR reductions decrease the frequency of violations and also shift peak PO_3 to lower NO_x.

Taken together, distinct behavior in the two temperature regimes provides evidence for two classes of VOCR sources in the Southern SJV. One class has decreased over the last twelve years and is a large VOCR source at moderate temperatures. Another class that dominates at high temperatures, has not decreased, and at high temperatures far exceeds the moderate temperature source.

3.1.4.2. Central San Joaquin Valley

The past decade has seen the 8-hour O_3 CAAQS exceedance probability in the Central SJV fall by almost 50% both on weekdays and weekends when temperatures are highest (Fig. 3.1.7; note that year increases right to left in analogy to the NO_2* concentration). In the last four years, at high temperatures exceedances became slightly less likely on weekends at all locations in the Central SJV suggesting O_3 conditions are transitioning to NO_x-limited chemistry. Unlike in the Southern SJV, in the Central SJV there is evidence for a significant role played by VOCR reductions in decreasing the number of violations at high temperatures (Fig. 3.1.8). In Fresno, we infer VOCR decreases from 1999–2002 to 2003–2006 have amounted to 20% fewer O_3 violations at the same NO_2* (Fig. 3.1.8b, top panel). From 2003–2006 to 2007–2010, VOCR changes again contributed a 20% decrease in O_3 exceedances. Similar trends are seen upwind in Madera and downwind in Parlier.

At moderate temperatures, the frequency of violations has decreased dramatically. In 2007–2010, the probability was less than 25% at all three locations, with the largest changes in Parlier, where violations occurred at a frequency of more than 75% on weekends a decade ago. We show this decrease in the exceedance probability is due to VOCR decreases, as exceedances are more likely on weekends (Fig. 3.1.7, bottom panel) and as probabilities consistently exhibit negative day-of-week slopes vs. NO_2* (Fig. 3.1.8, bottom panel). Fig. 3.1.8 suggests that the magnitude of the decrease in the likelihood of violations from 1999–2002 to 2003–2006 is approximately twice that at high temperatures. This is similar to the results for the Southern SJV (Fig. 3.1.6) and it again indicates the presence of two distinct classes of VOCR emissions, where at moderate temperatures, the controlled class is a larger fraction. These changes are explained if we assume that at high temperatures VOCR is a mixture of a controlled class and an uncontrolled class with both terms being important.

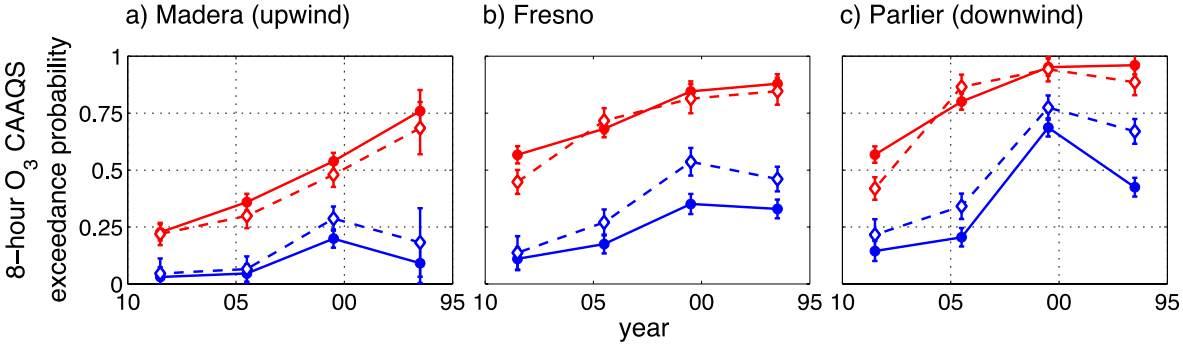

Figure 3.1.7. *Central SJV four-year median exceedance probabilities of the 8-hour O_3 CAAQS vs. year (increasing right to left) for Madera* ***(a)****, Fresno* ***(b)****, and Parlier* ***(c)****. Data are shown for 1995–1998, 1999–2002, 2003–2006, and 2007–2010 for high- (34–45°C) (red) and moderate- (28–33°C) (blue) temperature regimes and divided into weekdays (closed circles) and weekends (open diamonds). Uncertainties are calculated as counting errors and are typically less than ±0.04 (1σ) for weekdays and ±0.06 (1σ) for weekends. Over the past sixteen years there were on average 76 high-temperature days and 68 moderate-temperature days.*

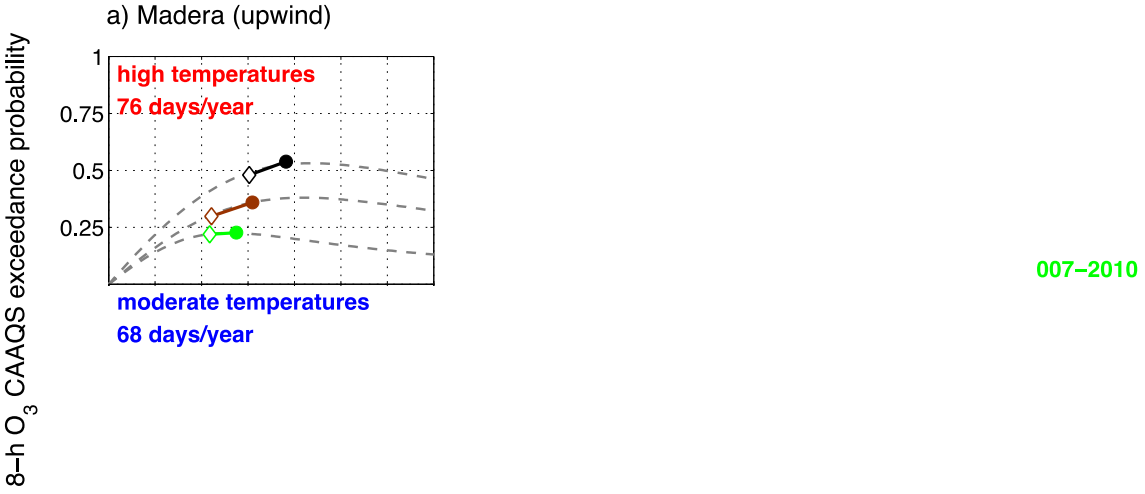

Figure 3.1.8. *Tethered four-year median weekday* ***(closed circles)*** *and weekend* ***(open diamonds)*** *8-hour O_3 CAAQS exceedance probabilities vs. NO_2* in the Central SJV for 1999–2002* ***(black)****, 2003–2006* ***(brown)****, and 2007–2010* ***(green)****. Data are separated into high-* ***(top)*** *and moderate-* ***(bottom)*** *temperature regimes for Madera* ***(a)****, Fresno* ***(b)****, and Parlier* ***(c)****. Uncertainties in the probability of violations are computed with counting statistics, are typically less than ±0.04 (1σ) for weekdays and ±0.06 (1σ) for weekends. Curves* ***(dashed grey lines)*** *were produced with an analytical model as for Fig. 3.1.6.*

3.1.4.3. Northern San Joaquin Valley

From 2007–2010 in Stockton, the upwind location of the Northern SJV region, there is a less than 10% probability that ozone concentrations will exceed the 8-hour CAAQS at high temperatures on either weekdays or weekends (Fig. 3.1.9a). Downwind, probabilities are higher. At all three sites, there have been steep weekday decreases in the last sixteen years: in Stockton from 20% to 5%, in Turlock from 75% to 35%, and in Merced from 95% to 55% (Figs. 3.1.9b and 3.1.9c). In Stockton and Turlock, more frequent weekend exceedances (Figs. 3.1.9a and 3.1.9b) and negative day-of-week slopes vs. NO_2* (Figs. 3.1.10a and 3.1.10b) show these locations are in a NO_x-suppressed chemical regime. In contrast, in Merced at high temperatures, chemistry became NO_x-limited in the last four years. Overall, in the Northern SJV, the observed decreases in the frequency of high O_3 apparently are due to VOCR reductions. However, Fig. 3.1.10c (top panel) indicates that the frequency of high O_3 in Merced will fall with continued NO_x reductions and Fig. 3.1.10b (top panel) shows that Turlock is near the threshold where NO_x reductions become effective.

Figure 3.1.9. *Northern SJV four-year median 8-hour O_3 CAAQS exceedance probabilities vs. year (increasing right to left) are plotted separated into high- (34–45°C) and moderate- (28–33°C) temperature regimes in* ***red*** *and* ***blue****, respectively and into weekdays* ***(circles)*** *and weekends* ***(diamonds)*** *for Stockton* ***(a)****, Turlock* ***(b)****, and Merced* ***(c)****. The average number of days with a maximum temperature in each temperature range over the past sixteen years is 48 (high) and 79 (moderate). Error bars are the uncertainties calculated as counting errors and are typically ±0.04 (1σ) for weekdays and ±0.06 (1σ) for weekends for four-year averages.*

At moderate temperatures, exceedances from 2007–2010 were highly unlikely, occurring on fewer than 10% of days at any of the three locations in the Northern SJV (Figs. 3.1.9 and 3.1.10). Violations were more frequent earlier in the record (e.g., Fig. 3.1.10c, bottom panel) and we infer the observed decreases are due to reductions in VOCR.

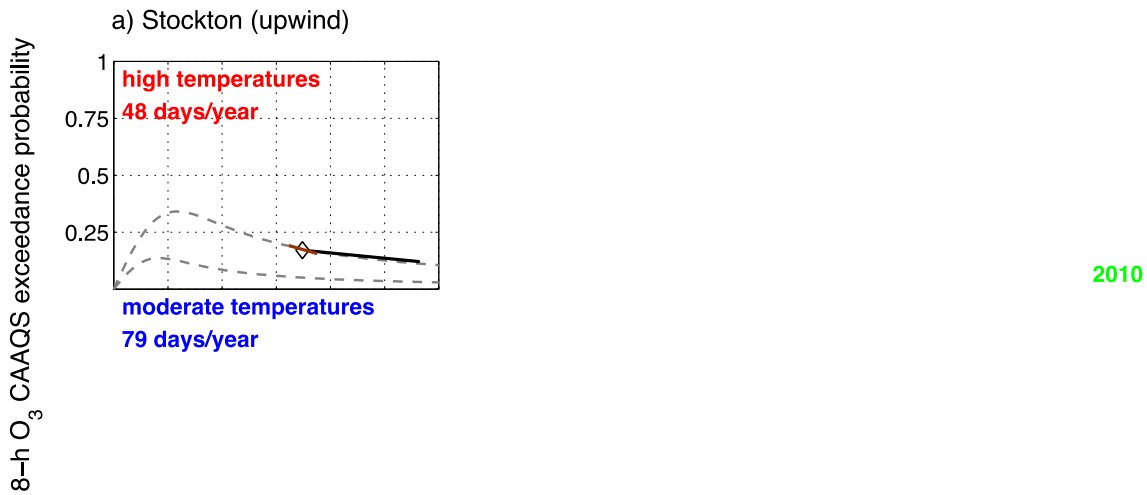

Figure 3.1.10. *Northern SJV four-year medians of 8-hour O_3 exceedance probabilities vs. NO_2* tethering weekdays* ***(circles)*** *and weekends* ***(diamonds)*** *for 1999–2002* ***(black)****, 2003–2006* ***(brown)****, and 2007–2010* ***(green)****. Data are separated into high-* ***(top)*** *and moderate-* ***(bottom)*** *temperature regimes for Stockton* ***(a)****, Turlock* ***(b)****, and Merced* ***(c)****. Uncertainties in the probability of violations are smaller than the observed year-to-year variability at ±0.04 (1σ) for weekdays and ±0.06 (1σ) for weekends. Curves* ***(dashed grey lines)*** *were produced as for Fig. 3.1.6.*

3.1.4.4. Evidence for local ozone production

There are two pieces of evidence that support local ozone production to be a large contributor to the frequency of high ozone days in the SJV. First, the observed exceedance probability is lowest for each of the upwind sites, Shafter (Southern SJV), Madera (Central SJV), and Stockton (Northern SJV), increases along the plume transect (in Bakersfield, Fresno, and Turlock), and is highest at the corresponding downwind locations, Arvin, Parlier, and Merced, respectively. In the Southern SJV in 2007–2010 at high temperatures, we see an increase in the probability of a violation by 45% on weekdays and by 40% on weekends between Shafter and Arvin. In the Central SJV, over the same time period and in the same temperature regime, the percentage of violations is shown to increase by 20% on weekends and 35% on weekdays from Madera to downwind Parlier. In the Northern SJV in 2007–2010 at high temperatures, the probability increases by 35% on weekdays and 45% on weekends between Stockton and downwind Merced. The second piece of evidence is that there is a ~10% drop in the exceedance percentage between Parlier (downwind Central) and Shafter (upwind Southern) and a ~20–35% decrease between Merced (downwind Northern) and Madera (upwind Central). If local production were not important, we would expect to observe a single Valley-wide ozone plume and therefore to see the exceedance probability to smoothly rise (or fall) the length of the SJV. This is not the case however. Rather, the exceedance probably increases across each sub-region but then decreases again at the next site to the south (at the upwind sites Shafter and Madera). Exceedances are presently unlikely at moderate temperatures in the Central and Northern SJV but a comparison of past four-year median exceedance probabilities also illustrates this effect.

3.1.5. Discussion

From 1995–2010, reductions in NO_x emissions in California have been mostly due to more stringent standards on stationary sources and light-duty vehicles. In contrast, emissions from heavy-duty diesel engines, the largest source of NO_x emissions in the SJV, have increased over the past fifteen years (Cox et al., 2009; Dallmann and Harley, 2010). Nationally new rules require heavy-duty diesel engines to meet more stringent NO_x emissions standards (Environmental Protection Agency, 2000); however, these engines have long service lifetimes and slow fleet turnover rates. In California, in an effort to expedite benefits from new diesel engine regulations, the California Air Resources Board (CARB) is requiring all vehicle owners to retrofit or replace older diesel engines by 2023 and half of the in-use heavy duty-engines in large fleets must meet new NO_x standards by 2014 (California Air Resources Board, 2007). Millstein and Harley (2010) show that in Los Angeles, as a result of this accelerated engine retrofit/replacement program, reductions in summertime diesel NO_x emissions could be greater than 50% over the five years from 2010 to 2015, with slower reductions (–20% in tons/day) predicted in the following ten years from 2015 to 2025. Additionally, the SJV Air Pollution Control District is also partnering with the Environmental Protection Agency (EPA) under the National Clean Diesel Campaign to replace diesel locomotives and diesel engines on agricultural equipment (Environmental Protection Agency, 2012a).

NO_x emissions reductions can still be expected from cars and light-duty trucks in the next twenty-five years. In 2012 CARB announced the Advanced Clean Cars Program, which aims to further reduce these NO_x emissions by 75% from 2014 levels through new emissions standards (in the 2015 model year) and by requiring one in seven news cars sold in California be zero-emission or plug-in hybrid vehicles by 2025 (Environmental Protection Agency, 2012b).

In summary, policymakers at the local (San Joaquin Valley Unified Air Pollution Control District), state (CARB), and federal level (EPA Region 9) have expressed a commitment to reducing NO_x emissions in the SJV and so we expect NO_x concentrations to continue to decrease Valley-wide.

The outlook for VOCR in the SJV is less clear. We show that at moderate temperatures, VOCR throughout the SJV has decreased over the last twelve years and that these decreases have resulted in fewer high O_3 days. This implies that the dominant sources of organic reactivity in this temperature regime are currently being controlled. VOC emissions from mobile sources have been thought to be largest source of O_3 forming organic precursors in the Valley (Hu et al., 2012). Regulatory efforts during our study window have focused on VOC emissions from light-duty vehicles and reduced these emissions through a combination of stricter standards and gasoline reformulation (Kirchstetter et al., 1999; Harley et al., 2006). At high temperatures in the Central and Northern SJV, we also show that reductions in VOCR have significantly decreased the frequency of violations. However, in the Central SJV these decreases in VOCR are smaller than those observed at moderate temperatures. This same temperature dependence is seen to a more dramatic extent in the Southern SJV, where over the last twelve years at high temperatures the VOCR in Bakersfield and Arvin has not changed. In this temperature regime, we therefore infer the existence of a VOCR source that both overwhelms the moderate-temperature source and that has gone unregulated over the last twelve years.

Recent model calculations have indicated non-mobile VOCR sources are important to PO_3 in the SJV, but to our knowledge this manuscript provides the first direct observational evidence. For

example, Steiner et al. (2009) computed the total reactivity in the SJV, finding that the biogenic VOC emissions important in most other locations, such as isoprene and monterpenes (α-pinene), were only a small fraction of the total VOCR in this region. The authors suggested that the regional reactivity was dominated by oxygenates, although they noted that the sources of these species were very poorly quantified. VOC emissions from animal feeds have been proposed to be a large component of SJV VOCR (Alanis et al., 2008; Howard et al. 2010a; Howard et al. 2010b; Malkina et al., 2011). This source is not currently included in official inventories. In a first step toward understanding their impacts, inclusion of animal feed emissions in a regional air quality model (focusing on a single O_3 episode July 24–August 2, 2000) found that they were less important than mobile source VOC emissions to PO_3, that PO_3 was still under-predicted SJV, and that there is still likely missing VOCR (Hu et al., 2012). Clearly more research is needed to identify the source(s) of VOCR in the SJV, but whatever the source, our analysis suggests it has been unchanged over the last decade.

With this background on the expected changes in San Joaquin emissions, we present policy-relevant conclusions for the Southern, Central, and Northern SJV below and address the impacts of additional NO_x and VOCR reductions on the frequencies of future CAAQS 8-hour O_3 exceedances in the region.

3.1.5.1. Southern San Joaquin Valley

When temperatures are hottest, ozone production in Bakersfield and Arvin has been at peak for much of the last sixteen years and at constant VOCR. This explains why, despite a decade of NO_x emission reductions, violations remain highly probable. At both sites ozone production has recently transitioned to NO_x-limited chemistry and, as a result, continued NO_x controls are poised to improve O_3 air quality. Sizable NO_x reductions are required before gains are seen in Arvin, as the exceedance probability at this site is still at peak on weekdays and very near unity. Current decreases in the high-temperature exceedance percentage in Arvin from 90% on weekdays to 70% on weekends suggest there will be 20% fewer weekday violations in response to the next 50% NO_x reduction. Fifty percent NO_x reductions will reduce the frequency of high ozone on weekdays in Bakersfield to 50% and in Shafter to 30%. At all three locations at moderate temperatures, ozone production is still at peak PO_3 or slightly NO_x-suppressed (with a small slope) and so NO_x reductions in this temperature regime will not immediately improve local O_3 air quality but will also not exacerbate it.

At the highest temperatures, observations suggest VOCR has not appreciably changed in the past decade. New strategies are therefore needed both to identify what organic molecules drive VOCR at the hottest temperatures and to reduce these precursor species. That said, because Southern SJV ozone production has transitioned to NO_x-limited chemistry at high temperatures, additional VOCR reductions will provide diminished returns. At moderate temperatures, there is still the potential for VOCR reductions to decrease the frequency of violations.

3.1.5.2. Central San Joaquin Valley

At high temperatures, the exceedance probability has in the last four years transitioned to NO_x-limited chemistry. It is difficult to be quantitative, but a comparison of the steepness of the 2007–2010 high-temperature slopes in Fig. 3.1.8 and Fig. 3.1.6 shows ozone chemistry in this region nearer to peak production than in the Southern SJV. As such, NO_x controls will improve O_3 air

quality but gains will lag those anticipated in the south. At moderate temperatures, NO_x reductions will be slow to decrease the frequency of exceedances because chemistry is still NO_x-suppressed.

VOCR reductions have been a powerful force in decreasing the exceedance probability under both high- and moderate-temperature conditions. Continued controls on mobile source emissions will further reduce the frequency of violations in both regimes but the impact of further controls is checked by the onset of NO_x-limited ozone chemistry and by the fraction of VOCR that is due to uncontrolled sources. This fraction is important at high temperatures.

3.1.5.3. Northern San Joaquin Valley

In Stockton, NO_2* abundances are high, the frequency of violations is NO_x-suppressed, and high O_3 days are uncommon. As a result, NO_x controls will not improve local O_3 air quality in this location. In Turlock under both high- and moderate-temperature conditions, the exceedance probability remains NO_x-suppressed. The payoff from continued NO_x reductions will be delayed until a transition to NO_x-limited chemistry takes place. The difference in the percentage of violations on weekdays and weekends is small and so chemistry is proximate to peak PO_3. This gives confidence that NO_x controls will not degrade Turlock O_3 air quality. In Merced, at high and moderate temperatures, PO_3 is NO_x-limited as of 2007–2010. We anticipate continued NO_x reductions will decrease the exceedance probability at this location and note that NO_x reductions upwind in Stockton and Turlock are important to decreasing NO_x abundances in Merced.

At high temperatures, continued reduction of VOC emissions is expected to decrease the frequency of high ozone days in Turlock. We predict that the impact of VOC emission reductions will be smaller than previously seen, as the decrease in O_3 exceedance probability in the last four years was only half that seen earlier in the decade. In Merced, in both temperature regimes, VOCR reductions have made profound improvements to O_3 air quality. At moderate temperatures, exceedances are below 15%. At the high temperatures, VOCR reductions have resulted in exceedances being 50% less probable than a decade ago. Now that ozone production is NO_x-limited further VOCR reductions will be unable to drive substantial decreases in the number of violations.

3.1.6. Conclusions

We describe ozone's dependence on NO_x and organic reactivity (VOCR) in San Joaquin Valley California using sixteen years of routine measurements of O_3, NO_2*, and temperature.

We show that local ozone production plays a large role in the frequency of high ozone days, as the exceedance percentage is seen to increase from upwind to downwind within each of our study regions and because the probability of a violation between regions is, in each case, higher at the downwind site to the north than at the receptor city to the south. This underscores the importance of controlling precursor emissions from local sources in the SJV.

We present location-specific policy-relevant conclusions for the Southern SJV, Central SJV, and Northern SJV in Sects. 3.1.5.1, 3.1.5.2, and 3.1.5.3, respectively. Broadly speaking, we show that in the Central and Northern SJV, decreases in VOCR have dramatically reduced the frequency of violations. We report a temperature dependence in the effects of VOCR reductions in the Central SJV, finding they are larger at moderate-range temperatures than at high. This is likewise true in the Southern SJV, where reductions in the VOCR have decreased the frequency of exceedances

at moderate temperatures but have made no impact when temperatures are hottest. That the VOCR has remained unchanged over the past twelve years at high temperatures in one region but not in the others reveals a need for detailed high-spatial resolution VOC emissions inventories in the SJV and a thorough analysis of the temperature dependence of each source. This evidence for two distinct types of VOCR sources frames an outstanding question for future research. *What organic molecules drive the temperature dependence of VOCR both within each region and Valley wide?*

We find that NO_x reductions are poised to improve ozone air quality where violations are most frequent—the Southern and Central SJV. We see that these regions have or soon will transition to NO_x-limited conditions when temperatures are highest and the likelihood of high ozone is greatest. We show that exceedances in the Southern SJV have remained highly probable despite NO_x emissions control efforts because the ozone chemistry in Bakersfield and Arvin has been near peak PO_3 and at constant VOCR for more than a decade.

Ozone, NO_2*, and temperature measurements have been collected across North America and around the world for more than a decade. We expect that the statistical approach described herein should be applicable to other isolated urban plumes. Even if wind directions are not as persistent as in the SJV, we imagine an analysis at the city center alone or one sorted by wind direction in addition to temperature will be interesting. We look forward to such analyses providing broader observational perspective on the effectiveness of NO_x and VOCR controls in other locations.

Appendix A: Measurements

CARB maintains an extensive network of ground-based monitors statewide. In this paper we use the 8-hour maximum O_3 and hourly NO_2 data from thirteen CARB sites in the San Joaquin Valley Air Basin. These sites are Arvin, Arvin-Bear Mountain Blvd (35.209, –118.779) (this site closed in November 2010); California Avenue, Bakersfield-5558 California Avenue (35.357, –119.063); Clovis, Clovis-N Villa Avenue (36.819, –119.716); Edison, Edison (35.346, –118.852); Drummond, Fresno-Drummond Street (36.705, –119.741); First Street, Fresno-1st Street (36.782, –119.773); Madera, Madera-Pump Yard (36.867, –120.010); Merced, Merced-S Coffee Avenue (37.282, –120.434); Parlier, Parlier (36.597, –119.504); Shafter, Shafter-Walker Street (35.503, –119.273); Skypark, Fresno-Sierra Skypark #2 (36.842, –119.883); Stockton, Stockton-Hazelton Street (37.952, –121.269); and Turlock, Turlock-S Minaret Street (37.488, –120.836). “Bakersfield” is the median of the California Avenue and Edison stations and “Fresno” is the median of the Skypark, First Street, Drummond, and Clovis stations. Data at Madera-Pump Yard are available starting in 1998 and data from Clovis in 2008 were not reported. Data at Merced-S Coffee Avenue are not available in 2000 (NO_2*) and 2006 (O_3). All data and detailed information about the location of each monitor are available for download on the CARB website: http://www.arb.ca.gov/adam/index.html.

We removed any concentration data exactly equal to 0.000 ppm believing this to be a physically unreasonable daytime concentration for either the 8-hour maximum O_3 or the hourly NO_2*. The daytime NO_2* concentration is the daily mean value between 10 am and 2 pm local time. The average NO_2* is not very sensitive to a change in this window and our work uses relative rather than absolute NO_2* concentration. For Fresno and Bakersfield we use medians of the individual sites and in the absence of data at a single site for a given day that day is omitted. Yearly NO_2* data are averaged for weekdays (Tuesdays–Fridays) and weekends (Saturdays–Sundays).

CARB NO_2* is measured by chemiluminescence coupled with a heated molybdenum catalyst. NO_2 measurements with this technique are attended by a known positive interference from higher oxides of nitrogen, for example organic nitrates and nitric acid, which also thermally decompose (Williams et al., 1998; Dunlea et al., 2007). Ammonia (NH_3) has also been seen to positively interfere (0–10%) with NO_2 chemiluminescence (Williams et al., 1998; Dunlea et al., 2007). NH_3 concentrations in the SJV are high (Clarisse et al., 2010) but we take confidence in the usefulness of the CARB NO_2* data, as the NO_2* abundances are decreasing across the Valley at rates similar to those observed from space by OMI (Russell et al., 2010). NO_2* data are reported by CARB to be accurate to at least 15%.

Temperature data are the 1-hour maximum daily temperatures and data are used from three sites, Merced-S Coffee Avenue (37.282, –120.434), Fresno Air Terminal (36.776, –119.718), and Bakersfield Airport (**35.325, –118.998);** one site in each of our three study areas. The average maximum temperature is not statistically different from 1995 to 2010. We do not separate NO_2* by temperature finding no significant temperature dependence in its concentration by day of week between high and moderate conditions.

Acknowledgements

This work is supported by the California Air Resources Board under grant CARB 08-316 and by the NASA under grant NNX10AR36G. We acknowledge the use of publically available data collected by the California Air Resources Board and the San Joaquin Valley Unified Air Pollution Control District. We thank Rynda Hudman and Brian LaFranchi for helpful discussions.

References for Pusede and Cohen, 2012:

Alanis, P., Ashkan, S., Krauter, C., Campbell, S., and Hasson, A.: Emissions of volatile fatty acids from feed at dairy facilities, Atmos. Environ., 44(39), 5084–5092, doi:10.1016/j.atmosenv.2010.09.017, 2010.

American Lung Association, State of the air: 2011 report: http://www.stateoftheair.org, last access: 5 March 2012, 2011.

Andreani-Aksoyoglu, S., Lu, C. H., Keller, J., Prevot, A. S. H., and Chang, J. S.: Variability of indicator values for ozone production sensitivity: a model study in Switzerland and San Joaquin Valley (California), Atmos. Environ., 35, 5593–5604, doi:10.1016/S1352-2310(01)00278-3, 2001.

Ban-Weiss, G. A., McLaughlin, J. P., Harley, R. A., Lunden, M. M., Kirchstetter, T. W., Kean, A. J., Strawa, A. W., Stevenson, E. D., and Kendall, G. R.: Long-term changes in emissions of nitrogen oxides and particulate matter from on-road gasoline and diesel vehicles, Atmos. Environ., 42, 220–232, doi:10.1016/j.atmosenv.2007.09.049, 2008.

Bishop, G. A. and Stedman, D. H.: A decade of on-road emissions measurements, Environ. Sci. Technol., 42, 1651–1656, doi:10.1021/es702413b, 2008.

California Air Resources Board, California air pollution control laws - 2011 bluebook: http://www.arb.ca.gov/bluebook/bluebook.htm, last access: 10 January 2012, 2011.

California Air Resources Board, Regulation to reduce emissions of diesel particulate matter, oxides of nitrogen and other criteria pollutants, from in-use heavy-duty diesel-fueled vehicles: http://www.arb.ca.gov/msprog/onrdiesel/regulation.htm, last access: 8 February 2012, 2008.

Cazorla, M., Brune, W. H., Ren, X., and Lefer, B.: Direct measurement of ozone production rates in Houston in 2009 and comparison with two estimation methods, Atmos. Chem. Phys., 12, 1203–1212, doi:10.5194/acp-12-1203-2012, 2012.

Clarisse, L., Shephard, M. W., Dentener, F., Hurtmans, D., Cady-Pereira, K., Karagulian, F., Van Damme, M., Clerbaux, C., and Coheur, P. F.: Satellite monitoring of ammonia: a case study of the San Joaquin Valley, J. Geophys. Res., 115, D13302, doi:10.1029/2009JD013291, 2010.

Cox, P., Delao, A., Komorniczak, A., and Weller, R.: The California almanac of emissions and air quality, California Air Resources Board, Sacramento, CA, 2009.

Dallmann, T. R. and Harley, R. A.: Evaluation of mobile source emission trends in the United States, J. Geophys. Res., 115, D14305, doi:10.1029/2010JD013862, 2010.

Di Carlo, P., Brune, W. H., Martinez, M., Harder, H., Lesher, R., Ren, X., Thornberry, T., Carroll, M. A., Young, V., Shepson, P. B., Riemer, D., Apel, E., and Campbell, C.: Missing OH reactivity in a forest: evidence for unknown reactive biogenic VOCs, Science, 304, 722–725, doi:10.1126/science.1094392, 2004.

Dunlea, E. J., Herndon, S. C., Nelson, D. D., Volkamer, R. M., San Martini, F., Sheehy, P. M., Zahniser, M. S., Shorter, J. H., Wormhoudt, J. C., Lamb, B. K., Allwine, E. J., Gaffney, J. S., Marley, N. A., Grutter, M., Marquez, C., Blanco, S., Cardenas, B., Retama, A., Villegas, C. R. R., Kolb, C. E., Molina, L. T., and Molina, M. J.: Evaluation of nitrogen dioxide chemiluminescence monitors in a polluted urban environment, Atmos. Chem. Phys., 7, 2691–2704, doi:10.5194/acp-7-2691-2007, 2007.

Environmental Protection Agency, National air quality and emissions trends report: 2003 special studies edition: http://www.epa.gov/airtrends/aqtrnd03, last access 5 March 2012, 2003.

Environmental Protection Agency, Clean diesel trucks, buses, and fuel: heavy-duty engine and vehicle standards and highway diesel fuel sulfur control requirements: http://www.epa.gov/otaq/highway-diesel/regs/2007-heavy-duty-highway.htm, last access February 2012, 2000.

Environmental Protection Agency, National clean diesel campaign (NCDC): http://www.epa.gov/cleandiesel/index.htm, last access February 2012, 2012a.

Environmental Protection Agency, California's advanced clean cars program: http://www.arb.ca.gov/msprog/clean_cars/clean_cars.htm, last access February 2012, 2012b.

Farmer, D. K., Perring, A. E., Wooldridge, P. J., Blake, D. R., Baker, A., Meinardi, S., Huey, L. G., Tanner, D., Vargas, O., and Cohen, R. C.: Impact of organic nitrates on urban ozone production, Atmos. Chem. Phys., 11, 4085–4094, doi:10.5194/acp-11-4085-2011, 2011.

Guenther, A. B., Zimmerman, P. R., Harley, P. C., Monson, R. K., and Fall, R.: Isoprene and monoterpene emission rate variability: model evaluations and sensitivity analyses, J. Geophys. Res., 98(D7), 12,609–12,617, doi:10.1029/93JD00527, 1993.

Harley, R. A., Marr, L. C., Lehner, J. K., and Giddings, S. N.: Changes in motor vehicle emissions on diurnal to decadal time scales and effects on atmospheric composition, Environ. Sci. Technol., 39, 5356–5362, doi:10.1021/es048172+, 2005.

Harley, R. A., Hooper, D. S., Kean, A. J., Kirchstetter, T. W., Hesson, J. M., Balberan, N. T., Stevenson, E. D., and Kendall, G. R.: Effects of reformulated gasoline and motor vehicle fleet on emissions and ambient concentrations of benzene, Environ. Sci. Technol., 40, 5084–5088, doi:10.1021/es0604820, 2006.

Howard, C. J., Kumar, A., Malkina, I., Mitloehner, F., Green, P. G., Flocchini, R. G., and Kleeman, M. J.: Reactive organic gas emissions from livestock feed contribute significantly to ozone production in Central California, Environ. Sci. Technol., 44, 2309–2314, doi:10.1021/es902864u, 2010a.

Howard, C. J., Kumar, A., Mitloehner, F., Stackhouse, K., Green, P. G., Flocchini, R. G., and Kleeman, M. J.: Direct measurements of the ozone formation potential from livestock and poultry waste emissions, Environ. Sci. Technol., 44, 2292–2298, doi:10.1021/es901916b, 2010b.

Hu, J., Howard, C. J., Mitloehner, F., Green, P. G., and Kleeman, M. J.: Mobile source and livestock feed contributions to regional ozone formation in Central California, Environ. Sci. Technol., ASAP, 2012.

Ingham, T., Goddard, A., Whalley, L. K., Furneaux, K. L., Edwards, P. M., Seal, C. P., Self, D. E., Johnson, G. P., Read, K. A., Lee, J. D., and Heard, D. E.: A flow-tube based laser-induced fluorescence instrument to measure OH reactivity in the troposphere, Atmos. Meas. Tech., 2, 465–477, 2009.

Jin, L., Tonse, S., Cohan, D. S., Mao, X., Harley, R. A., and Brown, N. J.: Sensitivity analysis of ozone formation and transport for a Central California air pollution episode, Environ. Sci. Technol., 42, 3683–3689, doi:10.1021/es072069d, 2008.

Kim, S.-W., Heckel, A., McKeen, S. A., Frost, G. J., Hsie, E. –Y., Trainer, M. K., Richter, A., Burrows, J. P., Peckham, S. E., and Grell, G. A.: Satellite-observed U.S. power plant NO_x emission reductions and their impact on air quality, Geophys. Res. Lett., 33, L22812, 5, doi:10.1029/2006GL027749, 2006.

Kim, S.-W., Heckel, A., Frost, G. J., Richter, A., Gleason, J., Burrows, J. P., McKeen, S., Hsie, E. Y., Granier, C., and Trainer, M.: NO_2 columns in the western United States observed from space and simulated by a regional chemistry model and their implications for NO_x emissions, J. Geophys. Res., 114, D11301, doi:10.1029/2008JD011343, 2009.

Kirchstetter, T. W., Singer, B. C., Harley, R. A., Kendall, G. R., and Hesson, J. M.: Impact of California reformulated gasoline on motor vehicle emissions: 2. volatile organic compound speciation and reactivity. Environ. Sci. Technol., 33, 329–336, 1999.

Kleinman, L. I., Daum, P. H., Lee, Y. N. Nunnermacker, L. J., Springston, S. R., Weinstein-Lloyd, J., and Rudolph, J.: A comparative study of ozone production in five U.S. metropolitan areas, J. Geophys. Res., 110(D2), D02301, doi:10.1029/2004JD005096, 2005.

Konolov, I. B., Beekman, M., Richter, A., Burrows, J. P., and Hilboll, A.: Multi-annual changes of NO_x emissions in megacity regions: nonlinear trend analysis of satellite measurement based estimates, Atmos. Chem. Phys., 10, 8481–8498, doi:10.5194/acp-10-8481/2010, 2010.

Kovacs, T. A. and Brune, W. H.: Total OH loss rate measurement, J. Atmos. Chem., 39, 105–122, doi:10.1023/A:1010614113786, 2001.

Kovacs, T. A., Brune, W. H., Harder, H., Martinez, M., Simpas, J. B., Frost, G. J., Williams, E., Jobson, T., Stroud, C., Young, V., Fried, A., and Wert, B.: Direct measurements of urban OH reactivity during Nashville SOS in summer 1999, J. Environ. Monit., 5, 68–74, doi:10.1039/B204339D, 2003.

LaFranchi, B. W., Goldstein, A. H., and Cohen, R. C.: Observations of the temperature dependent response of ozone to NO_x reductions in the Sacramento, CA urban plume, Atmos. Chem. Phys., 11, 6945–6960, doi:10.5194/acp-11-6945-2011, 2011.

Lou, S., Holland, F., Rohrer, F., Lu, K., Bohn, B., Brauers, T., Chang, C. C., Fuchs, H., Häseler, R., Kita, K., Kondo, Y., Li, X., Shao, M., Zeng, L., Wahner, A., Zhang, Y., Wang, W., and Hofzumahaus, A.: Atmospheric OH reactivities in the Pearl River Delta – China in summer 2006: measurement and model results, Atmos. Chem. Phys., 10, 11243–11260, doi:10.5194/acp-10-11243-2010, 2010.

Mahmud, A., Tyree, M., Cayan, D., Motallebi, N., and Kleeman, M. J.: Statistical downscaling of climate change impacts on ozone concentrations in California, J. Geophys. Res., 113(D21), D21103, doi:10.1029/2007JD009534, 2008.

Malkina, I. L., Kumar, A., Green, P. G., and Mitloehner, F. M.: Identification and quantification of volatile organic compounds emitted from dairy silage and other feedstuffs, J. Environ. Qual., 40(1), 28–36, 2011.

Marr, L. C., Black, D. R., and Harley, R. A.: Formation of photochemical air pollution in Central California - I. Development of a revised motor vehicle emission inventory, J. Geophys. Res., 107(D5–6), 4047, doi:10.1029/2001JD000689, 2002.

Marr, L. C. and Harley, R. A.: Modeling the effect of weekday-weekend differences in motor vehicle emissions on photochemical air pollution in Central California, Environ. Sci. Technol., 26, 4099–4106, doi:10.1021/es020629x, 2002.

Martin, R. V., Fiore, A. M., and Van Donkelaar, A.: Space-based diagnosis of surface ozone sensitivity to anthropogenic emissions, Geophys. Res. Lett., 31, L06120, doi:10.1029/2004GL019416, 2004.

Millstein, D. E. and Harley, R. A.: Effects of retrofitting emission control systems on in-use heavy diesel vehicles, Environ. Sci. Technol., 44, 5042–5048, doi:10.1021/es1006669, 2010.

Monks, P. S. Granier, C., Fuzzi, S., Stohl, A., Williams, M. L., Akimoto, H., Amann, M., Baklanov, A., Baltensperger, U., Bey, I., Blake, N., Blake, R. S., Carslaw, K., Cooper, O. R., Dentener, F., Fowler, D., Fragkou, E., Frost, G. J., Generoso, S., Ginoux, P., Grewe, V., Guenther, A., Hansson, H. C., Henne, S., Hjorth, J., Hofzumahaus, A., Huntrieser, H., Isaksen, I. S. A., Jenkin, M. E., Kaiser, J., Kanakidou, M., Klimont, Z., Kulmala, M., Laj, P., Lawrence, M. G., Lee, J. D., Liousse, C., Maione, M., McFiggans, G., Metzger, A., Mieville, A., Moussiopoulos, N., Orlando, J. J., O'Dowd, C. D., Palmer, P. I., Parrish, D. D., Petzold, A., Platt, U., Poschl, U., Prevot, A. S. H., Reeves, C. E., Reimann, S., Rudich, Y., Sellegri, K., Steinbrecher, R., Simpson, D., ten Brink, H., Theloke, J., van der Werf, G. R., Vautard, R., Vestreng, V., Vlachokostas, C., and von Glasow, R.: Atmospheric composition change - global

and regional air quality, Atmos. Environ., 43, 5268–5350, doi:10.1016/j.atmosenv.2009.08.021, 2009.

Murphy, J. G., Day, D. A., Cleary, P. A., Wooldridge, P. J., Millet, D. B., Goldstein, A. H., and Cohen, R. C.: The weekend effect within and downwind of Sacramento - part 2: observational evidence for chemical and dynamical contributions, Atmos. Chem. Phys. Discuss., 6, 11971–12019, doi:10.5194/acpd- 6-11971-2006, 2006.

Murphy, J. G., Day, D. A., Cleary, P. A., Wooldridge, P. J., Millet, D. B., Goldstein, A. H., and Cohen, R. C.: The weekend effect within and downwind of Sacramento - part 1: observations of ozone, nitrogen oxides, and VOC reactivity, Atmos. Chem. Phys., 7, 5327–5339, doi:10.5194/acp-7-5327-2007, 2007.

Ormeño, E., Gentner, D. R., Fares, S., Karlik, J., Park, J. H., and Goldstein, A. H.: Sesquiterpenoid emissions from agricultural crops: correlations to monoterpenoid emissions and leaf terpene content, Environ. Sci. Technol., 44, 3758–3764, doi:10.1021/es903674m, 2010.

Parrish, D. D., Trainer, M., Hereid, D., Williams, E. J., Olszyna, K. J., Harley, R. A., Meagher, J. F., and Fehsenfeld, F. C.: Decadal change in carbon monoxide to nitrogen oxide ratio in US vehicular emissions, J. Geophys. Res. 107(D12), 4140, doi:10.1029/2001JC000720, 2002.

Parrish, D. D.: Critical evaluation of US on-road vehicle emission inventories, 40, 2288–2300 doi:10.1016/j.atmosenv.2005.11.033, 2006.

Parrish, D. D., Singh, H. B., Molina, L., and Madronich, S.: Air quality progress in North American megacities: a review, Atmos. Environ., 45, 7015–7025, doi:10.1016/j.atmosenv.2011.09.039, 2011.

Pollack, I. B., Ryerson, T. B., Trainer, M., Parrish, D. D., Andrews, A. E., Atlas, E. L., Blake, D. R., Brown, S. S., Commane, R., Daube, B. C., de Gouw, J. A., Dubé, W. P., Flynn, J., Frost, G. J., Gilman, J. B., Grossberg, N., Holloway, J. S., Kofler, J., Kort, E. A., Kuster, W. C., Lang, P. M., Lefer, B., Lueb, R. A., Neuman, J. A., Nowak, J. B., Novelli, P. C., Peischl, J., Perring, A. E., Roberts, J. M., Santoni, G., Schwarz, J. P., Spackman, J. R., Wagner, N. L., Warneke, C., Washenfelder, R. A., Wofsy, S. C., and Xiang, B.: Airborne and ground-based observations of a weekend effect in ozone, precursors, and oxidation products in the California South Coast Air Basin, J. Geophys. Res., 117, D00V05, doi:10.1029/2011JD016772, 2012.

Rubin, J. I., Kean, A. J., Harley, R. A., Millet, D. B., and Goldstein, A. H.: Temperature dependence of volatile organic compound evaporative emissions from motor vehicles, J. Geophys. Res., 111(D3), D03305, doi:10.1029/2005JD006458, 2006.

Russell, A. R., Valin, L. C., Bucsela, E. J., Wenig, M. O., and Cohen, R. C.: Space-based constraints on spatial and temporal patterns of NO_x emissions in California, 2005–2008, Environ. Sci. Technol., 44, 3608–3615, doi:10.1021/es903451j, 2010.

Russell, A. R., Perring, A. E., Valin, L. C., Bucsela, E. J., Browne, E. C., Min, K.-E., Wooldridge, P. J., and Cohen, R. C.: A high spatial resolution retrieval of NO_2 column densities from OMI: method and evaluation, Atmos. Chem. Phys., 11, 8543–8554, doi:10.5194/acp-11-8543–2011, 2011.

Russell, A. R, Valin, L. C., and Cohen, R. C.: Trends in OMI NO_2 observations over the US: effects of emission control technology and the economic recession, Atmos. Chem. Phys. Discuss., 12, 15419–15452, doi:10.5194/acpd-12-15419-2012, 2012.

Sadanaga, Y., Yoshino, A., Watanabe, K., Yoshioka, A., Wakazono, Y., Kanaya, Y., and Kajii, Y.: Development of a measurement system of OH reactivity in the atmosphere by using a laser-induced pump and probe technique, Rev. Sci. Instrum., 75, 2648–2655, doi:10.1063/1.1775311, 2004.

San Joaquin Valley Unified Air Pollution Control District, Adopted 2007 ozone plan: http://www.valleyair.org/Air_Quality_Plans/AQ_Final_Adopted_Ozone2007.htm, last access February 2012, 2007.

Schade, G. W. and Goldstein, A. H.: Fluxes of oxygenated volatile organic compounds from a ponderosa pine plantation, J. Geophys. Res., 106(D3), 3111–3123, doi:10.1029/2000JD900592, 2001.

Sillman, S.: The use of NO_y, H_2O_2, and HNO_3 as indicators for ozone-NO_x-hydrocarbon sensitivity in urban locations, J. Geophys. Res. 100(D7), 14175–14188, doi:10.1029/94JD02953, 1995.

Sinha, V., Williams, J., Crowley, J. N., and Lelieveld J.: The Comparative Reactivity Method – a new tool to measure total OH reactivity in ambient air, Atmos. Chem. Phys., 8, 2213–2227, 2008.

Sinha, V., Williams, J., Lelieveld, J., Ruuskanen, T. M., Kajos, M. K., Patokoski, J., Hellen, H., Hakola, H., Mogensen, D., Boy, M., Rinne, J., and Kulmala, M.: OH reactivity measurements within a boreal forest: evidence for unknown reactive emissions, Environ. Sci. Technol., 44, 6614–6620, doi:10.1021/es101780b, 2010.

Steiner, A. L., Tonse, S., Cohen, R. C., Goldstein, A. H., and Harley, R. A.: Influence of future climate and emissions on regional air quality in California, J. Geophys. Res., 111(D18), D18303, doi:18310.11029/12005JD006935, 2006.

Steiner, A. L., Cohen, R. C., Harley, R. A., Tonse, S., Millet, D. B., Schade, G. W., and Goldstein, A. H.: VOC reactivity in central California: comparing an air quality model to ground-based measurements, Atmos. Chem. Phys., 8, 351–368, doi:10.5194/acp-8-351-2008, 2008.

Steiner, A. L., Davis, A. J., Sillman, S., Owen, R. C., Michalak, A. M., and Fiore A. M.: Observed suppression of ozone formation at extremely high temperatures due to chemical and biophysical feedbacks, Proc. Natl. Acad. Sci., 107, 19685–19690, doi:10.1073/pnas.1008336107, 2010.

Stephens, S., Madronich, S., Wu, F., Olson, J. B., Ramos, R., Retama, A., and Muñoz, R.: Weekly patterns of Mexico City's surface concentrations of CO, NO_x, PM_{10} and O_3 during 1986–2007, Atmos. Chem. Phys., 8, 5313–5325, 2008.

Thornton, J. A., Wooldridge, P. J., Cohen, R. C., Martinez, M., Harder, H., Brune, W. H., Williams, E. J., Roberts, J. M., Fehsenfeld, F. C., Hall, S. R., Shetter, R. E., Wert, B. P., and Fried, A.: Ozone production rates as a function of NO_x abundances and HO_x production rates in the Nashville urban plume, J. Geophys. Res., 107(D12), 4146, doi:10.1029/2001JD000932, 2002.

Trainer, M., Parrish, D. D., Goldan, P. D., Roberts, J., and Fehsenfeld, F. C.: Review of observation-based analysis of the regional factors influencing ozone concentrations, Atmos. Environ., 34, 2045–2061, doi:10.1016/S1352-2310(99)00459-8, 2000.

van der A., R. J., Eskes, H. J., Boersma, K. F., van Noije, T. P. C., Van Roozendael, M., De Smedt, I., Peters, D. H. M. U., and Meijer, E. W.: Trends, seasonal variability and dominate NO_x source derived from a ten year record of NO_2 measured from space, J. Geophys. Res., 113, D04302, doi:10.1029/2007JD009021, 2008.

Williams, E. J., Baumann, K., Roberts, J. M., Bertman, S. B., Norton, R. B., Fehsenfeld, F. C., Springston, S. R., Nunnermacker, L. J., Newman, L., Olszyna, K., Meagher, J., Hartsell, B., Edgerton, E., Pearson, J. R., and Rodgers, M. O.: Intercomparison of ground-based NO_y measurement techniques, J. Geophys. Res., 103(D17), D17, 22,261–22,280, doi:10.1029/98JD00074, 1998.

Wilson, R. C., Fleming, Z. L., Monks, P. S., Clain, G., Henne, S., Konovalov, I. B., Szopa, S., and Menut, L.: Have primary emission reduction measures reduced ozone across Europe? An analysis of European rural background ozone trends 1996–2005, Atmos. Chem. Phys., 12, 437–454, doi:10.5194/acp-12-437-2012, 2012.

Zhang, Q., Streets, D. G., He, K., Wang, Y., Richter, A., Burrows, J. P., Uno, I., Jang, C. J., Chen, D., Yao, Z., and Lei, Y.: NO_x emission trends for China, 1995-2004: the view from the ground and the view from space, J. Geophys. Res., 112(D22), D22306, doi:10.1029/2007JD008684, 2007.

Zhong, S. Y., Whiteman, C. D., and Bian, X. D.: Diurnal evolution of three-dimensional wind and temperature structure in California's Central Valley, 43 J. Appl. Meteorol., 43, 1679–1699, doi: 10.1175/JAM2154.1, 2004.

3.2. Evidence for NO_x control over nighttime SOA formation

Reproduced from: A. W. Rollins, E. C. Browne, K.-E. Min, S. E. Pusede, P. J. Wooldridge, D. Gentner, A. H. Goldstein, S. Liu, D. A. Day, L. M. Russell, and R. C. Cohen (2012) Evidence for NO_x Control over Nighttime SOA Formation, Science, 337, 1210-1212. The Supplimental Information is found at the end of the article.

CalNex study topics addressed: *sources of NO_X and VOC, nighttime chemistry, production and removal timescales of oxidation products, role of VOCs*

Abstract: Laboratory studies have established a number of chemical pathways by which nitrogen oxides (NO_x) affect atmospheric organic aerosol (OA) production. However, these effects have not been directly observed in ambient OA. We report measurements of particulate organic nitrates in Bakersfield, California, the nighttime formation of which increases with NO_x and is suppressed by high concentrations of organic molecules that rapidly react with nitrate radical (NO_3)—evidence that multigenerational chemistry is responsible for organic nitrate aerosol production. This class of molecules represents about a third of the nighttime increase in OA, suggesting that most nighttime secondary OA is due to the NO_3 product of anthropogenic NO_x emissions. Consequently, reductions in NO_x emissions should reduce the concentration of organic aerosol in Bakersfield and the surrounding region.

Introduction

Organic aerosol (OA) constitutes about half of the total submicrometer particulate mass in the troposphere (1–3). OA is emitted to the atmosphere both directly as particles (primary OA, POA) and produced in the atmosphere through oxidation of volatile molecules (secondary OA, SOA), although evidence suggests that SOA is dominant (4). Owing to the complexity of SOA chemistry, major gaps exist in our ability to predict the time evolution of the chemical, physical, and optical properties of aerosols. A key example is our inability to predict the response of SOA to changes in emissions of nitrogen oxides (NO_x). Although laboratory evidence shows that NO_x should substantially affect atmospheric SOA formation, a coherent understanding of the nonlinear SOA/NO relationship has not emerged (5). This issue is important because NO_x has decreased by 30% or more in the United States and United Kingdom in the last decade, while comparable increases have occurred in China (6–9). Direct evidence that these changes in NO_x affect aerosol would greatly aid in the understanding of SOA.

SOA is formed through the gas-phase oxidation of volatile organic compounds (VOCs) by reactions with the hydroxyl radical (OH), ozone (O_3), and the nitrate radical (NO_3), producing condensable material (10). Most laboratory (10, 11) and field [e.g., (2, 12)] SOA studies have focused on the role of oxidation via O_3 and OH as SOA sources. Reactions of organic compounds with NO_3 are also important for oxidizing unsaturated atmospheric compounds (13), and NO_3 is unique in that it is almost exclusively a by-product of anthropogenic NO emissions (reaction 1).

$$NO_2 + O_3 \rightarrow NO_3 + O_2 \qquad (1)$$

Due to its photolabile nature and rapid reaction with nitric oxide (NO), NO_3 is present primarily in the nighttime atmosphere. Oxidation products of nitrate radical chemistry have a unique

chemical signature due to the high yields, to form organic nitrates ($RONO_2$). Organic nitrates are also formed during the day by OH-initiated chemistry in the presence of NO, but with much lower yields. Laboratory studies of SOA from NO_3 have revealed both large aerosol yields, and the importance of multigenerational chemistry on compounds with multiple C-C double bonds. For example, Ng et al. (14) and Rollins et al. (15) studied the aerosol formed during NO_3 oxidation of isoprene. Both studies found large SOA yields (4 to 24%) and showed that the condensable compounds were formed not from the products of the initial NO_3 + isoprene reaction, but mostly from further oxidation of the first-generation products. Similar results were found for NO_3 + limonene (16).

Discussion

We have developed a fast, sensitive, and precise instrument capable of measuring the particulate total alkyl and multifunctional nitrates (pΣANs) (SI; 17). Using this instrument, we made observations of pΣANs along with key precursors (NO_2, O_3, VOC) and aerosol properties in Bakersfield, California, as part of the CalNex-2010 experiment. Bakersfield is of interest due to its location in California's San Joaquin Valley, with abundant sources of biogenic VOC (BVOC) and NO_x and (for the United States) relatively severe particulate matter (PM) air pollution. We interpret the observations as evidence for a substantial nighttime chemical source of pΣAN.

Air parcels arriving at the site had traveled typically through the agricultural San Joaquin Valley, and then through the Bakersfield urban center for 1 to 2 hours before reaching the site. During the experiment, OA concentrations exceeding 10 $\mu g/m^3$ were frequently observed at night. A possible contributor to these high concentrations is the reduction in the boundary layer (BL) depth before sunset in the San Joaquin Valley. At a site near Bakersfield, Bianco et al. (18) observed that during May and June, the BL on average would decrease from ≈1.7 km at noon to ≈300 m just before sunset. The nighttime increase in OA observed in this study, however, occurred after sunset (Fig. 3.2.1), and thus after the BL is thought to have reached its minimum depth. We do not know the extent to which the aerosol that we measured at the surface was mixed through the nocturnal BL; however, the diurnal patterns vary little from day to day, suggesting the observations shown in Fig. 3.2.1 are characteristic of a large spatial scale and not dominated by local surface layer plumes. There was no appreciable change in the prevailing wind direction (west-northwest) from 6 p.m. to 11 p.m., and back-trajectories for air arriving at this site in this time interval follow a common path arriving from the west-northwest (Fig. 3.2.4).

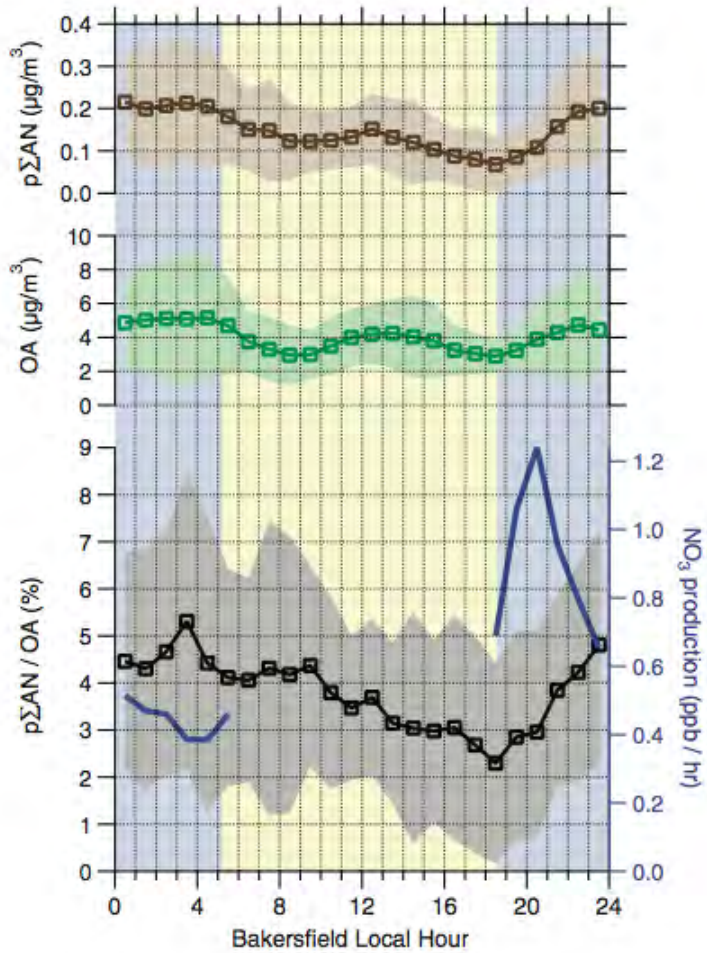

Figure 3.2.1. *Diurnal trends (means shown with T1s ranges in shading) in pΣAN (brown), OA (green), pΣAN/ OA (black), and NO_3 production rate (blue). Blue shading indicates nighttime (solar zenith angle > 85°), and yellow indicates daytime.*

The average diurnal trends in pΣAN, OA, and the ratio of these two are shown in Fig. 3.2.1. Additionally, diurnal averages in NO_2, O_3, temperature, and relative humidity are shown in Fig. 3.2.5. The OA and pΣAN have both a midday maximum and a nighttime/early morning maximum. The average OA maximum at night exceeds that of the midday by 24%, which is an unusual observation compared to studies in other large urban areas that have observed the daily OA maxima midday (19–21). Although aerosol mass spectrometer (AMS) data did not readily quantify POA and SOA individually at night, size distributions and tracers suggest that POA was at most 10 to 20% of OA (see materials and methods SI).

On average, the pΣAN nitrate groups increased from 2.3% of OA at sunset to 4.7% at 23:30 local time. The rapid increase in the pΣAN fraction begins immediately after sunset, when NO_3 chemistry becomes possible. Although temperature is expected to affect SOA through changes in vapor pressures, it does not appear to have played the dominant role in the trends; temperatures peaked near 15:00 local time and decreased significantly before sunset (Fig. 3.2.4). The $RONO_2$ contribution to OA is relatively constant in the morning hours between 6:00 and 9:30 before

obvious SOA production. After 10:00, when OA concentration is increasing, the observations indicate that as photochemistry generates SOA, pΣAN becomes a smaller fraction of the total OA mass. Factor analysis of AMS measurements are consistent with this interpretation. A unique nighttime factor was identified that becomes less important as the aerosol mass increases during daylight, and daytime SOA factors did not increase until after 9:00.

The observation that pΣAN and pΣAN/OA increase at night suggests not only that NO_3 chemistry is important for SOA production at night, but also that the organic nitrate tracers of this chemistry contribute appreciably to the total OA. Over the 5-hour time period after sunset (18:30 to 23:30), the average total OA increase was 1.54 $\mu g/m^3$. The added mass of $-ONO_2$ functional groups alone accounted for 0.129 $\mu g/m^3$ (8.4%) of this total mass. That this ratio increased continuously for 5 hours after sunset while Bakersfield is only 1 to 2 hours upwind suggests that the effect is somewhat regional. Assuming that the organic molecules with nitrate functional groups have an average molecular weight of 200 to 300 g/mol (22), we calculate that 27 to 40% of the OA growth was due to molecules with nitrate functionalities. This fraction of OA molecules that are nitrates is similar to the nitrate yields from a number of NO_3 + BVOC reactions (23). Thus, these numbers do not preclude all of the SOA production, including non-nitrates, being a result of NO_3 chemistry. The other potential source of nighttime SOA, O_3 + alkenes, is unlikely to be nearly as important because the rates of these reactions are typically at most one-tenth of the NO_3 rates (materials and methods S1.3).

To examine the role of NO_x emissions for SOA formation, we used observations of $[NO_2]$ and $[O_3]$ to calculate the nitrate radical production rates ($PNO_3 = k_1[NO_2][O_3]$) and compared these to the rate of net increase in pΣAN at night, defined as the difference ($\Delta p\Sigma AN = ([p\Sigma AN]_{23:30} - [p\Sigma AN]_{18:30})/5$ hours) on each night. Figure 3.2.2 compares ΔpΣAN to the average PNO3. The correlations with PNO3 are modest ($r = 0.44$). However, if we exclude those nights when the NO_3 lifetime to gas-phase reactions was short ($t < 65$ s), a much stronger correlation between the PNO_3 and ΔpΣAN ($r = 0.73$) is inferred. A linear fit to this data ($\Delta p\Sigma AN/PNO_3 = 0.015$) suggests that ~1.5% of NO_3 reacts to form particle-bound nitrates, a number that is somewhat lower than expected from chamber studies and could be used to estimate the efficacy of NO_x emission reductions for reducing fine PM at this location.

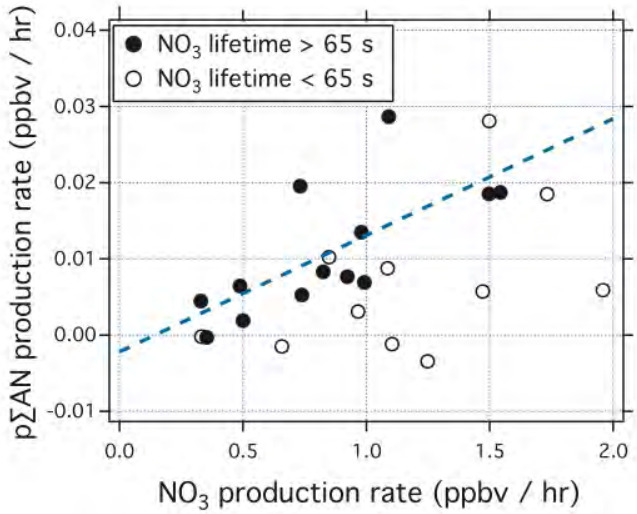

Figure 3.2.2. *Observations of trends in nighttime production rate of pΣAN with NO_3 production rate. Data are high NO_3 reactivity (open circles) and lower NO_3 reactivity (solid circles). Dashed blue line is a linear fit to low-reactivity data with a slope of 0.015 and r = 0.73.*

Generally, NO_3 reactivity at the site is dominated by BVOC from the valley and surrounding mountains (Fig. 3.2.6). When the NO_3 lifetime is short, we find that a larger fraction of the reactivity is due to primary biogenic VOC than on other nights, suggesting that BVOC can suppress aerosol formation. Previous in situ observations have shown that biogenics react rapidly with NO_3, reducing the NO_3 concentration (24). We believe this is the likely mechanism for aerosol suppression. The removal of NO_3 by primary VOC results in production of first-generation gas-phase nitrates with vapor pressures that are too high ($C^* \approx 103$ to 106 $\mu g/m^3$) for the molecules to be incorporated into aerosol to an appreciable extent. The condensable nitrates that we observe in the particle phase are likely second- or higher-generation oxidation products, produced by the slower oxidation of the first-generation products (15, 16). Based on the measurements of RH, and aerosol surface area and composition, we estimate that N_2O_5 heterogeneous loss has a small impact on NO_3 concentration (<10%), and thus NO_3 variability is dominated by its source term (reaction 1) and gas-phase reactivity. Figure 3.2.2 also shows that the kinetics of aerosol $RONO_2$ formation are approximately linear with PNO_3, indicating that aerosol precursors are abundant and that NO_3 production is rate limiting. Because this SOA is produced by reactions of NO_3, it can be considered anthropogenic. Although the carbon may be of biogenic origin, without high NO_x emissions it would not be produced.

The observation that VOC with high SOA yields may suppress SOA formation is surprising. To demonstrate that this is kinetically possible in the NO_x/VOC regime observed in Bakersfield, we modeled SOA formation from NO_3 oxidation of limonene (Fig. 3.2.3). We use limonene as an example VOC because of its relatively high concentrations in Bakersfield and its high SOA yield, and because we have some knowledge of the kinetics of its oxidation products (16). Details of the box model used are included in the materials and methods SI. We find that because the second-generation products have SOA yields ~2.5 times as large as those of the first-generation products and that high concentrations of limonene inhibit the formation of these less-volatile products, SOA production slows in the high-limonene regime. At the same time, given

sufficient O_3, increases in NO_2 always lead to more SOA owing to the higher NO_3 production rate.

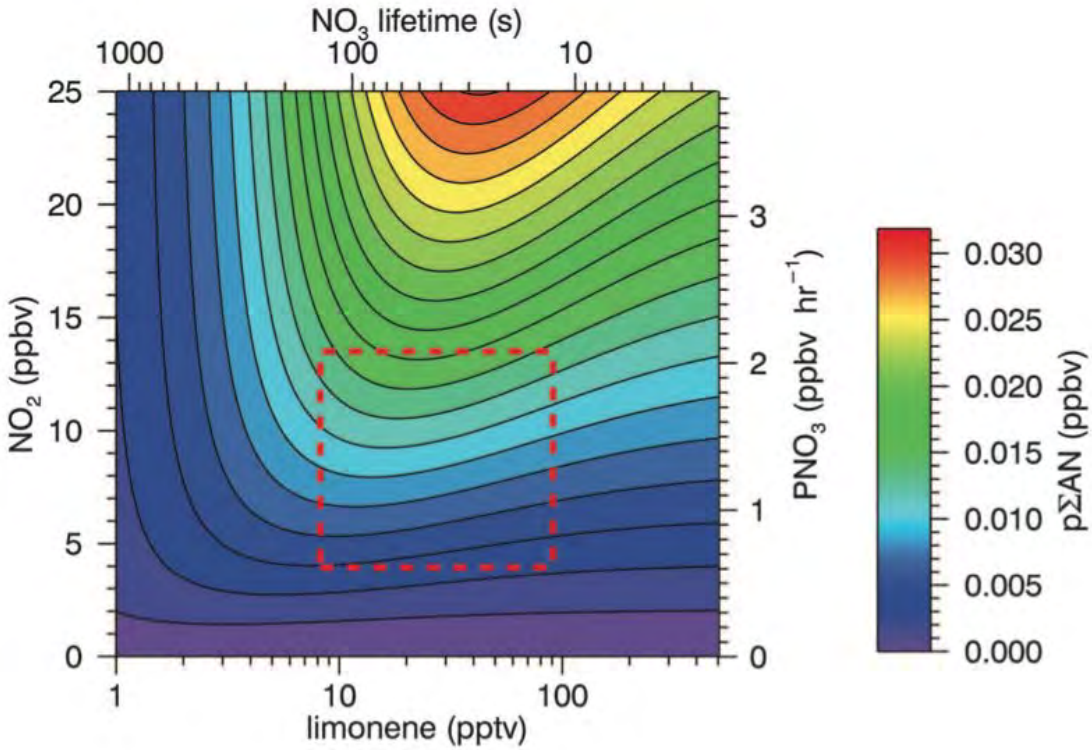

Figure 3.2.3. *Simulation of multigenerational SOA formation from the reaction of NO_3 with limonene as a function of NO_2 and limonene at 50 ppb O_3. We assume that Bakersfield (1 to 2 hours upwind) is the major NO_x source and therefore show contours that are ppb of pΣAN after 2-hour model runs. For longer runs (up to 5 hours), the pΣAN scaled approximately linearly with time. The production rates of NO_3 corresponding to the NO_2 concentration are shown on the right axis. Top axis shows the total NO_3 gas-phase lifetime with limonene at 34% of the total NO_3 loss. Red dashed box highlights the NO_2 and limonene concentration range typically observed in Bakersfield, showing that increases in limonene here are expected to lead to less aerosol production. [pptv (ppbv), parts per trillion (billion) by volume]*

Our findings suggest that SOA formation via nighttime nitrate radical chemistry in Bakersfield is a large PM source, which frequently results in the daily maximum OA concentration during the summer. The high concentrations of NO_2 and O_3 at night resulted in very high NO_3 production rates [frequently greater than 1 part per billion (ppb) hour^{-1}]. Nevertheless, concentrations of reactive BVOCs were frequently high enough that pΣAN formation was inhibited, suggesting that the pΣAN precursors are less reactive than the primary VOCs and have a somewhat reduced volatility. A good correlation between production rates of NO_3 and pΣAN was observed, suggesting that the targeted reductions in NO_x at this location should reduce OA mass. Although attributing sources of daytime SOA as biogenic or anthropogenic remains challenging, our results show that pΣANs are a large fraction of nighttime growth and likely a result of NO_3 chemistry. That this SOA would not be produced in the absence of NO_x makes nighttime pΣANs a clear tracer for anthropogenically controlled SOA, regardless of the carbon source.

Supplimentary Information for Rollins et al., 2012.

S1.1 CalNex site and measurements

Measurements reported here were performed at the Bakersfield supersite May 15–June 24 during CalNex-2010. This site was approximately 6 km southeast of the Bakersfield city center, which is at the southern end of the San Joaquin Valley in Central California. A map of the area near the measurement site is shown in Fig. 3.2.4. During the daytime, strong winds from the northwest were consistently observed. After dark the winds slowed, but typically maintained from the WNW until after midnight. The HYSPLIT model (1) was used to calculate typical back-trajectories of air masses arriving at the site between 19:00 and 23:00 local time and these trajectories agreed well with wind direction measured at the site. Air was transported down the San Joaquin Valley where both biogenic and anthropogenic VOC accumulate, and finally through the Bakersfield urban area before arriving at the measurement site. We estimate the largest NO_x inputs occurred within 1–2 hours of air arriving at the site.

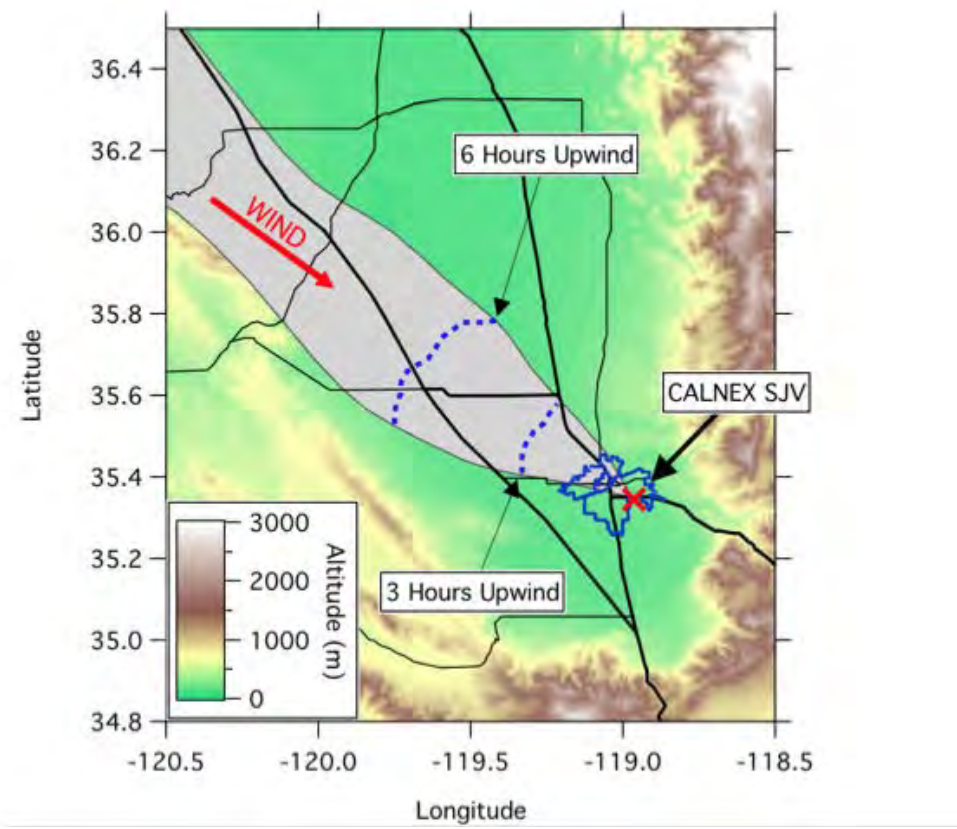

Figure 3.2.4. *Map of typical transport of air upwind of CalNex SJV site. Gray region shows typical back trajectories from 11PM local time generated using HYSPLIT from May and June 2010. Blue outlines the Bakersfield urban area. Black lines indicate freeways and major highways.*

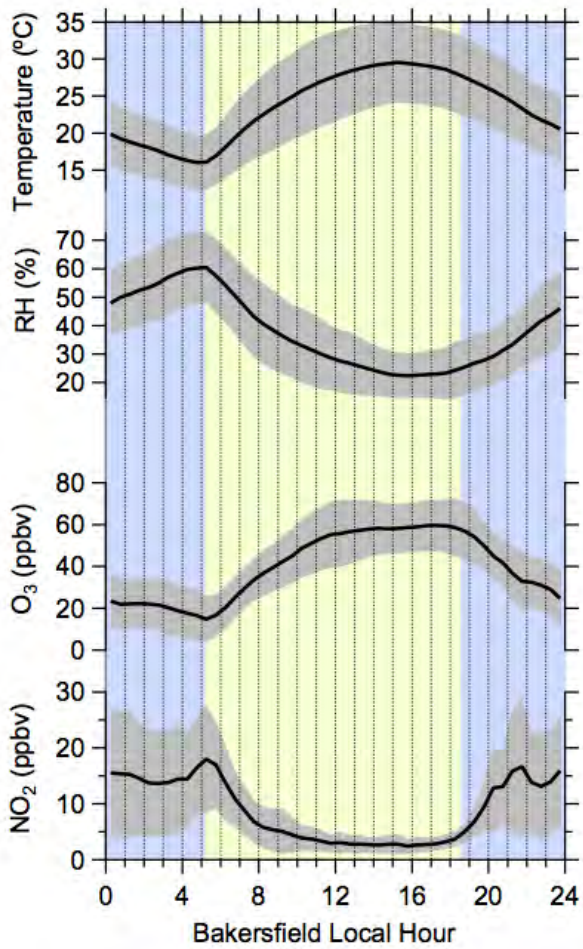

Figure 3.2.5. *Diurnal averages of, from top; temperature, relative humidity, O_3, and NO_2 measured at the site during the study period. For each quantity, dark line shows diurnal mean and gray shaded regions indicate ±1σ from mean. Blue background shading indicates nighttime (solar zenith angle > 85°) and yellow indicates daytime.*

TD-LIF: The inlet for the pΣAN and NO_2 measurements was located 5.5 m above ground level (AGL) on a scaffold tower. The pΣAN instrument uses an activated carbon denuder to remove gas phase NO_y prior to sampling into the TD-LIF instrument (2), which quantifies the mixing ratio sum of all nitrate groups in alkyl and multifunctional organic compounds (ΣANs, 3). Volume mixing ratios of ΣANs are converted to mass concentration using the molecular weight of the $–ONO_2$ group (62 amu). In the lab we have verified that gas phase NO_y compounds (e.g. NO_2, n-propyl nitrate, HNO_3) are completely removed by the denuder and that NH_4NO_3 aerosol are not detected as pΣANs. We used a PM2.5 cyclone on the TD-LIF inlet upstream of the denuder to reject larger particles. pΣAN measurements were reported every 1s and averaged to the AMS time resolution for analysis. Measurements at the site of aerosol $RONO_2$ were also made by FTIR analysis of filter samples collected for 3–6 hours for PM1 and for 24 hour samples of PM2.5. Comparison of the PM2.5 and PM1 FTIR suggested that 83% of the PM2.5 $RONO_2$ is in PM1, and so the TD-LIF data were scaled by this factor for comparison to AMS PM1 OA. A comparison between the aerosol $RONO_2$ techniques was performed by averaging the TD-LIF to the FTIR time resolution. The correlation coefficient was 0.70, and fit to the

datasets was TD-LIF = 1.39 x FTIR + 0.08 μ g/m^3. Uncertainties in the FTIR measurement are typically ±25% and those of the TD-LIF ±10%.

AMS: PM1 OA was measured with a time of flight Aerodyne Aerosol Mass Spectrometer (AMS), at 3 m AGL (4). A uniform collection efficiency of 80% was used for the AMS data, which was determined by comparing AMS mass with that calculated using a scanning mobility particle sizer. The comparison between OM measured with FTIR and AMS did not have a day/night dependence, and was not improved by using a composition-dependent CE (5) supporting the use of a uniform CE. AMS measurements were reported every 5–6 minutes. PMF analysis of the AMS data revealed a single factor associated with OA formation at night. This factor contained character both of POA and SOA. As has been seen both in chamber studies of nitrate radical generated SOA (6) and organic nitrate standards (7, 8), the CO_2^+ fragment from particulate $RONO_2$ is a relatively insignificant component of the AMS spectrum compared to other SOA making its AMS spectrum appear much closer to that of what is typically defined as the hydrocarbon like organic aerosol (HOA) and identified as POA. Therefore, we did not attempt to quantify POA and SOA at night using PMF.

We report the mass of OA calculated using what is currently the typical high resolution AMS data reduction method. This analysis excludes non-carbon containing fragments such as NO_x, SO_x, and NH_x from the analysis and therefore could potentially underestimate OA when these fragments are indeed of organic origin. This is a small underestimate, and significantly lower than the uncertainty in the AMS OA measurement (±30%). For example, the daily maximum organic nitrate mass we observed was 8.4%, which mostly fragments to NO_x in the AMS and therefore is disregarded as organic.

GC: VOC concentrations were measured via an automated in-situ gas chromatograph (Agilent 5890) equipped with a flame ionization detector and a mass spectrometer (Agilent 5971). The instrument operated in situ with a custom system that automated sample collection and analysis. Ambient samples were collected for the first half of every hour via an inlet at the top of the tower (18.6 m AGL). Ozone and particulate matter was removed at the inlet and the sample travelled down a 1⁄4” heated Silcosteel line at ~1 L min^{-1} to a preconcentration system, where a ~600 mL sample was concentrated on a custom-− - made adsorbent trap (glass beads: Tenax TA: Carbopak B: Carbopak X held in place by glass wool on each end) and thermally desorbed onto a DB-624 capillary column (60 m × 0.32 mm × 1.8 μm), and then analyzed by the mass spectrometer. An additional ~600 mL sample was concentrated on a adsorbent trap of glass beads, Carbopak B, Carbopak X, and Carboxen 1000 and thermally desorbed onto a Plot-Q capillary column (30 m × 0.32 mm × 20.0 μm), for analysis by the flame ionization detector. Calibrations were performed using gas-phase standards and liquid standards as part of daily calibration and zero checks, and multi-point calibrations at the beginning and end of the campaign. Limits of detection were at or near 1 pptv for most compounds.

S1.2 NO_3 reactivity calculations

The measurements of the individual VOCs were used to calculate the NO_3 gas phase loss. Reaction rate constants available in the literature were used for many of the compounds including those that dominated NO_3 reactivity. Reaction rate coefficients were estimated from

structural analogs for a number of less important species. Rate coefficients, used typical VOC concentrations and reactivities are listed in Table 3.2.1. Fig. 3.2.6 shows the total reactivity for each night of the campaign, and typical reactivity distributions for the high reactivity nights (NO_3 lifetime < 65 s) and low reactivity nights.

Table 3.2.1. *Reaction rate coefficients used in the calculation of NO_3 gas phase sinks. References rate coefficient references for most molecules are listed in the reference column. For molecules where no rate coefficient was available, a coefficient was estimated (est) based on coefficients for structurally similar molecules and the most relevant reference is listed. References for the MCM rates are 18–21.*

	Molecule	Mean Concentration (pptv)	Rate Coefficient (298 K)	Reference	Mean Reactivity (1/s)
Alkenes					
	1-methylcyclopentene	10	7.90E-12	est, (9)	1.97E-03
	2-methyl-2-pentene and c3-methyl-2-pentene	2	7.40E-12	est, (10)	3.39E-04
	1-methylcyclohexene	1	1.03E-11	(9)	2.61E-04
	c2-pentene	26	3.70E-13	MCM	2.45E-04
	unidentified C9 cycloalkene	9	7.20E-13	est, (9)	1.69E-04
	t2-butene	17	3.90E-13	MCM	1.47E-04
	c2-butene	18	3.50E-13	MCM	1.42E-04
	propene	301	9.54E-15	MCM	7.32E-05
	1-butene and isobutene	82	1.32E-14	MCM	2.75E-05
	C7 cyclopentenes, 2 isomers	2	5.42E-13	(9)	2.28E-05
	1-pentene	30	1.20E-14	MCM	8.53E-06
	1-hexene	26	1.20E-14	MCM	7.69E-06
Aromatics					
	phenol	32	2.81E-12	(10)	2.23E-03
	t2-butenylbenzene	4	1.50E-12	MCM styrene rate	1.35E-04
	indene	1	4.10E-12	(11)	8.12E-05
	1-ethenyl-2- and 3-methyl-benzene	1	1.50E-12	MCM styrene rate	2.59E-05
	1,2,4-trimethylbenzene	63	1.80E-15	MCM	3.14E-06
	m- and p-xylene	173	3.80E-16	MCM	1.73E-06
	1,2,3-trimethylbenzene	21	1.90E-15	MCM	1.17E-06
	1-ethyl-3- and 4-methylbenzene	56	6.60E-16	MCM	1.05E-06
	naphthalene	4	9.20E-15	(10)	9.38E-07
	indan	4	6.60E-15	(11)	7.26E-07
	o-xylene	59	4.60E-16	MCM	7.06E-07
	1,3,5-trimethylbenzene	24	8.80E-16	MCM	5.83E-07
	p-diethylbenzene	15	1.20E-15	est, MCM	5.03E-07
	2-methylindan	2	6.60E-15	use indan rate	3.73E-07
	p-cymene	11	9.90E-16	(12)	2.96E-07
	1-ethyl-2-methylbenzene	14	7.10E-16	MCM	2.71E-07
	1,4-dimethyl-2-ethylbenzene	4	2.10E-15	est, MCM	2.24E-07
	1,2,3,5-tetramethylbenzene	3	3.20E-15	est, MCM	2.14E-07

	1,3-dimethyl-4-ethylbenzene	4	2.10E-15	est, MCM	2.07E-07
	1-methylindan	2	6.60E-15	use indan rate	2.01E-07
	1,2,3,4-tetramethylbenzene	2	3.20E-15	est, MCM	1.74E-07
	1,2,4,5-tetramethylbenzene	2	3.20E-15	est, MCM	1.62E-07
	1,2-dimethyl-4-ethylbenzene	3	2.10E-15	est, MCM	1.61E-07
	ethylbenzene	47	1.20E-16	MCM	1.47E-07
	dimethylnaphthalenes	4	1.70E-15	(13), assume no2 = 10.7 ppb	1.46E-07
	1-methyl-3-n-propylbenzene	9	4.50E-16	use 1-methyl-3ethylbenzene rate, MCM	9.89E-08
	1,2-dimethyl-3-ethylbenzene	2	2.10E-15	est, MCM	8.00E-08
	1,3-dimethyl-2-ethylbenzene	1	2.10E-15	est, MCM	5.36E-08
	n-propyl-benzene	12	1.60E-16	MCM	5.29E-08
	m-cymene	1	9.90E-16	use p-cymene rate, (12)	3.46E-08
	o-diethylbenzene	1	1.00E-15	est, MCM	2.17E-08
	2-methylnaphthalene	3	2.70E-16	(13), assume no2 = 10.7 ppb	1.99E-08
	cumene	5	1.40E-16	MCM	1.80E-08
	1-methylethenylbenzene	1	7.60E-16	MCM	1.08E-08
	1-methylnaphthalene	2	1.90E-16	(13)	9.56E-09
	n-butyl_benzene	2	1.40E-16	use MCM propylbenzene	5.84E-09
	isobutylbenzene	1	1.40E-16	use MCM propylbenzene	3.79E-09
	m-diethylbenzene	4	6.40E-19	est, MCM	6.04E-11
	1-methyl-2-n-propylbenzene	2	7.60E-26	use 1-methyl-2ethylbenzene rate, MCM	3.90E-18
Aldehydes					
	hexanal	469	1.70E-14	(14)	1.90E-04
	pentanal	88	1.50E-14	MCM	2.99E-05
	methacrolien	81	3.40E-15	MCM	7.14E-06
	propanal	125	6.31E-15	MCM	2.01-05
	butanal	82	1.10E-14	MCM	2.16E-05
Terpenes					
	d-limonene	34	1.22E-11	MCM	1.10E-02
	alpha-pinene	45	6.21E-12	MCM	6.85E-03
	beta-myrcene	19	1.28E-11	(15)	4.23E-03
	delta-3-carene	13	8.10E-12	(16)	2.29E-03
	t-beta-ocimene	4	2.40E-11	(17)	2.11E-03
	sabinene	6	1.07E-11	(15)	1.80E-03
	isoprene	75	6.96E-13	MCM	1.25E-03
	gamma-terpinene	1	2.40E-11	(15)	6.19E-04
	camphene	8	2.51E-12	use b-pinene rate	5.42E-04
	alpha-thujene	3	6.21E-12	use a-pinene rate	5.06E-04
	beta-pinene	4	2.51E-12	MCM	2.55E-04

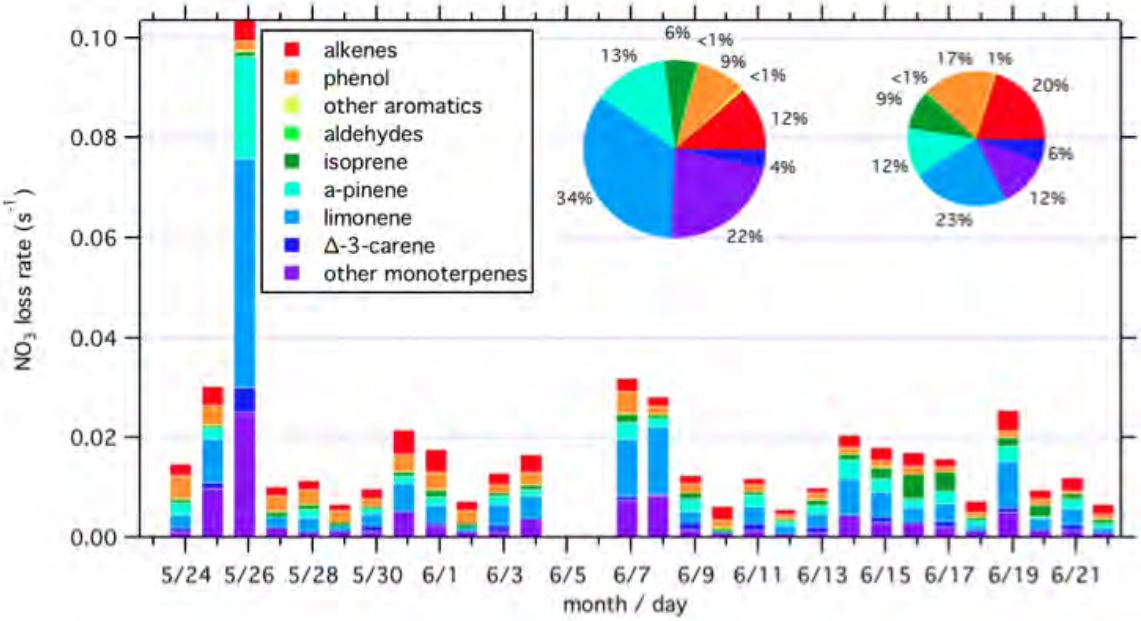

Figure 3.2.6. *Calculated average NO_3 reactivity for each night. Pie charts show distribution of NO_3 reactivity for* ***(left)*** *high reactivity nights and* ***(right)*** *low reactivity nights.*

S1.3 kinetics model

The kinetics model we used to simulate SOA formation from the oxidation of limonene is based on the work by Fry et al. (6). Our model is a reduced version that captures the essential NO_3 chemistry needed to resolve the multigenerational kinetics, while reducing the computational expense by lumping species with the same NO_3 rate constants and similar volatility (Fig. 3.2.7). The simulations are run with O_3 fixed at 50 ppbv, and NO_2 and limonene are also fixed throughout the model runs. The chemistry is integrated for 2 hours, which is the approximate time for transport of air parcels through the high-NO_x Bakersfield urban area. NO_3 and N_2O_5 are calculated online. An additional gas phase NO_3 sink is introduced to hold limonene at 34% of total NO_3 reactivity (Fig 3.2.6). Due to consistently low relative humidities (17–40%, mean of 30%), and high organic:sulfate ratios (8:1 typical), the N_2O_5 heterogeneous reaction probability (γ) in Bakersfield was likely below 0.01 (22). Aerosol surface area (SA) was on average 3 x 10^{-6} cm^2/cm^3. Using these SA and γ we calculate an N_2O_5 heterogeneous loss rate of k_{N2O5} = 2.0 x 10^{-4} s^{-1}. At this level and the high gas phase NO_3 reactivity, small variations in N_2O_5 heterogeneous loss have only minor (<10%) effects on NO_3 concentrations. Therefore we fixed k_{N2O5} at 2.0 x 10^{-4} s^{-1} in the simulations.

O_3 reactions with limonene are not considered in this model as they are too slow to be competitive with NO_3 as a sink for limonene in Bakersfield. The ratio of the reaction rates of NO_3 to O_3 for limonene (k_{NO3}/k_{O3}) at 298 K is 3.1 x 10^4. Thus, at an O_3 mixing ratio of 50 ppbv, an NO_3 mixing ratio of 16 pptv is sufficient for the NO_3 reaction to be 10 times as fast as that of O_3. Both steady state and kinetic calculations show that NO_3 was typically above this value at night.

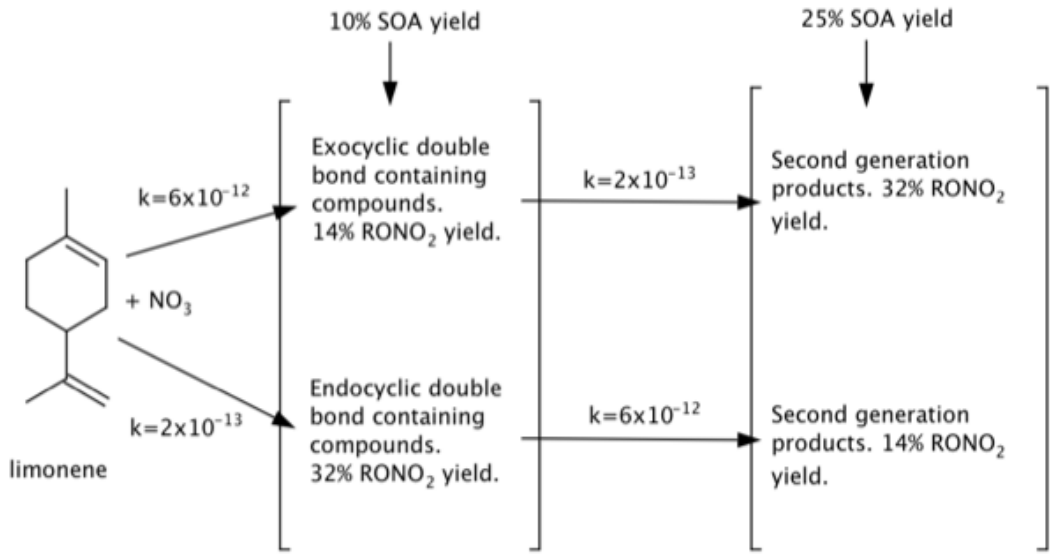

Figure 3.2.7. *Schematic of kinetics model. The two reaction sites in limonene react at different rates with NO_3, leaving one group of compounds with endocyclic double bonds, and another group with exocyclic double bonds. First generation products react with NO_3 at rates depending on the location of the remaining double bond. Condensed phase concentrations are calculated assuming 10% of first generation products condense, and 25% of second-generation products.*

References for Rollins et al., 2012:

1. Q. Zhang, et al. "Ubiquity and dominance of oxygenated species in organic aerosols in anthropogenically-influenced Northern Hemisphere midlatitudes." Geophys. Res. Lett., 34, L13801, doi:10.1029/2007GL029979, 2007A.
2. J. L. Jimenez, et al. "Evolution of Organic Aerosols in the Atmosphere." Science 326, 1525, doi:10.1126/science.11080353, 2009.
3. C. L. Heald, D. A. Ridley, S. M. Kreidenweis, and E. E. Drury. "Satellite observations cap the atmospheric organic aerosol budget." Geophys. Res. Lett. 37 (L24808), doi:10.1029/2010GL045095, 2010.
4. R. Volkamer, F. San Martini, L. T. Molina, D. Salcedo, J. L. Jimenez, and M. J. Molina. "A missing sink for gas-phase glyoxal in Mexico City: Formation of secondary organic aerosol." Geophys. Res. Lett. 34 (L19807), doi:10.1029/1007GL030752, 2007.
5. B. Ervens, B. J. Turpin, and R. J. Weber. "Secondary organic aerosol formation in cloud droplets and aqueous particles (aqSOA): a review of laboratory, field and model studies." Atmos. Chem. Phys. 11, 11069-11102, doi:10.5194/acp-11-11069-2011, 2011.
6. C. R. Hoyle, M. Boy, N. M. Donahue, J. L. Fry, M. Glasius, A. Guenther, A. G. Haller, K. Huff Hartz, M. D. Petters, T. Petaja, T. Rosenoern, and A. P. Sullivan. "A review of the anthropogenic influence on biogenic secondary organic aerosol." Atmos. Chem. Phys. 11, 321-343, doi:/10.5194/acp-11-321-2011, 2011.
7. Q. Zhang, D. G. Streets, K. He, Y. Wang, A. Richter, J. P. Burrows, I. Uno, C. J. Jang, D. Chen, Z. Yao, and Y. Lei. "NO_x emission trends for China, 1995-2004: The view from the ground and the view from space." J. Geophys. Res. 112(D22306), doi:10.1029/2007JD008684, 2007B.
8. US Environmental Protection Agency: Our Nation's Air – Status and Trends through 2008, Washington, DC, 2010.
9. D. C. Carslaw, S. D. Beevers, E. Westmoreland, M. L. Williams, J. E. Tate, T. Murrells, J. Stedman, Y. Li, S. Grice, A. Kent and I. Tsagatakis. "Trends in NO_x and NO_x emissions and ambient measurements in the UK." Version: July 2011.

10. B. W. LaFranchi, A. H. Goldstein, and R. C. Cohen. "Observations of the temperature dependent response of ozone to NO_x reductions in the Sacramento, CA urban plume." Atmos. Chem. Phys. 11, 6945-6960, doi:10.5194/acp-11-6945-2011, 2011.
11. M. Hallquist et al. "The formation, properties and impact of secondary organic aerosol: current and emerging issues." Atmos. Chem. Phys., 9, 5155-5236, 2009.
12. J. H. Kroll and J. H. Seinfeld. "Chemistry of secondary organic aerosol: Formation and evolution of low-volatility organics in the atmosphere." Atmos. Environ. 42, 3593-3624, 2008.
13. L. Hildebrandt, E. Kostenidou, N. Mihalopoulos, D. R. Worsnop, N. M. Donahue, and S. N. Pandis. "Formation of highly oxygenated organic aerosol in the atmosphere: Insights from the Finokalia Aerosol Measurement Experiments." Geophys. Res. Lett. 37 (L23801), doi:10.1029/2010GL045193, 2010.
14. A. M. Winer, R. Atkinson and J. N. Pitts, Jr. "Gaseous Nitrate Radical: Possible Nighttime Atmospheric Sink for Biogenic Organic Compounds." Science 224(4645) doi:10.1126/science.224.4645.156, 1984.
15. M. Sprengnether, K. L. Demerjian, N. M. Donahue, and J. G. Anderson. "Product analysis of the OH oxidation of isoprene and 1,3-butadiene in the presence of NO." J. Geophys. Res. 107(D15), doi:10.1029/2001JD000716, 2002.
16. F. Paulot, J. D. Crounse, H. G. Kjaergaard, J. H. Kroll, J. H. Seinfeld, and P. O. Wennberg. "Isoprene photooxidation: new insights into the production of acids and organic nitrates." Atmos. Chem. Phys. 9 1479-1501, 2009.
17. A. E. Perring, A. Wisthaler, M. Graus, P. J. Wooldridge, A. L. Lockwood, L. H. Mielke, P. B. Shepson, A. Hansel, and R. C. Cohen. "A product study of the isoprene + NO_3 reaction." Atmos. Chem. Phys. 9 4945-4956, 2009.
18. A. W. Rollins, A. Kiendler-Scharr, J. L. Fry, T. Brauers, S. S. Brown, H.-P. Dorn, W. P. Dube, H. Fuchs, A. Mensah, T. F. Mentel, F. Rohrer, R. Tillmann, R. Wegener, P. J. Wooldridge, and R. C. Cohen. "Isoprene oxidation by nitrate radical: alkyl nitrate and secondary organic aerosol yields." Atmos. Chem. Phys. 9, 6685-6703, 2009.
19. N. L. Ng, A. J. Kwan, J. D. Surratt, A. W. H. Chan, P. S. Chhabra, A. Sorooshian, H. O. T. Pye, J. D. Crounse, p. O. Wennberg, R. C. Flagan, and J. H. Seinfeld. "Secondary organic aerosol (SOA) formation from reaction of isoprene with nitrate radicals (NO_3)." Atmos. Chem. Phys. 8, 4117-4140, 2008.
20. J. L. Fry, A. Kiendler-Scharr, A. W. Rollins, T. Brauers, S. S. Brown, H.-P. Dorn, W. P. Dube, H. Fuchs, A. Mensah, F. Rohrer, R. Tillmann, A. Wahner, P. J. Wooldridge, and R. C. Cohen. "SOA from limonene: role of NO_3 in its generation and degradation." Atmos. Chem. Phys., 11, 3879-3894, doi:10.5194/acp-11-3879-2011, 2011.
21. D. A. Day, P. J. Wooldridge, M. B. Dillon, J. A. Thornton and R. C. Cohen. "A thermal dissociation laser-induced fluorescence instrument for in situ detection of NO_2, peroxy nitrates, alkyl nitrates and HNO_3." J. Geophys. Res. 107(D6) doi: 10.1029/2001JD000779, 2002.
22. A. W. Rollins, J. D. Smith, K. R. Wilson and R. C. Cohen. "Real time in situ detection of organic nitrates in atmospheric aerosols." Environ. Sci. Technol. 44, 5540-5545, 2010.
23. M. R. Canagaratna, J. T. Jayne, J. L. Jimenez, J. D. Allan, M. R. Alfarra, Q. Zhang, T. B. Onasch, F. Drewnick, H. Coe, A. Middlebrook, A. Delia, L. R. Williams, A. M. Trimborn, M. J. Northway, P. F. DeCarlo, C. E. Kolb, P. Davidovits, and D. R. Worsnop. "Chemical and microphysical characterization of ambient aerosols with the Aerodyne Aerosol Mass Spectrometer." Mass. Spec. Rev. 26, 185-222, 2007.
24. L. Bianco, I. V. Djalalova, C. W. King, and J. M. Wilczak. "Diurnal Evolution and Annual Variability of Boundary-Layer Height and Its Correlation to Other Meteorological Variables in California's Central Valley." Boundary-Layer Meteorol. 140, 491 – 511, doi:10.1007/s10546-011-9622-4 2011.
25. B. J. Williams, A. H. Goldstein, N. M. Kreisberg, S. V. Hering, D. R. Worsnop, I. M. Ulbrich, K. S. Docherty, and J. L. Jimenez. "Major components of atmospheric organic aerosol in southern California as determined by hourly measurements of source marker compounds." Atmos. Chem. Phys. 10, 11577-11603, doi:10.5194/acp-10-11577-2010, 2010.
26. A. C. Aiken, et al. "Mexico City aerosol analysis during MILAGRO using high resolution aerosol mass spectrometry at the urban supersite (T0) – Part 1: Fine particle composition and organic source apportionment." Atmos. Chem. Phys. 9, 6633-6653, 2009.
27. C. J. Hennigan, M. H. Bergin, A. G. Russell, A. Nenes, and R. J. Weber. "Gas/particle partitioning of water-soluble organic aerosol in Atlanta." Atmos. Chem. Phys. 9, 3613-3628, 2009.
28. M. Hallquist, I. Wängberg, E. Ljungström, I. Barnes, and K.-H. Becker. "Aerosol and Product Yields from NO_3 radical-initiated oxidation of selected monoterpenes." Environ. Sci. Technol. 33, 553-559, 1999.

29. M. Spittler, I. Barnes, I. Bejan, K. J. Brockmann, Th. Benter, and K. Wirtz. "Reactions of NO_3 radicals with limonene and A-pinene: Product and SOA formation." Atmos. Environ 40, S116-S127, 2006.
30. J. L. Fry, A. Kiendler-Scharr, A. W. Rollins, P. J. Wooldridge, S. S. Brown, H. Fuchs, W. Dubé, A. Mensah, M. dal Maso, R. Tillmann, H.-P. Dorn, T. Brauers, and R. C. Cohen. "Organic nitrate and secondary organic aerosol yield from NO_3 oxidation of B-pinene evaluated using a gas-phase kinetics/aerosol partitioning model." Atmos. Chem. Phys. 9, 1431-1449, doi:10.5194/acp-9-1431-2009, 2009.
31. S. S. Brown, J. A. deGouw, C. Warneke, T. B. Ryerson, W. P. Dube, E. Atlas, R. J. Weber, R. E. Peltier, J. A. Neuman, J. M. Roberts, A. Swanson, F. Flocke, S. a. McKeen, J. Brioude, R. Sommariva, M. Trainer, F. C. Fehsenfeld, and A. R. Ravishankara. "Nocturnal isoprene oxidation over the Northeast United States in summer and its impact on reactive nitrogen partitioning and secondary organic aerosol." Atmos. Chem. Phys. 9, 3027-3041, 2009.
32. F. J. Dentener and P. J. Crutzen. "Reaction of N_2O_5 on Tropospheric Aerosols: Impact on the Global Distributions of NO_x, O_3, and OH." J. Geophys. Res. 28(D4) 7149-7163, 1993.
33. T. H. Bertram, J. A. Thornton, T. P. Riedel, A. M. Middlebrook, R. Bahreini, T. S. Bates, P. K. Quinn, and D. J. Coffman. "Direct observations of N_2O_5 reactivity on ambient aerosol particles." Geophys. Res. Lett. 36(L19803) doi:10.1029/2009GL040248, 2009.
34. J. Lewis, R. De Young, R. Ferrare, and D. A. Chu. "Comparison of summer and winter California central valley aerosol distributions from lidar and MODIS measurements." Atmos. Environ 44 4510-4520, 2010.
35. I. Kind, T. Berndt, and O. Böge. "Gas-Phase rate constants for the reaction of NO_3 radicals with a series of cyclic alkenes, 2-ethyl-1-butene and 2,3-dimethyl-1,3,butadiene." Chem. Phys. Lett. 288, 111-118, 1998.
36. R. P. Wayne, I. Barnes, P. Biggs, J. P. Burrows, C. E. Canosa-Mas, J. Hjorth, G. Le Bras, G. K. Moortgat, D. Perner, G. Poulet, G. Restelli, and H. Sidebottom. "The Nitrate Radical: Physics, Chemistry, and the Atmosphere." Atmos. Environ. 25A (1) 1-203, 1991.
37. C. Bloss, V. Wagner, M. E. Jenkin, R. Volkamer, W. J. Bloss, J. D. Lee, D. E. Heard, K. Wirtz, M. Martin-Reviejo, G. Rea, J. C. Wenger, and M. J. Pilling. "Development of a detailed chemical mechanism (MCMv3.1) for the atmospheric oxidation of aromatic hydrocarbons." Atmos. Chem. Phys. 5 641-664, 2005.
38. M. E. Jenkin, S. M. Saunders, and M. J. Pilling. "The tropospheric degradation of volatile organic compounds: a protocol for mechanism development." Atmos. Environ. 31, 81-104, 1997.
39. M. E. Jenkin, S. M. Saunders, V. Wagner, and M. J. Pilling. "Protocol for the development of the Master Chemical Mechanism, MCM v3 (Part B): tropospheric degradation of aromatic volatile organic compounds." Atmos. Chem. Phys. 3, 181-193, 2003.
40. S. M. Saunders, M. E. Jenkin, R. G. Derwent, and M. J. Pilling. "Protocol for the development of the Master Chemical Mechanism. MCM v3 (Part A): tropospheric degradation of non-aromatic volatile organic compounds." Atmos. Chem. Phys. 3, 161-180, 2003.
41. E. S. . Kwok, R. Atkinson, and J. Arey. "Kinetics of the Gas-Phase Reactions of Indan, Indene, Fluorene and 9,10-Dihydroanthracene with OH Radicals, NO_3 Radicals, and O_3." Int'l. J. Chem. Kin. 29 (4) 299 – 309, doi: 10.1002/(SICI)1097-4601(1997)29:4<299::AID-KIN9>3.0.CO;2-P 1997.
42. S. B. Corchnoy and R. Atkinson. "Kinetics of the Gas-Phase Reactions of OH and NO_3 Radicals with 2-Carene, 1,8-Cineole, p-Cymene, and Terpinolene." Environ. Sci. Technol. 24 1497-1502, 1990.
43. P. T. Phousongphouang and J. Arey. "Rate Constants for the Gas-Phase Reactions of a Series of Alkylnaphthalenes with the Nitrate Radical." Environ. Sci. Technol. 37, 308-313, 2003.
44. J. Noda, C. Holm, G. Nyman, S. Langer, and E. Ljungström. "Kinetics of the Gas-Phase Reaction of n-C_6-C_{10} Aldehydes with the Nitrate Radical." Int'l. J. Chem. Kin. 35 (3), 120-129, 2003.

References for SI Rollins et al., 2012:

1. R. R. Draxler, G. D. Hess, An overview of the HYSPLIT_4 modeling system of trajectories, dispersion, and deposition. Aust. Meteorol. Mag. 47, 295 (1998).
2. A. W. Rollins, J. D. Smith, K. R. Wilson, R. C. Cohen, Real time in situ detection of organic nitrates in atmospheric aerosols. Environ. Sci. Technol. 44, 5540 (2010).
3. D. A. Day, P. J. Wooldridge, M. B. Dillon, J. A. Thornton, R. C. Cohen, A thermal dissociation laser-induced fluorescence instrument for in situ detection of NO_2, peroxy nitrates, alkyl nitrates and HNO_3. J. Geophys. Res. 107, (D6), 4046 (2002).
4. M. R. Canagaratna et al., Chemical and microphysical characterization of ambient aerosols with the aerodyne aerosol mass spectrometer. Mass Spectrom. Rev. 26, 185 (2007).

5. A. M. Middlebrook, R. Bahreini, J. L. Jimenez, M. R. Canagaratna, Evaluation of composition-dependent collection efficiencies for the aerodyne aerosol mass spectrometer using field data. Aerosol Sci. Technol. 46, 258 (2012).
6. J. L. Fry et al., SOA from limonene: Role of NO_3 in its generation and degradation. Atmos. Chem. Phys. 11, 3879 (2011).
7. A. W. Rollins et al., Elemental analysis of aerosol organic nitrates with electron ionization high-resolution mass spectrometry. Atmos. Meas. Tech. 3, 301 (2010).
8. D. K. Farmer et al., Response of an aerosol mass spectrometer to organonitrates and organosulfates and implications for atmospheric chemistry. Proc. Natl. Acad. Sci. U.S.A. 107, 6670 (2010).
9. I. Kind, T. Berndt, O. Böge, Gas-Phase rate constants for the reaction of NO_3 radicals with a series of cyclic alkenes, 2-ethyl-1-butene and 2,3-dimethyl-1,3,butadiene. Chem. Phys. Lett. 288, 111 (1998).
10. R. P. Wayne et al., The nitrate radical: Physics, chemistry, and the atmosphere. Atmos. Environ. 25A, 1 (1991).
11. E. S. C. Kwok, R. Atkinson, J. Arey, Kinetics of the gas-phase reactions of indan, indene, fluorene and 9,10-dihydroanthracene with OH radicals, NO_3 radicals, and O_3. Int. J. Chem. Kin. 29, 299 (1997).
12. S. B. Corchnoy, R. Atkinson, Kinetics of the gas-phase reactions of hydroxyl and nitrogen oxide (NO_3) radicals with 2-carene, 1,8-cineole, p-cymene, and terpinolene. Environ. Sci. Technol. 24, 1497 (1990).
13. P. T. Phousongphouang, J. Arey, Rate constants for the gas-phase reactions of a series of alkylnaphthalenes with the nitrate radical. Environ. Sci. Technol. 37, 308 (2003).
14. J. Noda, C. Holm, G. Nyman, S. Langer, E. Ljungström, Kinetics of the gas-phase reaction of n-c6-c10 aldehydes with the nitrate radical. Int. J. Chem. Kin. 35, 120 (2003).
15. E. Martínez, B. Cabañas, A. Aranda, P. Martín, S. Salgado, absolute rate coefficients for the gas-phase reactions of NO_3 radical with a series of monoterpenes at T=298 to 433 K. J. Atmos. Chem. 33, 265 (1999).
16. I. Barnes, V. Bastian, K. H. Becker, Z. Tong, Kinetics and products of the reactions of nitrate radical with monoalkenes, dialkenes, and monoterpenes. J. Phys. Chem. 94, 2413 (1990).
17. R. Atkinson, S. M. Aschmann, A. M. Winer, J. N. Pitts Jr., Kinetics and atmospheric implications of the gas-phase reactions of nitrate radicals with a series of monoterpenes and related organics at 294 ± 2K. Environ. Sci. Technol. 19, 159 (1985).
18. C. Bloss et al., Development of a detailed chemical mechanism (MCMv3.1) for the atmospheric oxidation of aromatic hydrocarbons. Atmos. Chem. Phys. 5, 641 (2005).
19. M. E. Jenkin, S. M. Saunders, M. J. Pilling, The tropospheric degradation of volatile organic compounds: A protocol for mechanism development. Atmos. Environ. 31, 81 (1997).
20. M. E. Jenkin, S. M. Saunders, V. Wagner, M. J. Pilling, Protocol for the development of the Master Chemical Mechanism, MCM v3 (Part B): Tropospheric degradation of aromatic volatile organic compounds. Atmos. Chem. Phys. 3, 181 (2003).
21. S. M. Saunders, M. E. Jenkin, R. G. Derwent, M. J. Pilling, Protocol for the development of the Master Chemical Mechanism. MCM v3 (Part A): Tropospheric degradation of non-aromatic volatile organic compounds. Atmos. Chem. Phys. 3, 161 (2003).
22. T. H. Bertram et al., Direct observations of N_2O_5 reactivity on ambient aerosol particles. Geophys. Res. Lett. 36, L19803 (2009).

3.3. Elucidating secondary organic aerosol from diesel and gasoline vehicles through detailed characterization of organic carbon emissions

Reproduced in part from: D.R. Gentner, G. Isaacman, D.R. Worton, A.W.H. Chan, T.R. Dallmann, L. Davis, S. Liu, D.A. Day, L.M. Russell, K.R. Wilson, R. Weber, A. Guha, R.A. Harley, A.H. Goldstein (2012) "Elucidating secondary organic aerosol from diesel and gasoline vehicles through detailed characterization of organic carbon emissions" Proc. Nat. Acad. Sci., 109, 18318-18323.

CalNex study topics addressed: *sources of NO_x and VOC, production and removal timescales of oxidation products, role of VOCs, SJVAB vs. SoCAB - particulate formation rate*

Abstract: Emissions from gasoline and diesel vehicles are predominant anthropogenic sources of reactive gas-phase organic carbon and key precursors to Secondary Organic Aerosol (SOA) in urban areas. Their relative importance for aerosol formation is a controversial issue with implications for air quality control policy and public health. We characterize the chemical composition, mass distribution, and organic aerosol formation potential of emissions from gasoline and diesel vehicles, and find diesel exhaust is 7 times more efficient at forming aerosol than gasoline exhaust. Yet, both sources are important for air quality; depending on a region's fuel use, diesel is responsible for 65-90% of vehicular-derived SOA, with substantial contributions from both aromatic and aliphatic hydrocarbons. Including these insights on source characterization and SOA formation will improve regional pollution control policies, fuel regulations, and methodologies for future measurement, laboratory, and modeling studies.

3.3.1. Introduction

Organic Aerosol (OA) in the atmosphere is detrimental to human health and represents a highly uncertain forcing of climate change (*1*). The use of petroleum-derived fuels is an important source of reactive gas-phase organic carbon that provides key precursors to the formation of Secondary Organic Aerosol (SOA) and tropospheric ozone (*1*). Controlling these emissions from gasoline and diesel vehicles is central to air quality mitigation policies in urban areas (*2*). Previous work has concluded that further research is necessary to elucidate all organic sources of SOA precursors (*3-4*). Significant controversy exists over the contributions of precursors from gasoline and diesel vehicles, and the relative importance of each for SOA formation remains in question, in part, due to insufficient chemical characterization of fuels and emissions, and the difficulty of ambient measurements of gas-phase compounds emitted from diesel sources (*1, 4-8*).

In the U.S., diesel fuel accounts for 21% of on-road fuel use (by volume), with off-road sources increasing diesel fuel usage to 28% of the total. In California, the diesel share of on-road fuel usage ranges from around 10% in coastal urban areas to over 30% in agricultural regions (Table 3.3.1) (*2, 9-10*). Non-combusted hydrocarbons from the fuels are emitted in the exhaust of gasoline and diesel engines, and also via evaporation from gasoline vehicles and service stations. These compounds in unburned gasoline and diesel fuel dominate vehicular emissions of reactive gas-phase carbon that have the potential to form SOA (*11-12*). Previous work has shown non-tailpipe emissions account for ~30% of gasoline-related emissions in urban regions, but limited work exists constraining the emissions and SOA formation potential of gas-phase organic carbon

from gasoline and diesel sources (*13*). Using extensive fuel analyses and field data from two sites that include many compounds with no prior *in situ* measurements, we present the most comprehensive data to date on the chemical composition, mass distribution, emissions, and SOA formation potential of non-tailpipe gasoline, gasoline exhaust, and diesel exhaust. We determine the relative importance of gasoline and diesel sources for SOA formation in, and downwind of, urban regions. We assess these results in the context of other studies over the past decade and discuss their significant implications for air pollution measurement, modeling, and control.

3.3.2. Results & Discussion

Forty gasoline and twelve diesel fuel samples from California were collected (coincident with field data) and characterized using several gas-chromatography methods, yielding the first comprehensive speciation of the "unresolved complex mixture" in diesel fuel. This was accomplished using soft photoionization techniques, and provides unprecedented detail on the molecular identification and mass distribution of hydrocarbons in diesel fuel (*14*). Gasoline and diesel fuel, and thus their emissions of unburned hydrocarbons, can be classified by vapor pressure and span the Volatile Organic Compound (VOC) range and the less volatile Intermediate-Volatility Organic Compound (IVOC) range (Figure 3.3.1). Gasoline hydrocarbons fall mostly within the VOC range with some aromatics extending into the IVOC range, whereas only 30% of diesel fuel hydrocarbons are in the VOC range. Diesel fuel is widely distributed across molecules containing 8 to 25 carbon atoms with a peak around 10-13 carbon atoms (Figure 3.3.2A). This peak is due to aromatics and cycloalkanes since straight and branched alkanes are evenly distributed between 10 and 20 carbon atoms. Aromatic and aliphatic hydrocarbons make up 23 and 68% of diesel fuel, respectively. By comparison, gasoline contains ~30% aromatics with the remainder of the non-ethanol fraction dominated by straight and branched alkanes with less than 10 carbon atoms (Table 3.3.2, Figure 3.3.2A).

In order to examine contributions from each source to reactive gas-phase organic carbon in both the ambient atmosphere and on-road emissions measured in a roadway tunnel, we used a chemical mass balance model with effective variance weighting on over-constrained least squares regressions (*15*). The model uses a subset of measured compounds and capitalizes on differences in the chemical composition of sources to assess the magnitude of total non-combusted hydrocarbon emissions from each source. The source profiles used as *a priori* information are constructed from liquid fuel data to represent gasoline and diesel exhaust, and vapor-liquid equilibrium calculations to represent non-tailpipe gasoline emissions. Equivalent chemical composition in exhaust and liquid fuel has been reported previously for gasoline and is demonstrated in this work for gasoline and diesel at both measurement sites (Figure 3.3.3) (*16*). Extensive diagnostics were used to assess model performance, including comparisons against independent compounds to confirm the model's ability to predict the behavior of reactive VOCs and IVOCs emitted by both gasoline and diesel sources (Figures 3.3.4-3.3.7).

Emission factors for non-combusted gas-phase organic carbon in exhaust were determined to be 0.38 ± 0.11 gC L^{-1} for gasoline and 0.86 ± 0.25 gC L^{-1} for diesel, which are consistent with values calculated using California's emissions model for the same period (*17*). With respect to contributions of non-combusted hydrocarbons from gasoline and diesel exhaust, diesel accounted for 24% at the tunnel study in a coastal city compared to 57% in the urban center of an agricultural region. Accounting for differences in emission factors and fuel densities, this is

consistent with on-road fuel sales data in both regions—11 and 33% diesel fuel by volume, respectively (Table 3.3.1) (*10*).

To assess the importance of gasoline and diesel sources for SOA in urban areas, we calculated bulk SOA yields for all 3 sources and compared them in context of our emission factors and source contributions. Data on SOA yields are limited for many of the hydrocarbons; the mass fraction of diesel, gasoline, and non-tailpipe gasoline emissions that have unknown yields are 66, 25, and 7%, respectively. Thus, we modeled high-NO_x SOA yields using published data (where available) and an estimation of yields and uncertainties for unknown values based on best estimates from various plausible scenarios (Figures 3.3.2B, 3.3.8).

For the same mass of unburned fuel emissions reacted, diesel exhaust forms 6.7 ± 2.9 times more SOA than gasoline exhaust (bulk SOA yields of 0.15 ± 0.05 and 0.023 ± 0.007 $\mu gSOA\ \mu g^{-1}$, respectively). Considering differences in emission factors, diesel exhaust is expected to form 15 times more SOA than gasoline per liter of fuel burned. For populated regions with 10 to 30% diesel fuel use, this implies that diesel exhaust is responsible for 2 to 7 times more SOA than gasoline exhaust (Figure 3.3.9). Non-tailpipe gasoline emissions were 39-77% lower than gasoline exhaust emissions and produce negligible SOA due to a substantially lower yield (0.0024 ± 0.0001).

Our methods also allowed us to examine the most important chemical classes and mass distribution of SOA formation. The vast majority of SOA from gasoline sources is due to its aromatic content, whereas diesel SOA is predicted to be 47 ± 7% from aliphatics with the remainder from aromatics (Figure 3.3.2B, Table 3.3.2).

Regional estimates of daytime SOA concentrations from both diesel and gasoline using our model results and calculated SOA yields are consistent with independent positive matrix factor analysis results for aromatic and aliphatic SOA from fossil fuel combustion in the San Joaquin Valley using Aerosol Mass Spectrometer (AMS) and Fourier Transform Infrared spectroscopy (FTIR) measurements. Based on our model results, we expect an average of 1.3 ± 0.4 $\mu gOA\ m^{-3}$ from motor vehicles compared to average $PM_{1.0}$ factor concentrations of 1.8 to 2.1 $\mu gOA\ m^{-3}$ from FTIR and AMS data, respectively (*18*). These independent data also support the predominance of diesel SOA in the San Joaquin Valley as young aerosol (oxygen:carbon (O:C) ratio = 0.27-0.36) was 58% aliphatic and 42% aromatic (*18*).

SOA models have made considerable progress using a parameterization known as the *volatility basis set* to estimate contributions from unmeasured intermediate and semi-volatile compounds (*5, 19*). Together with traditional explicit models for individual hydrocarbons in the VOC range, models are better able to predict the magnitude of observed SOA, but not all temporal patterns or physical/chemical characteristics (*3, 19, 27*). Here we evaluate the inclusion of SOA precursors in these models and their distribution in gasoline and diesel exhaust. Aromatics with single or multiple rings have rightfully received considerable attention historically, but their distribution between gasoline and diesel emissions has been relatively unexplored. Gasoline exhaust dominates emissions of C_7 and C_8 aromatics. C_9 aromatic content is four times greater in gasoline than diesel and there are nearly equivalent amounts of C_{10} aromatics. For an urban region with 15% diesel fuel use, this implies that gasoline emits over 90% of the C_9 aromatics

and 75% of the C_{10} aromatics. Gasoline SOA from C_9 and C_{10} aromatics represent 26% and 14% of total SOA from gasoline, respectively, and $C_{9\text{-}11}$ aromatics represent 5% of SOA from diesel exhaust (Table 3.3.2). Emissions of naphthalene and similar small Polycyclic Aromatic Hydrocarbons (PAHs) are shared by both gasoline and diesel vehicles, but represent only a minor contribution to potential SOA formation due to their minor weight fractions in the fuels (Figure 3.3.2, Tables 3.3.10-3.3.11).

We examined the compounds included in SOA models and found that 20-30% of the SOA formed from gasoline exhaust was not included in recent urban studies (*20-22*). Given the contributions of $C_{9\text{-}11}$ aromatics to SOA formation from gasoline and diesel vehicles, it is important that they are better represented in either explicit traditional SOA models or the extension of volatility basis set modeling to include the 10^7 and 10^8 $\mu g\ m^{-3}$ C° bins that fall in the VOC range (Figure 3.3.10) (*5, 19, 21*). For recent urban studies, scaling up traditional compound-explicit SOA models (without the volatility basis set) to include the missing 20-30% of gasoline SOA and contributions from diesel (assuming 15% diesel fuel use) produces a 5x increase in modeled SOA from vehicular exhaust. Such an inclusion dramatically improves model closure which has typically underestimated SOA in urban regions by 80-90% (*19*), but additional contributions from other sources of SOA precursors remain critical to model all observed SOA. Further chamber and modeling studies on SOA yields of aromatics with 9 or more carbon atoms are important to reduce uncertainties in the SOA-forming potential of gasoline and diesel exhaust emissions and their overall contribution to SOA in urban regions. Additional studies on the SOA yields of cyclic alkanes with 5- and 6-membered rings are also of interest since they are unstudied and comprise 37% of diesel and 11% of gasoline fuel.

In 1993, with the goal of mitigating emissions of particulates and nitrogen oxides, California regulated diesel fuel to have less than 10% single-ring aromatics and 1.4% PAHs, but concerns about engine performance and the cost of fuel production led the state to allow higher aromatic levels in diesel fuel (*23*). It is evident from our data (Table 3.3.1) that the vast majority of diesel fuels sold in California are certified alternative formulations that contain nearly double the aromatic content than initial regulations intended. While the fuel regulations were designed to help control primary particulate emissions (i.e., black carbon), this enhancement of aromatic content in diesel fuel increases the SOA potential of diesel emissions, especially for hydrocarbons with 9 to 17 carbon atoms. Significant progress is being made to improve heavy-duty diesel engine performance with post-combustion control technology, and may affect emissions of gas-phase organic carbon, but it is clear that attention to both gasoline and diesel fuel composition and emissions of reactive organic gases is necessary to control SOA precursor contributions from all vehicle classes. Furthermore, this work has focused on organic carbon emissions originating from fuels, but emissions of unburned motor oil from both gasoline and diesel vehicles represent an additional source of organic carbon. While total consumption of oil is minor relative to fuel, oil contributes gas and particle-phase compounds with lower volatilities than diesel fuel and should continue to be monitored in field, laboratory, and modeling studies.

Comparing observed concentrations of OA to carbon monoxide (CO) is a popular method for assessing the formation and behavior of SOA in the atmosphere (*6, 20, 24-25, 30-33*). Using derived SOA yields and emission factors for reactive gas-phase organic carbon and CO, we predict $\Delta OA/\Delta CO$ ratios for a mixture of gasoline and diesel fuel use for comparison to our

observations in the San Joaquin Valley (Bakersfield) and other urban studies over the past decade (Figure 3.3.11). Predicted ΔOA/ΔCO slopes for a range of typical fuel usage are consistent with observed ΔOA/ΔCO values in Los Angeles, Tokyo, and Mexico City after initial SOA formation occurring in the first six hours of processing (Figure 3.3.11A) (*6, 24-25*). We predict "young" ΔOA/ΔCO ratios well, but as air masses develop from a relatively young photochemical age of ~6 hours to ~1 day, ΔOA/ΔCO ratios increase. A 3-4x increase was observed in Mexico City, and the effect of increased processing can also be observed in Tokyo, where ΔOA/ΔCO slopes for multiple seasons depict a clear seasonal trend with the greatest slope occurring in the summer for processed air parcels while less-processed parcels remain consistent with expected ratios for a mix of gasoline and diesel emissions (*19, 24-25*).

In the San Joaquin Valley, the increase in ΔOA/ΔCO ratios appears to be coincident with the transition of young semi-volatile aerosols to more aged aerosols with lower volatility as shown by the increase in O:C ratios that peaks with ΔOA/ΔCO ratios in the afternoon (Figure 3.3.11) (*3, 19, 25*). Similarly, a greater fraction of low-volatility organic aerosol was observed in the summertime in Tokyo (*3*). Aged ΔOA/ΔCO ratios exceed our predictions despite our ability to predict overall observed vehicular OA concentrations. This suggests that the comprehension of all OA transformation processes is incomplete and further work remains to understand the development of low-volatility OA observed in urban plumes globally, a conclusion supported by recent observations and consideration of other mechanisms. (*3, 27-29*).

Examining differences between weekdays and weekends is another common and insightful metric for assessing emissions and chemical processes. We observed no weekday/weekend difference in the distribution of emissions between gasoline and diesel exhaust in Bakersfield as daytime values of both decreased by ~40% over the weekend (Figure 3.3.12). Yet, weekend OA concentrations (total and vehicular) were greater due to increased photochemical aging evidenced by higher ΔOA/ΔCO ratios (Figures 3.3.11C, 3.3.13). Recent work focused on Los Angeles reported that gasoline is vastly more important than diesel as a source of SOA precursors based on the observation that weekend ΔOA/ΔCO slopes were marginally similar to weekday slopes with similar photochemical ages despite large differences in diesel activity (*6*). Similar to Los Angeles, OA concentrations and ΔOA/ΔCO ratios are higher in Bakersfield over the weekend, but occurs despite no change in the relative use of gasoline and diesel, suggesting that increased OA at both locations over the weekend is a function of decreased diesel NO_x emissions leading to faster photochemical processing and is independent of changes in the mix of fuel use (*26*). The ubiquitous increase in ΔOA/ΔCO ratios with increased processing for both vehicular and total OA is independent of the mixture of gasoline and diesel, and ΔOA/ΔCO slopes alone are insufficient to discern organic SOA precursor contributions from gasoline vs. diesel given the variability in Los Angeles measurements (Figure 3.3.14) (*6*).

Non-vehicular anthropogenic and biogenic sources also lead to elevated ΔOA/ΔCO ratios with higher slopes occurring in regions with large non-vehicular sources, such as Mexico City, the Southeast U.S., and the Po Valley (Figure 3.3.11B). ΔOA/ΔCO ratios in the San Joaquin Valley span a broad range of values observed at other sites and the importance of other SOA sources is supported by elevated ΔOA/ΔCO ratios in aged air masses and episodic contributions of low O:C OA from other sources (Figures 3.3.11B, 3.3.15) (*6, 20, 24-25, 30-32*).

Our expanded measurement capabilities for gasoline and diesel compounds in both the liquid fuels and the ambient atmosphere produce a more complete picture of SOA formation from motor vehicles. Our methods provide the ability to predict emissions of SOA precursors and SOA formation that is consistent with fuel use data and ambient measurements. SOA from diesel sources outweighs gasoline contributions, and other sources provide significant precursors in many urban regions. The inclusion of our insights will allow for the development of more effective pollution control policies and inform the design of future studies in the ambient atmosphere, laboratory experiments, and modeling efforts.

3.3.3. Supporting materials and methods

3.3.3.1. Supporting in situ measurements

An extensive suite of instrumentation was deployed to both field studies (i.e., Caldecott Tunnel and CalNex-SJV) to characterize gas and particle species. In the Caldecott tunnel, Black Carbon (BC), carbon monoxide (CO), and carbon dioxide (CO_2) were measured at inlets co-located with gas-phase organic sampling. After passing through a 2.5 µm cyclone (URG Corporation, model 2000-30EN), BC was measured using an aethalometer (McGee Sci. model AE-16) and post-processed as described elsewhere (*36*). CO and CO_2 were measured via an infrared spectrometer (TECO Inc. Model 48) and non-dispersive infrared absorption (LI-COR, Lincoln, NE; model LI-820), respectively, with twice daily zero and calibration checks. Uncertainties are estimated to be ± 3 and 2%, respectively. Raw data were recorded at high-time resolution, but were averaged for this analysis to 30-min periods coincident with the VOC measurements.

At CalNex-Bakersfield, aerosol measurements were made using an Aerosol Mass Spectrometer (AMS) and Fourier Transform Infrared spectroscopy (FTIR) analysis of filters to assess $PM_{1.0}$ and $PM_{2.5}$ concentrations and composition; these methods have been described elsewhere (*18*). Carbon monoxide was measured from the top of the tower using a gas filter correlation infrared spectrometer (Teledyne, API M300EU2). Comparisons of Organic Aerosol (OA) to CO were done at 5-min time resolution with a $PM_{1.0}$ cutpoint. Vehicular OA, as presented in the paper, was determined as the sum of the four vehicular aerosol factors from the positive matrix factorization analysis of the AMS data: low O:C alkane, low O:C aromatic, high O:C alkane, and high O:C aromatic (*18*).

3.3.3.2 Fuel characterization

Forty samples of regular and premium grade gasoline, and twelve samples of diesel fuel were collected from service stations during the summer of 2010 (coincident with the field studies) in four California locations (Bakersfield, Pasadena, Sacramento, and Berkeley). Gasoline samples were analyzed at Chevron laboratories (Richmond, CA) by gas chromatography with dual flame ionization detectors. Additional analyses were performed to resolve co-eluting peaks. Over 400 compounds were quantified in the fuel samples via this method. Compositional averages for the State and each location were calculated assuming an 80:20 regular to premium usage.

To characterize the full range of compounds in diesel fuel, samples were analyzed by two methods. Samples were analyzed via direct injection on a traditional 1-dimensional gas chromatograph (HP 5890 Series II) with a quadrapole mass selective detector (HP 5971) on a

DB-624 column (60 m × 0.32 mm × 1.8 μm). Where available, liquid standards were used to calibrate traditionally-characterized components. Nine of the twelve diesel fuel samples were additionally run on a Rxi-5Sil MS column (60 m × 0.25 mm × 0.5 μm; Restek) coupled to a time-of-flight mass spectrometer (TOFMS; HTOF model, Tofwerk) with a custom modification to allow single-photon ionization. Effluent from the column was ionized using 10.5 eV vacuum-ultraviolet photons generated by synchrotron radiation at the Chemical Dynamics Beamline of the Advanced Light Source (ALS) at Lawrence Berkeley National Lab. Analysis of these data was performed following methods described previously (*14*), with improved quantification owing to the use of a more extensive suite of structurally-relevant standards.

Vapor-liquid equilibrium calculations were performed for each liquid gasoline sample to predict gasoline vapor composition, which were then averaged statewide and at each location using the same methodology as the liquid fuel. A detailed description of the non-ideal solution equilibrium calculations for gasoline has been published previously (*13, 37*). Uncertainties presented with all fuel data in this work have been propagated to reflect all anticipated variability in fuel samples.

3.3.3.3. Comparison of fuels to ambient and tunnel measurements

In order to compare expected versus measured source profiles for gas-phase organics, we compare gasoline and diesel fuel to both tunnel and ambient VOC/IVOC measurements. Isooctane and *n*-dodecane are selected as tracers for gasoline and diesel exhaust, respectively. Isooctane is a good tracer for gasoline exhaust because it is a trimethylpentane that is intentionally produced during the refining process and added to gasoline to comprise 3.6 ± 0.3 wt% of California gasoline (Summer 2010). Additionally, it will only be present as a minor component of evaporative gasoline emissions and diesel exhaust. *n*-dodecane is a good tracer for diesel exhaust because it is prevalent in diesel fuel and will be emitted only as a non-combusted hydrocarbon. It makes up only 0.01% of gasoline fuel and diesel emissions will greatly exceed any other urban VOC source of *n*-dodecane. From the fuels, expected ratios to tracers are derived by dividing the concentration (i.e., mol%) of a given compound by that of either isooctane or *n*-dodecane. For the tunnel and ambient data we performed linear regressions using a trust-region Levenberg-Marquardt least orthogonal distance method to account for uncertainties in both tracer measurements.

3.3.3.4 Chemical mass balance source receptor modeling and emission factor calculations

Previous work gives detailed descriptions of source receptor modeling and chemical mass balance methods (*13, 15*). For each hourly sample in the Caldecott tunnel (N=114) and at CalNex-Bakersfield (N=487), an over-constrained matrix system was constructed with 6 to 10 compounds to represent the source profiles of the three sources (i.e., gasoline, diesel, and gasoline evaporates). For each site, several confirmatory model runs with different sets of compounds were used to assess sensitivity of results. A summary of compounds used for modeling can be found in Tables 3.3.4-5. All compounds used in the model have authentic standards.

The gas-phase organic carbon data have numerous VOCs and IVOCs that act as source tracers either independently or in tandem with other compounds. With regards to gasoline and diesel emissions, emissions of most observed tracer compounds had not undergone significant

photochemistry that could bias the model over the timescales observed between emission and measurement at either field site. This is evidenced by roughly identical ratios for gasoline-related compounds in the ambient measurements compared to liquid gasoline collected in Bakersfield during the campaign (Fig. 3.3.3). If considerable aging with the ability to bias our model had occurred, these comparisons would be poor for compounds that have differences in OH reaction constants. Chemical losses were only really a concern at the Bakersfield site since the on-road emissions study was in close proximity to the source. At Bakersfield, evidence of chemical losses in the fresh emissions can occasionally be seen in comparisons of model results to independent compounds that are highly reactive, which is only an issue with the most reactive compounds that are not used in modeling for that reason. This lack of observable photochemical processing of the primary emissions used in the model allows us to effectively assess emissions from gasoline and diesel sources. Additionally, any minor biases that could be introduced due to chemical losses are minimized by selecting compounds for the model that have relatively similar reaction rates with OH and negligible reaction rates with ozone.

The source profiles used as inputs in the model were derived from the compound-specific fuel profiles presented in this work, with liquid fuels representing exhaust profiles and vapor-liquid equilibrium calculations determining the non-tailpipe profile. Previous work has shown compositional consistency for non-combusted gas-phase organics in liquid gasoline and gasoline exhaust (*16*). In addition to confirming this finding for gasoline, we also demonstrate compositional consistency for diesel fuel and exhaust (Fig. 3.3.3).

For Bakersfield, a fourth source representing fugitive light hydrocarbon ($C_{1\text{-}7}$) emissions from petroleum extraction and refining was necessary to properly model non-tailpipe gasoline emissions; data for this source came from U.S. geological surveys. Additionally, given the low volatility of hydrocarbons in diesel fuel, evaporative contributions of diesel fuel are expected to be negligible compared to exhaust emissions. Using IGOR Pro 6.22, a least-squares solution was determined for each over-constrained system to determine each hourly source contribution in ppbC using effective variance weighting methods described by Watson *et al.* and used by the U.S. EPA in their CMBv8.2 modeling platform (*15, 38*). To assess model performance, we calculated normalized biases and root mean squared errors for each compound used in the model and each independent compound. We also calculated the reduced chi-squared test and model R-squared for each hourly sample; results can be seen in Fig. 3.3.6. We verified the predictive capability of all compounds to independent compounds to confirm the ability of the model to predict the behavior of reactive VOCs and IVOCs that are emitted by both gasoline and diesel at both measurement sites. A selection of these compounds are shown in Figs. 3.3.4-5. Minor inconsistencies observed in a few of the panels are due to a combination of oxidation losses during the most photochemically-active periods of the day, other non-vehicular sources, and, in the case of IVOCs in the tunnel study, adsorptive losses on walls of the shared inlet.

Emission factors for non-combusted gas-phase organic carbon (expressed as GPOC in equations) were calculated using the modeling results and supporting in-situ measurements from the Caldecott tunnel study. The gasoline emission factor was first calculated by taking the average of hourly emission factors (the source contribution ($SC_{t,gasoline}$) over total carbon ($\Delta Total\ C_t$)) during the weekend when diesel traffic and contributions to total carbon were negligible, similar

to previous studies (*11*). Uncertainty is determined from the standard deviation of the emission factor.

$$EF_{GPOC,gasoline\ exhaust} = \frac{1}{N}\sum_{t=0}^{N}\left[\frac{SC_{t,gasoline}}{\Delta Total\ C_t}\right] f_{c,gasoline} d_{gasoline} \quad \text{(S1)}$$

$$\Delta Total\ C_t = [CO_2]_{t,tunnel} + [CO]_{t,tunnel} - [CO_2]_{t,ambient} - [CO]_{t,ambient} \quad \text{(S2)}$$

$$where:$$

$$SC_{t,gasoline} = \text{gC GPOC m}^{-3}\ (@25°\text{C})$$

$$\Delta Total\ C_t\ and\ concentrations = \text{kgC m}^{-3}$$

$$N : number\ of\ samples$$

$$f_{c,gasoline} : carbon\ fraction\ of\ gasoline$$

$$d_{gasoline} : liquid\ density\ of\ gasoline\ (@25°\text{C})$$

$$Assumption: SC_{t,gasoline,tunnel} \gg SC_{t,gasoline,ambient}$$

The results of this method were compared to a regression method where the slope of the source contribution vs. total carbon is used to calculate the emission factor and the uncertainty is determined from the standard deviation of the slope.

$$EF_{GPOC,gasoline\ exhaust} = \left[\frac{SC_{t,gasoline}}{Total\ C_t}\right]_{slope} f_{c,gasoline} d_{gasoline} \quad \text{(S3)}$$

The diesel emission factor is calculated similarly, but since the total carbon signal is dominated by gasoline in the tunnel, Black Carbon (BC) is used in its place since BC is largely from diesel. To correct for BC contributions from gasoline, BC measurements are adjusted to isolate the diesel signature using the gasoline source contribution and emission factors for non-combusted gas-phase organic carbon and BC from gasoline derived in this work and elsewhere (*36*). Data from weekdays and weekends are used in the regression.

$$EF_{GPOC,diesel\ exhaust} = \left[\frac{SC_{t,diesel}}{BC_{t,diesel}}\right]_{slope} EF_{BC,diesel\ exhaust} d_{diesel} \quad \text{(S4)}$$

$$BC_{t,diesel} = BC_{t,observed} - \frac{SC_{t,gasoline} EF_{BC,gasoline\ exhaust}}{EF_{GPOC,gasoline\ exhaust}} \quad \text{(S5)}$$

$$where:$$

$$EF_{BC,gasoline} = 0.020 \pm 0.003\ gBC\ kg^{-1} \quad \text{(Caldecott Tunnel Study)}$$

$$EF_{BC,diesel} = 0.54 \pm 0.07\ gBC\ kg^{-1} \quad \text{(Dallmann et al. (36))}$$

Emission factors are compared to those from the California emission factor model (EMFAC2011) as determined from statewide Summer 2010 data for running emissions and weighted for all vehicle models using vehicle miles traveled (VMT) (*17*). The resulting emission

factor is in gC GPOC L^{-1} and must be multiplied by ~0.73 to compare to the derived emission factors for non-combusted gas-phase organic carbon as 27% of reactive organic gas (ROG) emissions from gasoline are products of incomplete combustion (*11*). The exact ratio of products of incomplete combustion to total ROG emissions will vary depending on fuel type, oxygenate level and driving conditions. The value presented here is intended to check consistency with outside measurements and is not used in any of our calculations.

$$EF_{GPOC,gasoline} = \frac{\frac{\Sigma\left[EF_{ROG,vehicle\ type} VMT_{\ vehicle\ type}\right]}{\Sigma\left[VMT_{\ vehicle\ type}\right]} f_{c,gasoline} d_{gasoline}}{\frac{\Sigma\left[\left(EF_{CO,vehicle\ type}\frac{MW_C}{MW_{CO}} + EF_{CO2,vehicle\ type}\frac{MW_C}{MW_{CO2}}\right) VMT_{\ vehicle\ type}\right]}{\Sigma\left[VMT_{\ vehicle\ type}\right]}} \quad \text{(S6)}$$

$$EF_{CO,gasoline} = \frac{\frac{\Sigma\left[EF_{CO,vehicle\ type} VMT_{\ vehicle\ type}\right]}{\Sigma\left[VMT_{\ vehicle\ type}\right]} f_{c,gasoline} d_{gasoline}}{\frac{\Sigma\left[\left(EF_{CO,vehicle\ type}\frac{MW_C}{MW_{CO}} + EF_{CO2,vehicle\ type}\frac{MW_C}{MW_{CO2}}\right) VMT_{\ vehicle\ type}\right]}{\Sigma\left[VMT_{\ vehicle\ type}\right]}} \quad \text{(S7)}$$

Calculations to determine diesel emission factors for gas-phase organic carbon and CO are the same as for gasoline while using the diesel fuel properties.

3.3.3.5 Secondary organic aerosol yield determination methodology and associated calculations

To determine overall SOA yields for each source and the distribution of SOA formation from each source across molecular sizes and chemical classes, we first determined the distribution of mass in each source's emissions and organized it into 25 x 8 matrices ($W_{ij,source}$). The rows of the matrix represent carbon number (*i*) and the columns, chemical class (*j*) as shown in Tables 3.3.6-3.3.8. With the objective of determining average high-NO_X yields for the subset of isomers in each point in this matrix, we determined which values were well-known in the literature from chamber or modeling data, and which had insufficient data.

For all compounds, high-NO_x SOA yields for known and estimated compounds are calculated or modeled assuming an average organic particle concentration of 10 μg m^{-3}. This organic particle loading was used as a value relevant to chamber studies, urban areas, and downwind urban areas. As the organic loading decreases, the yields of IVOCs will also decrease slightly due to changes in partitioning of the reaction products. Straight and branched alkanes were considered to have known yields. Yields for *n*-alkanes were calculated using the model reported by Jordan *et al.* (*38*) and the product yields provided therein. The volatilities of those reaction products are assumed to decrease by a multiplicative factor of 0.35 per carbon number (*40*). Yields for branched alkanes were calculated using the same model assuming an average 30% alkoxy radical decomposition (*41*), yielding a product with the volatility of a ketone with 3/4 of the original carbon atoms. For all compounds, volatility was calculated using SIMPOL as described by Pankow *et al.* (*42*). We assumed branched aliphatic compounds have volatilities similar to an *n*-alkane with similar gas chromatographic retention times, which is a reasonable proxy for volatility within a compound class (*43, 44*). Modeled SOA yields for straight-chain and branched alkanes are shown in Table 3.3.9.

Estimates for SOA yields of other compound classes (straight-chain cycloalkanes (e.g. decylcyclohexane), branched cycloalkanes, bicycloalkanes, tricycloalkanes, aromatics, and PAHs) were estimated via a Monte Carlo analysis (discussed below) by combining various scenarios constrained by literature and model data. All unknown compounds are treated as branched. For all compound classes, one possible scenario posits an SOA yield of the *n*-alkane of a similar volatility, similar to the use of a volatility basis set model using *n*-alkanes as surrogate compounds, such as the analysis of Mexico City aerosol performed by Lee-Taylor *et al.* (*44*). Similarly, branched alkanes can be expected to be a reasonable surrogate for all branched aliphatic compounds, providing an alternate scenario. Furthermore, several additional schemes are available for estimating yields of cyclic aliphatic compounds based on the small amount of laboratory data available on cyclic alkanes (*41*). Most of these scenarios provide similar estimated SOA yields.

Small aromatic compounds are somewhat better constrained by laboratory data, though data for larger aromatics and PAHs are scarce. Small aromatics (C_6 through C_8) are assumed to be known and have the yields of benzene, toluene, and *m*-xylene found in the literature (*46, 47*). C_9 and larger aromatics can be estimated using extrapolations of the two-product models of toluene and *m*-xylene, assuming the products decrease in volatility using the carbon number multiplicative factor described above. These models provide conservative estimates as the yield for even the largest aromatics does not exceed 0.17 using these models. The literature model for naphthalene (*48*) provides yields closer to those expected based on volatility, so is used as an estimate for aromatics and PAHs. Alternate PAH scenarios assume C_{10} - C_{12} PAHs to have SOA yields of naphthalene, methylnaphthalene, and dimethylnaphthalene, based on literature values (*48*). Yields for larger PAHs are based on the extrapolation of these models. Extrapolations of models provide conservative upper and lower bounds for the least volatile aromatic compounds: 0.10 to 1.28 for C_{19}-C_{25} aromatics, 0.31 to 1.28 for C_{19}-C_{25} PAHs.

The Monte Carlo estimation does not give preference to any of the scenarios. For clarity, we provide a summary of the scenarios used to model unknown yields. Scenarios 3-6 for the cycloalkanes and scenarios 3-4 for the multi-ring cycloalkanes are based on laboratory data for three measured cyclohexanes (*41*).

Cycloalkanes:

1) Yields of *n*-alkanes of similar volatility (*38*)
2) Yields of branched alkanes of similar volatility
3) Yields of branched alkanes with 2 more carbon atoms
4) Yields of branched alkanes with 1 less carbon atom
5) $C_{5\text{-}10}$ have yields of branched alkanes with 2 more carbon atoms, while C_{16} and larger have yields with 1 less carbon atom. Yields for $C_{11\text{-}15}$ are interpolated
6) Yields extrapolated from C_6 (branched alkane with 2 more carbon atoms) and C_{16} (branched alkane with 1 less carbon atom)

Bicycloalkanes & Tricycloalkanes:

1) Yields of *n*-alkanes of similar volatility (*38*)
2) Yields of branched alkanes of similar volatility
3) $C_{5\text{-}10}$ have yields of branched alkanes with 2 more carbon atoms, while C_{16} and larger have yields with 1 less carbon atom. Yields for $C_{11\text{-}15}$ are interpolated

4) Yields extrapolated from C_6 (branched alkane with 2 more carbon atoms) and C_{16} (branched alkane with 1 less carbon atom)

Aromatics (C_9 and larger):

1) Yields of *n*-alkanes of similar volatility (*38*)
2) Yields extrapolated from toluene two-product model (*46*)
3) All yields are 0.10 based on Chan *et al.* (*48*)
4) Yields extrapolated from naphthalene two-product model (*48*)

PAHs:

1) Yields of *n*-alkanes of similar volatility (*38*)
2) Yields extrapolated from naphthalene two-product model (*48*)
3) Yields for C_{12} and larger extrapolated from methylnaphthalene two-product model with $C_{10\text{-}11}$ having known yields (*48*)
4) Yields for C_{12} and larger assumed to be that of dimethylnaphthalene with $C_{10\text{-}11}$ having known yields (*48*)

We performed a Monte Carlo analysis to determine both bulk yields for each source and the distribution of those yields in each source to determine the most important compounds for SOA formation. If the yield for a given carbon number and chemical class point in the matrix was well-known, then the known yield did not change and no uncertainty is reported (Table 3.3.9). For unknown or understudied yields, for each iteration we randomly selected a scenario (*k*) from the constructed scenarios and added up to ±10% Gaussian-distributed noise (represented as $Y_{estimate,ijk}*gnoise(0.1)$ in Equation S8). Each iteration of known and randomly selected unknown yield values (Y'_{ij}) is multiplied by the known and constant weight percent matrix from each source ($W_{ij,source}$). The average of 10,000 iterations provides the distribution of SOA formation across each source ($Y_{ij,source}$) weighted by the chemical composition of the source. Uncertainties for all points in the matrices ($\sigma_{Yij,source}$) are determined by assessing the deviation of values across the 10,000 simulations (M=10,000).

$$Y'_{ij} = \begin{cases} Y_{known,ij}, & if\ known\ value\ exists \\ Y_{estimate,ijk} + Y_{estimate,ijk} * gnoise(0.1), & if\ no\ known\ value\ exists \end{cases} \quad \text{(S8)}$$

$$where\ k\ is\ selected\ by\ a\ random\ number\ generator$$

$$Y_{ij,source} = \frac{1}{M}\sum^{M}\left[W_{ij,source} * Y'_{ij}\right]\frac{1}{100} \quad \text{(S9)}$$

$$\sigma_{ij,Y_{source}} = \sqrt{\frac{1}{M}\left(\sum^{M}\left[Y^2_{ij,source}\right] - M\bar{Y}^2_{ij,source}\right)} \quad \text{(S10)}$$

The bulk SOA yield for a source (y_{source}) is calculated by summing the distribution of SOA yields from the entire matrix to provide a value that can be multiplied by total non-combusted organic carbon from a source to determine the predicted SOA. The uncertainty of the bulk yield value ($\sigma_{y,source}$) is determined by assessing the deviation of all values in the simulations and is shown in Figure 3.3.8.

$$y_{source} = \sum_i \sum_j Y_{ij,source} \quad \text{(S11)}$$

$$\sigma_{y_{source}} = \sum_i \sum_j \sqrt{\frac{1}{M}\left(\sum^M [y_{source}^2] - M\bar{y}_{source}^2\right)} \quad \text{(S12)}$$

Uncertainties presented in Table 3.3.1 and throughout the analyses have been propagated to reflect all uncertainties associated with the calculation and comparison of values.

The estimation of expected total SOA from gasoline and diesel presented in the paper (1.3 ± 0.4 μgOA m^{-3}) for comparison to AMS data was calculated by taking the daytime (8:00-19:30 PST) average of source contributions from gasoline and diesel (13.5 ± 9.3 and 9.8 ± 7.1 ppbC, respectively (N=270)) and determining the predicted SOA from both using the derived bulk SOA yields. Our CMB modeling method allows us to assess emissions from gasoline and diesel sources within several hours of transport to the site, and compare them to SOA production from a slightly larger scale of regional emissions and photochemistry as measured by the AMS. While, this does not act as a direct comparison since the observed SOA by the AMS is somewhat decoupled from the fresh emissions used to calculate the expected SOA, it does provide supporting evidence for the consistency of our calculations with observations. There were no significant multi-day OA events with accumulation of precursors or aerosol since concentrations decreased substantially on a daily basis due to meteorology. Dry-deposition of $PM_{1.0}$ OA would not have been a significant loss process, nor would coagulation of particles given particle number concentrations.

In the paper we examine the inclusion of SOA formation from gasoline in several traditional SOA modeling studies (MILAGRO, TORCH, NEAQS) and find that 20% of the SOA from gasoline is missing in the compound explicit models used at the TORCH and NEAQS campaigns, and 30% at the MILAGRO/MCMA studies (*20-22*). This was determined using the published list of compounds included in their models with our average liquid gasoline profile and determined SOA yields shown in Tables 3.3.7 and 3.3.9.

3.3.3.6. Calculation of ΔOA/ΔCO slopes

For the purposes of comparison to a broad set of urban studies, we estimate ΔOA/ΔCO slopes using derived bulk SOA yields and emission factors for non-combusted gas-phase organic carbon and CO:

$$\left[\frac{\Delta OA}{\Delta CO}\right]_{Predicted} = \left[\frac{\Delta POA}{\Delta CO}\right] + \frac{y_{gasoline} EF_{GPOC,gasoline} V_{gasoline} + y_{diesel} EF_{GPOC,diesel} V_{diesel}}{EF_{CO,gasoline} V_{gasoline} + EF_{CO,diesel} V_{diesel}} \quad \text{(S13)}$$

where $V_{gasoline}$ and V_{diesel} are the fraction of gasoline and diesel sold by volume and:

$$V_{gasoline} + V_{diesel} = 1 \quad \text{(S14)}$$

The emission factors for non-combusted gas-phase organic carbon and CO were:

$EF_{VOC,gasoline} = 0.45\ gGPOC\ L^{-1}$ (from this work, consistent with EMFAC2011 (*17*))

$EF_{VOC,diesel} = 1.01\ gGPOC\ L^{-1}$ (from this work, consistent with EMFAC2011 (*17*))

$EF_{CO,gasoline} = 12{,}750\ ppmv\ L^{-1}$ (from EMFAC2011 (*17*))

$$EF_{CO,diesel} = 3890\ ppmv\ L^{-1}$$ (from EMFAC2011 (*17*))

The [ΔPOA/ΔCO] constant is the average observed slope reported previously (9.4 μg m^{-3} $ppmv^{-1}$ CO) and is similar for most urban studies (*20, 33*).

Additional derivations of the OA/ΔCO equation that include non-tailpipe gasoline VOC emissions with no associated CO emissions have a negligible effect on predicted ΔOA/ΔCO values. Similarly, including cold start emissions, which has a slightly different ΔOA/ΔCO ratio than the running emission factors used (i.e. more CO in cold start emissions), does not have a substantial effect on the predicted ratio. Therefore, the simplified version (Equation S13) was used to calculate ΔOA/ΔCO ratios.

3.3.4. Supporting results

3.3.4.1. Characterization of gasoline and diesel fuel

We present the most comprehensive chemical speciation of diesel fuel to date with over 90% mass closure as part of an overall assessment of gasoline and diesel fuel. In this work, we supply unprecedented detail on both the overall mass and chemical distribution of both fuels and in-depth compound specific speciation data for use in future analyses and models such as those presented in this work. Composition data for hundreds of individual hydrocarbons in both fuels is shown in Tables 3.3.10-3.3.12 with average values for the state of California and site-specific data for the four regions from which fuel data were collected. Ten gasoline samples and three diesel samples were analyzed for each location and standard deviations represent the variability between fuel samples. Gasoline, with 10 wt% ethanol additive, had an average density of 740 ± 7 g L^{-1}, and a carbon fraction of 0.824. Diesel fuel had an average density of 852 ± 10 g L^{-1} and a carbon fraction of 0.866. Gasoline composition was relatively homogeneous across the state in terms of mass distribution and percentages of chemical classes with minor differences in concentrations of individual compounds. Diesel fuel showed some heterogeneity with a few samples being slightly shifted in mass distribution. Overall, the composition was similar, but not as homogeneous as gasoline likely due to differences in regulations between gasoline and diesel fuel. The standard deviations in Tables 3.3.1 and 3.3.3 reflect this variability. Future work with the supplied data must recognize that both regional and seasonal differences in fuel can significantly affect the ratios of specific compounds and caution should be taken when extrapolating detailed data outside of the timeframe and locations presented here.

The volatility basis set defines VOCs as compounds with saturation concentrations (C°) > 10^6 μg m^{-3}, IVOCs as C° = 10^3-10^6 μg m^{-3}, and a third class Semi-Volatile Organic Compounds (SVOCs) as C° = 1–100 μg m^{-3} (*5*). A small fraction (~5%) of diesel fuel extends into the SVOC range (Figure 3.3.11). For the purposes of comparison to *a priori* information used in SOA models to represent diesel POA, IVOCs, and SVOCs, we present the composition of diesel fuel in terms of the volatility basis set used in many SOA models (Figure 3.3.11) (*5, 19-21*).

Following the U.S. Clean Air Act of 1990, gasoline composition was reformulated numerous times over the following 2 decades. Currently, California reformulated gasoline, similar to U.S. reformulated gasoline, is regulated to contain less than 25% aromatics and 6% alkenes (by

volume) largely due to their ozone formation potential (*23*). Across our four sampling locations we measured a range of 24-29 wt% aromatics and 2-5 wt% olefins. During the summer, vapor pressure is also regulated to reduce non-tailpipe evaporative emissions. All of California is required to use reformulated gasoline and most U.S. regions that fail to meet air quality standards are required to use U.S. reformulated gasoline. Across the whole U.S., about a third of the gasoline sold is reformulated (*9*). Conventional gasoline, compared to reformulated gasoline can contain greater amounts of aromatics and olefins, which are likely to increase its reactivity and SOA formation potential (*2*).

Diesel fuel has been regulated nationally for sulfur content, but only in California has the organic composition been regulated. Starting in 1993, diesel fuels distributed in California have been regulated to contain less than 10% aromatics by volume and 1.4% PAHs by weight (*23*). A provision contained within the regulations allows for producers and importers of diesel fuel to sell an alternative diesel formulation if they can prove that emissions from a heavy-duty diesel engine using their fuel are similar or lower for nitrogen oxides, particulate matter, and soluble organic fraction of particulate matter. Such "Certified Diesel Fuel Formulations" contain 15 to 25% aromatics and 2 to 5% PAHs (*23*).

3.3.4.2 CMB analysis results and comparison of emission factors to EMFAC2011

Over a mix of weekdays and weekends, diesel exhaust constituted 24 ± 14% of gas-phase organic carbon from motor vehicle exhaust emissions at the Caldecott tunnel, and 57 ± 16% of total exhaust at the Bakersfield supersite in the San Joaquin Valley. Diesel fuel sales data are consistent with model results at both sites when accounting for differences in emission factors since 11% and 33% of on-road fuel use is diesel in the San Francisco Bay Area and Kern County, respectively (*10*). It is important to note that off-road use of diesel represents a non-negligible amount of diesel fuel use and will increase total diesel fuel use by a few percent on a state and national level. On-road diesel usage is 4-6x greater than off-road on these scales, but county-level data do not exist at this time.

The contributions of non-tailpipe gasoline (i.e., evaporative) emissions were slightly different than previous work showing that non-tailpipe gasoline was responsible for ~30% of gasoline-related VOC emissions in the South Coast Air Basin (*13*). 17 ± 9% of gasoline-related emissions were from non-tailpipe sources in the Caldecott tunnel, which is not unexpected since emissions from service stations and resting emissions from vehicles would not play a role in the tunnel environment. In Bakersfield, non-tailpipe gasoline was 38 ± 20 % of emissions from gasoline vehicles—slightly higher than previous work.

In terms of the overall contribution to non-combusted gas-phase organic carbon emissions at Bakersfield, diesel exhaust, gasoline exhaust, and non-tailpipe gasoline comprised 46 ± 15%, 34 ± 13%, and 20 ± 11 of motor vehicle emissions, respectively. Additional analysis examining the impact of petroleum operations (e.g. production & refining) is detailed in Section 3.5. At the Caldecott tunnel, diesel exhaust, gasoline exhaust, and non-tailpipe gasoline comprised 20 ± 12%, 66 ± 13%, and 14 ± 7 of motor vehicle emissions, respectively.

Atypical of many urban areas, weekday/weekend differences were not strong in Bakersfield with regard to the distribution of emissions between gasoline and diesel exhaust as daytime values of both decreased by ~40% on the weekends (Figure 3.3.12).

From the tunnel study, emissions of non-combusted gas-phase organic carbon were determined to be 0.38 ± 0.11 gC L^{-1} for gasoline exhaust and 0.86 ± 0.25 gC L^{-1} for diesel exhaust. Values calculated using California's emissions model for the same period (*17*) are 0.36 gC L^{-1} and 0.75 gC L^{-1} before adjusting for products of incomplete combustion for gasoline and diesel, respectively. The gasoline emission factor is close to gasoline emission factors calculated by both methods (0.30 ± 0.11 gC L^{-1} using the regression method), but diesel is somewhat different with our value being slightly higher. Differences in gasoline and diesel fleet distribution across varying vehicle classes, ages, and levels of maintenance in the tunnel versus that of EMFAC may be responsible for these differences, as "high-emitters" are sometimes self-selected out of dynamometer testing.

Calculated exhaust emission factors are lower bounds since they do not include products of incomplete combustion or cold start emissions. The calculated values are focused on unburned hydrocarbons, which are considerably more important for SOA formation. While many products of incomplete combustion are highly reactive and important for overall OH reactivity and ozone formation, most of them are not currently expected to form SOA with the exception of larger carbonyls that make up a minor fraction of emissions (*11-12*). Continued work is necessary to understand their emissions, but for these reasons they are not included in the emission factors derived and used in this study.

The methods applied in this work include the ability to examine emissions and concentrations of individual compounds in addition to overall source contributions. Emission factors for any individual compound in gasoline and/or diesel fuel (or set of compounds) can be estimated by adjusting the reported emission factors for non-combusted gas-phase organic carbon by the compound's compositional fraction in the fuel (e.g., $EF_{n\text{-}dodecane,diesel} = EF_{GPOC,diesel} * WtC\%_{n\text{-}dodecane,diesel} /100$). Similarly, the ambient concentration of any compound can be estimated by multiplying the source contributions (ppbC) by the compound's composition (WtC%) in the sources and summing the terms. Additionally, estimates of SOA from each source can be obtained my multiplying emission factors or calculated emissions by bulk SOA yields.

3.3.4.3. ΔOA/ΔCO ratios

Emissions of SOA precursors are dominated by diesel, whereas CO emissions are dominated by gasoline, so ΔOA/ΔCO ratios are sensitive to changes in fuel use. In urban areas which have a mixture of diesel and gasoline use, gasoline CO overwhelms the ΔOA/ΔCO relationship as gasoline mobile sources are responsible for 30x more than diesel (*49*). In urban regions such as the South Coast Air Basin, 90% of CO emissions are from mobile sources versus 65% statewide (*17, 49*). The ΔOA/ΔCO ratio presented for gasoline is an upper bound given the relatively slow reaction rates for benzene and toluene.

Weekday values in Los Angeles were centered on 14 μg m^{-3} $ppmv^{-1}$ CO and we predict a very similar value of 13 μg m^{-3} $ppmv^{-1}$ CO for a reported 17% diesel fraction of total fuel usage cited in their work. Photochemical ages reported in Los Angeles during the weekend are greater due to

faster photochemical processing likely associated with lower NO_x emissions from diesel sources (*6, 26*). Adjusting observed weekend ΔOA/ΔCO values from Los Angeles for photochemical aging results in a ΔOA/ΔCO slope very similar to that expected from a gasoline-dominated fleet (*6*). Based on previous work, a 3-4x increase in the ΔOA/ΔCO slope occurs from photochemical ages of ~6 hours to 1 day at a roughly linear rate (*19, 25*). Thus, ages of 12 and 24 hours should correspond to increases of 2x and 4x, respectively. Observed weekend ratios ranged from 22 to 70 μg m^{-3} $ppmv^{-1}$ CO (Figure 3.3.14) (*6*). The corresponding range of photochemical ages shown over the weekend extend from 12 hours to just over 24 hours as determined by toluene/benzene ratios of 2.0 through 1.0 (*6, 30*). Adjusting the observed ΔOA/ΔCO values of 22 to 70 μg m^{-3} $ppmv^{-1}$ CO, by factors of 2 to 4, respectively, produces ΔOA/ΔCO values around 11 to 17 μg m^{-3} $ppmv^{-1}$ CO at ~6 hours of photochemical processing, and does not consider the influence of other sources of SOA precursors. Similarly, in Figure 3.3.14, we estimate aged weekend ΔOA/ΔCO values based on a fuel mixture of 5-10% diesel and see general agreement with reported measurements. We contend that ΔOA/ΔCO slopes alone are not sufficiently sensitive to effectively discern the contributions of gasoline vs. diesel, and given the variability in data from the Los Angeles study, it is difficult to separate the effects of changes in SOA precursor emissions, CO emissions, and increased photochemical processing.

Non-vehicular anthropogenic and biogenic sources contribute SOA precursors without CO and will vary depending on the characteristics of an urban region as shown by enhanced ΔOA/ΔCO slopes in Mexico City, the Southeast U.S., and the Po Valley (despite outlier filtering for major non-vehicular events in some studies) (*25, 30-32*).

Our derived SOA yields are intended to model the first several generations of photochemical oxidation, which corresponds to the extent of oxidation effectively constrained by experimental measurements. It is highly plausible that the continued increase in ΔOA/ΔCO ratios beyond our predictions is caused by the continued oxidation of multi-generation oxidation products in the gas-phase. In this study, we have refrained from estimating SOA yields for these highly-aged air masses as doing so would require excessive extrapolation with high uncertainties. A re-evaluation of gasoline and diesel SOA yields is encouraged once these data become available.

References and Notes for Gentner et al., 2012:

1 M. Hallquist *et al.*, The formation, properties and impact of secondary organic aerosol: current and emerging issues. *Atmos. Chem. Phys.* **9**, 5155 (2009).

2 U.S. Environmental Protection Agency, *U.S. Clean Air Act (and subsequent amendments/rulings)* (http://www.epa.gov/air/caa/)

3 J. L. Jimenez *et al*., Evolution of Organic Aerosols in the Atmosphere. *Science* **326**, 1525 (2009).

4 D. R. Worton *et al*., Embracing Complexity: Deciphering Origins and Transformations of Atmospheric Organics through Speciated Measurements (Viewpoint). *Environ. Sci. Technol.* **46**, 5265 (2012).

5 A. L. Robinson *et al*., Rethinking organic aerosols: Semivolatile emissions and photochemical aging. *Science* **315**, 1259 (2007).

6 R. Bahreini *et al*., Gasoline emissions dominate over diesel in formation of secondary organic aerosol mass. *Geophys. Res. Lett.* **39**, L06805 (2012).

7 E. A. Weitkamp *et al*., Laboratory Measurements of the Heterogeneous Oxidation of Condensed-Phase Organic Molecular Makers for Motor Vehicle Exhaust. *Environ. Sci. Technol.* **42**, 7950 (2008).

8 H. O. T. Pye, G. A. Pouliot, Modeling the Role of Alkanes, Polycyclic Aromatic Hydrocarbons, and Their Oligomers in Secondary Organic Aerosol Formation. *Environ. Sci. Technol.* **46**, 6041 (2012).

9 U.S. Energy Information Administration, *National fuel sales data* (2010 data, http://www.eia.gov/dnav/pet/pet_cons_prim_dcu_nus_a.htm)
10 California Department of Transportation, *California Motor Vehicle Stock Travel, and Fuel Forecast (MVSTAFF) 2008 Report* (http://www.dot.ca.gov/hq/tsip/smb/documents/mvstaff/mvstaff08.pdf)
11 T. W. Kirchstetter *et al*., Impact of Oxygenated Gasoline Use on California Light-Duty Vehicle Emissions. *Environ. Sci. Technol.* **30**, 661 (1996).
12 J. J. Schauer *et al.*, Measurement of Emissions from Air Pollution Sources. 2. C1 through C30 Organic Compounds from Medium Duty Diesel Trucks. *Environ. Sci. Technol.* **33**, 1578 (1999).
13 D. R. Gentner *et al*., Diurnal and Seasonal Variability of Gasoline-Related Volatile Organic Compound Emissions in Riverside, California. *Environ. Sci. Technol.* **43**, 4247 (2009).
14 G. Isaacman *et al.*, Improved resolution of hydrocarbon structures and constitutional isomers in complex mixtures using gas chromatography-vacuum ultraviolet-mass spectrometry. *Anal. Chem.* **84**, 2335 (2012).
15 J. G. Watson *et al.*, The effective variance weighting for least squares calculations applied to the mass balance receptor model. *Atmos. Env.* **18**, 1347 (1984).
16 W. R. Leppard *et al.*, "Effects of gasoline composition on vehicle engineout and tailpipe hydrocarbon emissions," *SAE Tech. Pap. Ser. No. 920329* (1992).
17 California Air Resources Board, *Motor Vehicle Emission Factor/Emission Inventory Model - EMFAC 2011* (http://www.arb.ca.gov/msei/msei.htm)
18 S. Liu *et al*., Secondary organic aerosol formation from fossil fuel sources contribute majority of summertime organic mass at Bakersfield. *J. Geophys. Res.* in review.
19 A. Hodzic *et al.*, Modeling organic aerosols in a megacity: potential contribution of semi-volatile and intermediate volatility primary organic compounds to secondary organic aerosol formation. *Atmos. Chem. Phys.* **10**, 5491 (2010).
20 J. A. de Gouw *et al.*, Sources of particulate matter in the northeastern United States: 1. Direct emissions and secondary formation of organic matter in urban plumes. *J. Geophys. Res.* **113**, D08301 (2008).
21 K. Dzepina *et al.*, Modeling the Multiday Evolution and Aging of Secondary Organic Aerosol During MILAGRO 2006. *Environ. Sci. Technol.* **45**, 3496 (2011).
22 D. Johnson *et al*., Simulating regional scale secondary organic aerosol formation during the TORCH 2003 campaign in the southern UK. *Atmos. Chem. Phys.* **6**, 403 (2006).
23 California Air Resources Board, *California Diesel Fuel and Reformulated Gasoline Regulations (with subsequent amendments)* (http://www.arb.ca.gov/fuels/fuels.htm)
24 N. Takegawa *et al*., Seasonal and diurnal variations of submicron organic aerosol in Tokyo observed using the Aerodyne aerosol mass spectrometer. *J. Geophys. Res.* **111**, D11206 (2006).
25 L. I. Kleinman *et al.*, The time evolution of aerosol composition over the Mexico City plateau. *Atmos. Chem. Phys.* **8**, 1559 (2008).
26 A. R. Russell *et al.*, Space-based Constraints on Spatial and Temporal Patterns of NO*x* Emissions in California, 2005-2008. *Environ. Sci. Technol.* **44**, 3608 (2010).
27 C. D. Cappa, K. R. Wilson, Multi-generation gas-phase oxidation, equilibrium partitioning, and the formation and evolution of secondary organic aerosol. *Atmos. Chem. Phys. Discuss.* **12**, 3295 (2012).
28 B. Ervens, B. J. Turpin, R. J. Weber, Secondary organic aerosol formation in cloud droplets and aqueous particles (aqSOA): a review of laboratory, field and model studies. *Atmos. Chem. Phys.* **11**, 11069 (2011).
29 A. W. Rollins *et al*., Nighttime growth of particulate organic nitrates: a significant source of atmospheric secondary organic aerosols. *Science* in review.
30 R. J. Weber *et al.*, A study of secondary organic aerosol formation in the anthropogenic-influenced southeastern United States. *J. Geophys. Res.* **112**, D13302 (2007).
31 P. F. DeCarlo *et al.*, Fast airborne aerosol size and chemistry measurements above Mexico City and Central Mexico during the MILAGRO Campaign. *Atmos. Chem. Phys.* **8**, 4027 (2008).
32 J. Crosier *et al.*, Chemical composition of summertime aerosol in the Po Valley (Italy), northern Adriatic and Black Sea. *Q. J. R. Meteorol. Soc.* **113**, 61 (2007).
33 J. de Gouw, J. L. Jimenez, Organic aerosols in the Earth's atmosphere. *Environ. Sci. Technol.* **43**, 7614 (2009).
34 J. Pollmann, J. Ortega, D. Helmig, Analysis of atmospheric sesquiterpenes: Sampling losses and mitigation of ozone interferences, *Environ. Sci. Technol*., **39**, 9620 (2005).
35 D. B. Millet *et al.*, Atmospheric volatile organic compound measurements during the Pittsburgh Air Quality Study: Results, interpretations, and quantification of primary and secondary contributions. *J. Geophys. Res.* **110**, D07S07 (2005).

36 T. R. Dallmann *et al*., On-Road Measurement of Gas and Particle Phase Pollutant Emission Factors for Individual Heavy-Duty Diesel Trucks. *Environ. Sci. Technol.* in review.
37 R. A. Harley, S. C. Coulter-Burke, T. S. Yeung, Relating liquid fuel and headspace vapor composition in California reformulated gasoline samples containing ethanol. *Environ. Sci. Technol.* **34**, 4088 (2000).
38 U.S. Environmental Protection Agency, *EPA-CMB8.2* (http://www.epa.gov/scram001/receptor_cmb.htm)
39 C. E. Jordan *et al*., Modeling SOA formation from OH reactions with C8–C17 n-alkanes. *Atmos. Environ.* **42**, 8015 (2008).
40 J. H. Kroll, J. H. Seinfeld, Chemistry of secondary organic aerosol: Formation and evolution of low-volatility organics in the atmosphere. *Atmos. Environ.* **42**, 3593 (2008).
41 Y. B. Lim, P. J. Ziemann, Effects of molecular structure on aerosol yields from OH radical-initiated reactions of linear, branched, and cyclic alkanes in the presence of NOx. *Environ. Sci. Technol.* **43**, 2328 (2009).
42 J. F. Pankow, W. E. Asher, SIMPOL.1: a simple group contribution method for predicting vapor pressures and enthalpies of vaporization of multifunctional organic compounds. *Atmos. Chem. Phys*., **8**, 2773 (2008).
43 G. Isaacman *et al.*, Understanding evolution of product composition and volatility distribution through in-situ GC × GC analysis: a case study of longifolene ozonolysis. *Atmos. Chem. Phys*., **11**, 5335 (2011).
44 D. A. Hinckley *et al.*, Determination of Vapor Pressures for Nonpolar and Semipolar Organic Compounds from Gas Chromatographic Retention Data. *J. Chem. Eng. Data* **35**, 232 (1990).
45 J. Lee-Taylor *et al.*, Explicit modeling of organic chemistry and secondary organic aerosol partitioning for Mexico City and its outflow plume. *Atmos. Chem. Phys*., **11**, 13219 (2011).
46 N. L. Ng *et al*., Secondary organic aerosol formation from *m*-xylene, toluene, and benzene. *Atmos. Chem. Phys.* **7**, 3909 (2007).
47 K. P. Wyche *et al.*, Gas phase precursors to anthropogenic secondary organic aerosol: detailed observations of 1,3,5-trimethylbenzene photooxidation, *Atmos. Chem. Phys.*, **9**, 635 (2009).
48 A. W. H. Chan et al., Secondary organic aerosol formation from photooxidation of naphthalene and alkylnaphthalenes: implications for oxidation of intermediate volatility organic compounds (IVOCs). *Atmos. Chem. Phys*. **9**, 3049 (2009).
49 California Air Resources Board, *Estimated annual average emissions, 2010*. (http://www.arb.ca.gov/ei/emsmain/emsmain.htm).

Figures and Tables for Gentner et al., 2012:

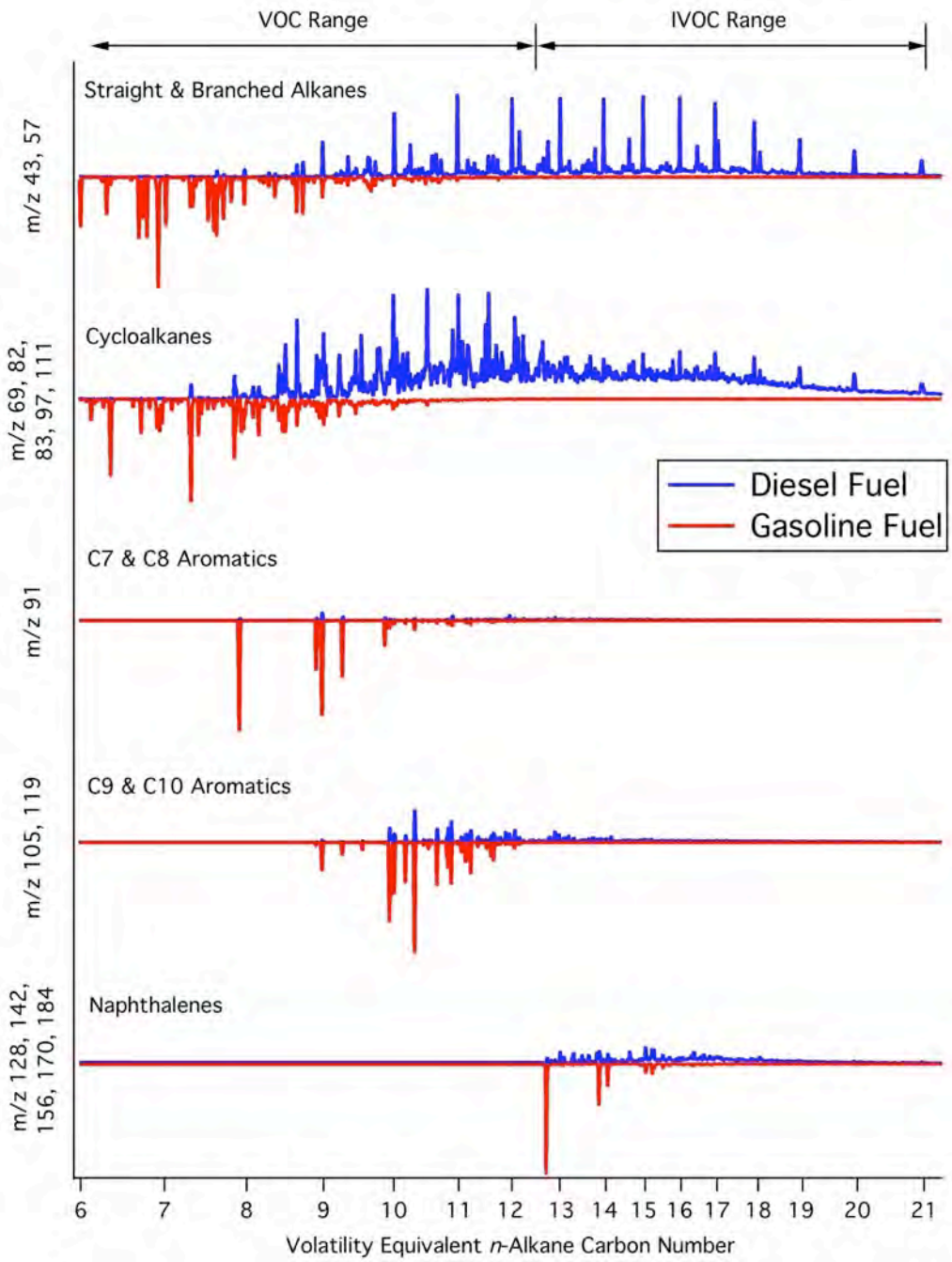

Figure 3.3.1. *Distributions of chemical classes for diesel (blue) and gasoline (red) are distinct with some overlap as shown via gas chromatography/mass spectrometry for representative fuel samples. Fuels span both the VOC and IVOC volatility ranges. Chemical classes are represented by their dominant mass fragments and shown as a function of n-alkane carbon number.*

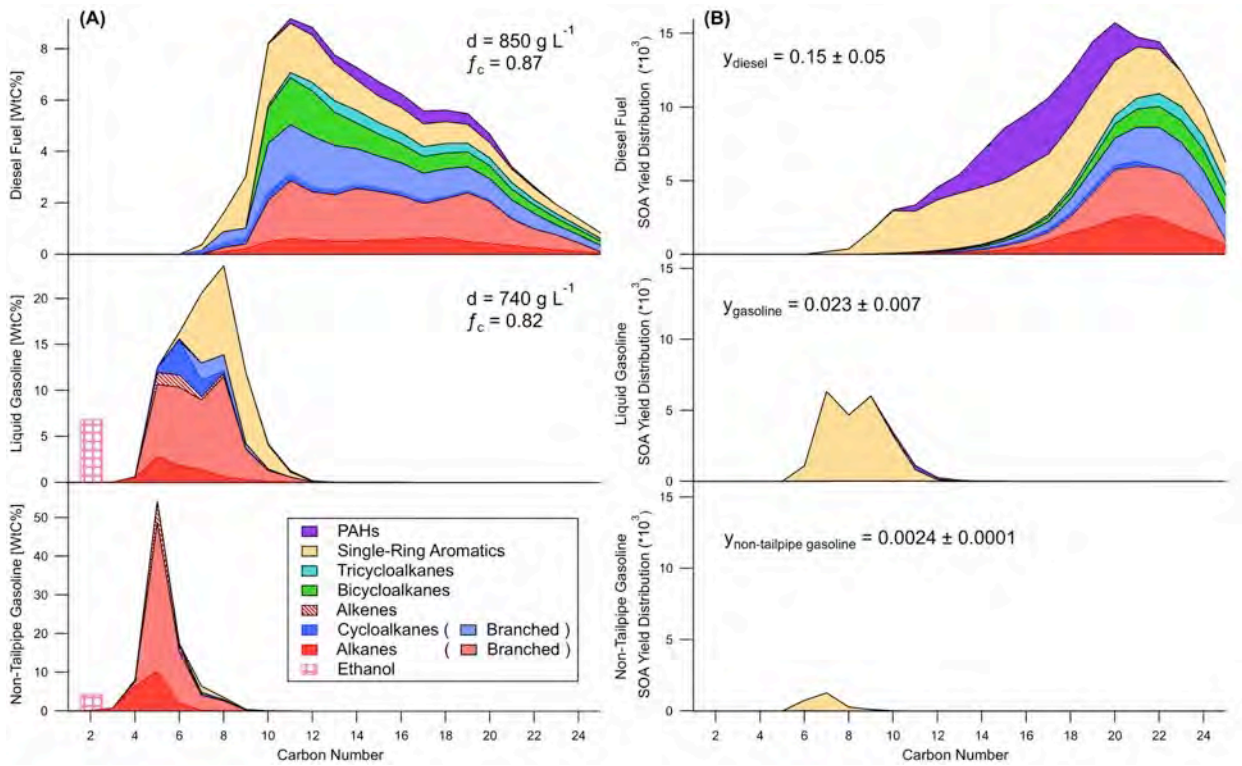

Figure 3.3.2. *Distribution of mass* ***(A)*** *and SOA formation potential [μgSOA μg^{-1}]* ***(B)*** *in diesel and gasoline fuel (representative of exhaust) and non-tailpipe gasoline emissions. Distributions in both panels are colored by chemical class. Fuel properties (density, carbon fraction) and bulk SOA yields (at M = 10 μg m^{-3}) are superposed on panels A and B, respectively. Predicted SOA from gasoline exhaust is much lower than diesel and dominated solely by aromatic content, whereas diesel SOA is produced from a mix of aromatic and aliphatic compounds. A distribution of the SOA potential uncertainties can be found in Fig. 3.3.8.*

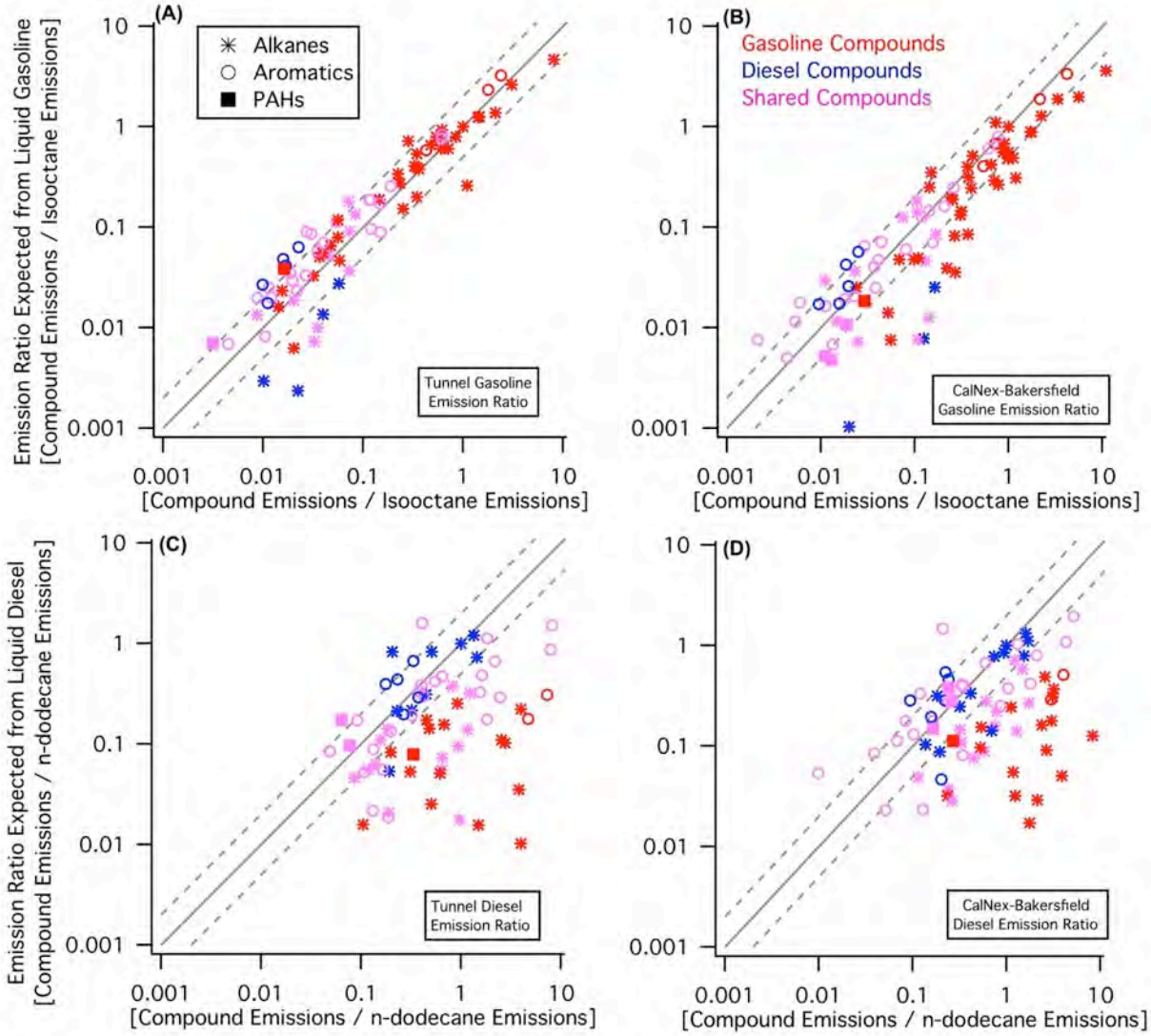

Figure 3.3.3. *Demonstration of compositional consistency between gasoline and diesel fuel to gasoline and diesel exhaust, respectively, at both* **(A, C)** *the Caldecott tunnel and Bakersfield* **(B, D)** *using regressions to gasoline (iso-octane) and diesel (n-dodecane) tracers. Similar to Figure 3.3.1, compounds dominated by gasoline (red) are most consistent with the liquid gasoline profile. Conversely, those dominated by diesel (blue) agree most with diesel fuel. Compounds shared by gasoline and diesel (pink) vary in degree of covariance with each source depending on relative content in each fuel and relative magnitude of each source at each field site.*

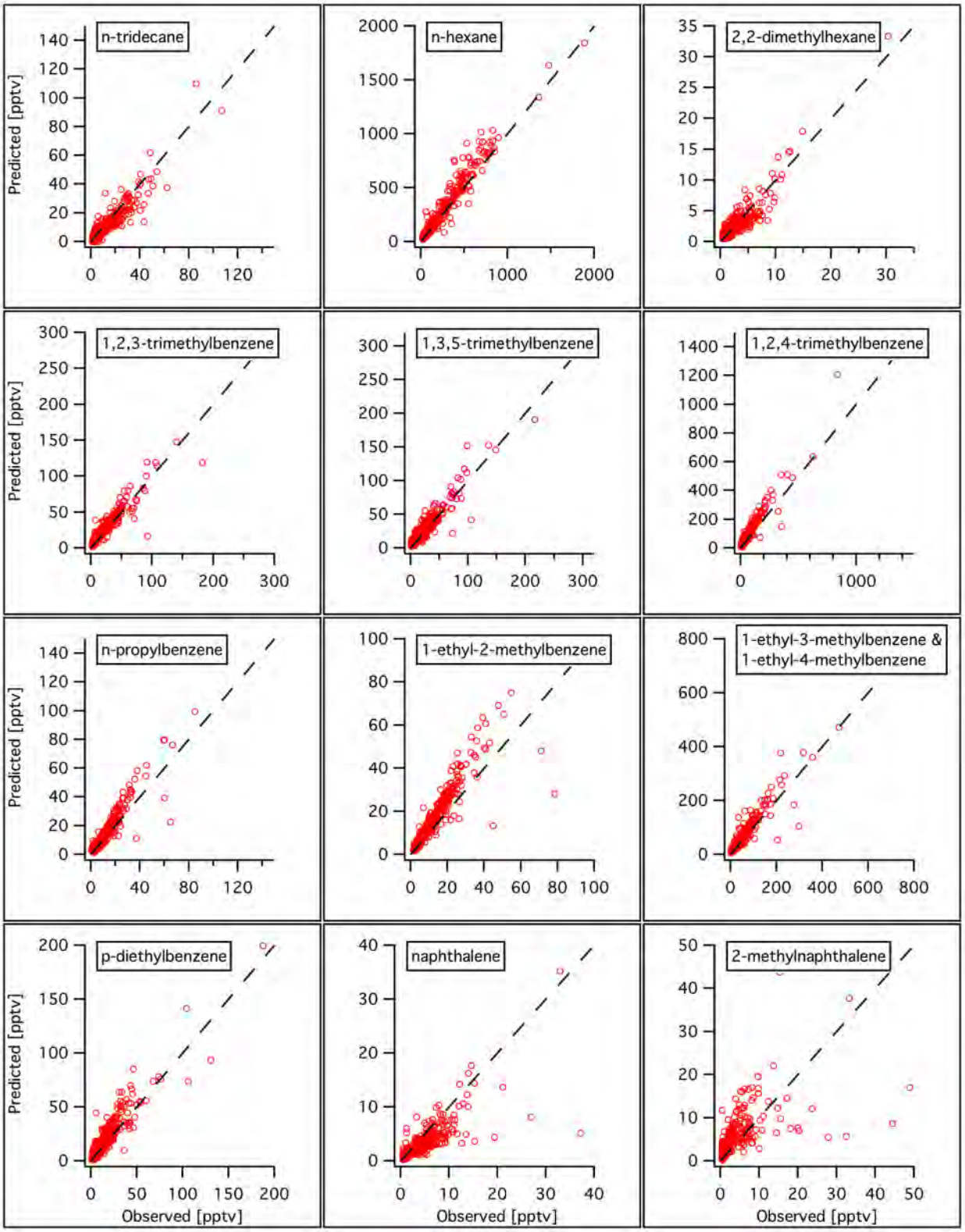

Figure 3.3.4. *Verification of model perfomance at CalNex-SJV by comparing predicted compound concentrations with observations of independent compounds not included in model. The 1:1 line is shown in each panel as a dashed line.*

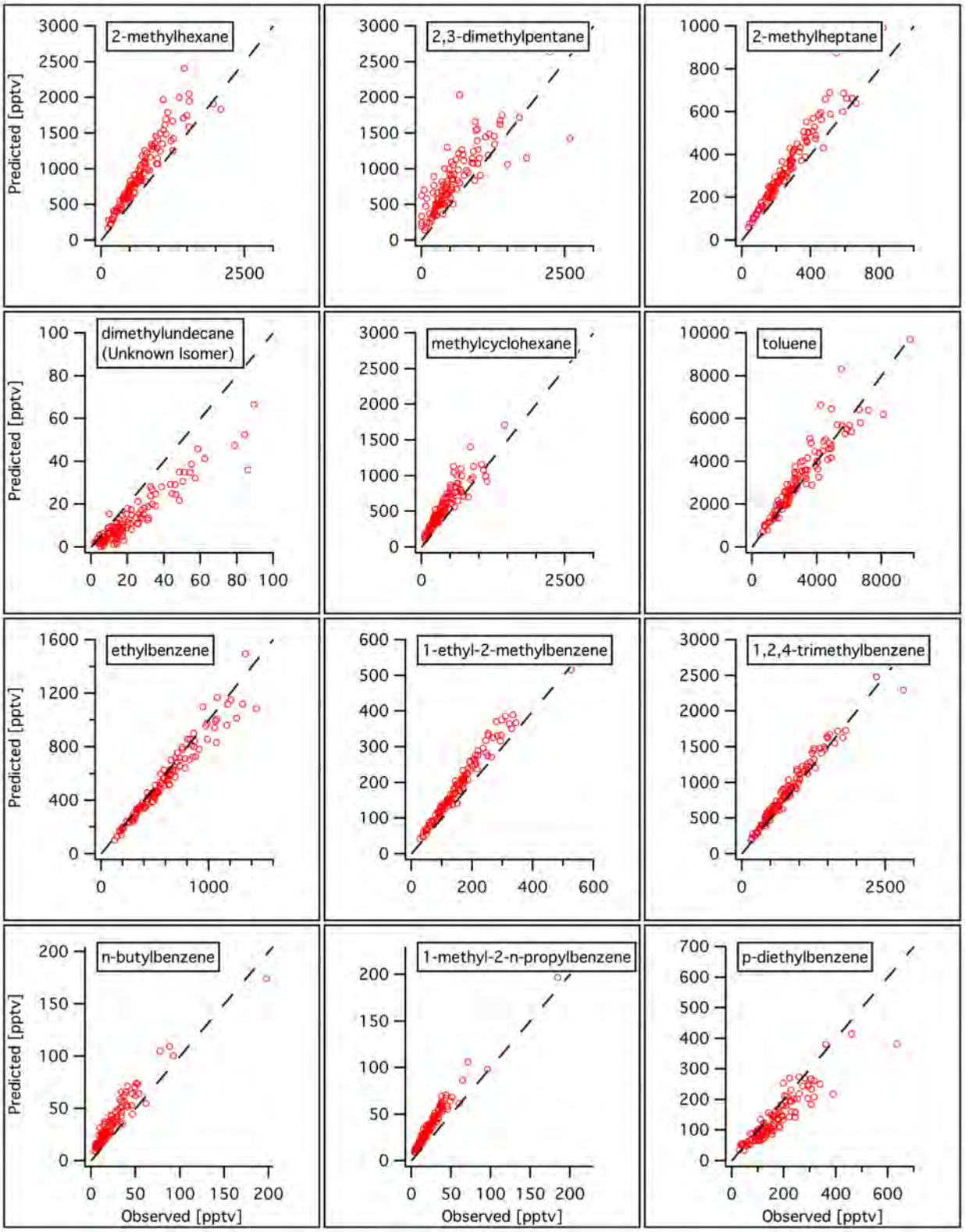

Figure 3.3.5. *Verification of model perfomance at the Caldecott Tunnel (Oakland, CA) by comparing predicted compound concentrations with observations of independent compounds not included in model. The 1:1 line is shown in each panel as a dashed line.*

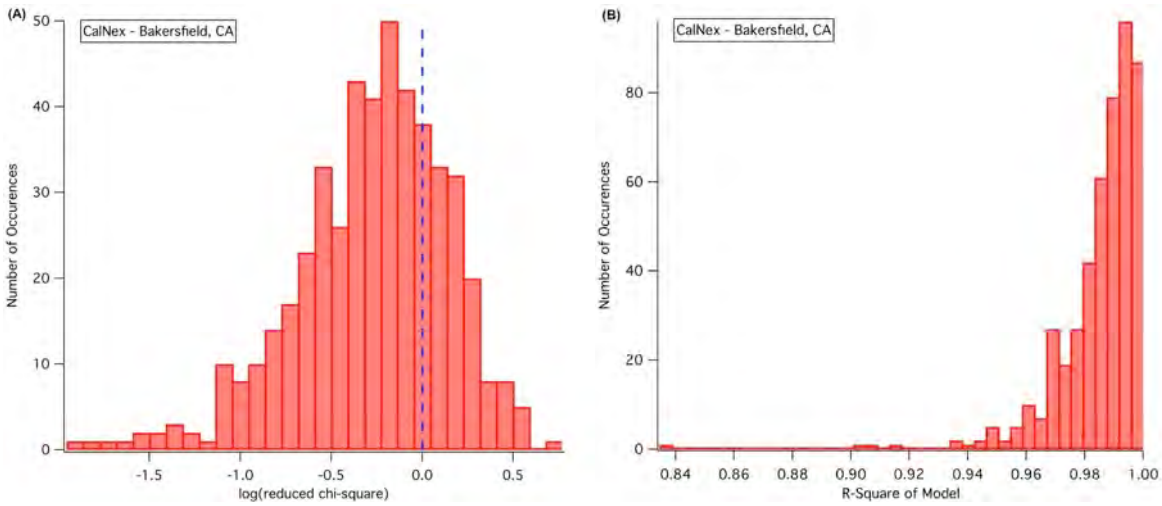

Figure 3.3.6. *Internal model diagnostics for CalNex-Bakersfield site (N=476). Panel A shows the log of the reduced chi-square test where ≤ 0 indicates a good fit of model data. Similarly, Panel B shows the overall coefficient of determination (r^2) of compounds used in the model and values close to 1.0 indicate robust model performance.*

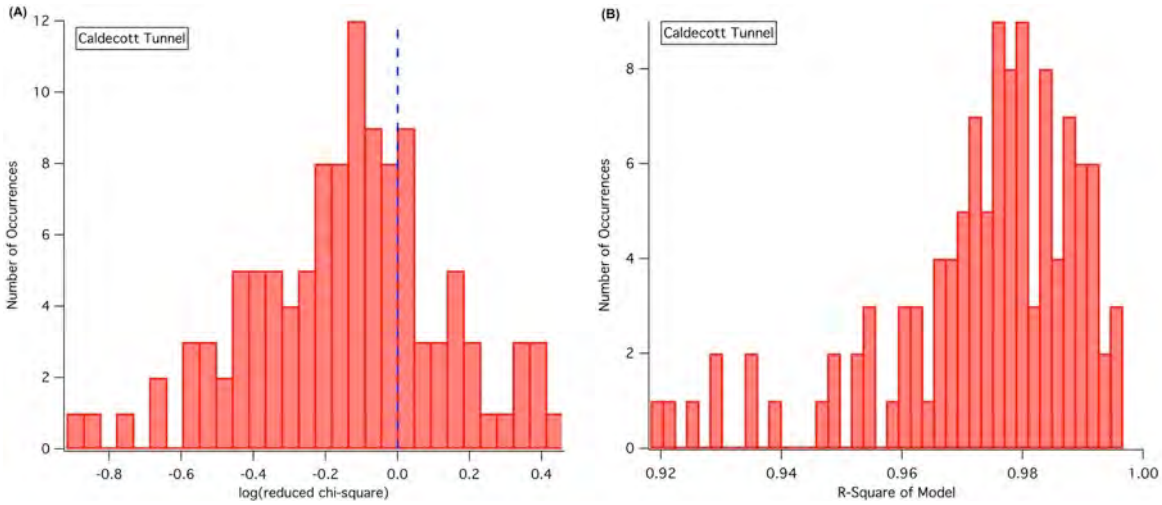

Figure 3.3.7. *Internal model validation for the Caldecott tunnel (N=114). Description same as Figure 3.3.6*

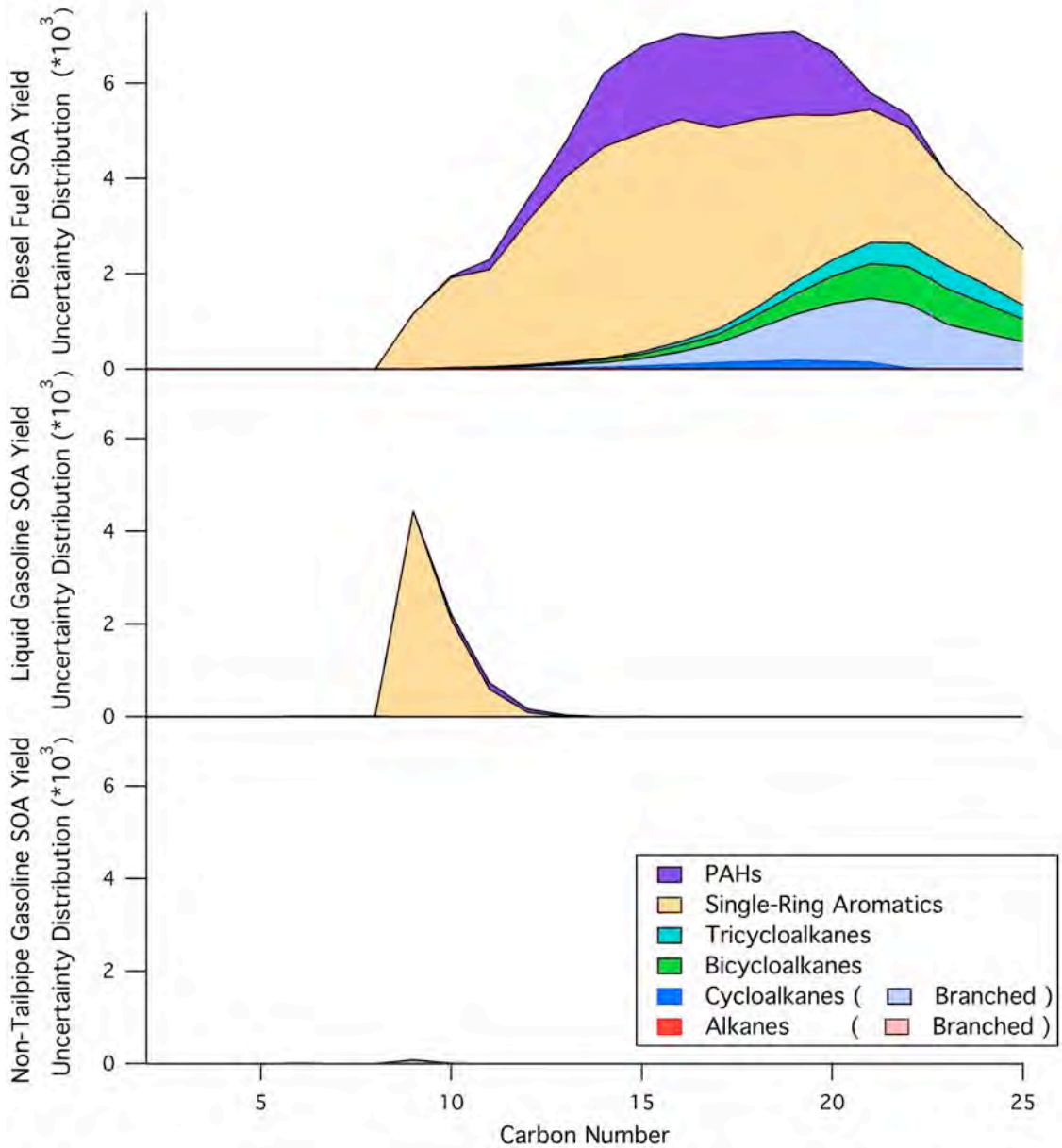

Figure 3.3.8. *Distibutions of SOA yield uncertainties [μgSOA μg^{-1}] from each source where uncertainties are based on Monte Carlo anlaysis. Diesel exhasut has greatest uncertainty due to insufficent studies on intermediate volatility compounds likely to form SOA, with the exception of straight and branched alkanes.*

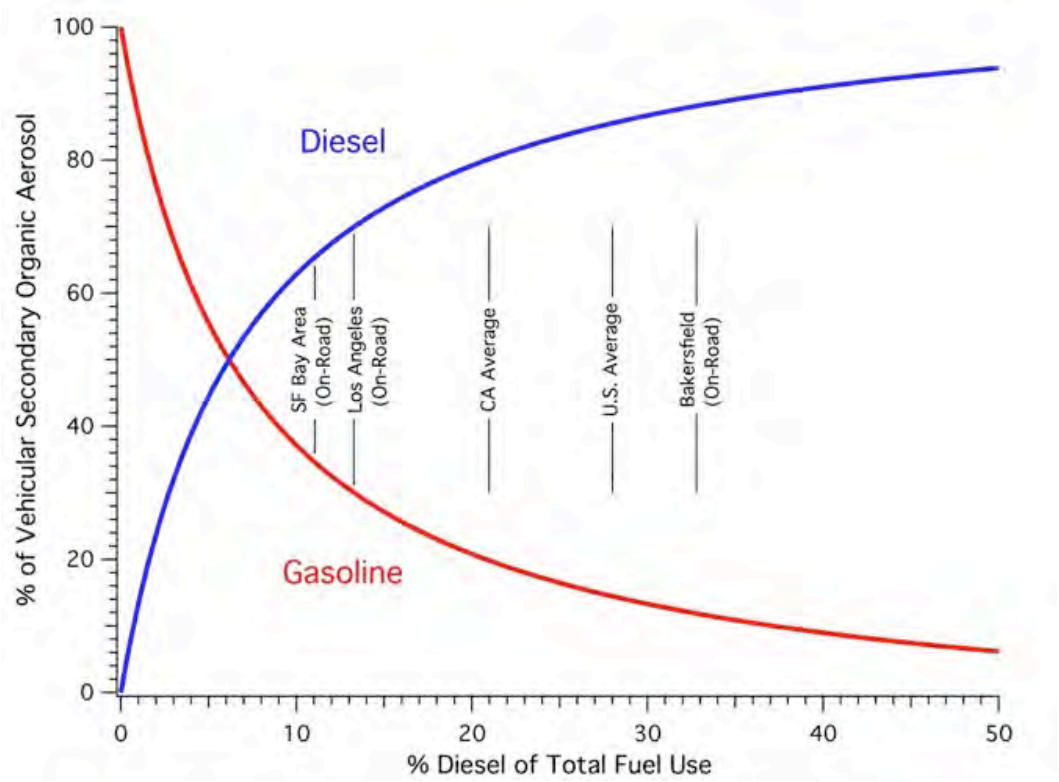

Figure 3.3.9. *The percent contribution of gasoline and diesel exhaust to SOA over 0-50% diesel fuel use demonstrates the predominance of diesel sources for SOA formation. SOA contributions form the two sources are equivalent at 6% diesel fuel use. The U.S. and CA state averages shown are based on total on- and off-road use. The urban areas in CA shown are for on-road fuel use only; off-road contributions will increase the diesel fraction of total use by several percent, but are not available at this scale.*

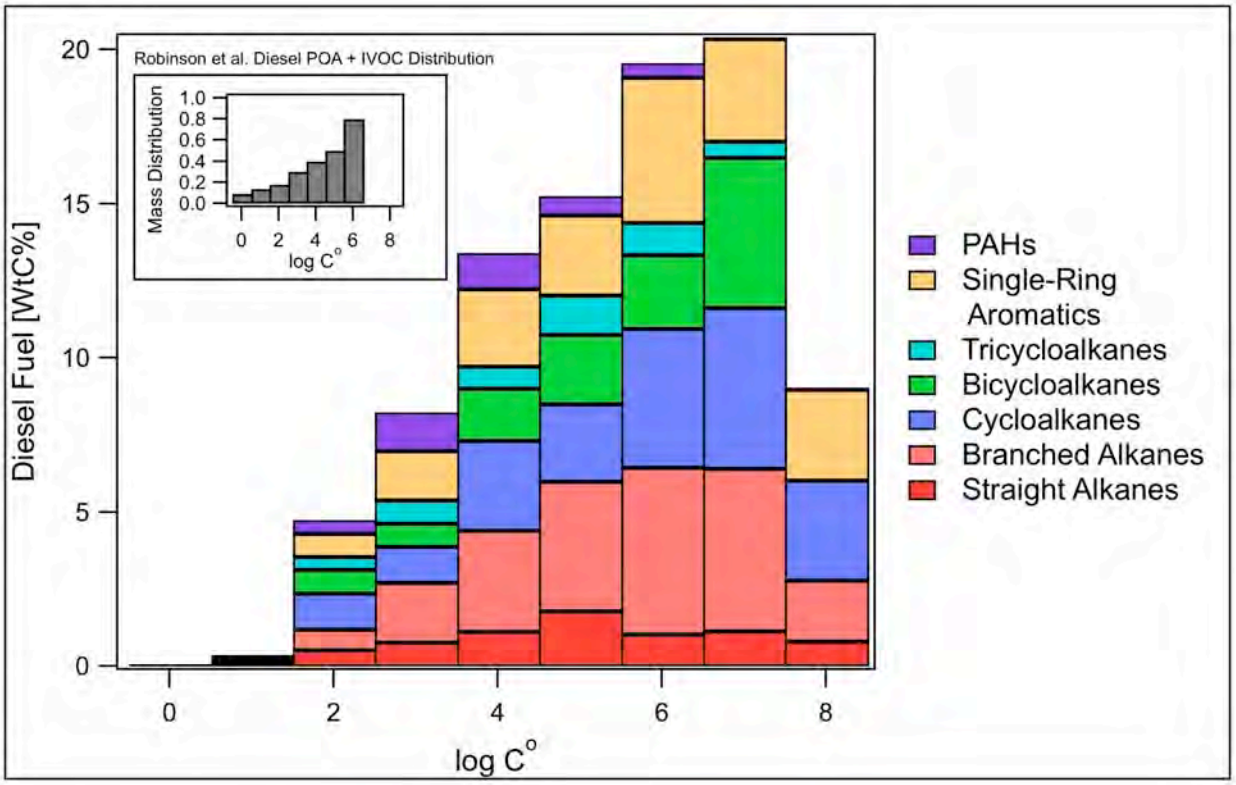

Figure 3.3.10. *Volatility basis set distribution of diesel fuel broken down by chemical class. Inset shows SVOC and IVOC distribution used in current models (5), which does not include the* $C°=10^7$ *μg* m^{-3} *and* $C°=10^8$ *μg* m^{-3} *volatility bins, which contain* $C_{9\text{-}11}$ *aromatics. The magnitude of the* $C°=1$ *μg* m^{-3} *and* $C°=10$ *μg* m^{-3} *volatility bins are accurately larger in current models as they include primary gases and particles eminating from motor oil.*

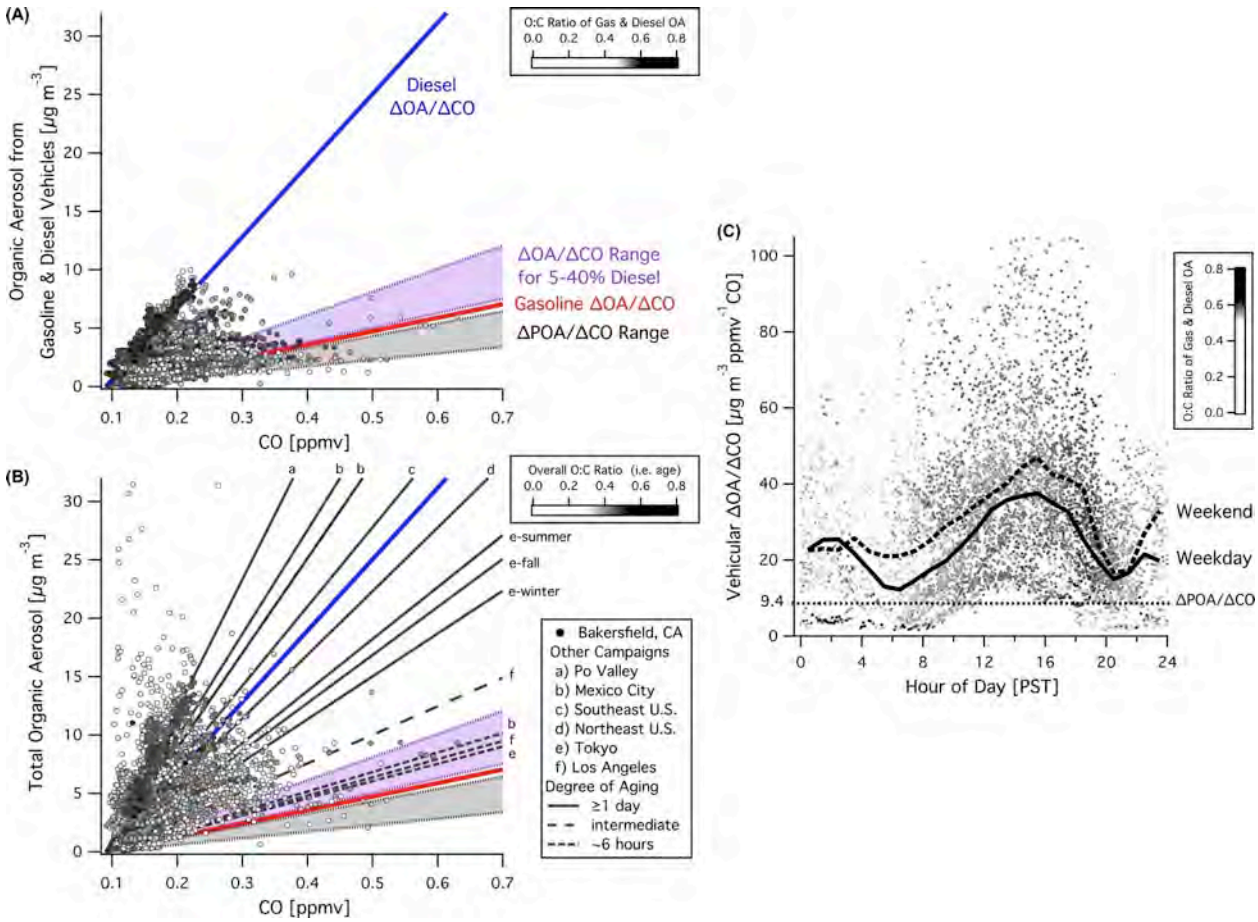

Figure 3.3.11. *Comparisons of Organic Aerosol (OA) vs. carbon monoxide (CO) show the behavior of primary and secondary OA in the atmosphere and are used to examine vehicular OA and total OA in the San Joaquin Valley (Bakersfield) and numerous other urban sites (6, 18, 20, 24-32). Photochemical aging increases ΔOA/ΔCO ratios and is represented by increased oxygen:carbon (O:C) ratios shaded in each panel.* ***(A)*** *Best estimates for ΔOA/ΔCO ratios expected for pure gasoline and diesel emissions are added to a ΔPOA/ΔCO value of 9.4 μg m^{-3} $ppmv^{-1}$ CO to account for primary OA and shown with a range of ΔPOA/ΔCO values (20, 33). Vehicular OA is determined from AMS factor analysis and observations are well constrained at Bakersfield with the exception of the most aged air parcels whose ΔOA/ΔCO ratios are greater than expected for the mix of gasoline and diesel usage.* ***(B)*** *Predicted ΔOA/ΔCO slopes for a range of fuel mixtures ranging from 5 to 40% diesel agree with observations of relatively young aerosol in urban areas and vehicular OA at Bakersfield. Observed ΔOA/ΔCO ratios increase with degree of aging and/or the influence of other SOA precursor sources that do not emit CO, which are prominent at Bakersfield and sites a-c.* ***(C)*** *Weekday and weekend diurnal averages of vehicular ΔOA/ΔCO show greater ratios in the afternoon and over the weekend due to increased photochemical aging. Ratios are calculated with a 90 ppbv CO background (NOAA GMD at Trinedad Head, CA) and standard deviations are shown in Fig. 3.3.13.*

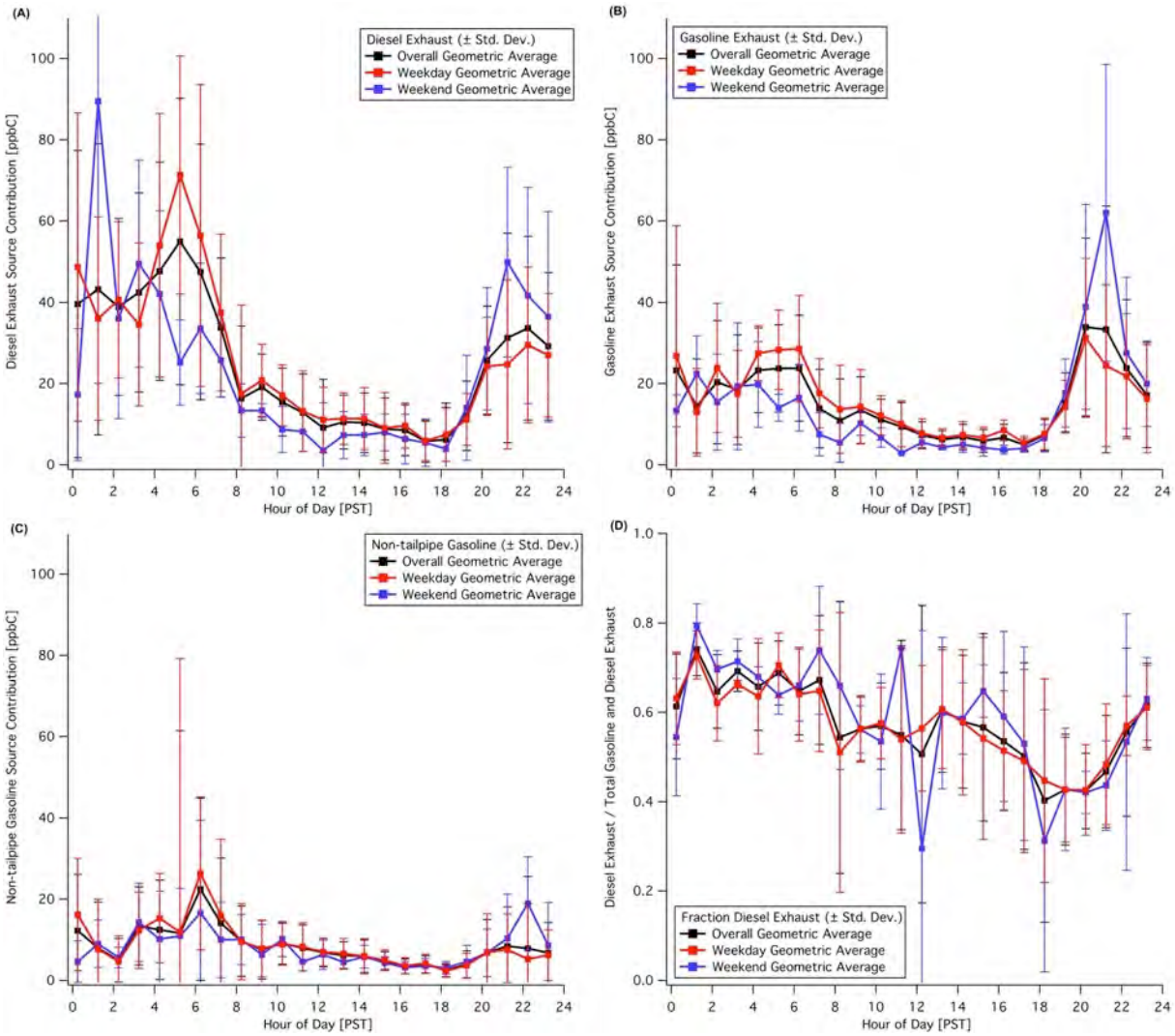

Figure 3.3.12. *Weekday/weekend diurnal profiles of of diesel exhaust* ***(A)****, gasoline exhaust* ***(B)****, and non-tailpipe gasoline source contributions* ***(C)****, and ratio of diesel to gasoline exhaust* ***(D)*** *during the early summer in Bakersfield (includes 5 weekends). The source contributions of gasoline and diesel (A-B) have greater daytime values during the week. The diesel exhaust fraction* ***(D)*** *shows some diurnal variablity, there is no strong weekday/weekend effect in the relative fraction of each fuel due to equivalent decreases in both gasoline and diesel.*

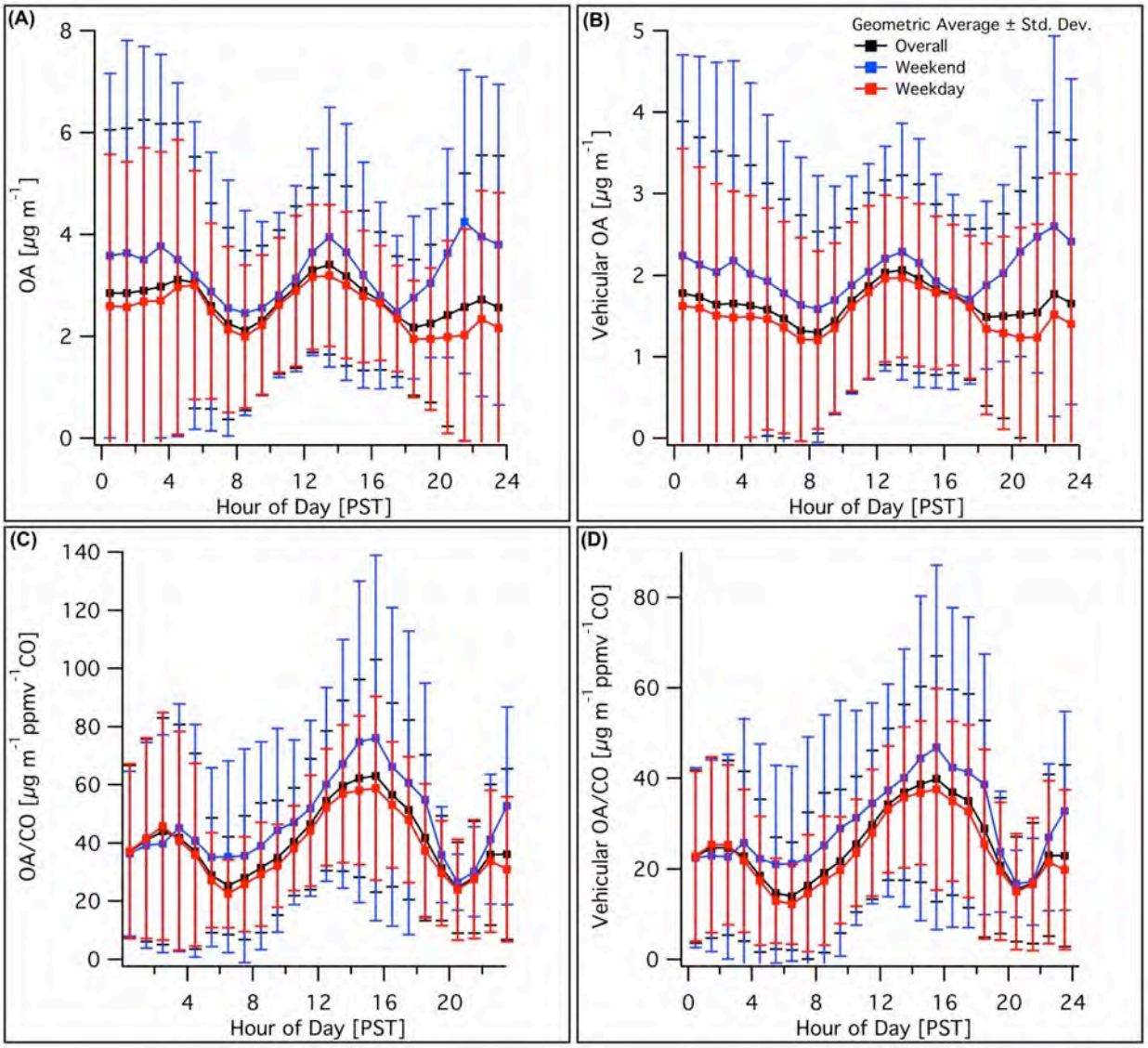

Figure 3.3.13. (A-B) *Overall, weekday, and weekend diurnal patterns for total and vehicular organic aerosol at Bakersfield, CA during the early summer. Vehicular OA is determined from AMS positive matrix factor analysis (18).* ***(C-D)*** *Overall, weekday, and weekend diurnal patterns for ΔOA/ΔCO ratios for total and vehicular organic aerosol. In all cases, daytime weekend values are higher, but within the large variability observed across the 6-week campaign. Total and vehicular OA are higher over the weekend due to increased photochemical processing (as shown by increased ΔOA/ΔCO ratios) associated with decreased* NO_x *emissions from diesel sources and is not a function of changes in the distribution of fuel use.*

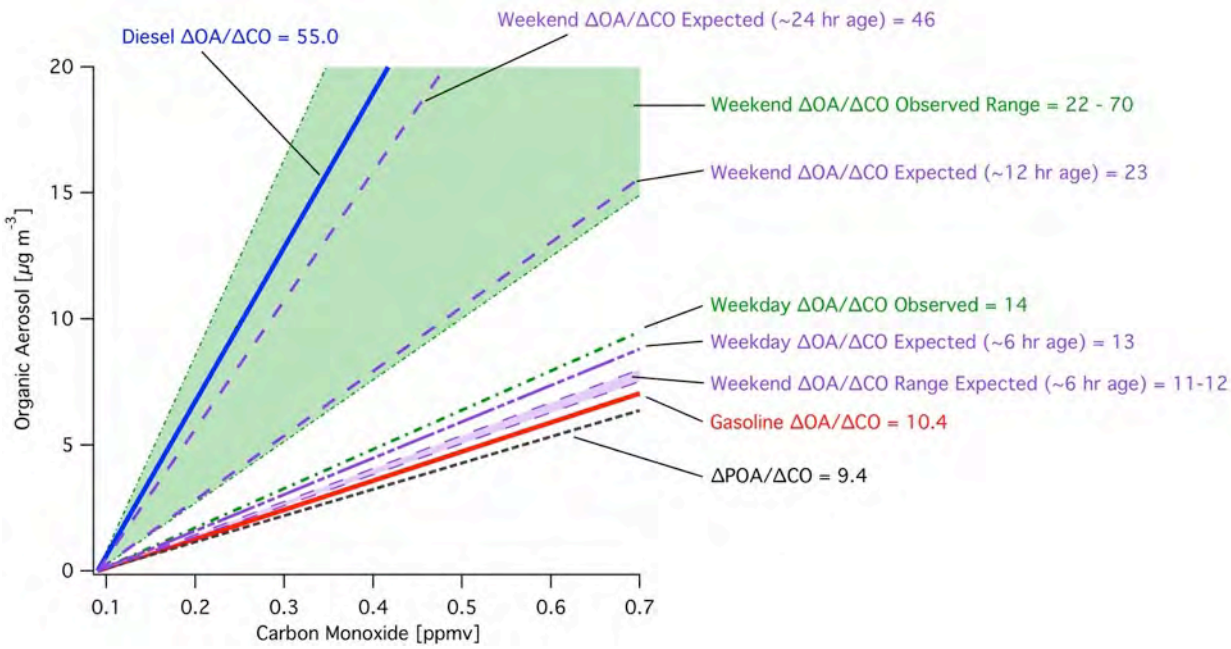

Figure 3.3.14. *Weekday/weekend behavior of ΔOA/ΔCO ratios in Los Angeles, CA (Summer 2010) with best estimates for ΔOA/ΔCO ratios expected for pure gasoline and diesel emissions added to an average POA/CO value of 9.4 μg m^{-3} $ppmv^{-1}$ CO (20). Calculated weekday ΔOA/ΔCO slope (17% diesel) for Los Angeles agrees with observed value. Weekend values show varying degrees of aging ranging from 12 hours to 1 day based on reported photochemical ages, which roughly correspond to a 2-4x increase in ΔOA/ΔCO ratios (6, 19, 25). Approximate aged weekend values with 5-10% diesel use are shown and are consistent with observations. While Los Angeles is dominated by motor vehicle emissions, contributions of SOA precursors from other non-CO related sources would elevate predicted ΔOA/ΔCO ratios further.*

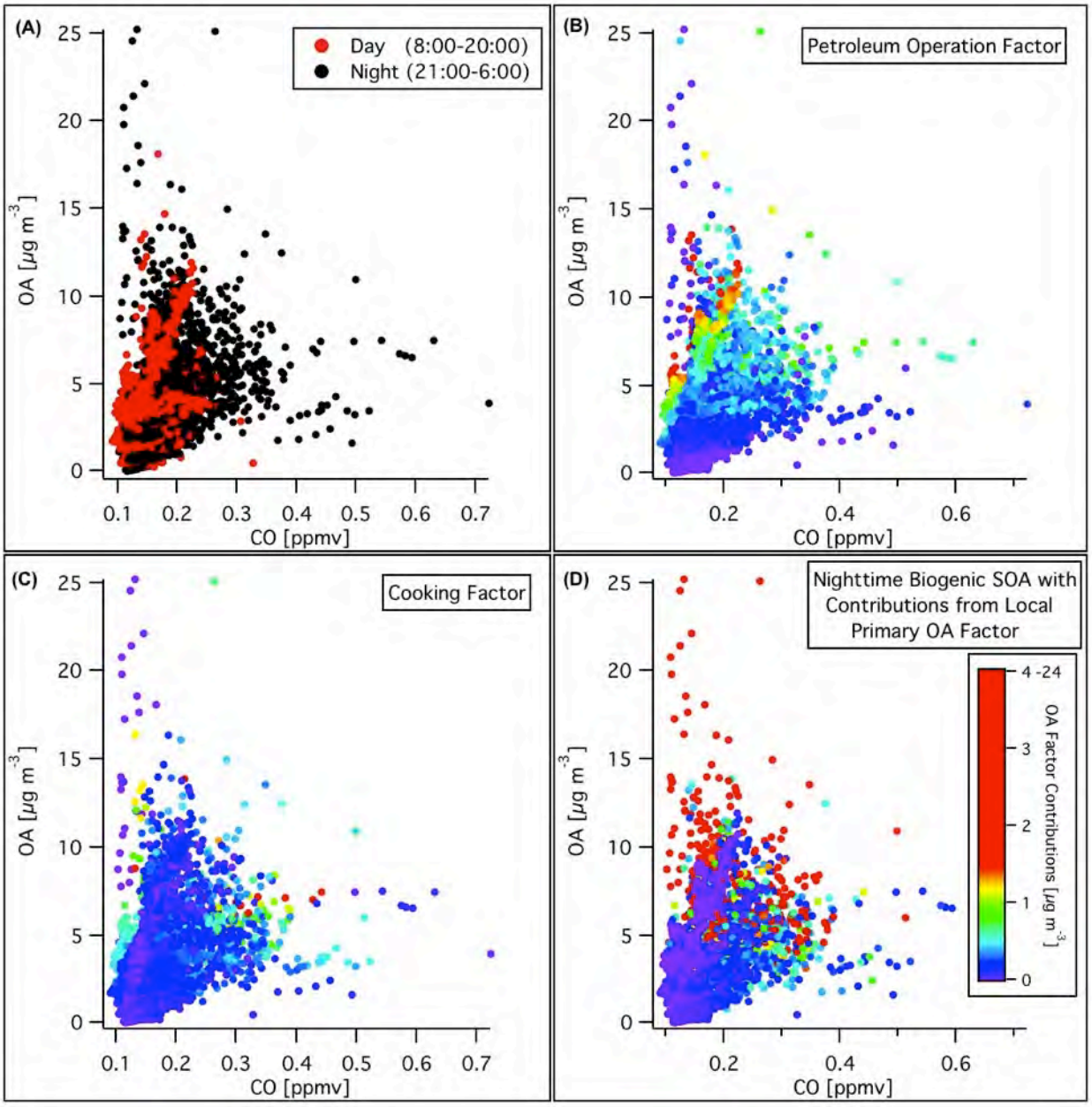

Figure 3.3.15. *Observed organic aerosol vs. carbon monoxide at Bakersfield, CA during the early summer. Panel A shows day and night ratios, with increased daytime ΔOA/ΔCO slopes associated with greater aging, while nighttime values show less aged air masses and episodic contributions to OA without CO from non-vehicular sources. Panels B-D show color-shaded contributions for major non-vehicular sources as determined by factor analysis of AMS data (18).*

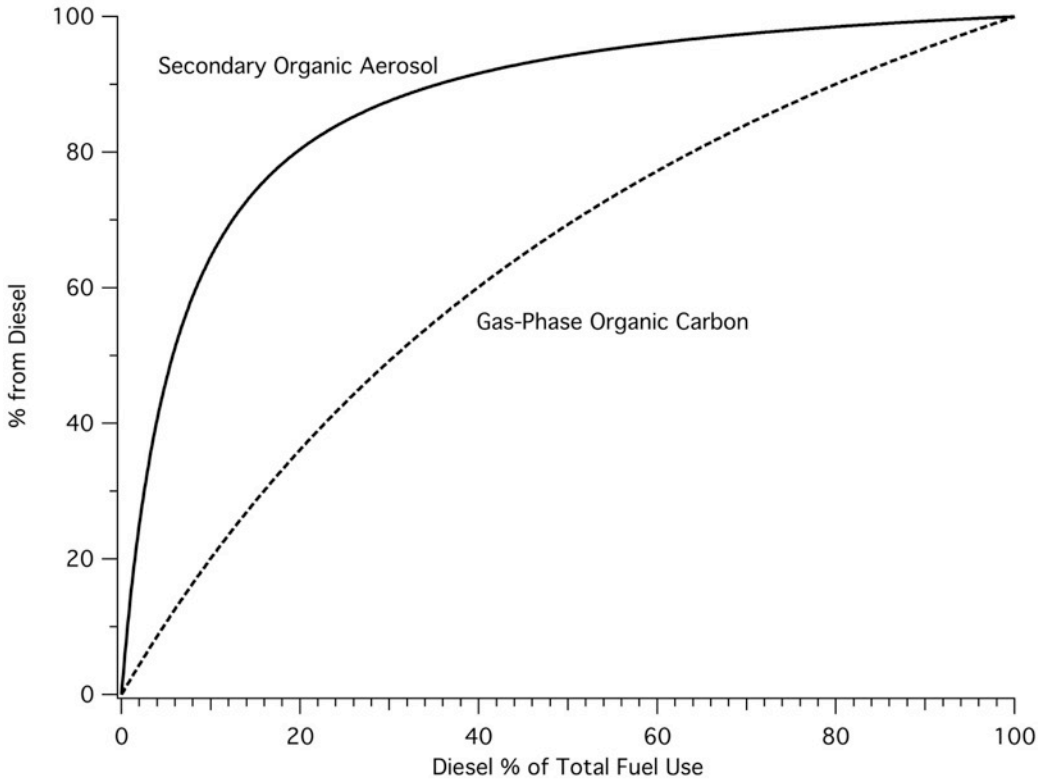

Figure 3.3.16. *The percent contribution of diesel exhaust to SOA over percent diesel fuel use. The percent diesel contribution to gas-phase organic carbon is shown as well and has greater contributions from gasoline with a equivalence point at 31% diesel fuel use. The percent contribution from gasoline can be determined via the difference of diesel. The gas-phase organic carbon line does not consider contributions from non-tailpipe gasoline sources since contributions will vary depending on location and time of year.*

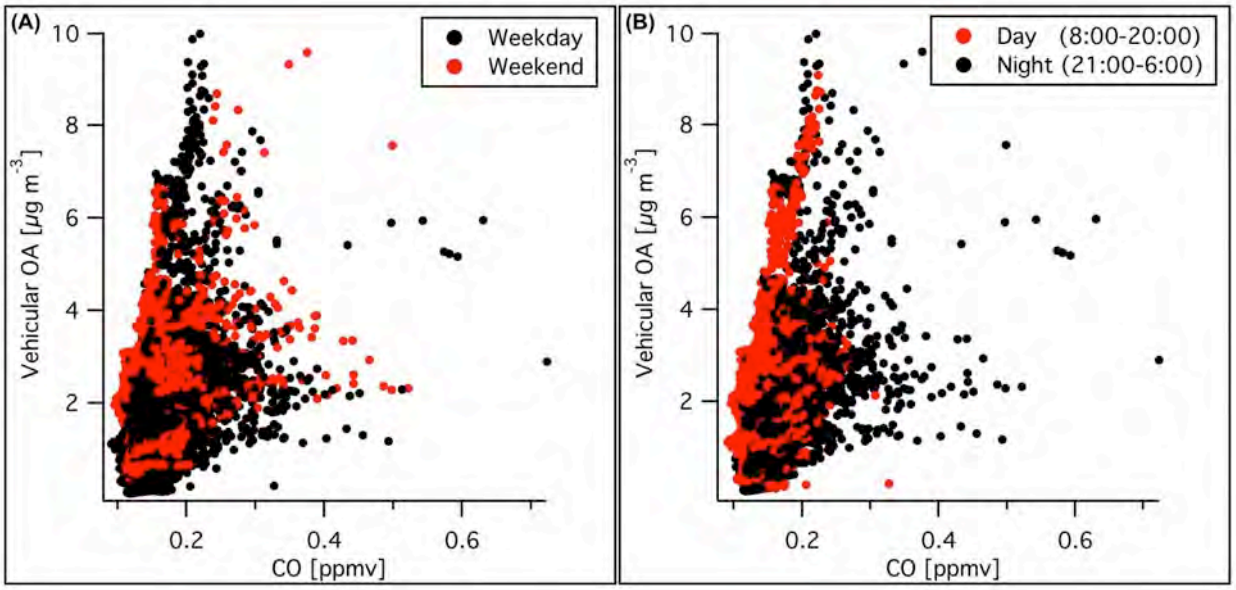

Figure 3.3.17. *Vehicular organic aerosol vs. carbon monoxide at Bakersfield, CA during the early summer. Vehicular OA is determined from AMS positive matrix factor analysis (18). Panel A shows minor weekday/weekend differences with considerable variability and is better displayed in Figure 3.3.13D. Panel B shows day and night ratios, with increased daytime ΔOA/ΔCO slopes associated with greater aging, while nighttime values show a mix of air mass ages.*

Table 3.3.1. *Sales of on-road gasoline and diesel fuel in California and its counties (10).*

COUNTY	Total Gas and Diesel Sales [10^6 gallons annually]	Percent Gasoline (by volume)	Percent Diesel (by volume)
ALAMEDA	772	84.2%	15.8%
ALPINE	3	89.5%	10.5%
AMADOR	24	86.8%	13.2%
BUTTE	97	85.3%	14.7%
CALAVERAS	21	89.0%	11.0%
COLUSA	43	64.6%	35.4%
CONTRA COSTA	432	89.4%	10.6%
DEL NORTE	16	77.8%	22.2%
EL DORADO	86	89.7%	10.3%
FRESNO	497	76.6%	23.4%
GLENN	40	57.7%	42.3%
HUMBOLDT	72	81.9%	18.1%
IMPERIAL	129	71.4%	28.6%
INYO	32	77.5%	22.5%
KERN	565	67.3%	32.7%
KINGS	92	71.0%	29.0%
LAKE	32	85.2%	14.8%
LASSEN	34	69.7%	30.3%
LOS ANGELES	4251	86.8%	13.2%
MADERA	102	71.0%	29.0%
MARIN	145	92.3%	7.7%
MARIPOSA	13	95.8%	4.2%
MENDOCINO	67	82.4%	17.6%
MERCED	164	73.1%	26.9%
MODOC	15	65.1%	34.9%
MONO	17	84.7%	15.3%
MONTEREY	213	79.5%	20.5%
NAPA	62	90.3%	9.7%
NEVADA	71	77.8%	22.2%
ORANGE	1415	89.3%	10.7%
PLACER	194	83.2%	16.8%
PLUMAS	23	71.9%	28.1%
RIVERSIDE	1154	78.6%	21.4%
SACRAMENTO	644	85.5%	14.5%
SAN BENITO	33	71.2%	28.8%
SAN BERNARDINO	1301	76.3%	23.7%
SAN DIEGO	1460	88.7%	11.3%
SAN FRANCISCO	171	93.9%	6.1%
SAN JOAQUIN	413	73.4%	26.6%
SAN LUIS OBISPO	161	85.4%	14.6%
SAN MATEO	336	92.3%	7.7%
SANTA BARBARA	203	86.8%	13.2%
SANTA CLARA	790	89.6%	10.4%
SANTA CRUZ	102	89.7%	10.3%
SHASTA	120	76.1%	23.9%
SIERRA	7	74.7%	25.3%
SISKIYOU	72	60.9%	39.1%
SOLANO	252	86.2%	13.8%
SONOMA	220	87.2%	12.8%
STANISLAUS	250	76.3%	23.7%
SUTTER	50	85.0%	15.0%
TEHAMA	64	71.0%	29.0%
TRINITY	13	68.8%	31.2%
TULARE	232	74.4%	25.6%
TUOLUMNE	35	85.8%	14.2%
VENTURA	364	87.2%	12.8%
YOLO	120	79.2%	20.8%
YUBA	36	86.4%	13.6%
TOTAL	**18344**	**83.5%**	**16.5%**

Table 3.3.2. *Distribution of mass and SOA potential by chemical class for diesel exhaust, gasoline exhaust, and non-tailpipe gasoline.*

	Weight Percent by Carbon [WtC%]			Potential SOA Formation [Wt% SOA]		
Compound Class	**Diesel Exhaust**	**Gasoline Exhaust**	**Non-Tailpipe Gasoline**	**Diesel Exhaust**	**Gasoline Exhaust**	**Non-Tailpipe Gasoline**
Total Aliphatic	68 ± 8	58 ± 2	85 ± 4	47 ± 4	0.38 ± 0.07	0.9 ± 0.4
Straight-chain Alkanes	*7 ± 1*	*7.7 ± 0.3*	*20 ± 1*	*11 ± 2*	*0.09 ± 0.003*	*0.02 ± 0.001*
Branched Alkanes	*23 ± 2*	*40 ± 1*	*60 ± 3*	*14 ± 2*	*0.12 ± 0.003*	*0.13 ± 0.01*
Cycloalkanes (Single Straight Alkyl Chain)	*2.5 ± 0.2*	*4.3 ± 0.1*	*1.03 ± 0.04*	*1.2 ± 0.3*	*0.13 ± 0.07*	*0.7 ± 0.4*
Cycloalkanes (Branched or Multiple Alkyl Chain(s))	*18 ±2*	*6.2 ± 0.3*	*5.0 ± 0.2*	*11 ± 2*	*0.04 ± 0.02*	*0.05 ± 0.03*
Bicycloalkanes	*13 ± 1*	*0*	*0*	*6 ± 1*	*0*	*0*
Tricycloalkanes	*4.8 ± 0.6*	*0*	*0*	*4 ± 1*	*0*	*0*
Single-ring Aromatics	19 ± 2	29 ± 1	2.7 ±0.1	36 ± 9	96 ± 22	99 ± 6
Polycyclic Aromatic Compounds	4 ± 2	0.32 ± 0.02	0.0003	17 ± 8	3.2 ± 0.9	0.01 ± 0.01
Alkenes (Straight, Branched, & Cyclic)	0	3.6 ± 0.1	7.4 ± 0.3	0	0	0
Ethanol	0	6.9 ± 0.5	4.4 ± 0.4	0	0	0

Note: Wt% by total mass for each source can be found in Table 3.3.3.

Table 3.3.3. *Chemical class distribution of sources by total mass.*

	Weight Percent by mass (± St. Dev)		
Compound Class	**Diesel Fuel**	**Liquid Gasoline**	**Non-Tailpipe Gasoline**
Straight-chain Alkanes	7.3 ± 1.2	7.6 ± 0.3	19 ± 0.9
Branched Alkanes	23 ± 2.5	39 ± 0.9	58 ± 3
Cycloalkanes (Single Straight Alkyl Chain)	2.5 ± 0.2	4.2 ± 0.1	0.98 ± 0.04
Cycloalkanes (Branched or Multiple Alkyl Chain(s))	18 ± 1.8	6.0 ± 0.3	4.8 ± 0.2
Bicycloalkanes	12 ± 1.3	0	0
Tricycloalkanes	4.7 ± 0.6	0	0
Single-ring Aromatics	17.7 ± 1.6	26.7 ± 0.7	2.5 ± 0.1
Polycyclic Aromatic Compounds	3.8 ±1.6	0.29 ± 0.02	0.0003
Alkenes (Straight, Branched, & Cyclic)	0	3.5 ± 0.1	7.0 ± 0.3
Ethanol	0	10.9 ± 0.9	6.9 ± 0.6

Table 3.3.4. *Summary of compounds used in source receptor modeling at Bakersfield.*

Master Set	Confirmation Set #1	Confirmation Set #2	Confirmation Set #3	Confirmation Set #4
n-butane isopentane n-pentane n-heptane isooctane m&p-xylene o-xylene n-nonane n-undecane n-dodecane	n-butane n-pentane isopentane n-heptane isooctane m&p-xylene n-nonane n-undecane	n-butane isopentane 2,2-dimethylbutane n-heptane 2-methylhexane 3-methylhexane m&p-xylene n-nonane n-tridecane	n-butane n-pentane 2,2-dimethylbutane methylcyclopentane n-heptane isooctane m&p-xylene n-nonane 1-ethyl-3(+4)-methylbenzene n-dodecane	n-butane n-pentane isopentane toluene isooctane o-xylene n-undecane n-dodecane naphthalene

Table 3.3.5. *Summary of compounds used in source receptor modeling at the Caldecott Tunnel.*

Master Set	Confirmation Set #1	Confirmation Set #2	Confirmation Set #3	Confirmation Set #4
isopentane isooctane m&p-xylene o-xylene n-nonane 1,2,3-trimethylbenzene 1,3,5-trimethylbenzene n-propylbenzene n-undecane n-dodecane	isopentane n-hexane isooctane m&p-xylene o-xylene n-nonane n-dodecane	n-pentane 2,2-dimethylbutane n-hexane 3-methylpentane o-xylene n-nonane 1,2,4-trimethylbenzene 1-ethyl-2-methylbenzene n-tridecane	n-pentane 2,2-dimethylbutane n-hexane 3-methylpentane ethylcyclopentane methylcyclohexane 2,3-dimethylheptane 1-ethyl-2-methylbenzene n-tridecane	n-pentane n-heptane n-nonane 1,2,3-trimethylbenzene n-undecane n-tridecane

Table 3.3.6. *Mass and chemical class distribution of diesel fuel (in weight percent by carbon).*

Carbon Number	Straight-chain Alkanes	Branched Alkanes	Cycloalkanes (Single Straight Alkyl Chain)	Cycloalkanes (Branched or Multiple Alkyl Chain(s))	Bicycloalkanes	Tricycloalkanes	Aromatics	Polycyclic Aromatic Compounds
1	0	0	0	0	0	0	0	0
2	0	0	0	0	0	0	0	0
3	0	0	0	0	0	0	0	0
4	0	0	0	0	0	0	0	0
5	0	0	0	0	0	0	0	0
6	0	0	0	0	0	0	0	0
7	0	0	0.15	0	0	0	0.21	0
8	0.10	0.17	0.19	0.42	0	0	0.73	0
9	0.21	0.20	0.26	0.35	0	0	2.02	0
10	0.50	1.60	0.35	1.87	1.38	0.11	2.38	0.03
11	0.60	2.27	0.29	1.90	1.82	0.21	1.91	0.18
12	0.55	1.89	0.20	1.96	1.76	0.34	1.83	0.30
13	0.51	1.81	0.17	1.74	1.30	0.44	1.46	0.32
14	0.51	2.06	0.15	1.39	1.00	0.49	1.18	0.49
15	0.56	1.89	0.15	1.22	0.86	0.45	1.03	0.56
16	0.58	1.70	0.14	1.14	0.74	0.44	0.99	0.51
17	0.64	1.35	0.12	1.05	0.65	0.39	0.89	0.50
18	0.62	1.55	0.10	1.06	0.62	0.37	0.84	0.45
19	0.50	1.90	0.08	0.94	0.57	0.34	0.73	0.42
20	0.43	1.63	0.06	0.82	0.50	0.30	0.61	0.32
21	0.34	1.03	0.05	0.70	0.42	0.25	0.53	0.08
22	0.25	0.73	0.01	0.59	0.33	0.21	0.45	0.06
23	0.16	0.60	0	0.38	0.26	0.17	0.35	0
24	0.11	0.34	0	0.31	0.21	0.14	0.28	0
25	0.06	0.04	0	0.25	0.16	0.11	0.22	0

Table 3.3.7. *Mass and chemical class distribution of liquid gasoline (in weight percent by carbon).*

Carbon Number	Straight-chain Alkanes	Branched Alkanes	Cycloalkanes (Single Straight Alkyl Chain)	Cycloalkanes (Branched or Multiple Alkyl Chain(s))	Bicycloalkanes	Tricycloalkanes	Aromatics	Polycyclic Aromatic Compounds
1	0	0	0	0	0	0	0	0
2	0.0003	0	0	0	0	0	0	0
3	0.014	0	0	0	0	0	0	0
4	0.500	0.057	0	0	0	0	0	0
5	2.84	7.83	0.475	0	0	0	0	0
6	1.84	8.51	3.75	0	0	0	0.750	0
7	1.39	7.60	1.76	1.89	0	0	7.59	0
8	0.621	10.89	0.214	1.78	0	0	9.69	0
9	0.278	3.33	0.043	0.536	0	0	7.74	0
10	0.116	1.20	0	0.126	0	0	2.63	0.130
11	0.063	0.516	0	0	0	0	0.558	0.127
12	0.017	0.040	0	0	0	0	0.060	0.048
13	0.008	0	0	0	0	0	0	0.016
14	0.004	0.007	0	0	0	0	0.001	0
15	0.004	0.006	0	0	0	0	0	0.002
16	0	0	0	0	0	0	0	0.0004
17	0	0	0	0	0	0	0	0
18	0	0	0	0	0	0	0	0
19	0	0	0	0	0	0	0	0
20	0	0	0	0	0	0	0	0
21	0	0	0	0	0	0	0	0
22	0	0	0	0	0	0	0	0
23	0	0	0	0	0	0	0	0
24	0	0	0	0	0	0	0	0
25	0	0	0	0	0	0	0	0

Table 3.3.8. *Mass and chemical class distribution of non-tailpipe gasoline (in weight percent by carbon).*

Carbon Number	Straight-chain Alkanes	Branched Alkanes	Cycloalkanes (Single Straight Alkyl Chain)	Cycloalkanes (Branched or Multiple Alkyl Chain(s))	Bicycloalkanes	Tricycloalkanes	Aromatics	Polycyclic Aromatic Compounds
1	0	0	0	0	0	0	0	0
2	0.0987	0	0	0	0	0	0	0
3	0.690	0	0	0	0	0	0	0
4	6.54	1.07	0	0	0	0	0	0
5	10.3	38.4	1.07	0	0	0	0	0
6	1.97	13.4	3.35	0	0	0	0.506	0
7	0.137	3.89	0.562	0.774	0	0	1.52	0
8	0.0616	2.59	0.0194	0.257	0	0	0.564	0
9	0.0085	0.262	0.0014	0	0	0	0.139	0
10	0.0012	0	0	0.0003	0	0	0.0085	0.0002
11	0.0002	0	0	0	0	0	0.0001	0
12	0	0	0	0	0	0	0	0
13	0	0	0	0	0	0	0	0
14	0	0	0	0	0	0	0	0
15	0	0	0	0	0	0	0	0
16	0	0	0	0	0	0	0	0
17	0	0	0	0	0	0	0	0
18	0	0	0	0	0	0	0	0
19	0	0	0	0	0	0	0	0
20	0	0	0	0	0	0	0	0
21	0	0	0	0	0	0	0	0
22	0	0	0	0	0	0	0	0
23	0	0	0	0	0	0	0	0
24	0	0	0	0	0	0	0	0
25	0	0	0	0	0	0	0	0

Table 3.3.9. *Average high-NO_x SOA yields with uncertainties (± st. dev) constructed from scenarios and Monte Carlo analysis.*

Carbon Number	Straight-chain Alkanes	Branched Alkanes	Cycloalkanes (Single Straight Alkyl Chain)	Cycloalkanes (Branched or Multiple Alkyl Chain(s))	Bicycloalkanes	Tricycloalkanes	Aromatics	Polycyclic Aromatic Compounds
1	--	--	--	--	--	--	--	--
2	--	--	--	--	--	--	--	--
3	--	--	--	--	--	--	--	--
4	--	--	--	--	--	--	--	--
5	--	--	--	--	--	--	--	--
6	--	--	0.0004 ± 0.0003	--	--	--	0.14	--
7	--	--	0.0007 ± 0.0006	0.0001 ± 0.0001	--	--	0.083	--
8	0.0006	0.0001	0.0015 ± 0.0011	0.0002 ± 0.0002	--	--	0.048	--
9	0.0012	0.0002	0.0031 ± 0.0020	0.0005 ± 0.0003	0.0005 ± 0.0002	--	0.077 ± 0.057	--
10	0.0026	0.0004	0.0059 ± 0.0039	0.0010 ± 0.0006	0.0010 ± 0.0005	--	0.12 ± 0.08	0.17 ± 0.09
11	0.0053	0.0008	0.010 ± 0.006	0.0018 ± 0.0011	0.0018 ± 0.0008	--	0.15 ± 0.11	0.23 ± 0.11
12	0.010	0.0017	0.016 ± 0.010	0.0034 ± 0.0022	0.0031 ± 0.0015	0.0032 ± 0.0015	0.19 ± 0.16	0.28 ± 0.15
13	0.019	0.0035	0.026 ± 0.016	0.0062 ± 0.0042	0.0056 ± 0.0029	0.0057 ± 0.0030	0.26 ± 0.27	0.40 ± 0.23
14	0.033	0.0070	0.041 ± 0.026	0.011 ± 0.008	0.0097 ± 0.0056	0.0098 ± 0.0057	0.33 ± 0.38	0.49 ± 0.31
15	0.055	0.013	0.064 ± 0.042	0.019 ± 0.014	0.016 ± 0.010	0.017 ± 0.010	0.39 ± 0.45	0.62 ± 0.32
16	0.089	0.024	0.099 ± 0.071	0.031 ± 0.024	0.026 ± 0.017	0.027 ± 0.018	0.43 ± 0.47	0.70 ± 0.35
17	0.14	0.042	0.16 ± 0.11	0.053 ± 0.039	0.044 ± 0.028	0.045 ± 0.028	0.46 ± 0.48	0.75 ± 0.37
18	0.23	0.073	0.24 ± 0.17	0.088 ± 0.065	0.072 ± 0.045	0.073 ± 0.045	0.51 ± 0.47	0.79 ± 0.40
19	0.37	0.12	0.36 ± 0.23	0.14 ± 0.10	0.12 ± 0.07	0.12 ± 0.07	0.56 ± 0.48	0.82 ± 0.42
20	0.56	0.20	0.50 ± 0.26	0.22 ± 0.15	0.19 ± 0.12	0.19 ± 0.12	0.61 ± 0.50	0.82 ± 0.42
21	0.77	0.32	0.66 ± 0.27	0.33 ± 0.19	0.29 ± 0.17	0.30 ± 0.18	0.65 ± 0.52	0.82 ± 0.42
22	0.96	0.47	0.82 ± 0.26	0.45 ± 0.23	0.43 ± 0.24	0.43 ± 0.24	0.67 ± 0.54	0.82 ± 0.42
23	1.08	0.61	0.94 ± 0.23	0.57 ± 0.25	0.56 ± 0.28	0.57 ± 0.28	0.68 ± 0.55	0.82 ± 0.42
24	1.14	0.70	1.03 ± 0.20	0.67 ± 0.25	0.66 ± 0.29	0.67 ± 0.30	0.68 ± 0.55	0.82 ± 0.42
25	1.16	0.75	1.09 ± 0.17	0.73 ± 0.23	0.74 ± 0.28	0.74 ± 0.28	0.68 ± 0.55	0.82 ± 0.42

Table 3.3.10. *Compound specific liquid gasoline speciation for California in Summer 2010.*

	Weight percentage in fuel [% weight by carbon (± St. Dev)]					Molar percentage in fuel [% mol (± St. Dev)]				
Compound	Statewide	Bakersfield	Berkeley	Pasadena	Sacramento	Statewide	Bakersfield	Berkeley	Pasadena	Sacramento
ethane	0.000±0.000	0.001±0.000	0.000±0.000	0.000±0.000	0.000±0.000	0.001±0.000	0.004±0.001	0.000±0.000	0.001±0.000	0.000±0.000
propane	0.014±0.001	0.030±0.003	0.006±0.002	0.006±0.001	0.012±0.003	0.027±0.002	0.060±0.006	0.012±0.003	0.011±0.002	0.024±0.006
n-butane	0.500±0.038	0.692±0.049	0.420±0.074	0.478±0.098	0.411±0.074	0.747±0.057	1.025±0.073	0.626±0.110	0.722±0.148	0.615±0.110
n-pentane	2.839±0.220	3.920±0.207	2.487±0.484	2.582±0.533	2.366±0.459	3.376±0.261	4.635±0.247	2.957±0.574	3.080±0.634	2.830±0.548
n-hexane	1.837±0.156	2.117±0.037	1.715±0.351	1.841±0.386	1.674±0.341	1.821±0.155	2.085±0.037	1.698±0.347	1.832±0.383	1.668±0.340
n-heptane	1.385±0.116	1.538±0.026	1.652±0.329	1.093±0.214	1.257±0.248	1.177±0.099	1.299±0.022	1.403±0.279	0.933±0.182	1.074±0.211
n-octane	0.621±0.052	0.690±0.015	0.710±0.141	0.493±0.097	0.593±0.119	0.462±0.039	0.510±0.011	0.527±0.105	0.368±0.072	0.444±0.089
n-nonane	0.278±0.024	0.303±0.012	0.298±0.061	0.237±0.047	0.275±0.056	0.184±0.016	0.199±0.008	0.197±0.040	0.158±0.031	0.182±0.037
n-decane	0.116±0.011	0.100±0.003	0.099±0.020	0.147±0.030	0.117±0.023	0.069±0.006	0.059±0.002	0.059±0.012	0.088±0.018	0.070±0.014
n-undecane	0.063±0.007	0.034±0.002	0.054±0.012	0.098±0.022	0.065±0.013	0.034±0.004	0.018±0.001	0.029±0.006	0.054±0.012	0.036±0.007
n-dodecane	0.017±0.003	0.004±0.000	0.010±0.002	0.045±0.011	0.011±0.003	0.009±0.001	0.002±0.000	0.005±0.001	0.022±0.005	0.006±0.001
n-tridecane	0.008±0.001	0.002±0.000	0.002±0.000	0.025±0.005	0.004±0.001	0.004±0.001	0.001±0.000	0.001±0.000	0.012±0.003	0.002±0.000
n-tetradecane	0.004±0.001	0.001±0.000	0.001±0.000	0.011±0.002	0.002±0.000	0.002±0.000	0.000±0.000	0.000±0.000	0.005±0.001	0.001±0.000
n-pentadecane	0.004±0.001	0.002±0.000	0.003±0.001	0.007±0.002	0.003±0.000	0.002±0.000	0.001±0.000	0.001±0.000	0.003±0.001	0.001±0.000
2-methylpropane	0.057±0.006	0.085±0.009	0.043±0.011	0.078±0.018	0.023±0.004	0.085±0.009	0.125±0.014	0.064±0.017	0.119±0.027	0.034±0.006
2-methylbutane	7.821±0.646	7.166±0.192	8.426±1.555	7.475±1.393	8.216±1.508	9.321±0.770	8.470±0.219	10.032±1.849	8.946±1.661	9.838±1.803
2,2-dimethylpropane	0.008±0.001	0.009±0.001	0.007±0.001	0.007±0.002	0.008±0.001	0.009±0.001	0.011±0.001	0.009±0.002	0.009±0.002	0.010±0.002
2-methylpentane	3.858±0.344	3.283±0.246	4.323±0.832	3.922±0.776	3.906±0.736	3.829±0.341	3.231±0.238	4.287±0.824	3.904±0.769	3.895±0.733
3-methylpentane	2.412±0.212	2.097±0.135	2.664±0.511	2.408±0.474	2.479±0.466	2.394±0.210	2.064±0.131	2.642±0.505	2.399±0.470	2.473±0.464
2,2-dimethylbutane	0.902±0.106	0.585±0.107	1.303±0.304	0.728±0.201	0.991±0.186	0.894±0.105	0.575±0.104	1.291±0.300	0.721±0.199	0.989±0.185
2,3-dimethylbutane	1.341±0.109	1.196±0.064	1.327±0.237	1.418±0.254	1.423±0.256	1.333±0.109	1.178±0.062	1.318±0.235	1.417±0.253	1.421±0.255
2-methylhexane	1.339±0.137	1.164±0.078	1.813±0.386	1.090±0.266	1.288±0.270	1.136±0.116	0.981±0.065	1.538±0.328	0.925±0.225	1.100±0.230
3-methylhexane	1.981±0.174	1.883±0.053	2.368±0.474	1.850±0.359	1.823±0.355	1.685±0.148	1.590±0.044	2.011±0.402	1.579±0.305	1.557±0.303
3-ethylpentane	0.087±0.011	0.108±0.012	0.142±0.036	0.054±0.019	0.045±0.016	0.074±0.010	0.091±0.010	0.120±0.031	0.045±0.016	0.038±0.014
2,2-dimethylpentane	0.113±0.010	0.129±0.002	0.121±0.027	0.113±0.024	0.089±0.017	0.096±0.008	0.109±0.002	0.103±0.023	0.096±0.020	0.076±0.014
2,3-dimethylpentane	2.720±0.218	3.048±0.124	1.999±0.348	3.581±0.671	2.251±0.418	2.324±0.188	2.579±0.107	1.704±0.296	3.086±0.580	1.927±0.358
2,4-dimethylpentane	1.200±0.093	1.292±0.051	0.874±0.148	1.516±0.269	1.116±0.204	1.025±0.080	1.093±0.044	0.745±0.126	1.304±0.232	0.956±0.174
3,3-Dimethylpentane	0.112±0.010	0.133±0.002	0.111±0.029	0.112±0.023	0.093±0.018	0.095±0.009	0.112±0.001	0.094±0.025	0.096±0.019	0.080±0.015
2,2,3-Trimethylbutane	0.044±0.003	0.044±0.000	0.042±0.007	0.044±0.008	0.044±0.008	0.037±0.003	0.037±0.000	0.036±0.006	0.038±0.007	0.038±0.007
2-Methylheptane	0.940±0.078	0.990±0.013	0.976±0.191	0.913±0.176	0.882±0.171	0.700±0.058	0.731±0.010	0.726±0.141	0.683±0.132	0.660±0.128
3-Methylheptane	1.014±0.083	1.115±0.015	1.089±0.213	0.917±0.180	0.936±0.181	0.754±0.062	0.824±0.011	0.809±0.158	0.684±0.134	0.700±0.135
4-Methylheptane	0.427±0.034	0.456±0.005	0.443±0.085	0.399±0.076	0.409±0.077	0.318±0.026	0.337±0.004	0.330±0.063	0.299±0.056	0.306±0.058
2,2-dimethylhexane	0.059±0.005	0.080±0.004	0.068±0.015	0.045±0.009	0.045±0.008	0.044±0.004	0.059±0.003	0.050±0.011	0.033±0.007	0.033±0.006
2,4-dimethylhexane	0.622±0.047	0.630±0.011	0.575±0.099	0.638±0.112	0.645±0.114	0.464±0.035	0.466±0.008	0.429±0.074	0.479±0.084	0.483±0.086
2,5-dimethylhexane	0.604±0.046	0.599±0.012	0.544±0.092	0.585±0.101	0.688±0.121	0.451±0.034	0.443±0.009	0.406±0.069	0.439±0.075	0.516±0.091
3,3-dimethylhexane	0.070±0.006	0.097±0.005	0.078±0.016	0.050±0.010	0.054±0.010	0.052±0.004	0.072±0.004	0.058±0.012	0.037±0.007	0.041±0.008
2-Me-3-Et-pentane	0.572±0.043	0.577±0.011	0.503±0.086	0.596±0.104	0.611±0.109	0.427±0.032	0.427±0.009	0.375±0.064	0.448±0.078	0.458±0.081
2,2,3-triMe-pentane	0.167±0.014	0.152±0.005	0.146±0.026	0.145±0.025	0.226±0.040	0.125±0.010	0.113±0.004	0.109±0.019	0.109±0.019	0.170±0.030
2,2,4-triMe-pentane	3.639±0.293	3.171±0.123	2.871±0.496	4.106±0.706	4.406±0.786	2.724±0.220	2.346±0.090	2.148±0.371	3.094±0.532	3.306±0.590
2,3,3-triMe-pentane	1.374±0.112	1.261±0.042	1.168±0.205	1.161±0.202	1.904±0.340	1.026±0.084	0.934±0.031	0.873±0.153	0.871±0.152	1.428±0.255
2,3,4-triMe-pentane	1.405±0.111	1.330±0.043	1.153±0.195	1.325±0.227	1.810±0.324	1.050±0.083	0.985±0.032	0.862±0.146	0.998±0.171	1.357±0.243
2,2,5-trimethylhexane	0.894±0.083	0.896±0.041	0.874±0.205	0.656±0.117	1.148±0.228	0.594±0.055	0.590±0.028	0.582±0.137	0.438±0.078	0.767±0.152
2,3,5-trimethylhexane	0.183±0.016	0.194±0.008	0.174±0.038	0.141±0.025	0.225±0.043	0.122±0.010	0.128±0.005	0.116±0.025	0.094±0.017	0.150±0.028

2,4,4-trimethylhexane	0.089±0.008	0.072±0.003	0.072±0.014	0.109±0.021	0.104±0.019	0.059±0.005	0.047±0.002	0.048±0.009	0.073±0.014	0.069±0.013
2,4-dimethylheptane	0.115±0.009	0.144±0.007	0.118±0.023	0.090±0.018	0.105±0.019	0.076±0.006	0.095±0.004	0.078±0.015	0.060±0.012	0.070±0.013
2,6-dimethylheptane	0.186±0.018	0.165±0.003	0.168±0.035	0.227±0.050	0.184±0.036	0.123±0.012	0.108±0.002	0.111±0.023	0.152±0.033	0.122±0.024
2,5-dimethylheptane	0.009±0.001	0.010±0.000	0.010±0.002	0.008±0.002	0.010±0.002	0.006±0.001	0.006±0.000	0.006±0.001	0.005±0.001	0.007±0.001
3,5-dimethylheptane	0.391±0.031	0.448±0.016	0.360±0.069	0.383±0.073	0.375±0.071	0.259±0.021	0.294±0.010	0.238±0.046	0.255±0.049	0.249±0.047
2,3-dimethylheptane	0.121±0.009	0.130±0.004	0.119±0.022	0.108±0.020	0.129±0.023	0.080±0.006	0.085±0.003	0.079±0.014	0.071±0.013	0.086±0.016
3,4-dimethylheptane	0.058±0.005	0.057±0.001	0.053±0.010	0.063±0.013	0.060±0.011	0.038±0.003	0.037±0.001	0.035±0.007	0.042±0.008	0.040±0.007
3,3-dimethylheptane	0.039±0.004	0.029±0.001	0.028±0.006	0.059±0.013	0.039±0.008	0.026±0.003	0.019±0.001	0.019±0.004	0.040±0.009	0.026±0.005
4,4-dimethylheptane	0.030±0.003	0.024±0.002	0.022±0.004	0.047±0.010	0.027±0.006	0.020±0.002	0.016±0.001	0.014±0.003	0.032±0.007	0.018±0.004
2-methyloctane	0.323±0.027	0.343±0.007	0.313±0.063	0.322±0.063	0.314±0.063	0.214±0.018	0.225±0.005	0.207±0.042	0.214±0.042	0.209±0.042
3-methyloctane	0.400±0.033	0.437±0.014	0.382±0.076	0.389±0.074	0.393±0.076	0.265±0.022	0.287±0.009	0.253±0.050	0.259±0.049	0.261±0.050
4-methyloctane	0.274±0.023	0.312±0.011	0.269±0.054	0.260±0.051	0.257±0.051	0.182±0.015	0.205±0.007	0.178±0.036	0.173±0.034	0.171±0.034
3-ethylheptane	0.090±0.008	0.098±0.003	0.092±0.019	0.078±0.017	0.094±0.019	0.060±0.005	0.064±0.002	0.061±0.012	0.051±0.011	0.062±0.013
4-ethylheptane	0.054±0.004	0.064±0.003	0.053±0.010	0.048±0.009	0.051±0.010	0.036±0.003	0.043±0.002	0.035±0.007	0.032±0.006	0.034±0.007
2,2-dimethylheptane	0.024±0.002	0.040±0.003	0.024±0.005	0.015±0.003	0.017±0.003	0.016±0.001	0.026±0.002	0.016±0.003	0.010±0.002	0.011±0.002
3-Me-4-Et-hexane	0.029±0.002	0.037±0.002	0.030±0.006	0.020±0.004	0.028±0.005	0.019±0.001	0.024±0.001	0.020±0.004	0.013±0.003	0.019±0.003
2,2,3-trimethylhexane	0.020±0.003	0.047±0.005	0.022±0.009	0.000±0.000	0.012±0.004	0.013±0.002	0.031±0.003	0.014±0.006	0.000±0.000	0.008±0.002
2-methylnonane	0.111±0.010	0.101±0.002	0.105±0.022	0.120±0.025	0.119±0.025	0.066±0.006	0.060±0.001	0.062±0.013	0.072±0.015	0.071±0.015
3-methylnonane	0.110±0.010	0.108±0.004	0.104±0.022	0.114±0.023	0.113±0.023	0.065±0.006	0.064±0.002	0.062±0.013	0.068±0.014	0.068±0.014
4-methylnonane	0.145±0.015	0.207±0.006	0.116±0.030	0.074±0.023	0.182±0.046	0.086±0.009	0.123±0.004	0.069±0.018	0.044±0.014	0.109±0.027
3-ethyloctane	0.004±0.001	0.000±0.000	0.001±0.001	0.010±0.003	0.005±0.002	0.003±0.000	0.000±0.000	0.001±0.000	0.006±0.002	0.003±0.001
4-ethyloctane	0.048±0.004	0.044±0.002	0.043±0.008	0.054±0.011	0.050±0.010	0.029±0.003	0.026±0.001	0.026±0.005	0.033±0.006	0.030±0.006
2,2-dimethyloctane	0.055±0.005	0.057±0.003	0.050±0.010	0.058±0.012	0.055±0.011	0.033±0.003	0.034±0.002	0.030±0.006	0.035±0.007	0.033±0.007
2,3-dimethyloctane	0.042±0.004	0.038±0.002	0.035±0.007	0.053±0.012	0.040±0.008	0.025±0.003	0.022±0.001	0.021±0.004	0.032±0.008	0.024±0.005
2,6-dimethyloctane	0.019±0.003	0.004±0.001	0.011±0.004	0.037±0.010	0.024±0.006	0.011±0.002	0.002±0.001	0.006±0.002	0.022±0.006	0.014±0.004
4,4-dimethyloctane	0.022±0.002	0.021±0.001	0.020±0.004	0.026±0.005	0.023±0.005	0.013±0.001	0.012±0.000	0.012±0.002	0.015±0.003	0.014±0.003
2-methyldecane	0.046±0.004	0.053±0.002	0.031±0.006	0.043±0.008	0.059±0.011	0.025±0.002	0.029±0.001	0.017±0.003	0.024±0.004	0.032±0.006
3-methyldecane	0.033±0.004	0.020±0.001	0.030±0.008	0.048±0.011	0.036±0.008	0.018±0.002	0.010±0.001	0.016±0.004	0.026±0.006	0.020±0.004
2,6-dimethylnonane	0.025±0.004	0.012±0.001	0.018±0.004	0.047±0.012	0.024±0.005	0.014±0.002	0.007±0.000	0.010±0.002	0.026±0.007	0.013±0.003
C-11 Isoparaffins	0.012±0.001	0.009±0.000	0.010±0.002	0.017±0.003	0.013±0.002	0.006±0.001	0.005±0.000	0.005±0.001	0.009±0.002	0.007±0.001
C-11 Isoparaf alky	0.026±0.003	0.019±0.001	0.018±0.004	0.041±0.010	0.026±0.006	0.014±0.002	0.011±0.001	0.010±0.002	0.022±0.006	0.014±0.003
223-triMethylheptane	0.068±0.006	0.070±0.003	0.062±0.012	0.070±0.014	0.069±0.014	0.041±0.003	0.042±0.002	0.037±0.007	0.042±0.008	0.041±0.008
224-triMe-heptane	0.031±0.002	0.029±0.001	0.026±0.005	0.030±0.005	0.039±0.007	0.019±0.001	0.017±0.001	0.016±0.003	0.018±0.003	0.023±0.004
225-triMe-heptane	0.067±0.007	0.046±0.010	0.067±0.014	0.085±0.017	0.069±0.013	0.040±0.004	0.027±0.006	0.040±0.008	0.051±0.011	0.041±0.008
236-triMe-heptane	0.077±0.006	0.082±0.004	0.058±0.010	0.088±0.016	0.079±0.014	0.046±0.004	0.049±0.002	0.035±0.006	0.053±0.009	0.047±0.008
244-triMe-heptane	0.152±0.019	0.093±0.007	0.124±0.029	0.235±0.058	0.157±0.039	0.091±0.011	0.055±0.004	0.074±0.017	0.142±0.035	0.094±0.023
245-triMe-heptane	0.029±0.002	0.026±0.001	0.021±0.004	0.036±0.007	0.030±0.005	0.017±0.001	0.016±0.001	0.013±0.002	0.022±0.004	0.018±0.003
246-triMe-heptane	0.026±0.003	0.022±0.000	0.020±0.004	0.035±0.008	0.028±0.005	0.016±0.002	0.013±0.000	0.012±0.002	0.021±0.005	0.017±0.003
255-triMe-heptane	0.120±0.010	0.116±0.005	0.089±0.015	0.147±0.027	0.128±0.023	0.072±0.006	0.069±0.003	0.053±0.009	0.088±0.016	0.077±0.014
335-triMe-heptane	0.000±0.000	0.000±0.000	0.000±0.000	0.001±0.000	0.000±0.000	0.000±0.000	0.000±0.000	0.000±0.000	0.000±0.000	0.000±0.000
22466pentMe-heptane	0.008±0.002	0.000±0.000	0.005±0.002	0.019±0.006	0.007±0.002	0.004±0.001	0.000±0.000	0.003±0.001	0.010±0.003	0.004±0.001
C-10 Isoparaffin O	0.027±0.003	0.019±0.001	0.016±0.003	0.047±0.010	0.027±0.005	0.016±0.002	0.011±0.000	0.010±0.002	0.029±0.006	0.016±0.003
2-Me-3-Et-heptane	0.047±0.006	0.018±0.004	0.049±0.010	0.066±0.017	0.057±0.012	0.028±0.004	0.011±0.002	0.029±0.006	0.040±0.011	0.034±0.007
2,6-diMe-hendecane	0.007±0.001	0.005±0.000	0.006±0.001	0.012±0.002	0.006±0.001	0.004±0.000	0.002±0.000	0.003±0.001	0.006±0.001	0.003±0.001
2,6,10triM-hendecane	0.007±0.001	0.004±0.000	0.004±0.001	0.014±0.003	0.007±0.001	0.004±0.000	0.002±0.000	0.002±0.000	0.007±0.001	0.003±0.001
2,6,10triMe-dodecane	0.006±0.001	0.001±0.000	0.005±0.001	0.011±0.002	0.005±0.001	0.003±0.000	0.000±0.000	0.002±0.001	0.005±0.001	0.002±0.000
C-9 Naphthenes	0.047±0.004	0.047±0.001	0.045±0.009	0.047±0.009	0.050±0.009	0.031±0.003	0.031±0.001	0.029±0.006	0.031±0.006	0.033±0.006

Cyclopentane	0.475±0.037	0.615±0.028	0.466±0.092	0.385±0.079	0.432±0.081	0.565±0.044	0.727±0.033	0.554±0.109	0.459±0.094	0.518±0.097
Methylcyclopentane	2.669±0.220	3.037±0.051	2.734±0.550	2.470±0.491	2.435±0.482	2.648±0.219	2.992±0.052	2.708±0.544	2.463±0.488	2.428±0.480
Ethylcyclopentane	0.332±0.029	0.369±0.009	0.299±0.063	0.346±0.070	0.314±0.064	0.283±0.024	0.312±0.007	0.254±0.054	0.297±0.060	0.269±0.055
1T2-diMecyclopentane	0.617±0.050	0.986±0.079	0.529±0.118	0.483±0.101	0.470±0.096	0.525±0.042	0.833±0.067	0.450±0.100	0.414±0.087	0.402±0.082
1C3-diMecyclopentane	0.679±0.058	0.814±0.031	0.655±0.146	0.638±0.128	0.610±0.124	0.578±0.050	0.687±0.026	0.557±0.124	0.547±0.110	0.521±0.106
1T3-diMecyclopentane	0.592±0.050	0.741±0.032	0.558±0.124	0.555±0.112	0.515±0.105	0.504±0.043	0.626±0.027	0.474±0.105	0.475±0.096	0.440±0.090
Propylcyclopentane	0.024±0.002	0.024±0.001	0.018±0.004	0.029±0.006	0.023±0.005	0.018±0.002	0.018±0.000	0.013±0.003	0.022±0.005	0.018±0.003
112-triMeCyPentane	0.007±0.001	0.006±0.001	0.005±0.001	0.011±0.002	0.006±0.001	0.005±0.001	0.004±0.000	0.004±0.001	0.008±0.002	0.005±0.001
113-triMeCyPentane	0.146±0.012	0.204±0.010	0.111±0.023	0.154±0.032	0.117±0.024	0.109±0.009	0.151±0.007	0.083±0.017	0.116±0.024	0.087±0.018
1C2C3-triMeCypentane	0.004±0.000	0.003±0.000	0.003±0.001	0.005±0.001	0.004±0.001	0.003±0.000	0.002±0.000	0.002±0.001	0.004±0.001	0.003±0.001
1C2T3-triMeCyPentane	0.013±0.001	0.016±0.000	0.013±0.003	0.013±0.003	0.011±0.002	0.010±0.001	0.012±0.000	0.009±0.002	0.010±0.002	0.009±0.002
1T2C3-triMeCyPentane	0.149±0.012	0.221±0.015	0.104±0.022	0.156±0.034	0.113±0.023	0.111±0.009	0.164±0.011	0.078±0.016	0.117±0.026	0.084±0.017
1C2C4-triMeCyPentane	0.005±0.001	0.004±0.001	0.003±0.001	0.008±0.002	0.003±0.001	0.003±0.000	0.002±0.000	0.002±0.001	0.006±0.001	0.003±0.001
1T2C4-triMeCyPentane	0.239±0.021	0.268±0.007	0.189±0.040	0.288±0.060	0.211±0.044	0.178±0.016	0.198±0.005	0.141±0.030	0.216±0.045	0.158±0.033
Cyclohexane	1.076±0.100	1.147±0.044	1.313±0.289	0.820±0.178	1.024±0.210	1.066±0.099	1.130±0.044	1.299±0.285	0.815±0.177	1.021±0.209
Methylcyclohexane	1.424±0.123	1.542±0.028	1.361±0.284	1.473±0.299	1.322±0.267	1.212±0.105	1.302±0.023	1.157±0.241	1.262±0.256	1.129±0.228
Ethylcyclohexane	0.191±0.022	0.125±0.011	0.134±0.032	0.312±0.070	0.192±0.043	0.142±0.017	0.092±0.008	0.100±0.024	0.235±0.053	0.144±0.032
1,1-diMecyclohexane	0.031±0.003	0.041±0.002	0.026±0.006	0.031±0.007	0.026±0.005	0.023±0.002	0.030±0.002	0.019±0.004	0.023±0.005	0.019±0.004
1C2-diMecyclohexane	0.060±0.006	0.045±0.002	0.047±0.011	0.089±0.020	0.062±0.013	0.045±0.005	0.033±0.002	0.035±0.008	0.067±0.015	0.046±0.010
1T2-diMecyclohexane	0.121±0.012	0.113±0.005	0.094±0.019	0.164±0.035	0.111±0.022	0.090±0.009	0.083±0.004	0.070±0.014	0.123±0.027	0.083±0.016
1C3-diMecyclohexane	0.259±0.027	0.220±0.014	0.204±0.044	0.375±0.082	0.239±0.050	0.193±0.020	0.163±0.010	0.151±0.033	0.281±0.062	0.178±0.037
1T3-diMecyclohexane	0.208±0.022	0.157±0.011	0.161±0.036	0.311±0.066	0.204±0.042	0.155±0.016	0.115±0.008	0.120±0.027	0.233±0.050	0.152±0.032
1C4-diMecyclohexane	0.051±0.005	0.043±0.004	0.032±0.007	0.085±0.018	0.046±0.009	0.038±0.004	0.032±0.003	0.024±0.005	0.064±0.014	0.034±0.007
Propylcyclohexane	0.043±0.005	0.027±0.001	0.032±0.007	0.069±0.017	0.044±0.010	0.029±0.003	0.018±0.000	0.021±0.005	0.046±0.011	0.029±0.006
iso-Bu-Cyclohexane	0.004±0.000	0.003±0.000	0.004±0.001	0.004±0.001	0.006±0.001	0.003±0.000	0.002±0.000	0.002±0.001	0.003±0.001	0.004±0.001
sec-Bu-Cyclohexane	0.017±0.002	0.011±0.000	0.014±0.003	0.023±0.005	0.019±0.004	0.010±0.001	0.007±0.000	0.008±0.002	0.014±0.003	0.011±0.002
113-t4-tetraMeCyPent	0.113±0.011	0.108±0.002	0.090±0.020	0.143±0.030	0.111±0.023	0.075±0.007	0.071±0.001	0.060±0.014	0.096±0.020	0.074±0.015
1Me-1EtCyclopentane	0.100±0.010	0.109±0.004	0.072±0.017	0.136±0.031	0.082±0.020	0.074±0.008	0.080±0.003	0.053±0.013	0.103±0.023	0.061±0.015
1Me-C2EtCyclopentane	0.055±0.006	0.040±0.002	0.050±0.012	0.069±0.014	0.063±0.013	0.041±0.004	0.030±0.001	0.037±0.009	0.052±0.011	0.047±0.010
1MeC3EtCyclopentane	0.165±0.016	0.143±0.005	0.135±0.031	0.219±0.046	0.165±0.035	0.123±0.012	0.106±0.003	0.100±0.023	0.165±0.034	0.123±0.026
1-M-t-3-Et Cycpentane	0.164±0.016	0.149±0.005	0.126±0.028	0.223±0.045	0.161±0.033	0.123±0.012	0.110±0.004	0.093±0.020	0.167±0.034	0.120±0.024
1MeC3Etcyclohexane	0.082±0.008	0.095±0.004	0.055±0.011	0.086±0.018	0.091±0.022	0.054±0.005	0.063±0.003	0.037±0.008	0.057±0.012	0.061±0.015
1MeC4EtCyclohexane	0.011±0.001	0.007±0.001	0.009±0.002	0.015±0.003	0.013±0.002	0.007±0.001	0.005±0.000	0.006±0.001	0.010±0.002	0.009±0.002
1MeT4Etcyclohexane	0.032±0.003	0.025±0.000	0.026±0.006	0.044±0.010	0.034±0.007	0.022±0.002	0.016±0.000	0.017±0.004	0.030±0.007	0.023±0.005
113-triMecyclohexane	0.048±0.004	0.045±0.001	0.043±0.009	0.056±0.011	0.048±0.009	0.032±0.003	0.030±0.000	0.029±0.006	0.037±0.007	0.032±0.006
1C2C3-triMeCyhexane	0.000±0.000	0.000±0.000	0.000±0.000	0.000±0.000	0.000±0.000	0.000±0.000	0.000±0.000	0.000±0.000	0.000±0.000	0.000±0.000
1C2T3-triMeCyhexane	0.023±0.002	0.021±0.002	0.018±0.004	0.029±0.006	0.023±0.005	0.015±0.001	0.014±0.001	0.012±0.003	0.019±0.004	0.015±0.003
1C3T5-triMeCyhexane	0.142±0.015	0.105±0.004	0.106±0.022	0.215±0.047	0.144±0.028	0.095±0.010	0.069±0.003	0.070±0.014	0.144±0.032	0.096±0.018
1-M-t2-PropCyHexane	0.062±0.006	0.049±0.002	0.042±0.007	0.089±0.017	0.069±0.012	0.037±0.003	0.029±0.001	0.025±0.004	0.053±0.010	0.041±0.007
C-9 Naphthene A	0.013±0.001	0.010±0.001	0.009±0.002	0.019±0.004	0.014±0.003	0.008±0.001	0.006±0.001	0.006±0.002	0.013±0.003	0.009±0.002
C-9 Naphthene B	0.011±0.001	0.011±0.000	0.008±0.002	0.014±0.003	0.011±0.002	0.007±0.001	0.007±0.000	0.005±0.001	0.009±0.002	0.007±0.001
C-9 Naphthene I	0.014±0.002	0.012±0.003	0.014±0.004	0.004±0.001	0.025±0.005	0.009±0.001	0.008±0.002	0.009±0.002	0.003±0.001	0.017±0.003
C-10 Cyclohexane AA	0.014±0.002	0.003±0.001	0.009±0.003	0.029±0.008	0.013±0.003	0.009±0.002	0.002±0.001	0.006±0.002	0.019±0.005	0.009±0.002
C-10 Cyclohexane BB	0.027±0.004	0.013±0.001	0.017±0.004	0.054±0.016	0.025±0.005	0.016±0.003	0.008±0.000	0.010±0.002	0.032±0.009	0.015±0.003
2MePropylCyclohexane	0.001±0.001	0.000±0.000	0.000±0.000	0.005±0.003	0.000±0.000	0.001±0.000	0.000±0.000	0.000±0.000	0.003±0.002	0.000±0.000
Benzene	0.750±0.063	0.800±0.017	0.725±0.145	0.805±0.154	0.669±0.134	0.744±0.062	0.788±0.017	0.719±0.143	0.804±0.153	0.667±0.133
Toluene	7.523±0.596	9.344±0.470	8.219±1.614	5.710±1.100	6.818±1.280	6.397±0.506	7.904±0.400	6.980±1.368	4.874±0.935	5.829±1.093

Ethylbenzene	1.433±0.124	1.280±0.041	1.677±0.324	1.302±0.251	1.475±0.278	1.067±0.092	0.946±0.030	1.246±0.240	0.973±0.187	1.103±0.208
o-Xylene	2.209±0.186	2.148±0.027	2.455±0.474	1.984±0.382	2.251±0.423	1.645±0.138	1.588±0.020	1.825±0.352	1.483±0.284	1.684±0.316
m-Xylene	4.881±0.409	4.831±0.069	5.533±1.077	4.191±0.804	4.969±0.933	3.633±0.305	3.571±0.053	4.113±0.800	3.132±0.598	3.717±0.698
p-Xylene	1.168±0.094	1.196±0.010	1.228±0.232	1.082±0.203	1.165±0.216	0.869±0.070	0.884±0.008	0.913±0.173	0.809±0.151	0.871±0.162
Cumene	0.097±0.009	0.090±0.004	0.114±0.022	0.088±0.018	0.096±0.018	0.064±0.006	0.059±0.002	0.076±0.015	0.058±0.012	0.064±0.012
1-Me-2-Et-benzene	0.545±0.046	0.519±0.011	0.609±0.118	0.494±0.096	0.556±0.106	0.360±0.031	0.341±0.007	0.403±0.078	0.328±0.064	0.370±0.070
1-Me-3-Et-benzene	1.575±0.133	1.501±0.015	1.739±0.337	1.434±0.274	1.626±0.309	1.042±0.088	0.986±0.010	1.149±0.223	0.953±0.181	1.081±0.205
1-Me-4-Et-benzene	0.681±0.057	0.667±0.006	0.748±0.145	0.614±0.118	0.695±0.132	0.451±0.038	0.438±0.004	0.494±0.096	0.408±0.078	0.462±0.087
123-triMe-benzene	0.587±0.049	0.581±0.012	0.606±0.117	0.575±0.111	0.586±0.112	0.388±0.032	0.382±0.007	0.400±0.077	0.382±0.073	0.389±0.074
124-TriMe-benzene	2.629±0.213	2.824±0.044	2.705±0.522	2.417±0.463	2.568±0.485	1.739±0.141	1.856±0.029	1.787±0.344	1.606±0.307	1.708±0.322
135-triMe-benzene	0.800±0.065	0.881±0.028	0.836±0.163	0.704±0.133	0.781±0.148	0.530±0.043	0.579±0.019	0.552±0.108	0.468±0.088	0.519±0.098
Butylbenzene	0.071±0.008	0.027±0.008	0.084±0.019	0.077±0.017	0.095±0.020	0.042±0.005	0.016±0.005	0.050±0.011	0.047±0.010	0.057±0.012
Isobutylbenzene	0.085±0.007	0.071±0.002	0.072±0.012	0.112±0.021	0.087±0.016	0.051±0.004	0.042±0.001	0.043±0.007	0.068±0.013	0.052±0.009
Sec-butylbenzene	0.042±0.004	0.029±0.002	0.050±0.010	0.036±0.008	0.051±0.011	0.025±0.002	0.017±0.001	0.030±0.006	0.022±0.005	0.031±0.006
T-butylbenzene	0.006±0.003	0.000±0.000	0.000±0.000	0.024±0.012	0.000±0.000	0.004±0.002	0.000±0.000	0.000±0.000	0.015±0.007	0.000±0.000
o-Cymene	0.019±0.002	0.012±0.001	0.016±0.003	0.033±0.007	0.014±0.003	0.011±0.001	0.007±0.001	0.010±0.002	0.020±0.005	0.008±0.002
m-Cymene	0.066±0.006	0.046±0.004	0.071±0.014	0.075±0.014	0.073±0.014	0.040±0.004	0.027±0.003	0.043±0.008	0.045±0.009	0.044±0.008
p-Cymene	0.020±0.002	0.014±0.001	0.021±0.004	0.022±0.004	0.022±0.004	0.012±0.001	0.008±0.001	0.013±0.003	0.013±0.003	0.013±0.003
1234-tetMe-benzene	0.071±0.006	0.068±0.002	0.063±0.013	0.084±0.016	0.067±0.013	0.042±0.004	0.041±0.001	0.038±0.007	0.050±0.009	0.040±0.007
1235-tetMe-benzene	0.230±0.019	0.226±0.004	0.229±0.044	0.249±0.047	0.214±0.040	0.137±0.011	0.134±0.002	0.137±0.026	0.149±0.028	0.128±0.024
1245-tetMe-benzene	0.170±0.014	0.168±0.003	0.173±0.033	0.178±0.033	0.159±0.030	0.101±0.008	0.099±0.002	0.103±0.020	0.107±0.020	0.095±0.018
Pentamethylbenzene	0.015±0.001	0.012±0.000	0.011±0.002	0.023±0.004	0.012±0.002	0.008±0.001	0.007±0.000	0.006±0.001	0.013±0.002	0.007±0.001
Propylbenzene	0.499±0.043	0.453±0.008	0.557±0.109	0.488±0.093	0.498±0.096	0.330±0.029	0.297±0.005	0.368±0.072	0.325±0.062	0.331±0.064
1,3-diethylbenzene	0.108±0.010	0.081±0.004	0.120±0.024	0.113±0.021	0.117±0.023	0.064±0.006	0.048±0.002	0.071±0.014	0.068±0.013	0.070±0.014
1-Me-3-Pr-benzene	0.291±0.026	0.238±0.008	0.321±0.063	0.298±0.057	0.307±0.060	0.174±0.016	0.141±0.005	0.191±0.037	0.179±0.034	0.184±0.036
1-Me-4-Pr-benzene	0.182±0.016	0.172±0.003	0.197±0.039	0.186±0.035	0.175±0.033	0.109±0.009	0.102±0.002	0.117±0.023	0.111±0.021	0.104±0.020
Indan	0.274±0.024	0.255±0.006	0.278±0.055	0.265±0.050	0.298±0.059	0.181±0.016	0.167±0.004	0.184±0.037	0.176±0.033	0.198±0.039
1,4-diethylbenzene	0.329±0.029	0.279±0.005	0.349±0.068	0.347±0.066	0.341±0.065	0.196±0.017	0.165±0.003	0.208±0.040	0.208±0.039	0.204±0.039
1-Me-2-Pr-benzene	0.099±0.009	0.077±0.004	0.106±0.021	0.113±0.022	0.100±0.019	0.059±0.005	0.045±0.002	0.063±0.012	0.068±0.013	0.060±0.011
14-diMe2Et-benzene	0.237±0.022	0.187±0.006	0.253±0.051	0.255±0.049	0.253±0.050	0.141±0.013	0.110±0.003	0.151±0.030	0.153±0.029	0.151±0.030
13-diMe4Et-benzene	0.193±0.017	0.160±0.004	0.207±0.041	0.201±0.038	0.203±0.039	0.115±0.010	0.095±0.002	0.123±0.024	0.120±0.023	0.122±0.023
12-diMe4Et-benzene	0.297±0.026	0.256±0.005	0.326±0.064	0.305±0.058	0.302±0.058	0.177±0.015	0.151±0.003	0.194±0.038	0.182±0.034	0.180±0.035
13-diMe2Et-benzene	0.026±0.002	0.020±0.001	0.025±0.005	0.033±0.007	0.027±0.005	0.016±0.001	0.012±0.001	0.015±0.003	0.020±0.004	0.016±0.003
Indene	0.035±0.003	0.027±0.001	0.027±0.005	0.051±0.011	0.035±0.007	0.023±0.002	0.018±0.001	0.018±0.003	0.035±0.007	0.023±0.004
12-diMe3Et-benzene	0.087±0.008	0.065±0.003	0.091±0.018	0.104±0.020	0.089±0.017	0.052±0.005	0.039±0.002	0.054±0.011	0.062±0.012	0.053±0.010
1-Me35diEt-benzene	0.032±0.003	0.018±0.001	0.030±0.007	0.047±0.010	0.033±0.007	0.017±0.002	0.010±0.001	0.017±0.004	0.026±0.005	0.018±0.004
1-Phenyl-2Me butane	0.031±0.003	0.021±0.001	0.030±0.005	0.040±0.008	0.035±0.006	0.017±0.002	0.011±0.001	0.016±0.003	0.022±0.004	0.019±0.003
1-Phenyl-3Me butane	0.014±0.001	0.011±0.000	0.010±0.002	0.019±0.004	0.016±0.003	0.008±0.001	0.006±0.000	0.006±0.001	0.010±0.002	0.009±0.002
124-triMe-5Etbenzene	0.026±0.002	0.022±0.001	0.022±0.004	0.036±0.007	0.025±0.005	0.014±0.001	0.012±0.000	0.012±0.002	0.020±0.004	0.013±0.003
123-triMe-5Etbenzene	0.024±0.003	0.015±0.000	0.018±0.004	0.045±0.009	0.018±0.004	0.013±0.001	0.008±0.000	0.010±0.002	0.025±0.005	0.010±0.002
124-triMe-3Etbenzene	0.006±0.001	0.003±0.000	0.004±0.001	0.011±0.002	0.006±0.001	0.003±0.000	0.002±0.000	0.002±0.000	0.006±0.001	0.003±0.001
12-diMe-3Pr-benzene	0.040±0.004	0.029±0.001	0.039±0.008	0.054±0.011	0.038±0.008	0.022±0.002	0.015±0.000	0.021±0.005	0.030±0.006	0.021±0.004
135-triMe-2Etbenzene	0.026±0.002	0.022±0.001	0.022±0.004	0.030±0.005	0.029±0.005	0.014±0.001	0.012±0.000	0.012±0.002	0.016±0.003	0.016±0.003
Tetralin	0.010±0.002	0.001±0.000	0.001±0.000	0.027±0.009	0.011±0.004	0.006±0.001	0.000±0.000	0.001±0.000	0.016±0.005	0.007±0.002
1-Me-3Bu-benzene	0.054±0.006	0.034±0.002	0.054±0.011	0.079±0.018	0.048±0.010	0.029±0.003	0.018±0.001	0.029±0.006	0.043±0.010	0.026±0.005
12-diMe-4Pr-benzene	0.055±0.005	0.045±0.002	0.044±0.008	0.069±0.012	0.061±0.011	0.033±0.003	0.027±0.001	0.026±0.005	0.041±0.007	0.036±0.006
125-triMe-3Etbenzene	0.027±0.003	0.020±0.001	0.024±0.005	0.039±0.007	0.024±0.005	0.016±0.002	0.012±0.000	0.014±0.003	0.023±0.004	0.014±0.003

123-triMe4Et-benzene	0.004±0.001	0.002±0.000	0.003±0.001	0.009±0.003	0.004±0.001	0.003±0.000	0.001±0.000	0.002±0.000	0.006±0.002	0.002±0.000
C-11 Aromatic K	0.017±0.002	0.013±0.001	0.013±0.002	0.026±0.005	0.017±0.003	0.011±0.001	0.008±0.000	0.008±0.001	0.016±0.003	0.010±0.002
Cis-hydrindane	0.015±0.001	0.014±0.001	0.013±0.003	0.017±0.004	0.016±0.003	0.010±0.001	0.009±0.000	0.009±0.002	0.012±0.002	0.010±0.002
C-7 cyclopentene A	0.036±0.004	0.026±0.003	0.019±0.005	0.064±0.013	0.034±0.007	0.030±0.003	0.022±0.002	0.016±0.004	0.055±0.011	0.029±0.006
C-7 cyclopentene B	0.034±0.004	0.025±0.003	0.018±0.005	0.062±0.013	0.033±0.007	0.029±0.003	0.021±0.002	0.015±0.004	0.053±0.011	0.028±0.006
C-11 Aromatic E	0.059±0.006	0.032±0.002	0.057±0.012	0.086±0.018	0.061±0.013	0.033±0.003	0.018±0.001	0.032±0.007	0.048±0.010	0.033±0.007
C-12 Aromatic A	0.002±0.000	0.003±0.000	0.001±0.000	0.003±0.002	0.001±0.000	0.001±0.000	0.001±0.000	0.000±0.000	0.002±0.001	0.001±0.000
C-12 Aromatic E	0.001±0.000	0.000±0.000	0.001±0.000	0.004±0.002	0.000±0.000	0.001±0.000	0.000±0.000	0.000±0.000	0.002±0.001	0.000±0.000
C-12 Aromatic F	0.005±0.001	0.003±0.000	0.003±0.001	0.011±0.002	0.004±0.001	0.003±0.000	0.001±0.000	0.002±0.000	0.006±0.001	0.002±0.000
Octylbenzene	0.001±0.000	0.000±0.000	0.000±0.000	0.001±0.000	0.001±0.000	0.000±0.000	0.000±0.000	0.000±0.000	0.000±0.000	0.000±0.000
1-Methylindane	0.101±0.010	0.068±0.003	0.097±0.020	0.136±0.028	0.101±0.020	0.060±0.006	0.040±0.002	0.058±0.012	0.081±0.017	0.061±0.012
2-Methylindane	0.151±0.015	0.102±0.004	0.149±0.030	0.202±0.041	0.151±0.031	0.090±0.009	0.061±0.002	0.089±0.018	0.122±0.025	0.090±0.018
4-Methylindane	0.002±0.000	0.002±0.001	0.004±0.001	0.000±0.000	0.002±0.001	0.001±0.000	0.001±0.001	0.003±0.001	0.000±0.000	0.001±0.001
Dimethylindane A	0.017±0.002	0.011±0.000	0.013±0.002	0.031±0.006	0.014±0.003	0.009±0.001	0.006±0.000	0.007±0.001	0.017±0.003	0.008±0.001
Dimethylindane B	0.029±0.004	0.012±0.001	0.021±0.005	0.056±0.012	0.025±0.005	0.016±0.002	0.006±0.000	0.012±0.003	0.031±0.007	0.014±0.003
Dimethylindane C	0.016±0.002	0.006±0.000	0.011±0.003	0.034±0.008	0.014±0.003	0.009±0.001	0.003±0.000	0.006±0.001	0.019±0.004	0.007±0.002
Dimethylindane E	0.020±0.003	0.009±0.000	0.013±0.003	0.040±0.009	0.017±0.004	0.011±0.001	0.004±0.000	0.007±0.002	0.022±0.005	0.009±0.002
Dimethylindane F	0.030±0.003	0.017±0.001	0.021±0.004	0.057±0.012	0.024±0.005	0.016±0.002	0.009±0.000	0.012±0.002	0.031±0.006	0.013±0.002
Dimethylindane G	0.021±0.003	0.009±0.001	0.011±0.002	0.055±0.011	0.011±0.002	0.012±0.002	0.005±0.000	0.006±0.001	0.030±0.006	0.006±0.001
C-11 Indane H	0.012±0.002	0.006±0.000	0.008±0.002	0.029±0.006	0.008±0.002	0.007±0.001	0.003±0.000	0.004±0.001	0.016±0.003	0.004±0.001
Biphenyl	0.005±0.001	0.002±0.000	0.004±0.001	0.007±0.002	0.007±0.001	0.003±0.000	0.001±0.000	0.002±0.000	0.003±0.001	0.004±0.001
Naphthalene	0.130±0.013	0.073±0.005	0.140±0.029	0.179±0.035	0.129±0.026	0.078±0.008	0.043±0.003	0.083±0.017	0.108±0.021	0.077±0.016
1-Methylnaphthalene	0.038±0.004	0.022±0.001	0.028±0.006	0.069±0.014	0.032±0.006	0.021±0.002	0.012±0.001	0.015±0.004	0.037±0.007	0.017±0.003
2-Methylnaphthalene	0.090±0.010	0.047±0.002	0.075±0.016	0.168±0.034	0.069±0.013	0.049±0.005	0.025±0.001	0.041±0.008	0.092±0.019	0.038±0.007
12-DiMe-naphthalene	0.003±0.000	0.002±0.000	0.002±0.001	0.006±0.001	0.003±0.001	0.002±0.000	0.001±0.000	0.001±0.000	0.003±0.001	0.001±0.000
13-DiMe-naphthalene	0.014±0.002	0.008±0.000	0.012±0.003	0.025±0.005	0.011±0.002	0.007±0.001	0.004±0.000	0.006±0.001	0.013±0.003	0.006±0.001
14-DiMe-naphthalene	0.000±0.000	0.000±0.000	0.001±0.000	0.001±0.000	0.001±0.000	0.000±0.000	0.000±0.000	0.000±0.000	0.000±0.000	0.000±0.000
15-DiMe-naphthalene	0.001±0.000	0.000±0.000	0.000±0.000	0.002±0.000	0.001±0.000	0.000±0.000	0.000±0.000	0.000±0.000	0.001±0.000	0.000±0.000
16-DiMe-naphthalene	0.008±0.001	0.005±0.000	0.006±0.001	0.014±0.003	0.007±0.001	0.004±0.000	0.002±0.000	0.003±0.001	0.007±0.001	0.003±0.001
17-DiMe-naphthalene	0.000±0.000	0.000±0.000	0.000±0.000	0.000±0.000	0.000±0.000	0.000±0.000	0.000±0.000	0.000±0.000	0.000±0.000	0.000±0.000
18-DiMe-naphthalene	0.000±0.000	0.000±0.000	0.000±0.000	0.001±0.000	0.000±0.000	0.000±0.000	0.000±0.000	0.000±0.000	0.000±0.000	0.000±0.000
23-DiMe-naphthalene	0.007±0.001	0.004±0.000	0.006±0.001	0.012±0.003	0.006±0.001	0.003±0.000	0.002±0.000	0.003±0.001	0.006±0.001	0.003±0.001
26-DiMe-naphthalene	0.002±0.000	0.002±0.000	0.001±0.000	0.003±0.001	0.001±0.000	0.001±0.000	0.001±0.000	0.000±0.000	0.002±0.000	0.001±0.000
27-DiMe-naphthalene	0.001±0.000	0.001±0.000	0.001±0.000	0.002±0.000	0.002±0.001	0.001±0.000	0.001±0.000	0.000±0.000	0.001±0.000	0.001±0.000
1-Ethylnaphthalene	0.003±0.000	0.002±0.000	0.001±0.000	0.006±0.001	0.003±0.001	0.002±0.000	0.001±0.000	0.001±0.000	0.003±0.001	0.002±0.000
2-Ethylnaphthalene	0.006±0.001	0.003±0.000	0.006±0.001	0.011±0.002	0.004±0.001	0.003±0.000	0.001±0.000	0.003±0.001	0.005±0.001	0.002±0.000
Acenaphthylene	0.000±0.000	0.000±0.000	0.000±0.000	0.000±0.000	0.000±0.000	0.000±0.000	0.000±0.000	0.000±0.000	0.000±0.000	0.000±0.000
Acenaphthene	0.001±0.000	0.001±0.000	0.000±0.000	0.001±0.000	0.001±0.000	0.000±0.000	0.000±0.000	0.000±0.000	0.000±0.000	0.000±0.000
Ethanol	6.925±0.549	7.038±0.031	6.854±1.261	6.929±1.277	6.877±1.267	20.638±1.639	20.808±0.084	20.396±3.745	20.763±3.819	20.584±3.787
Propene	0.000±0.000	0.000±0.000	0.000±0.000	0.001±0.000	0.000±0.000	0.001±0.000	0.001±0.000	0.000±0.000	0.002±0.000	0.001±0.000
1-butene	0.005±0.001	0.003±0.000	0.003±0.001	0.009±0.002	0.004±0.001	0.007±0.001	0.005±0.000	0.005±0.001	0.013±0.003	0.006±0.001
Cis-2-butene	0.027±0.004	0.017±0.002	0.015±0.005	0.055±0.013	0.020±0.005	0.040±0.005	0.025±0.002	0.022±0.007	0.084±0.019	0.029±0.007
Trans-2-butene	0.025±0.003	0.015±0.001	0.018±0.005	0.044±0.010	0.022±0.005	0.037±0.005	0.022±0.002	0.026±0.008	0.067±0.015	0.033±0.008
2-methylpropene	0.003±0.000	0.002±0.000	0.002±0.001	0.006±0.001	0.003±0.001	0.005±0.001	0.003±0.000	0.003±0.001	0.009±0.002	0.004±0.001
1-pentene	0.102±0.012	0.061±0.007	0.075±0.023	0.168±0.033	0.103±0.023	0.122±0.014	0.072±0.009	0.089±0.027	0.203±0.040	0.124±0.027
Cis-2-pentene	0.161±0.018	0.097±0.011	0.121±0.032	0.261±0.051	0.164±0.036	0.192±0.021	0.114±0.013	0.144±0.038	0.314±0.061	0.197±0.043
trans-2-pentene	0.310±0.035	0.177±0.021	0.252±0.066	0.473±0.092	0.339±0.077	0.371±0.041	0.209±0.025	0.300±0.078	0.569±0.111	0.405±0.092

2-methyl-1-butene	0.200±0.023	0.113±0.015	0.154±0.045	0.324±0.064	0.208±0.046	0.239±0.028	0.134±0.018	0.183±0.053	0.391±0.078	0.249±0.055
3-methyl-1-butene	0.029±0.004	0.016±0.003	0.024±0.009	0.045±0.009	0.031±0.007	0.034±0.004	0.018±0.003	0.028±0.010	0.054±0.011	0.037±0.009
2-methyl-2-butene	0.447±0.049	0.243±0.028	0.386±0.097	0.665±0.130	0.494±0.109	0.534±0.059	0.287±0.033	0.459±0.115	0.800±0.157	0.591±0.130
1-hexene	0.037±0.004	0.029±0.003	0.024±0.005	0.063±0.012	0.031±0.006	0.037±0.004	0.028±0.003	0.024±0.005	0.063±0.012	0.031±0.006
Cis-2-hexene	0.074±0.007	0.058±0.006	0.053±0.011	0.100±0.019	0.086±0.015	0.074±0.007	0.057±0.006	0.053±0.011	0.100±0.019	0.086±0.015
Trans-2-hexene	0.171±0.016	0.131±0.017	0.135±0.030	0.178±0.033	0.238±0.044	0.170±0.016	0.130±0.017	0.135±0.030	0.178±0.033	0.238±0.045
Cis-3-hexene	0.097±0.009	0.076±0.009	0.071±0.015	0.123±0.023	0.117±0.021	0.097±0.009	0.075±0.008	0.071±0.015	0.123±0.023	0.118±0.021
2-Me-1-pentene	0.099±0.009	0.075±0.008	0.077±0.017	0.126±0.024	0.118±0.021	0.099±0.009	0.074±0.008	0.077±0.016	0.127±0.024	0.118±0.021
4-methyl-1-pentene	0.044±0.004	0.031±0.003	0.033±0.007	0.066±0.013	0.046±0.008	0.044±0.004	0.031±0.003	0.033±0.007	0.066±0.013	0.046±0.008
2-methyl-2-pentene	0.324±0.037	0.246±0.047	0.293±0.075	0.207±0.039	0.548±0.112	0.322±0.037	0.243±0.047	0.291±0.075	0.207±0.039	0.548±0.112
C-3Me-2-pentene	0.073±0.008	0.054±0.006	0.048±0.012	0.123±0.023	0.067±0.014	0.073±0.007	0.053±0.006	0.047±0.012	0.123±0.023	0.067±0.014
T-3Me-2-pentene	0.104±0.012	0.062±0.013	0.061±0.019	0.196±0.037	0.096±0.022	0.103±0.012	0.061±0.013	0.061±0.019	0.196±0.037	0.096±0.022
C-4Me-2-pentene	0.016±0.002	0.010±0.002	0.013±0.004	0.011±0.003	0.030±0.008	0.016±0.002	0.010±0.002	0.013±0.004	0.011±0.003	0.030±0.008
T-4Me-2-pentene	0.148±0.018	0.108±0.024	0.138±0.037	0.077±0.015	0.269±0.057	0.147±0.018	0.107±0.023	0.137±0.037	0.077±0.015	0.269±0.057
2-Et-1-butene	0.026±0.003	0.020±0.002	0.017±0.004	0.046±0.009	0.022±0.004	0.026±0.003	0.020±0.002	0.017±0.004	0.047±0.009	0.022±0.004
2,3-dimethyl-1-butene	0.037±0.003	0.026±0.003	0.030±0.007	0.043±0.008	0.048±0.009	0.037±0.003	0.025±0.003	0.030±0.007	0.043±0.008	0.048±0.009
3,3-dimethylbutene	0.003±0.000	0.002±0.000	0.002±0.001	0.005±0.001	0.003±0.001	0.003±0.000	0.002±0.000	0.002±0.001	0.005±0.001	0.003±0.001
2,3-dimethyl-2-butene	0.053±0.005	0.039±0.006	0.044±0.010	0.050±0.009	0.078±0.015	0.053±0.005	0.039±0.006	0.044±0.010	0.050±0.009	0.078±0.015
Nonenes	0.009±0.001	0.012±0.000	0.008±0.002	0.009±0.002	0.007±0.002	0.006±0.000	0.008±0.000	0.005±0.001	0.006±0.001	0.005±0.001
Undecenes	0.001±0.000	0.000±0.000	0.000±0.000	0.000±0.000	0.003±0.001	0.001±0.000	0.000±0.000	0.000±0.000	0.000±0.000	0.002±0.001
Tridecenes	0.001±0.000	0.001±0.000	0.001±0.000	0.001±0.001	0.000±0.000	0.000±0.000	0.000±0.000	0.000±0.000	0.001±0.000	0.000±0.000
Tetradecenes	0.002±0.000	0.002±0.000	0.001±0.000	0.002±0.000	0.002±0.000	0.001±0.000	0.000±0.000	0.000±0.000	0.001±0.000	0.001±0.000
C-1,3-pentadiene	0.003±0.000	0.002±0.000	0.003±0.001	0.005±0.001	0.003±0.001	0.004±0.000	0.002±0.000	0.003±0.001	0.006±0.001	0.004±0.001
T-1,3-pentadiene	0.006±0.001	0.004±0.000	0.005±0.001	0.009±0.002	0.006±0.001	0.007±0.001	0.004±0.000	0.006±0.002	0.011±0.002	0.008±0.002
2-Me-1,3-butadiene	0.006±0.001	0.004±0.000	0.005±0.002	0.009±0.002	0.007±0.001	0.007±0.001	0.004±0.000	0.006±0.002	0.011±0.002	0.008±0.002
T-1Me-1,3-pentadiene	0.000±0.000	0.000±0.000	0.000±0.000	0.000±0.000	0.000±0.000	0.000±0.000	0.000±0.000	0.000±0.000	0.000±0.000	0.000±0.000
1,7-Octadiene	0.001±0.000	0.001±0.000	0.001±0.000	0.003±0.001	0.001±0.000	0.001±0.000	0.001±0.000	0.001±0.000	0.002±0.000	0.001±0.000
Cyclopentadiene	0.004±0.000	0.002±0.000	0.003±0.001	0.007±0.001	0.004±0.001	0.005±0.001	0.003±0.000	0.003±0.001	0.008±0.002	0.005±0.001
1-Me-cyclopentadiene	0.006±0.002	0.000±0.000	0.011±0.004	0.011±0.005	0.000±0.000	0.005±0.002	0.000±0.000	0.011±0.004	0.011±0.005	0.000±0.000
Octadiene A	0.029±0.003	0.020±0.002	0.020±0.005	0.041±0.008	0.034±0.007	0.021±0.002	0.014±0.002	0.015±0.004	0.031±0.006	0.025±0.005
23-diMe-1-pentene	0.009±0.001	0.007±0.001	0.006±0.001	0.017±0.003	0.007±0.001	0.008±0.001	0.006±0.001	0.005±0.001	0.014±0.003	0.006±0.001
24-dime-1-pentene	0.006±0.001	0.005±0.001	0.003±0.001	0.012±0.002	0.004±0.001	0.005±0.001	0.004±0.001	0.003±0.001	0.010±0.002	0.003±0.001
33-DiMe-1-pentene	0.002±0.000	0.002±0.000	0.002±0.000	0.004±0.001	0.002±0.000	0.002±0.000	0.002±0.000	0.001±0.000	0.004±0.001	0.002±0.000
3,4-Dimethyl-2-Pentene	0.000±0.000	0.000±0.000	0.001±0.000	0.000±0.000	0.000±0.000	0.000±0.000	0.000±0.000	0.001±0.000	0.000±0.000	0.000±0.000
44-diMe-1-pentene	0.009±0.001	0.004±0.001	0.005±0.001	0.024±0.005	0.003±0.001	0.008±0.001	0.003±0.001	0.004±0.001	0.021±0.004	0.003±0.001
23-diMe-2-pentene	0.037±0.004	0.028±0.004	0.025±0.006	0.061±0.011	0.036±0.008	0.032±0.003	0.024±0.003	0.021±0.005	0.052±0.010	0.031±0.006
24Dimethyl-2-Pentene	0.002±0.000	0.002±0.000	0.001±0.000	0.004±0.001	0.001±0.000	0.002±0.000	0.001±0.000	0.001±0.000	0.004±0.001	0.001±0.000
34-diMe-c2-pentene	0.009±0.001	0.007±0.001	0.007±0.002	0.015±0.003	0.009±0.002	0.008±0.001	0.006±0.001	0.006±0.001	0.013±0.002	0.008±0.002
44-diMe-c2-pentene	0.004±0.000	0.003±0.000	0.002±0.000	0.008±0.002	0.003±0.001	0.004±0.000	0.003±0.000	0.002±0.000	0.007±0.001	0.003±0.001
3-Et-1-pentene	0.000±0.000	0.000±0.000	0.000±0.000	0.001±0.000	0.000±0.000	0.000±0.000	0.000±0.000	0.000±0.000	0.000±0.000	0.000±0.000
3-Et-2-pentene	0.075±0.008	0.055±0.007	0.046±0.011	0.128±0.025	0.070±0.014	0.064±0.007	0.046±0.006	0.040±0.010	0.110±0.021	0.060±0.012
2-Me-1-hexene	0.020±0.002	0.016±0.002	0.012±0.003	0.036±0.007	0.015±0.003	0.017±0.002	0.014±0.002	0.011±0.003	0.031±0.006	0.013±0.003
3-Me-1-hexene	0.003±0.000	0.002±0.000	0.002±0.001	0.006±0.001	0.002±0.001	0.003±0.000	0.002±0.000	0.002±0.000	0.005±0.001	0.002±0.000
5-Me-1-hexene	0.012±0.001	0.010±0.001	0.008±0.002	0.021±0.004	0.010±0.002	0.011±0.001	0.008±0.001	0.007±0.002	0.018±0.003	0.009±0.002
2-Me-2-hexene	0.041±0.004	0.031±0.004	0.027±0.007	0.065±0.012	0.038±0.008	0.035±0.004	0.026±0.003	0.023±0.006	0.056±0.010	0.033±0.007
5-Me-t2-hexene	0.000±0.000	0.000±0.000	0.000±0.000	0.001±0.000	0.000±0.000	0.000±0.000	0.000±0.000	0.000±0.000	0.001±0.000	0.000±0.000
2-Me-t3-hexene	0.020±0.002	0.016±0.002	0.012±0.003	0.037±0.007	0.015±0.003	0.017±0.002	0.013±0.002	0.011±0.003	0.032±0.006	0.013±0.003

3-Me-c3-hexene	0.028±0.003	0.021±0.003	0.019±0.005	0.045±0.009	0.027±0.006	0.024±0.002	0.018±0.002	0.016±0.004	0.039±0.007	0.023±0.005
3-Me-t3-hexene	0.017±0.002	0.013±0.002	0.012±0.003	0.028±0.005	0.016±0.003	0.015±0.002	0.011±0.001	0.010±0.003	0.024±0.005	0.013±0.003
1-Heptene	0.019±0.002	0.015±0.003	0.010±0.003	0.033±0.007	0.016±0.004	0.016±0.002	0.013±0.003	0.008±0.003	0.028±0.006	0.014±0.003
Cis-2-heptene	0.000±0.000	0.000±0.000	0.000±0.000	0.001±0.000	0.000±0.000	0.000±0.000	0.000±0.000	0.000±0.000	0.001±0.000	0.000±0.000
Trans-2-heptene	0.002±0.000	0.005±0.001	0.000±0.000	0.001±0.000	0.000±0.000	0.001±0.000	0.004±0.000	0.000±0.000	0.001±0.000	0.000±0.000
T3-Heptene	0.025±0.003	0.015±0.004	0.012±0.004	0.051±0.009	0.022±0.005	0.021±0.003	0.013±0.003	0.011±0.004	0.043±0.008	0.019±0.004
C2-Octene	0.015±0.001	0.011±0.002	0.012±0.003	0.015±0.003	0.021±0.004	0.011±0.001	0.008±0.001	0.009±0.002	0.011±0.002	0.016±0.003
C4-Octene	0.001±0.000	0.002±0.001	0.001±0.001	0.002±0.001	0.000±0.000	0.001±0.000	0.001±0.001	0.001±0.001	0.002±0.001	0.000±0.000
25-Dimethyl-1-hexene	0.000±0.000	0.000±0.000	0.000±0.000	0.001±0.000	0.000±0.000	0.000±0.000	0.000±0.000	0.000±0.000	0.001±0.000	0.000±0.000
4-M-1-Heptene	0.058±0.005	0.075±0.003	0.041±0.008	0.065±0.013	0.050±0.010	0.042±0.003	0.055±0.003	0.030±0.006	0.048±0.010	0.037±0.007
t-4-M-2-Heptene	0.001±0.000	0.001±0.000	0.002±0.000	0.001±0.000	0.002±0.000	0.001±0.000	0.001±0.000	0.001±0.000	0.001±0.000	0.002±0.000
C-2-m-3-heptene	0.137±0.014	0.114±0.009	0.107±0.023	0.202±0.043	0.126±0.026	0.102±0.011	0.084±0.006	0.079±0.017	0.151±0.033	0.095±0.019
c-6-M-2-Heptene	0.002±0.000	0.002±0.000	0.002±0.000	0.004±0.001	0.002±0.000	0.002±0.000	0.001±0.000	0.001±0.000	0.003±0.001	0.002±0.000
t-6-M-2-Heptene	0.001±0.001	0.000±0.000	0.000±0.000	0.000±0.000	0.004±0.002	0.001±0.000	0.000±0.000	0.000±0.000	0.000±0.000	0.003±0.002
2-Methyl-2-heptene	0.042±0.004	0.034±0.001	0.032±0.007	0.058±0.012	0.043±0.009	0.031±0.003	0.025±0.001	0.023±0.005	0.043±0.009	0.032±0.007
2235TetMethylhexane	0.000±0.000	0.000±0.000	0.001±0.000	0.000±0.000	0.000±0.000	0.000±0.000	0.000±0.000	0.000±0.000	0.000±0.000	0.000±0.000
C-7 Olefin A	0.006±0.001	0.005±0.001	0.003±0.001	0.011±0.002	0.004±0.001	0.005±0.001	0.004±0.001	0.003±0.001	0.010±0.002	0.003±0.001
C-7 Olefin B	0.001±0.000	0.001±0.000	0.000±0.000	0.002±0.000	0.001±0.000	0.001±0.000	0.001±0.000	0.000±0.000	0.001±0.000	0.000±0.000
C-7 Olefin D	0.002±0.000	0.002±0.000	0.001±0.000	0.004±0.001	0.001±0.000	0.002±0.000	0.001±0.000	0.001±0.000	0.004±0.001	0.001±0.000
Octene B	0.003±0.000	0.002±0.000	0.002±0.000	0.005±0.001	0.003±0.001	0.002±0.000	0.002±0.000	0.001±0.000	0.004±0.001	0.003±0.001
Octene C	0.006±0.001	0.004±0.000	0.003±0.001	0.012±0.002	0.005±0.001	0.005±0.001	0.003±0.000	0.002±0.001	0.009±0.002	0.003±0.001
Octene D	0.008±0.001	0.006±0.001	0.004±0.001	0.016±0.003	0.007±0.001	0.006±0.001	0.004±0.001	0.003±0.001	0.012±0.003	0.005±0.001
Octene F	0.001±0.000	0.001±0.000	0.000±0.000	0.005±0.001	0.000±0.000	0.001±0.000	0.000±0.000	0.000±0.000	0.004±0.001	0.000±0.000
Octene G	0.001±0.000	0.001±0.000	0.001±0.000	0.002±0.000	0.001±0.000	0.001±0.000	0.001±0.000	0.001±0.000	0.002±0.000	0.001±0.000
Octene H	0.007±0.001	0.006±0.001	0.005±0.001	0.012±0.002	0.007±0.001	0.006±0.001	0.004±0.000	0.004±0.001	0.009±0.002	0.006±0.001
Octene I	0.011±0.001	0.008±0.001	0.008±0.002	0.016±0.003	0.010±0.002	0.008±0.001	0.006±0.001	0.006±0.001	0.012±0.002	0.008±0.002
C-8 Olefin K	0.013±0.001	0.024±0.002	0.008±0.002	0.012±0.003	0.008±0.002	0.009±0.001	0.017±0.001	0.006±0.001	0.009±0.002	0.006±0.001
C-8 Olefin M	0.027±0.003	0.021±0.002	0.022±0.005	0.034±0.007	0.031±0.006	0.020±0.002	0.015±0.001	0.016±0.004	0.025±0.005	0.022±0.005
44DiMe2neopen1pentene	0.001±0.001	0.000±0.000	0.002±0.001	0.004±0.002	0.000±0.000	0.001±0.000	0.000±0.000	0.001±0.000	0.002±0.001	0.000±0.000
22466PentaMe3heptene	0.000±0.000	0.000±0.000	0.001±0.001	0.000±0.000	0.000±0.000	0.000±0.000	0.000±0.000	0.001±0.000	0.000±0.000	0.000±0.000
T-2-T-4-hexadiene	0.005±0.001	0.004±0.000	0.003±0.001	0.010±0.002	0.004±0.001	0.004±0.000	0.003±0.000	0.002±0.000	0.009±0.002	0.003±0.001
Cyclopentene	0.065±0.007	0.041±0.004	0.042±0.011	0.114±0.023	0.063±0.013	0.078±0.009	0.048±0.005	0.050±0.013	0.138±0.028	0.076±0.016
1-Me-cyclopentene	0.143±0.016	0.105±0.012	0.074±0.020	0.262±0.052	0.133±0.027	0.126±0.014	0.091±0.010	0.065±0.018	0.231±0.046	0.116±0.024
3-Me-cyclopentene	0.036±0.004	0.026±0.003	0.020±0.005	0.072±0.014	0.027±0.005	0.032±0.004	0.023±0.003	0.017±0.004	0.064±0.013	0.024±0.005
Sum of Unclassified Compounds	2.589±0.007	1.417±0.000	1.540±0.003	3.174±0.014	2.113±0.006	1.433±0.002	0.782±0.000	0.849±0.001	1.755±0.004	1.174±0.002

Note: Compounds for which an exact isomer could not be determined are denoted and differentiated by a CAPITAL suffix.

Table 3.3.11. *Compound specific diesel fuel speciation for California in Summer 2010.*

	Weight percentage in fuel [% weight by carbon (± St. Dev)]				
Compound	**Statewide**	**Bakersfield**	**Berkeley**	**Pasadena**	**Sacramento**
n-octane	0.104±0.069	0.046±0.003	0.057±0.045	0.180±0.071	0.132±0.035
n-nonane	0.209±0.111	0.120±0.031	0.125±0.095	0.330±0.095	0.263±0.012
n-decane	0.444±0.169	0.353±0.066	0.315±0.228	0.588±0.122	0.519±0.098
n-undecane	0.581±0.183	0.456±0.039	0.573±0.312	0.695±0.168	0.602±0.114
n-dodecane	0.478±0.115	0.364±0.032	0.520±0.167	0.565±0.094	0.466±0.033
n-tridecane	0.440±0.091	0.337±0.029	0.469±0.102	0.517±0.091	0.436±0.005
n-tetradecane	0.439±0.081	0.322±0.020	0.503±0.021	0.493±0.018	0.437±0.061
n-pentadecane	0.524±0.106	0.414±0.033	0.560±0.076	0.605±0.104	0.518±0.121
n-hexadecane	0.552±0.162	0.395±0.041	0.588±0.090	0.645±0.188	0.579±0.216
n-heptadecane	0.628±0.189	0.542±0.102	0.659±0.131	0.646±0.257	0.665±0.297
n-octadecane	0.556±0.161	0.507±0.083	0.600±0.117	0.543±0.243	0.576±0.236
n-nonadecane	0.400±0.182	0.215±0.028	0.506±0.130	0.413±0.217	0.464±0.209
n-eicosane	0.386±0.175	0.233±0.021	0.511±0.128	0.351±0.215	0.450±0.197
2-5-dimethylhexane	0.009±0.004	0.012±0.002	0.005±0.004	0.009±0.002	0.010±0.003
2-4-dimethylhexane	0.006±0.002	0.005±0.002	0.004±0.002	0.006±0.002	0.007±0.003
2-methylheptane	0.057±0.021	0.047±0.008	0.038±0.030	0.075±0.007	0.067±0.013
4-methylheptane	0.017±0.008	0.012±0.003	0.012±0.010	0.023±0.007	0.023±0.004
3-methylheptane	0.052±0.022	0.034±0.003	0.036±0.026	0.070±0.010	0.068±0.014
2,6-dimethylheptane	0.051±0.026	0.032±0.004	0.028±0.021	0.078±0.022	0.063±0.005
3-5-dimethylheptane	0.028±0.015	0.014±0.002	0.019±0.011	0.040±0.012	0.041±0.011
2,3-dimethyheptane	0.013±0.005	0.012±0.002	0.007±0.005	0.017±0.003	0.017±0.001
4&2-methyloctane	0.056±0.031	0.024±0.005	0.037±0.024	0.081±0.018	0.084±0.012
3-methyloctane+3-ethylheptane	0.079±0.039	0.038±0.007	0.054±0.038	0.117±0.011	0.108±0.005
C10 Branched alkanes A	0.057±0.020	0.043±0.008	0.040±0.015	0.067±0.020	0.076±0.010
2-6-dimethyloctane	0.035±0.016	0.029±0.006	0.023±0.018	0.045±0.018	0.042±0.016
C10 Branch alkanes B	0.316±0.118	0.206±0.032	0.243±0.092	0.405±0.113	0.408±0.054
C11 Branched Alkanes A	0.046±0.014	0.030±0.002	0.050±0.006	0.049±0.022	0.054±0.002
C11 Branched Alkanes B	0.018±0.008	0.007±0.002	0.017±0.005	0.024±0.005	0.023±0.002
dimethylundecane A	0.174±0.067	0.225±0.012	0.176±0.083	0.163±0.088	0.133±0.055
dimethyundecane B	0.129±0.049	0.191±0.009	0.120±0.048	0.111±0.046	0.093±0.024
methylcyclohexane	0.127±0.050	0.156±0.025	0.067±0.050	0.142±0.031	0.141±0.048
Ethylcyclopentane	0.025±0.010	0.029±0.008	0.016±0.011	0.032±0.010	0.025±0.007
n-propylcyclopentane	0.031±0.016	0.018±0.002	0.018±0.011	0.051±0.014	0.036±0.002

ethylcyclohexane	0.157±0.068	0.111±0.021	0.088±0.053	0.221±0.045	0.207±0.017
propylcyclohexane	0.256±0.095	0.270±0.047	0.147±0.053	0.312±0.112	0.294±0.083
cumene	0.029±0.009	0.036±0.005	0.022±0.017	0.030±0.001	0.029±0.004
n-propyl_benzene	0.090±0.020	0.092±0.017	0.069±0.021	0.099±0.019	0.101±0.012
1-ethyl-4(and3)-methylbenzene	0.389±0.091	0.348±0.049	0.339±0.107	0.452±0.131	0.415±0.029
1-3-5-trimethylbenzene	0.150±0.045	0.197±0.027	0.114±0.057	0.145±0.034	0.145±0.022
1-ethyl-2-methylbenzene	0.136±0.023	0.129±0.018	0.128±0.035	0.149±0.029	0.137±0.015
1-2-4-trimethylbenzene	0.699±0.222	0.984±0.111	0.589±0.255	0.605±0.122	0.617±0.120
1-ethenyl-2-(or3)-methylbenzene	0.019±0.009	0.020±0.002	0.020±0.015	0.021±0.012	0.015±0.002
isobutylbenzene	0.009±0.003	0.012±0.002	0.008±0.003	0.007±0.002	0.010±0.003
m-cymene	0.040±0.015	0.054±0.007	0.035±0.028	0.037±0.006	0.035±0.007
p-cymene	0.039±0.021	0.065±0.007	0.029±0.026	0.031±0.010	0.030±0.011
m-diethylbenzene	0.589±0.244	0.588±0.047	0.693±0.504	0.545±0.171	0.531±0.130
1-methyl-3-n-propylbenzene	0.267±0.076	0.279±0.024	0.287±0.144	0.267±0.088	0.233±0.014
indan	0.142±0.060	0.152±0.015	0.150±0.104	0.152±0.083	0.112±0.013
p-diethylbenzene	0.415±0.172	0.417±0.034	0.487±0.357	0.383±0.120	0.374±0.088
n-butylbenzene	0.132±0.053	0.103±0.014	0.146±0.093	0.150±0.066	0.128±0.013
o-diethylbenzene	0.034±0.006	0.038±0.002	0.037±0.009	0.033±0.002	0.028±0.001
1-methyl-2-n-propylbenzene	0.071±0.018	0.076±0.007	0.083±0.030	0.062±0.016	0.063±0.009
1,4-dimethyl-2-ethylbenzene	0.162±0.047	0.164±0.022	0.204±0.078	0.149±0.027	0.130±0.022
1,3-dimethyl-4-ethylbenzene	0.164±0.046	0.203±0.017	0.182±0.071	0.145±0.025	0.127±0.023
1,2-dimethyl-4-ethylbenzene	0.108±0.040	0.116±0.007	0.130±0.080	0.098±0.023	0.088±0.015
Trans-1-butenylbenzene	0.009±0.003	0.012±0.002	0.009±0.004	0.008±0.002	0.007±0.002
1,3-dimethyl-2-ethylbenzene	0.071±0.030	0.096±0.007	0.075±0.057	0.057±0.006	0.055±0.003
1,2-dimethyl-3-ethylbenzene	0.052±0.016	0.069±0.004	0.058±0.022	0.042±0.005	0.040±0.006
1-2-4-5-tetramethylbenzene	0.078±0.038	0.108±0.014	0.086±0.069	0.061±0.017	0.057±0.017
1-2-3-5-tetramethylbenzene	0.114±0.046	0.160±0.014	0.126±0.066	0.087±0.022	0.082±0.020
C11 Aromatics A	0.020±0.007	0.026±0.005	0.023±0.012	0.017±0.002	0.016±0.002
1-methylindan	0.113±0.072	0.085±0.015	0.171±0.131	0.114±0.060	0.083±0.009
C11 Aromatics B	0.010±0.003	0.015±0.001	0.010±0.003	0.008±0.002	0.008±0.001
1-2-3-4-tetramethylbenzene	0.183±0.084	0.301±0.012	0.190±0.073	0.122±0.016	0.119±0.021
2-methylindan	0.217±0.092	0.215±0.018	0.289±0.168	0.200±0.069	0.164±0.010
toluene	0.214±0.102	0.252±0.043	0.106±0.074	0.242±0.122	0.256±0.108
ethylbenzene	0.093±0.043	0.063±0.010	0.061±0.033	0.132±0.044	0.115±0.033
m&p-xylene	0.475±0.154	0.467±0.069	0.321±0.158	0.575±0.186	0.538±0.098
o-xylene	0.164±0.056	0.151±0.021	0.107±0.040	0.202±0.070	0.195±0.038

123-trimethylbenzene	0.286±0.178	0.564±0.075	0.189±0.090	0.190±0.040	0.199±0.060
dimethylnaphthalenes	0.182±0.167	0.456±0.007	0.125±0.021	0.067±0.015	0.082±0.010
trimethylnapthalenes	0.153±0.134	0.370±0.007	0.112±0.030	0.056±0.022	0.073±0.012
naphthalene	0.045±0.037	0.103±0.017	0.034±0.010	0.022±0.007	0.020±0.003
2-methylnaphthalene	0.124±0.120	0.319±0.029	0.082±0.032	0.046±0.019	0.050±0.009
1-methylnaphthalene	0.066±0.062	0.166±0.013	0.046±0.013	0.024±0.008	0.027±0.005
C9 Cycloalkene A	0.052±0.026	0.065±0.007	0.028±0.007	0.047±0.026	0.068±0.039
ctc-1-2-4-trimethylcyclopentane	0.016±0.006	0.023±0.004	0.009±0.005	0.017±0.002	0.016±0.002
ctc-1,2,3-trimethylcyclopentane	0.040±0.020	0.066±0.014	0.018±0.013	0.041±0.014	0.036±0.007
ctt-1-2-4-trimethylcyclopentane	0.010±0.004	0.012±0.001	0.006±0.003	0.013±0.005	0.010±0.001
cis-1,3 & 1,1-dimethylcyclohexane	0.099±0.043	0.072±0.010	0.054±0.036	0.135±0.027	0.135±0.010
trans-1-2-dimethylcyclohexane	0.118±0.048	0.100±0.010	0.060±0.041	0.154±0.027	0.157±0.013
trans-1-3-dimethylcyclohexane	0.078±0.034	0.050±0.005	0.049±0.030	0.112±0.024	0.100±0.006
isopropylcyclopentane	0.010±0.006	0.007±0.001	0.006±0.003	0.017±0.007	0.011±0.001
ccc-1-3-5-trimethylcyclohexane	0.052±0.048	0.020±0.003	0.025±0.014	0.065±0.045	0.100±0.066
cis-1-2-dimethylcyclohexane	0.049±0.025	0.030±0.005	0.029±0.015	0.078±0.024	0.060±0.011
1-1-3-trimethylcyclohexane	0.096±0.047	0.128±0.018	0.043±0.029	0.105±0.050	0.109±0.050
1-1-4-trimethylcyclohexane	0.027±0.011	0.020±0.002	0.018±0.007	0.031±0.004	0.040±0.010
ctt-1,2,4-trimethylcyclohexane	0.018±0.013	0.011±0.001	0.010±0.004	0.018±0.009	0.031±0.018
ctc-1-2-4-trimetylcyclohexane	0.099±0.057	0.091±0.014	0.056±0.022	0.102±0.046	0.149±0.091
C9 cycloalkanes A	0.008±0.003	0.007±0.001	0.005±0.001	0.011±0.004	0.010±0.001
methyl-ethylcyclohexane isomer A	0.010±0.004	0.011±0.002	0.008±0.002	0.010±0.007	0.012±0.005
isopropylcyclohexane	0.039±0.014	0.052±0.007	0.022±0.009	0.041±0.011	0.041±0.012
C10 cyclohexanes A	0.126±0.050	0.129±0.014	0.094±0.014	0.134±0.073	0.148±0.075

Note: This list only comprises a fraction of compounds in diesel. Compounds for which an exact isomer could not be determined are denoted and differentiated by a CAPITAL suffix.

Table 3.3.12. *Compound specific non-tailpipe gasoline speciation for California in Summer 2010.*

	Weight percentage in fuel [% weight by carbon (± St. Dev)]					Molar percentage in fuel [% mol (± St. Dev)]				
Compound	**Statewide**	**Bakersfield**	**Berkeley**	**Pasadena**	**Sacramento**	**Statewide**	**Bakersfield**	**Berkeley**	**Pasadena**	**Sacramento**
ethane	0.099±0.011	0.310±0.042	0.015±0.006	0.069±0.014	0.000±0.000	0.235±0.026	0.735±0.099	0.037±0.015	0.169±0.033	0.000±0.000
propane	0.690±0.059	1.534±0.156	0.315±0.088	0.287±0.063	0.624±0.143	1.105±0.095	2.430±0.242	0.511±0.141	0.461±0.100	1.020±0.234
n-butane	6.542±0.499	8.944±0.646	5.472±0.961	6.326±1.301	5.426±0.973	7.929±0.603	10.652±0.740	6.734±1.182	7.652±1.561	6.676±1.197
n-pentane	10.313±0.801	14.100±0.768	9.068±1.766	9.362±1.924	8.723±1.690	10.060±0.787	13.484±0.685	8.950±1.746	9.210±1.899	8.595±1.666
n-hexane	1.970±0.168	2.245±0.044	1.837±0.374	1.976±0.413	1.823±0.372	1.605±0.138	1.797±0.030	1.511±0.308	1.617±0.338	1.497±0.306
n-heptane	0.137±0.012	0.150±0.003	0.164±0.033	0.108±0.021	0.126±0.025	0.096±0.008	0.103±0.002	0.116±0.023	0.075±0.015	0.088±0.017
n-octane	0.062±0.005	0.067±0.002	0.071±0.014	0.049±0.010	0.059±0.012	0.038±0.003	0.040±0.001	0.044±0.009	0.030±0.006	0.037±0.007
n-nonane	0.008±0.001	0.009±0.000	0.009±0.002	0.007±0.001	0.008±0.002	0.005±0.000	0.005±0.000	0.005±0.001	0.004±0.001	0.005±0.001
n-decane	0.001±0.000	0.001±0.000	0.001±0.000	0.001±0.000	0.001±0.000	0.001±0.000	0.000±0.000	0.000±0.000	0.001±0.000	0.001±0.000
2-methylpropane	1.072±0.111	1.569±0.176	0.807±0.212	1.484±0.341	0.428±0.076	1.293±0.134	1.859±0.206	0.994±0.260	1.791±0.408	0.527±0.094
2-methylbutane	38.367±3.173	34.577±0.809	41.426±7.644	36.647±6.790	40.817±7.477	37.582±3.129	33.334±0.935	40.855±7.546	35.930±6.675	40.209±7.370
2,2-dimethylpropane	0.072±0.006	0.083±0.005	0.066±0.012	0.066±0.014	0.074±0.013	0.071±0.006	0.080±0.004	0.065±0.012	0.065±0.014	0.073±0.013
2-methylpentane	5.814±0.519	4.856±0.345	6.545±1.260	5.893±1.158	5.961±1.121	4.756±0.427	3.923±0.298	5.384±1.038	4.821±0.950	4.895±0.921
3-methylpentane	3.247±0.286	2.774±0.169	3.598±0.688	3.235±0.633	3.381±0.634	2.655±0.235	2.238±0.147	2.960±0.567	2.646±0.519	2.776±0.521
2,2-dimethylbutane	2.051±0.241	1.295±0.232	3.006±0.703	1.628±0.448	2.276±0.426	1.688±0.199	1.060±0.194	2.483±0.582	1.341±0.370	1.869±0.350
2,3-dimethylbutane	2.247±0.183	1.967±0.099	2.231±0.399	2.377±0.425	2.413±0.433	1.834±0.151	1.583±0.087	1.835±0.329	1.937±0.347	1.980±0.356
2-methylhexane	0.625±0.064	0.535±0.034	0.852±0.182	0.504±0.122	0.610±0.128	0.439±0.045	0.370±0.026	0.601±0.129	0.356±0.087	0.430±0.090
3-methylhexane	0.867±0.076	0.811±0.020	1.042±0.209	0.808±0.156	0.808±0.157	0.607±0.054	0.559±0.017	0.735±0.148	0.566±0.110	0.568±0.111
3-ethylpentane	0.036±0.005	0.044±0.005	0.059±0.015	0.022±0.008	0.019±0.007	0.025±0.003	0.030±0.003	0.042±0.011	0.015±0.006	0.013±0.005
2,2-dimethylpentane	0.085±0.008	0.095±0.001	0.092±0.021	0.084±0.017	0.068±0.013	0.059±0.005	0.065±0.001	0.065±0.015	0.059±0.012	0.048±0.009
2,3-dimethylpentane	1.338±0.108	1.474±0.061	0.985±0.171	1.775±0.334	1.118±0.208	0.929±0.075	1.007±0.040	0.693±0.121	1.229±0.230	0.786±0.146
2,4-dimethylpentane	0.844±0.066	0.894±0.036	0.615±0.104	1.075±0.191	0.794±0.145	0.587±0.046	0.612±0.024	0.432±0.073	0.746±0.132	0.558±0.102
3,3-Dimethylpentane	0.066±0.006	0.077±0.001	0.066±0.018	0.066±0.013	0.056±0.010	0.046±0.004	0.053±0.001	0.047±0.013	0.046±0.009	0.039±0.007
2,2,3-Trimethylbutane	0.032±0.002	0.032±0.000	0.031±0.006	0.032±0.006	0.032±0.006	0.022±0.002	0.022±0.000	0.022±0.004	0.022±0.004	0.023±0.004
2-Methylheptane	0.137±0.011	0.142±0.002	0.143±0.028	0.133±0.026	0.130±0.025	0.084±0.007	0.085±0.001	0.088±0.017	0.081±0.016	0.080±0.016
3-methylheptane	0.140±0.012	0.152±0.002	0.151±0.030	0.127±0.025	0.131±0.025	0.086±0.007	0.091±0.001	0.093±0.018	0.078±0.015	0.081±0.016
4-Methylheptane	0.062±0.005	0.066±0.001	0.065±0.012	0.058±0.011	0.060±0.011	0.038±0.003	0.039±0.000	0.040±0.008	0.036±0.007	0.037±0.007
2,2-dimethylhexane	0.014±0.001	0.019±0.001	0.016±0.004	0.011±0.002	0.011±0.002	0.009±0.001	0.011±0.001	0.010±0.002	0.007±0.001	0.007±0.001
2,4-dimethylhexane	0.135±0.010	0.134±0.003	0.125±0.022	0.139±0.024	0.141±0.025	0.082±0.006	0.081±0.001	0.077±0.013	0.085±0.015	0.087±0.015
2,5-dimethylhexane	0.131±0.010	0.128±0.003	0.118±0.020	0.127±0.022	0.151±0.026	0.080±0.006	0.076±0.001	0.073±0.012	0.078±0.013	0.093±0.016
3,3-dimethylhexane	0.014±0.001	0.020±0.001	0.016±0.003	0.010±0.002	0.011±0.002	0.009±0.001	0.012±0.001	0.010±0.002	0.006±0.001	0.007±0.001
2-Me-3-Et-pentane	0.097±0.007	0.097±0.002	0.086±0.015	0.102±0.018	0.105±0.019	0.059±0.005	0.058±0.001	0.053±0.009	0.062±0.011	0.065±0.012
2,2,3-triMe-pentane	0.038±0.003	0.034±0.001	0.033±0.006	0.033±0.006	0.052±0.009	0.023±0.002	0.020±0.001	0.020±0.004	0.020±0.004	0.032±0.006
2,2,4-triMe-pentane	1.287±0.104	1.101±0.042	1.013±0.175	1.465±0.252	1.571±0.280	0.785±0.064	0.658±0.024	0.624±0.108	0.893±0.154	0.967±0.172
2,3,3-triMe-pentane	0.265±0.022	0.240±0.008	0.224±0.039	0.224±0.039	0.371±0.066	0.162±0.013	0.144±0.005	0.138±0.024	0.137±0.024	0.229±0.041
2,3,4-triMe-pentane	0.271±0.022	0.253±0.008	0.222±0.038	0.257±0.044	0.353±0.063	0.165±0.013	0.151±0.005	0.137±0.023	0.157±0.027	0.217±0.039
2,2,5-trimethylhexane	0.106±0.010	0.105±0.005	0.104±0.024	0.078±0.014	0.138±0.027	0.058±0.005	0.056±0.002	0.057±0.013	0.042±0.008	0.075±0.015
2,3,5-trimethylhexane	0.022±0.002	0.023±0.001	0.021±0.004	0.017±0.003	0.027±0.005	0.012±0.001	0.012±0.000	0.011±0.002	0.009±0.002	0.015±0.003
2,4,4-trimethylhexane	0.011±0.001	0.008±0.000	0.008±0.002	0.013±0.003	0.012±0.002	0.006±0.001	0.004±0.000	0.005±0.001	0.007±0.001	0.007±0.001
2,4-dimethylheptane	0.009±0.001	0.011±0.001	0.009±0.002	0.007±0.001	0.008±0.002	0.005±0.000	0.006±0.000	0.005±0.001	0.004±0.001	0.005±0.001
2,6-dimethylheptane	0.015±0.001	0.013±0.000	0.013±0.003	0.018±0.004	0.015±0.003	0.008±0.001	0.007±0.000	0.007±0.001	0.010±0.002	0.008±0.002
3,5-dimethylheptane	0.031±0.002	0.035±0.001	0.028±0.005	0.030±0.006	0.030±0.006	0.017±0.001	0.018±0.001	0.015±0.003	0.016±0.003	0.016±0.003
2,3-dimethylheptane	0.009±0.001	0.010±0.000	0.009±0.002	0.008±0.002	0.010±0.002	0.005±0.000	0.005±0.000	0.005±0.001	0.005±0.001	0.006±0.001

3,4-dimethylheptane	0.005±0.000	0.004±0.000	0.004±0.001	0.005±0.001	0.005±0.001	0.002±0.000	0.002±0.000	0.002±0.000	0.003±0.001	0.003±0.000
3,3-dimethylheptane	0.003±0.000	0.002±0.000	0.002±0.000	0.005±0.001	0.003±0.001	0.002±0.000	0.001±0.000	0.001±0.000	0.003±0.001	0.002±0.000
4,4-dimethylheptane	0.002±0.000	0.002±0.000	0.002±0.000	0.004±0.001	0.002±0.000	0.001±0.000	0.001±0.000	0.001±0.000	0.002±0.000	0.001±0.000
2-methyloctane	0.015±0.001	0.016±0.000	0.014±0.003	0.015±0.003	0.015±0.003	0.008±0.001	0.008±0.000	0.008±0.002	0.008±0.002	0.008±0.002
3-methyloctane	0.018±0.002	0.020±0.001	0.018±0.003	0.018±0.003	0.018±0.004	0.010±0.001	0.011±0.000	0.010±0.002	0.010±0.002	0.010±0.002
4-methyloctane	0.013±0.001	0.014±0.001	0.012±0.002	0.012±0.002	0.012±0.002	0.007±0.001	0.008±0.000	0.007±0.001	0.007±0.001	0.007±0.001
2,2-dimethylheptane	0.002±0.000	0.003±0.000	0.002±0.000	0.001±0.000	0.001±0.000	0.001±0.000	0.002±0.000	0.001±0.000	0.001±0.000	0.001±0.000
2,2,3-trimethylhexane	0.002±0.000	0.004±0.000	0.002±0.001	0.000±0.000	0.001±0.000	0.001±0.000	0.002±0.000	0.001±0.000	0.000±0.000	0.001±0.000
Cyclopentane	1.070±0.084	1.371±0.065	1.056±0.209	0.864±0.177	0.988±0.186	1.044±0.083	1.312±0.057	1.043±0.207	0.850±0.174	0.973±0.183
Methylcyclopentane	2.602±0.216	2.923±0.055	2.669±0.536	2.409±0.477	2.408±0.477	2.119±0.177	2.339±0.036	2.194±0.441	1.967±0.390	1.977±0.391
Ethylcyclopentane	0.095±0.008	0.104±0.003	0.084±0.018	0.099±0.020	0.091±0.019	0.066±0.006	0.071±0.001	0.059±0.012	0.069±0.014	0.064±0.013
1T2-diMecyclopentane	0.279±0.023	0.441±0.036	0.239±0.053	0.219±0.046	0.216±0.044	0.193±0.016	0.300±0.023	0.168±0.037	0.153±0.032	0.152±0.031
1C3-diMecyclopentane	0.228±0.020	0.270±0.011	0.220±0.049	0.215±0.043	0.208±0.042	0.159±0.014	0.185±0.007	0.154±0.034	0.150±0.030	0.146±0.030
1T3-diMecyclopentane	0.268±0.023	0.331±0.015	0.252±0.056	0.251±0.051	0.236±0.048	0.186±0.016	0.226±0.009	0.177±0.039	0.175±0.035	0.166±0.034
Propylcyclopentane	0.002±0.000	0.002±0.000	0.002±0.000	0.003±0.001	0.002±0.000	0.001±0.000	0.001±0.000	0.001±0.000	0.002±0.000	0.001±0.000
112-triMeCyPentane	0.001±0.000	0.001±0.000	0.001±0.000	0.002±0.000	0.001±0.000	0.001±0.000	0.001±0.000	0.001±0.000	0.001±0.000	0.001±0.000
113-triMeCyPentane	0.041±0.003	0.057±0.003	0.031±0.006	0.044±0.009	0.034±0.007	0.025±0.002	0.034±0.002	0.019±0.004	0.027±0.006	0.021±0.004
1C2T3-triMeCyPentane	0.003±0.000	0.004±0.000	0.003±0.001	0.003±0.001	0.003±0.001	0.002±0.000	0.002±0.000	0.002±0.000	0.002±0.000	0.002±0.000
1T2C3-triMeCyPentane	0.034±0.003	0.051±0.004	0.024±0.005	0.036±0.008	0.027±0.005	0.021±0.002	0.030±0.002	0.015±0.003	0.022±0.005	0.016±0.003
1T2C4-triMeCyPentane	0.055±0.005	0.061±0.002	0.044±0.009	0.067±0.014	0.050±0.010	0.034±0.003	0.037±0.001	0.027±0.006	0.041±0.008	0.031±0.006
Cyclohexane	0.747±0.070	0.787±0.031	0.915±0.202	0.567±0.122	0.722±0.148	0.611±0.058	0.632±0.027	0.754±0.167	0.465±0.101	0.593±0.122
Methylcyclohexane	0.468±0.041	0.500±0.009	0.445±0.092	0.486±0.099	0.441±0.089	0.326±0.028	0.343±0.005	0.313±0.065	0.339±0.069	0.310±0.063
Ethylcyclohexane	0.017±0.002	0.011±0.001	0.012±0.003	0.029±0.006	0.018±0.004	0.011±0.001	0.007±0.001	0.007±0.002	0.017±0.004	0.011±0.002
1,1-diMecyclohexane	0.005±0.000	0.006±0.000	0.004±0.001	0.005±0.001	0.004±0.001	0.003±0.000	0.004±0.000	0.003±0.001	0.003±0.001	0.003±0.001
1C2-diMecyclohexane	0.006±0.001	0.004±0.000	0.004±0.001	0.009±0.002	0.006±0.001	0.004±0.000	0.003±0.000	0.003±0.001	0.005±0.001	0.004±0.001
1T2-diMecyclohexane	0.017±0.002	0.015±0.001	0.013±0.003	0.023±0.005	0.016±0.003	0.010±0.001	0.009±0.000	0.008±0.002	0.014±0.003	0.010±0.002
1C3-diMecyclohexane	0.040±0.004	0.033±0.002	0.031±0.007	0.057±0.013	0.037±0.008	0.024±0.002	0.020±0.001	0.019±0.004	0.035±0.008	0.023±0.005
1T3-diMecyclohexane	0.032±0.003	0.024±0.002	0.024±0.005	0.048±0.010	0.032±0.007	0.020±0.002	0.014±0.001	0.015±0.003	0.029±0.006	0.020±0.004
1C4-diMecyclohexane	0.007±0.001	0.006±0.000	0.004±0.001	0.011±0.002	0.006±0.001	0.004±0.000	0.003±0.000	0.003±0.001	0.007±0.001	0.004±0.001
Propylcyclohexane	0.001±0.000	0.001±0.000	0.001±0.000	0.002±0.001	0.001±0.000	0.001±0.000	0.000±0.000	0.001±0.000	0.001±0.000	0.001±0.000
1Me-1EtCyclopentane	0.014±0.001	0.015±0.001	0.010±0.002	0.019±0.004	0.012±0.003	0.009±0.001	0.009±0.000	0.006±0.001	0.012±0.003	0.007±0.002
Benzene	0.506±0.042	0.532±0.012	0.491±0.098	0.544±0.103	0.457±0.091	0.412±0.035	0.426±0.008	0.404±0.081	0.445±0.085	0.375±0.075
Toluene	1.521±0.121	1.878±0.099	1.665±0.328	1.149±0.220	1.393±0.261	1.061±0.085	1.286±0.066	1.174±0.232	0.806±0.155	0.980±0.184
Ethylbenzene	0.097±0.008	0.086±0.003	0.114±0.022	0.088±0.017	0.102±0.019	0.060±0.005	0.052±0.002	0.071±0.014	0.054±0.010	0.062±0.012
o-Xylene	0.104±0.009	0.100±0.001	0.116±0.022	0.094±0.018	0.108±0.020	0.064±0.005	0.060±0.001	0.072±0.014	0.057±0.011	0.066±0.012
m-Xylene	0.289±0.024	0.282±0.005	0.329±0.064	0.248±0.047	0.298±0.056	0.177±0.015	0.169±0.003	0.203±0.040	0.152±0.029	0.183±0.034
p-Xylene	0.073±0.006	0.073±0.001	0.077±0.015	0.067±0.013	0.073±0.014	0.044±0.004	0.044±0.000	0.047±0.009	0.041±0.008	0.045±0.008
Cumene	0.003±0.000	0.003±0.000	0.004±0.001	0.003±0.001	0.003±0.001	0.002±0.000	0.002±0.000	0.002±0.000	0.002±0.000	0.002±0.000
1-Me-2-Et-benzene	0.010±0.001	0.010±0.000	0.012±0.002	0.009±0.002	0.011±0.002	0.006±0.000	0.005±0.000	0.006±0.001	0.005±0.001	0.006±0.001
1-Me-3-Et-benzene	0.035±0.003	0.033±0.000	0.039±0.008	0.032±0.006	0.037±0.007	0.019±0.002	0.018±0.000	0.021±0.004	0.017±0.003	0.020±0.004
1-Me-4-Et-benzene	0.015±0.001	0.014±0.000	0.016±0.003	0.013±0.003	0.015±0.003	0.008±0.001	0.008±0.000	0.009±0.002	0.007±0.001	0.008±0.002
123-triMe-benzene	0.007±0.001	0.007±0.000	0.007±0.001	0.007±0.001	0.007±0.001	0.004±0.000	0.004±0.000	0.004±0.001	0.004±0.001	0.004±0.001
124-TriMe-benzene	0.041±0.003	0.043±0.001	0.042±0.008	0.038±0.007	0.040±0.008	0.022±0.002	0.023±0.000	0.023±0.004	0.020±0.004	0.022±0.004
135-triMe-benzene	0.015±0.001	0.016±0.001	0.016±0.003	0.013±0.002	0.015±0.003	0.008±0.001	0.009±0.000	0.009±0.002	0.007±0.001	0.008±0.002
Propylbenzene	0.012±0.001	0.011±0.000	0.014±0.003	0.012±0.002	0.012±0.002	0.007±0.001	0.006±0.000	0.008±0.001	0.007±0.001	0.007±0.001
1,4-diethylbenzene	0.002±0.000	0.002±0.000	0.003±0.001	0.003±0.000	0.003±0.000	0.001±0.000	0.001±0.000	0.001±0.000	0.001±0.000	0.001±0.000
Ethanol	4.387±0.351	4.363±0.014	4.392±0.810	4.374±0.805	4.421±0.815	10.726±0.863	10.485±0.035	10.831±2.000	10.701±1.973	10.885±2.008

Propene	0.029±0.004	0.031±0.002	0.012±0.004	0.047±0.014	0.025±0.006	0.046±0.006	0.049±0.004	0.020±0.006	0.076±0.022	0.041±0.010
1-butene	0.077±0.010	0.052±0.004	0.048±0.014	0.142±0.033	0.067±0.016	0.094±0.012	0.062±0.005	0.059±0.017	0.173±0.040	0.082±0.019
Cis-2-butene	0.307±0.041	0.192±0.018	0.168±0.051	0.643±0.147	0.227±0.054	0.374±0.050	0.233±0.023	0.206±0.062	0.779±0.176	0.279±0.066
2-methylpropene	0.052±0.007	0.033±0.002	0.033±0.009	0.096±0.023	0.048±0.011	0.063±0.008	0.039±0.003	0.040±0.011	0.116±0.028	0.059±0.013
1-pentene	0.461±0.053	0.271±0.033	0.329±0.100	0.769±0.153	0.475±0.106	0.451±0.052	0.264±0.033	0.324±0.098	0.750±0.149	0.468±0.104
Cis-2-pentene	0.568±0.063	0.335±0.038	0.419±0.108	0.930±0.182	0.589±0.130	0.556±0.061	0.325±0.038	0.412±0.106	0.907±0.177	0.580±0.128
trans-2-pentene	1.118±0.125	0.626±0.075	0.889±0.229	1.718±0.336	1.239±0.281	1.095±0.123	0.609±0.075	0.875±0.226	1.676±0.327	1.219±0.277
2-methyl-1-butene	0.871±0.101	0.484±0.064	0.653±0.187	1.428±0.284	0.920±0.205	0.853±0.098	0.471±0.064	0.642±0.183	1.392±0.276	0.906±0.202
3-methyl-1-butene	0.185±0.024	0.097±0.017	0.147±0.054	0.292±0.060	0.203±0.047	0.181±0.023	0.095±0.017	0.144±0.053	0.284±0.058	0.200±0.047
2-methyl-2-butene	1.959±0.217	1.044±0.121	1.659±0.414	2.939±0.577	2.196±0.485	1.919±0.213	1.014±0.121	1.634±0.407	2.866±0.561	2.163±0.477
1-hexene	0.049±0.005	0.037±0.004	0.032±0.007	0.084±0.016	0.041±0.008	0.040±0.004	0.030±0.003	0.026±0.006	0.068±0.013	0.034±0.006
Cis-2-hexene	0.079±0.007	0.061±0.006	0.056±0.012	0.107±0.020	0.093±0.017	0.065±0.006	0.049±0.005	0.046±0.010	0.087±0.016	0.076±0.014
Trans-2-hexene	0.188±0.018	0.143±0.019	0.148±0.033	0.197±0.037	0.266±0.050	0.154±0.015	0.116±0.016	0.120±0.027	0.161±0.030	0.218±0.041
Cis-3-hexene	0.114±0.010	0.087±0.010	0.083±0.018	0.145±0.027	0.140±0.025	0.093±0.009	0.071±0.008	0.068±0.015	0.118±0.022	0.114±0.021
2-Me-1-pentene	0.111±0.010	0.082±0.009	0.086±0.018	0.143±0.027	0.135±0.024	0.091±0.008	0.067±0.008	0.070±0.015	0.116±0.022	0.110±0.020
4-methyl-1-pentene	0.050±0.005	0.034±0.003	0.037±0.008	0.075±0.014	0.053±0.009	0.041±0.004	0.028±0.003	0.030±0.007	0.061±0.012	0.043±0.008
2-methyl-2-pentene	0.363±0.042	0.273±0.053	0.323±0.083	0.234±0.044	0.624±0.127	0.296±0.034	0.222±0.043	0.263±0.067	0.190±0.036	0.510±0.104
C-3Me-2-pentene	0.082±0.008	0.059±0.006	0.053±0.014	0.138±0.026	0.076±0.016	0.067±0.007	0.048±0.005	0.044±0.011	0.112±0.021	0.062±0.013
T-3Me-2-pentene	0.103±0.012	0.060±0.013	0.061±0.019	0.196±0.037	0.097±0.022	0.084±0.010	0.049±0.011	0.050±0.016	0.159±0.030	0.080±0.018
C-4Me-2-pentene	0.028±0.004	0.018±0.004	0.022±0.008	0.019±0.005	0.053±0.014	0.023±0.003	0.015±0.003	0.018±0.006	0.015±0.004	0.044±0.011
T-4Me-2-pentene	0.235±0.029	0.169±0.037	0.214±0.057	0.123±0.023	0.432±0.091	0.191±0.024	0.138±0.030	0.174±0.046	0.100±0.019	0.354±0.074
2,3-dimethyl-1-butene	0.066±0.006	0.046±0.006	0.053±0.012	0.078±0.015	0.087±0.016	0.054±0.005	0.037±0.005	0.044±0.009	0.063±0.012	0.071±0.013
3,3-dimethylbutene	0.009±0.001	0.006±0.001	0.007±0.002	0.015±0.003	0.008±0.002	0.007±0.001	0.005±0.000	0.005±0.001	0.012±0.002	0.007±0.001
2,3-dimethyl-2-butene	0.047±0.005	0.034±0.005	0.039±0.009	0.045±0.008	0.070±0.013	0.038±0.004	0.028±0.004	0.032±0.007	0.036±0.007	0.057±0.011
C-1,3-pentadiene	0.009±0.001	0.006±0.001	0.007±0.002	0.015±0.003	0.009±0.002	0.009±0.001	0.006±0.001	0.007±0.002	0.014±0.003	0.009±0.002
T-1,3-pentadiene	0.017±0.002	0.010±0.001	0.014±0.004	0.027±0.005	0.019±0.004	0.017±0.002	0.010±0.001	0.013±0.004	0.026±0.005	0.019±0.004
2-Me-1,3-butadiene	0.024±0.003	0.014±0.002	0.020±0.006	0.036±0.007	0.027±0.006	0.024±0.003	0.014±0.002	0.019±0.006	0.035±0.007	0.026±0.006
1-Heptene	0.007±0.001	0.006±0.001	0.004±0.001	0.013±0.003	0.006±0.001	0.005±0.001	0.004±0.001	0.003±0.001	0.009±0.002	0.005±0.001
Trans-2-heptene	0.001±0.000	0.002±0.000	0.000±0.000	0.000±0.000	0.000±0.000	0.000±0.000	0.001±0.000	0.000±0.000	0.000±0.000	0.000±0.000
T3-Heptene	0.010±0.001	0.006±0.001	0.005±0.002	0.020±0.004	0.009±0.002	0.007±0.001	0.004±0.001	0.004±0.001	0.014±0.003	0.006±0.001
C2-Octene	0.002±0.000	0.001±0.000	0.001±0.000	0.002±0.000	0.002±0.000	0.001±0.000	0.001±0.000	0.001±0.000	0.001±0.000	0.002±0.000
Cyclopentene	0.177±0.020	0.109±0.011	0.112±0.028	0.312±0.064	0.174±0.036	0.173±0.019	0.105±0.011	0.110±0.028	0.304±0.062	0.171±0.036

3.4. Evidence for emissions from petroleum operations in California's San Joaquin Valley

In preparation for submission to a peer reviewed journal: D.R. Gentner, T.B. Ford, A. Guha, J. Brioude, W. Angevine, D.R. Blake, R.A. Harley, and A.H. Goldstein

CalNex study topics addressed: *sources of NO_x and VOC, role of VOCs.*

Abstract: Petroleum operations are prominent in the southern San Joaquin Valley and concentrations of many associated hydrocarbons are well above other urban areas. Using a source receptor model with chemical mass balancing of Volatile Organic Compound (VOC) measurements from the CalNex-Bakersfield supersite, we present evidence of a large source of paraffinic hydrocarbons associated with unrefined petroleum gas. We present results for numerous VOCs, including many branched and cyclic alkanes, having limited previous *in situ* measurements and not having been associated with petroleum operations in the past. We used novel statistical modeling with Flexpart (backward air mass trajectory runs using meteorological data and ground-based air quality data to assess the spatial distribution of emissions in the southern San Joaquin Valley. The results are consistent with aircraft measurements of propane and the locations of oil wells. Methane emissions associated with the petroleum gas are not significant despite very good agreement of other hydrocarbons associated with the unrefined natural gas composition as measured at wells by the U.S. Geological Survey. These results suggest that the emissions are predominantly from condensate storage tanks containing the non-methane liquids separated from the associated gas. The abundance of non-methane hydrocarbons due to petroleum gas was 82 ± 74% of emissions from motor vehicles by carbon mass in Bakersfield, and ranged widely 30-150% depending on meterology and time of day. The non-methane hydrocarbon emissions from the petroleum gas source are an important source of hydrocarbon mass in the region and, given a calculated normalized reactivity of 0.67 $gO_3\ g^{-1}$, may have a minor effect on atmospheric chemistry. A rough comparison with the California Air Resources Board emission inventory validates the relative emissions of reactive organic gases compared to motor vehicles in the San Joaquin Valley and Kern County, specifically, where the CalNex-SJV site was located.

3.4.1. Introduction

California's San Joaquin Valley is an important region for oil and natural gas production in the United States. Operations include extraction, storage, transport, and processing; all of which may have varying degrees of fugitive emissions of methane and other gas-phase organic carbon, such as Volatile Organic Compounds (VOCs) (1, 2). Crude oil and unrefined natural gas are composed of a broad suite of organic compounds that span a range of vapor pressures, and are either produced by thermogenic or biogenic processes (3). Thermogenic gas is produced via the cracking of larger compounds in oil and can either be termed associated or non-associated depending on the presence of oil (3). The vast majority of wells in the San Joaquin Valley are oil wells and most have associated gas, also known as wet thermogenic gas (3). Thermogenic wet gas is predominately found in oil wells as the gas is geochemically produced from the cracking of larger molecules in oil, and thus contains substantial amounts of non-methane hydrocarbons ranging from 3 to 40% C_2 and greater content (Table 3.4.1) (3). Crude oil production in Kern

County within the San Joaquin Valley is 450,000 barrels day^{-1}, which represents 69% of production within California and 8% of national production (4, 5).

Previous studies in the urban area of Houston, a prominent region for petroleum imports and refining have reported considerable emissions attributed to oil/gas operations and petrochemical production of other chemicals (1, 2). One evident source, termed oil/natural gas evaporation from refineries, was comprised of C_{2-7} straight and branched alkanes, as well as cyclopentane, cyclohexane, and methylcyclopentane. In one study, this source accounted for 27% of observed VOC mass at the urban site outside of the Houston shipping channel, and ranged from 10-40 ppbC diurnally (1).

The objective of this analysis was to examine the existence and magnitude of hydrocarbon emissions from petroleum operations in the San Joaquin Valley. This is accomplished using multiple VOC data sets and novel methods to assess the spatial distribution of sources (i.e., a statistical source footprint) via meteorological modeling. We also examined the potential of petroleum operation emissions to impact air quality relative to motor vehicle emissions, and compare my results to the California Air Resources Board (CARB) emission inventory.

3.4.2. Materials and methods

Using six weeks of VOC data collected in Bakersfield, CA as part of the CalNex (California at the Nexus of Air Quality and Climate Change) campaign, we assessed emissions from petroleum operations during Summer 2010. The magnitude of petroleum gas observed at the site was determined using source receptor modeling with chemical mass balancing; details on these methods and data collection have been described previously (Section 3.3). *A priori* source profile information for the model was constructed using U.S. Geological Survey data on associated thermogenic natural gas composition from wells in the San Joaquin Valley (Table 3.4.1) (3). The compounds used in the over-constrained model were propane, n-butane, n-pentane, iso-pentane, m/p-xylene, o-xylene, isooctane, n-nonane, n-undecane, n-dodecane to model motor vehicle and petroleum gas sources. Propane and n-butane were corrected for background values of 500 and 100 pptv, respectively. Standard errors were used as uncertainties in the model for the petroleum gas source as their standard deviations were ±80-300%, given the variability between wells and sampling methods in the data complied by the U.S.G.S. This was an order of magnitude greater than motor vehicle source profiles and would have otherwise been insufficient to constrain the petroleum source, so standard errors were used in this case to model the petroleum gas source.

Emissions of additional compounds from petroleum operations are inferred from an array of hydrocarbons not present in the initial limited petroleum gas profile that episodically exceed predicted concentrations from gasoline and diesel vehicles based on coincident fuel data from Bakersfield (Chapter 4). The residuals, or excess concentrations beyond contributions from motor vehicles, were filtered for values that exceed the uncertainties of model calculations, which are determined in part by the 10-20% variability in fuels. Measurements of a few light VOCs not measured *in situ* are included from canister measurements to further characterize the observed sources. Canisters were taken as 3-hour averages in the morning (5-8 PST) and analyzed via U.S. EPA methods for an array of organic compounds. Supporting methane measurements were made using integrated cavity output spectroscopy (Los Gatos Research, Fast

Greenhouse Gas Analyzer) with 1-min time resolution. OH reactivities and ozone formation potentials are examined using literature OH reaction constants, and Maximum Incremental Reactivities (MIRs) (6, 7).

The spatial distribution of emissions is examined via two methods, using canister samples taken on NOAA's P3 aircraft and using ground measurements from the CalNex-SJV site coupled with meteorological modeling to assess the ground-level footprint of each 30-minute sample over the previous 6-12 hours. We generated back-trajectory footprints for each hourly sample using the Flexpart Lagrangian dispersion meteorological modeling package (Figure 3.4.1). Here, we present the first integration of this meteorological modeling method with statistical back-trajectory analysis to explore the distribution and relative magnitude of VOC sources at ground level. We contend that this method is superior to using single back trajectories (i.e., HYSPLIT), which do not directly inform the residence time of an air parcel at ground level or the distribution of residence time along a back trajectory or a collection of back trajectories during a campaign.

We generated 6- and 12-hour back-trajectory footprints with 4 km resolution for each hourly sample using the FLEXPART Lagrangian dispersion meteorological modeling package developed by the NOAA Earth Sciences Research Laboratory. Simulations were initiated from the top of the 18 m tower and further details of FLEXPART modeling can be found elsewhere (8, 9). We present the first integration of this meteorological modeling method with statistical back-trajectory analysis to explore the distribution of VOC sources and their surface level contribution. We contend that our method is superior to using HYSPLIT single back trajectories, which do not directly inform the residence time of an air parcel at ground level. Utilizing concentration weighted trajectory analysis allows us to find the average concentration of a compound in a cell, $\overline{C_{ij}}$:

$$\overline{C_{ij}} = \frac{1}{\sum_0^t (\tau_{ijt})} \sum_0^t (c_{ijt} \cdot \tau_{ijt}) \qquad (1)$$

where τ_{ij} is the time the trajectory spends at ground level (<100 m) in the ijth cell and c_{ij} is the concentration of a compound in each trajectory. Each cell has a corresponding n_{ij} value, the number of t_{ij} values contributing to a cell (10). To correct for the exaggerated contributions of low n_{ij} values, a weighting function multiplies $\overline{C_{ij}}$ with n_{ij} values above the Q_{90}, Q_{75}, Q_{50} and below the Q_{50} percentiles by 1, 0.7, 0.4, and 0.05 respectively (11). Contour maps were then plotted using these final $\overline{C_{ij}}$ values and appended on top of a 1 arc second elevation map obtained from the USGS National Map Seamless Server.

3.4.3. Results and discussion

The reported non-methane composition of thermogenic wet gas (Table 3.4.1) accurately represented the observed petroleum gas source. The composition of the natural gas has substantial variability among all the wells sampled, but is consistent with atmospheric observations using both *in situ* and canister data at Bakersfield. The relative ratios of hydrocarbons in our *in situ* data, the canister data, and the thermogenic wet gas profile data are compared to strengthen the argument for petroleum gas as the observed source. Additionally, the ratios are also compared to a similar petroleum source factor from one of the Houston studies (1). The ethane to propane ratio expected from the thermogenic wet wells in the San Joaquin

Valley is 1.2 in terms of mass carbon, which is similar to canister measurements at the Bakersfield site (1.4) (Figure 3.4.2), and also to measurements in Houston (1.0). Propane to n-butane ratios are all similar with 2.9, 3.0, 2.2 and 2.0 in the oil well data, in Houston, and at Bakersfield in canister and *in situ* data, respectively. Ratios of n-butane to isobutane also support the conclusion of a petroleum gas source as they are 1.7, 2.9, and 2.0 in the oil well, in Houston, and in canister measurements from Bakersfield. Comparisons of these ratios have considerable uncertainty when considering the variability among oil/gas wells within a region and compared to other regions.

The 25th percentiles for propane and n-butane are similar to other urban ground sites during the summer, but higher concentrations were observed for the 50th and 75th percentiles, by up to a factor of 2 compared to Pittsburgh, PA (2002) (12). The 75th percentiles in the San Joaquin Valley are even higher by 25-50% than values from Riverside, CA, a much more populated region, in summer 2005 (data from Chapter 3).

The over-constrained chemical mass balance model used in Chapter 4 effectively modeled emissions of most compounds in the tunnel study and many of the compounds that are most prevalent in gasoline and diesel at Bakersfield. Yet, in addition to the compounds known to be in natural gas, the model under-predicted numerous alkanes. These compounds are summarized in Table 3.4.2 and Figure 3.4.3, which shows their average unexplained concentrations and the percent of total mass that is unexplained as determined by the residuals in the source receptor model. Most of the mass of unexplained alkanes was well correlated ($r \geq 0.75$) with the petroleum gas signal, so it is attributed to this source (Figures 3.4.3C-D & Figures 3.4.4). The presence of the branched and cyclic alkanes in unrefined petroleum gas is not surprising as there are significant amounts of C_{5-7} straight chain alkanes in the reported composition (Table 3.4.1). Many of these compounds are reported here as *in-situ* measurements for the first time, especially many of the cyclic alkanes.

We assessed our model output to check for contributions from products of incomplete combustion. The only considerable impact was from cyclopentane as emissions in the Caldecott tunnel were higher than expected based on the abundance of cyclopentane in liquid gasoline. We determined that emissions of cyclopentane in gasoline exhaust due to formation from other precursors in the fuel were equivalent to those from cyclopentane present in unburned fuel, such that doubling the emission factor of cyclopentane accurately modeled emission in the on-road tunnel study. A similar, but larger increase is known for benzene (13). We did not observe any significant emission enhancement for cyclohexane.

The additional compounds attributed to the petroleum gas source profile increase the mass of emissions by 10% as shown by the regression of the correlated unexplained compounds with the petroleum gas source ($r=0.95$) (Figure 3.4.6). The weight fraction of each correlated compound in the "unexplained" mass is shown in Table 3.4.2 with similar fractions in the overall source profile as the known C_{5-7} compounds in petroleum gas. Using this new source profile, the ozone forming potential is calculated to be 0.67 $gO_3\ g^{-1}$ with the new compounds increasing the reactivity from 0.58 $gO_3\ g^{-1}$. In all, the interquartile range of the unrefined natural gas source contribution was 8.3-90 ppbC (Table 3.4.3), with a diurnal pattern that was strongly dependent on meteorological dilution (Figure 3.4.5). The mass concentration of compounds from unrefined

natural gas ranged from 30-40% to 100-150% of the sum of compounds from motor vehicles during the afternoon and nighttime, respectively (Figure 3.4.7).

The remaining branched and cyclic compounds that were not highly correlated with the petroleum gas source represent a relatively small amount of mass and a source could not be inferred for these compounds. The excess C_{13-16} branched alkanes were well-correlated ($r \geq 0.80$) with each other, but not with any of the other compounds. The excess concentrations of C_{10-11} branched alkanes are correlated with each other, and one of the compounds, 2,6-dimethyloctane, is well-correlated ($r \geq 0.80$) with the three C_9 cycloalkanes that do not correlate well with the petroleum gas source. These remaining compounds have ozone formation potentials similar to other observed compounds, ranging from 0.6 to 1.6 $gO_3\ g^{-1}$, but their excess concentrations after modeling were minimal—average values from 0 to 0.15 ppbC (Figure 3.4.3).

Using Flexpart and the meteorological data for the region, distributions of back-trajectories were calculated for 6 and 12 hours prior to arrival and measurement at the Bakersfield site. Overall averages, as well as day and nighttime averages are shown for the entire campaign in Figure 3.4.1. At all times, the influence of local emissions near the site is important. Daytime measurements are largely impacted by the north-northwest winds (direction from which the wind blows) due to consistent up-valley flows during the day. In contrast, at night the wind speeds and direction are more variable and irregular with flows that arrive from all directions, but originate from up-valley flows from the north-northwest. Extensive reviews of meteorology and flow patterns in the San Joaquin Valley found elsewhere are consistent with the results presented in this work (14, 15). Statistical meteorological modeling using ground site data resulted in a spatial distribution of petroleum gas emissions similar to that of oil wells in the southern San Joaquin Valley (Figure 3.4.8). Additionally, canister samples taken via aircraft in the region show higher propane (a major component of the source profile) concentrations for some points in the southern part of the valley (Figure 3.4.8C). Given the co-location of oil wells in the region and the spatial distribution of elevated concentrations of petroleum gas compounds, it is very likely that emissions occur at or near the wells during extraction/storage in addition to other potential emissions in downstream operations.

Observations of methane and the petroleum gas source are not well correlated (Figure 3.4.9) and the potential methane emissions expected from the thermogenic wet gas source profile would be equivalent to all of the methane enhancements above background concentrations. However, since non-methane compound ratios and chemical mass balance modeling agreed well with source profile for petroleum gas extracted in the region, We are confident that the source originates from unrefined petroleum gas, but excludes the methane. Our observation of a major petroleum gas source with minimal coincident methane is consistent with measurements of emissions from condensate tanks, which contain the separated non-methane liquids and have been shown in two Texas-based studies to be dominated by non-methane hydrocarbons (16, 17). The studies demonstrated that condensate tanks emit 4-6 times more VOCs than methane whereas all other emission pathways emit 3-15 times more methane than VOCs, and methane was on average only 15±11 wt% of 20 vent gas samples from condensate tanks (16, 17).

A comparison of methane to non-vehicular ethanol (calculated via the CMB model) supports this claim that methane emissions from the petroleum source are relatively minor in the San Joaquin

Valley as the two compounds are well correlated with no major methane spikes above the ratio inferred from the regression (Figure 3.4.10). Additionally, coloring the points by the petroleum gas factor showed no pattern towards higher ratios of methane to non-vehicular ethanol (not shown). Additional ethanol contributions are evident and have the strongest coincidence with high concentrations of chloroform. Carbon disulfide and ethanethiol (not shown) also show a similar trend as chloroform, but for different points that diverge from the line in Figure 3.4.10. Thus, it is evident that emissions of methane are dominated by the same source as non-vehicular ethanol and are relatively minor from the petroleum gas source. The reason methane is not co-emitted with other compounds in this source profile is because of the minor concentrations of methane in condensate storage tanks. Further work underway by CARB focused on quantifying emissions from these tanks will further constrain the source and strengthen the case for control through either vapor recovery systems or vent flares (18).

On a mass basis, emissions of petroleum gas are important at the Bakersfield site as observed concentrations of petroleum gas were 30-40% of that from motor vehicles during the day and 100-150% at night. Yet, they represent a relatively minor contribution to potential ozone formation, as the MIR value is 3-5 times less than that of gasoline sources. Secondary organic aerosol (SOA) formation from petroleum sources is likely to be minimal given that the yields for all of the alkanes with 8 or less carbon atoms is at most 0.002 gSOA g^{-1}, with an organic particle loading of 10 μg m^{-3} (Section 3.3). The CARB emissions inventory for the San Joaquin Valley reports an average of 35 tons ROG per day, which is equal to 28% of mobile source emissions in the air basin (19). This value is roughly consistent with the daytime ratio observed at the Bakersfield site, but is expectedly lower than nighttime ratios as Bakersfield is in much closer proximity to potential sources than most other portions of the air basin. A comparison on a smaller scale for the portion of Kern County in the San Joaquin Valley supports this as the CARB inventory has petroleum operations emitting 132% that of mobile sources with much of the San Joaquin Valley's petroleum operation emission in this county (19). This observation is consistent with the statistical footprints shown in this work as daytime footprints encompass a larger footprint that stretches into other counties while nighttime footprints are more heavily influenced by local emissions. This intercomparison, while rough, provides some validation of the CARB emission inventory for petroleum operations in the San Joaquin Valley.

References for Gentner et al., in preparation:

1. Leucher M. and Rappengluck B. (2010) VOC source-receptor relationships in Houston during TexAQS-II, *Atmos. Envron.*, 44, 4056-4067.
2. Buzcu B. and Fraser M.P. (2006) Source identification and apportionment of volatile organic compounds in Houston, TX, *Atmos. Envron.*, 40, 2385-2400.
3. U.S. Geological Survey, Petroleum Systems of the San Joaquin Basin Province—Geochemical Characteristics of Gas Types by P.G. Lillis, A. Warden, G.E. Claypool, and L.B. Magoon, Chapter 10 in "Petroleum Systems and Geologic Assessment of Oil and Gas in the San Joaquin Basin Province, California" A.H. Scheirer ed., 2007 (http://pubs.usgs.gov/pp/pp1713/).
4. U.S. Energy Information Administration, *U.S. Crude Oil Production by State, 2004.* (http://www.eia.gov/dnav/pet/PET_CRD_CRPDN_ADC_MBBLPD_A.htm).
5. California Energy Commission, *California Crude Oil Production and Imports, 2006,* by M. Sheridan. (http://www.energy.ca.gov/2006publications/CEC-600-2006-006/CEC-600-2006-006.PDF).
6. Carter, W. P. L.: SAPRC Atmospheric Chemical Mechanisms and VOC Reactivity Scales (available at: http://www.engr.ucr.edu/~carter/SAPRC/)

7. Atkinson, R. and Arey, J. (2003) Atmospheric degradation of volatile organic compounds, *Chem. Rev.*, 103, 4605-4638.
8. Brioude, J., W.M. Angevine, S.A. McKeen, and E.Y. Hsie (2012) Numerical uncertainty at mesoscale in a Lagrangian model in complex terrain, *Geosci. Model Dev. Discuss.*, 5, 967–991, doi:10.5194/gmdd-5-967-2012.
9. Metcalf, A.R., J.S. Craven, J.J. Ensberg et al. (2012) Black carbon aerosol over the Los Angeles Basin during CalNex, *J. Geophys. Res.*, 117, D00V13, doi: 10.1029/2011JD017255.
10. Seibert, P., H. Kromp-Kolb, U. Baltensperger et al. (1994) Trajectory analysis of aerosol measurements at high alpine sites. In: B.P. M., B. P., C. T. and S. W. (Editors), Transport and Transformation of Pollutants in the Troposphere. Academic Publishing, Den Haag, pp. 689-693, 1994.
11. Polissar, A.V., P.K. Hopke and J.M. Harris (2001) Source regions for atmospheric aerosol measured at Barrow, Alaska, *Environ. Sci. Technol*., 35:4214-4226.
12. Millet DB *et al.* (2005) Atmospheric volatile organic compound measurements during the Pittsburgh Air Quality Study: Results, interpretations, and quantification of primary and secondary contributions. *J. Geophys. Res.* 110:D07S07.
13. Leppard WR *et al.* (1992) Effects of gasoline composition on vehicle engineout and tailpipe hydrocarbon emissions. *SAE Tech. Pap. Ser.* No. 920329.
14. Bao J.W. *et al*. (2007) Observed and simulated low-level winds in a high ozone episode during the central California ozone study, *J. Applied Met. & Climate.*, 47, 2372-2394.
15. Beaver S. and Palazoglu A. (2009) Influence of synoptic and mesoscale meteorology on ozone pollution potential for San Joaquin Valley of California, *Atmos. Envron.*, 43, 1779-1788.
16. Armendariz A., "Emissions from Natural Gas Production in the Barnett Shale Area and Opportunities for Cost-Effective Improvements," Jan. 26, 2009. (http://www.edf.org/sites/default/files/9235_Barnett_Shale_Report.pdf) Accessed Oct. 2012.
17. Hendler A., Nunn J., Lundeen J., McKaskle R. "VOC Emissions from Oil and Condensate Storage Tanks – Final Report," a report prepared for the Houston Advanced Research Center. October 31, 2006. (http://files.harc.edu/Projects/AirQuality/Projects/H051C/H051CFinalReport.pdf) Accessed Oct. 2012.
18. California Air Resources Board, "Determination of Methane, Carbon Dioxide, and Volatile Organic Compounds from Crude Oil and Natural Gas Separation and Storage Tank Systems," June, 2012 Draft. (http://www.arb.ca.gov/cc/oil-gas/flash_protocol_dec29.pdf) Accessed Oct. 2012.
19. California Air Resources Board, *Estimated annual average emissions, 2010*. (http://www.arb.ca.gov/ei/emsmain/emsmain.htm) Accessed May 2012.

Tables and Figures

Table 3.4.1. *Unrefined natural gas profile for thermogenic wet wells in the San Joaquin Valley from U.S.G.S. samples (N=49 wells).*

	wtC%	Std. Dev.	k_{OH}	MIR
Methane	82.3	9.2	0.0064	0.014
Ethane	5.33	3.46	0.248	0.28
Propane	4.42	3.50	1.09	0.49
isobutane	0.920	0.837	2.12	1.23
n-butane	1.55	2.17	2.36	1.15
isopentane	0.223	0.401	3.60	1.45
n-pentane	0.273	0.405	3.80	1.31
neo-pentane	0.061	0.182	0.825	0.67
n-hexane	0.105	0.108	5.20	1.24
n-heptane	0.049	0.041	6.76	1.07

Notes: k_{OH} is in $cm^3\ s^{-1}$ $molecules^{-1} \times 10^{12}$ and are from Ref. 7
MIR is in $gO_3\ g^{-1}$ and are from Ref. 6

Table 3.4.2. *Interquartile ranges and MIRs for alkanes discussed in this work*

Compound Name	# in Fig. 3.4.3	Interquartile Range [pptv]	WtC% of Unexplained Mass	MIR [$gO_3\ g^{-1}$]
Propane	-	1133 - 5602		0.49
n-butane	-	230 - 6397		1.15
n-pentane	-	221 - 2127		1.31
2-2-dimethylbutane	1	28.0 - 76.6		1.17
2-methylpentane & 2,3-dimethylbutane	2	121.6 - 501.0	9.02	1.2
3-methylpentane	3	50.1 - 253.9	7.41	1.80
2,4- & 2,2-dimethylpentane	4	13.7 - 54.7		1.3
3,3-dimethylpentane	5	4.0 - 16.6		1.20
2,3-dimethylpentane	6	19.7 - 93.0		1.34
2-methylhexane	7	23.2 - 90.3	2.76	1.19
3-methylhexane	8	28.0 - 124.6	3.48	1.61
2,2-dimethylhexane	9	1.0 - 4.0		1.02
2,5-dimethylhexane	10	6.2 - 35.8	1.50	1.46
2,4-dimethylhexane	11	7.4 - 32.0	0.88	1.73
2,2,3-trimethylpentane	12	2.7 - 12.1		1.22
iso-octane	13	39.1 - 115.3		1.26
2,3,4-trimethylpentane & ctc-1,2,3-trimethylcyclopentane	14	31.6 - 160.2	7.57	1.3
2,3,3-trimethylpentane & 2,3-dimethylhexane	15	11.3 - 32.8		1.1
2-methylheptane	16	10.2 - 48.8	1.34	1.07
4-methylheptane	17	4.3 - 20.7		1.25
3-methylheptane	18	9.3 - 43.6	1.84	1.24
2,2,5-trimethylhexane	19	5.4 - 16.3		1.13
2,6-dimethylheptane	20	5.4 - 30.7	1.91	1.04
3,5-dimetylheptane	21	2.2 - 10.3		1.56
2,3-dimethylheptane	22	0.9 - 4.7		1.09
2- & 4-methyloctane	23	2.9 - 12.7		0.9
3-methyloctane & 4-ethylheptane	24	3.1 - 12.9		1.1
2,2,5-trimethylheptane	25	0.7 - 1.7		1.26
2,2,4-trimethylheptane	26	0.8 - 2.6		1.16
C10 branched alkanes (5 unknown isomers)	27	3.0 - 11.5		0.94
2,6-dimethyloctane	28	0.7 - 3.2		1.08
2- & 3- & 4-methylnonane & 3- & 4-ethyloctane & 2,3-dimetyloctane	29	6.9 - 24.6		0.94
C11 branched alkanes (3 unknown isomers)	30	0.7 - 2.6		0.73
C11 branched alkanes (10	31	5.4 - 17.5		0.73

unknown isomers)						
dimethylundecane isomer #1	32	0.8	-	3.3		0.6
dimethylundecane isomer #2	33	0.8	-	2.6		0.6
C13 branched alkanes (2 unknown isomers)	34	2.3	-	5.8		0.6
C14 branched alkanes (6 unknown isomers)	35	4.4	-	11.3		0.55
C16 branched alkane (unknown)	36	1.3	-	3.1		0.47
Cyclopentane	37	36.7	-	164.5	4.04	2.39
Methylcyclopentane	38	57.4	-	315.3	8.86	2.19
cis-1,3-dimethylcyclopentane	39	14.8	-	100.1	5.23	1.94
trans-1,3-dimethylcyclopentane	40	16.4	-	177.7	7.86	1.94
Ethylcyclopentane	41	7.9	-	44.4	1.93	2.01
ctc-1,2,4-trimethylcyclopentane	42	5.4	-	52.2	4.19	1.53
ctt-1,2,4-trimethylcyclopentane	43	1.7	-	15.5	1.32	1.53
Unknown methylethylcyclopentane	44	0.7	-	4.3		1.6
iso-propylcyclopentane	45	1.1	-	5.9	0.35	1.69
n-propylcyclopentane	46	2.1	-	10.0	0.58	1.69
Cyclohexane	47	27.5	-	154.0	6.22	1.25
Methylcyclohexane	48	20.4	-	147.0	7.30	1.70
cis-1,3- & 1,1-dimethylcyclohexane	49	4.6	-	38.4	3.02	1.4
trans-1,2-dimethylcyclohexane	50	4.6	-	42.4	3.37	1.41
trans-1,3-dimethylcyclohexane	51	2.9	-	17.8	0.95	1.52
cis-1,2-dimethylcyclohexane	52	1.9	-	9.8	0.52	1.41
Ethylcyclohexane	53	4.8	-	31.9	2.36	1.47
ccc-1,3,5-trimethylcyclohexane	54	1.0	-	6.6		1.15
1,1,3-trimethylcyclohexane	55	2.0	-	20.4	2.32	1.19
1,1,4-trimethylcyclohexane	56	1.1	-	8.8		1.2
ctt-1,2,4- & cct-1,3,5-trimethylcyclohexane	57	0.7	-	3.9		1.2
ctc-1,2,4-trimethylcyclohexane	58	1.2	-	9.6		1.2
1,1,2-trimethylcyclohexane and isobutylcyclopentane	59	0.7	-	2.0		1.3
methylethylcyclohexane isomer #1	60	0.8	-	4.5	0.32	1.4
methylethylcyclohexane	61	0.7	-	3.7	0.28	1.4

isomer #2						
iso-propylcyclohexane	62	0.9	-	5.2		1.3
n-propylcyclohexane	63	2.9	-	15.5		1.29
unidentified C10 cyclohexane	64	2.5	-	7.8		1.07
unidentified C10 cyclohexanes	65	0.7	-	2.7		1.07
unidentified C9 cycloalkane	66	1.2	-	11.0	1.26	1.36

Table 3.4.3. *Quartiles [ppbC] for ambient concentrations of VOCs from major petroleum-based sources measured at the Bakersfield site*

	Q_{25}	Q_{50}	Q_{75}
Gasoline Exhaust	8.2	13.9	23.1
Diesel Exhaust	11.0	20.6	39.9
Non-tailpipe Gasoline	4.2	8.4	20.4
Petroleum Gas Source (ROG)	8.2	20.2	89.8

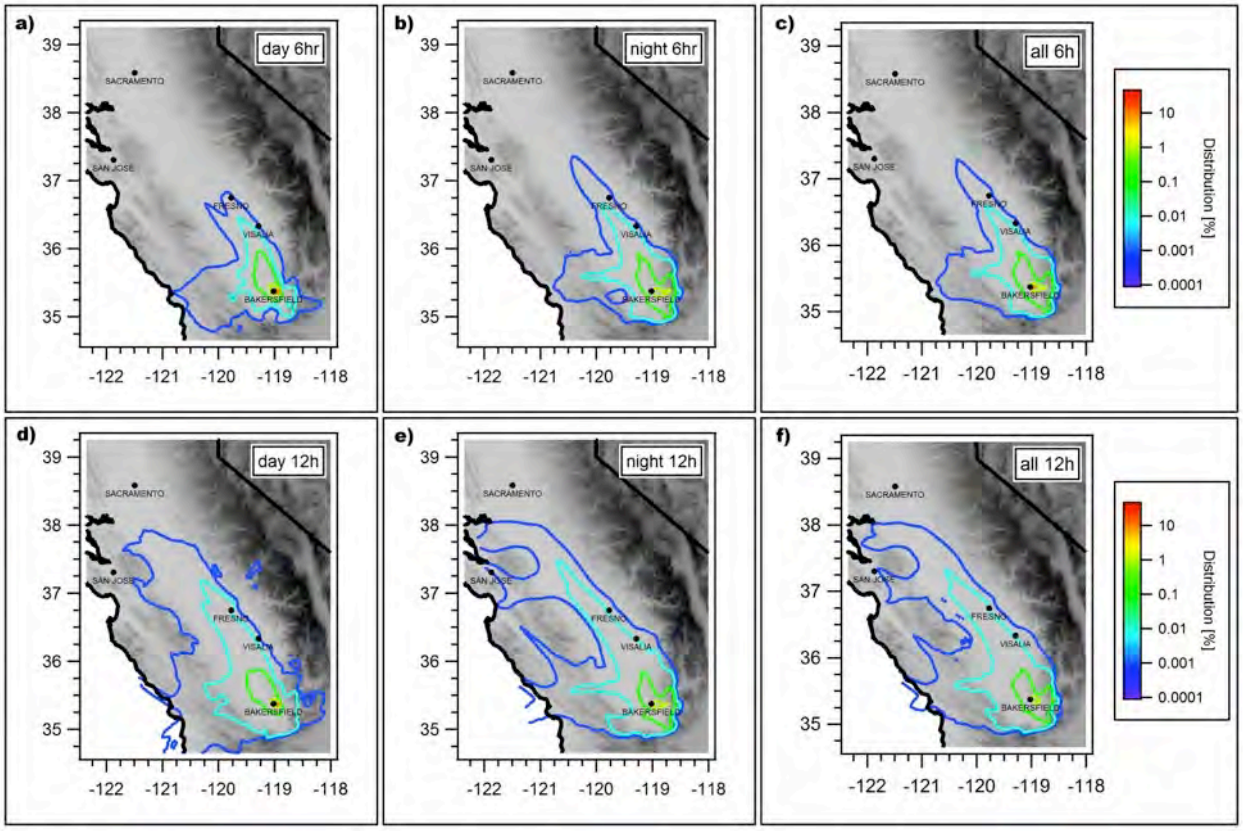

Figure 3.4.1. *6 and 12 hour statistical VOC footprints for the Bakersfield ground site averaged across the entire CalNex campaign. Day* ***(a, d)*** *and nighttime* ***(b, e)*** *averages are filtered for 08:00-20:00 PST and 21:00-06:00 PST, respectively, and are shown with overall averages* ***(c, f)****.*

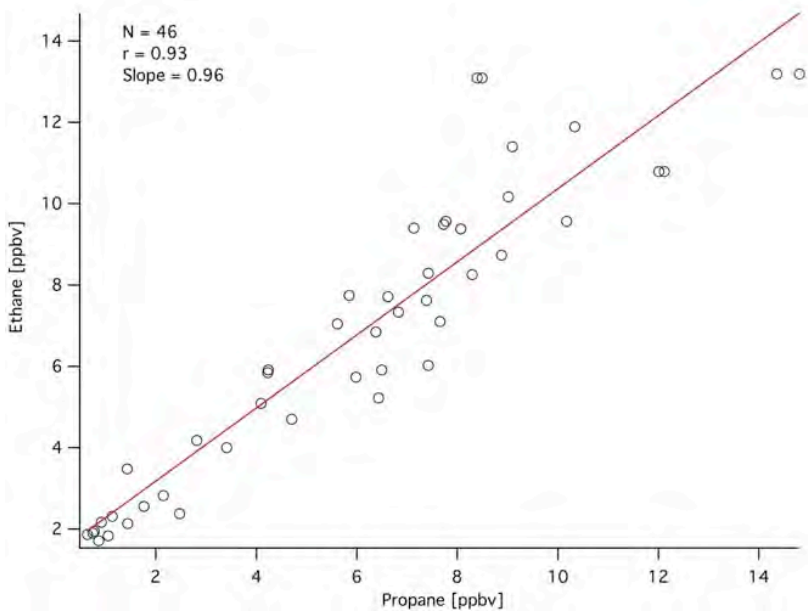

Figure 3.4.2. *Observations of ethane vs. propane using canister measurements (5-8 PST) are well correlated with a ratio similar to that expected based on the petroleum gas source profile.*

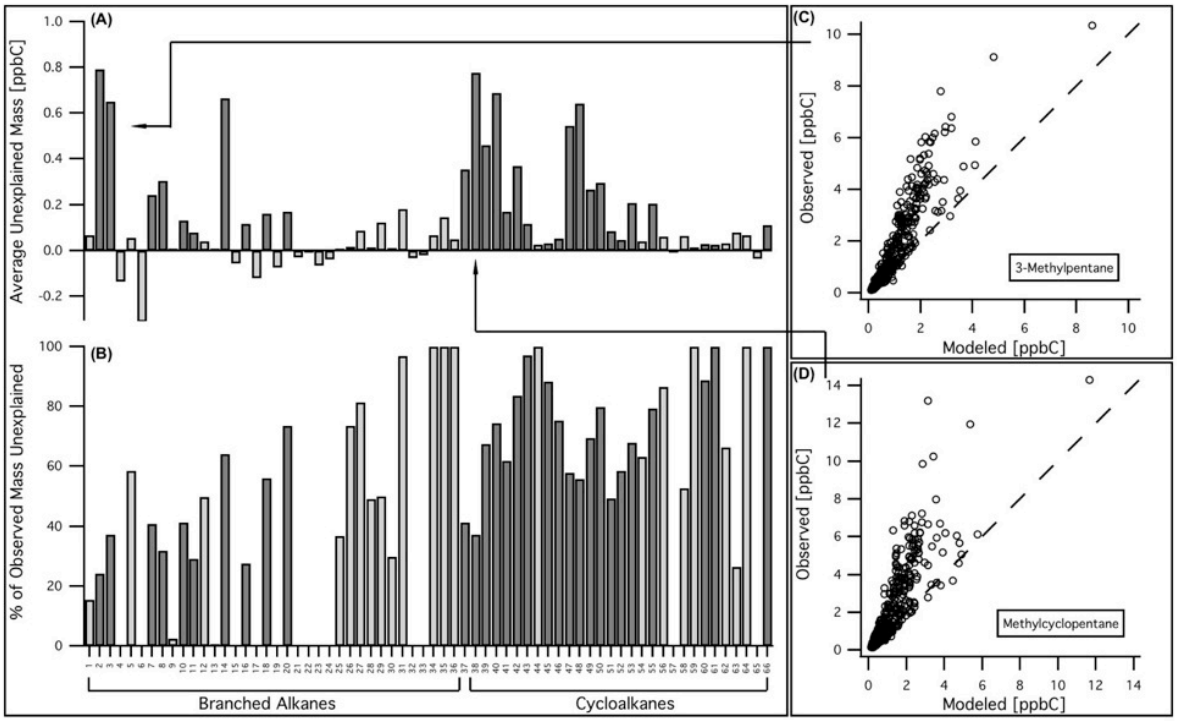

Figure 3.4.3. *Many branched and cyclic alkanes exceeded predicted concentrations based on source profiles for motor vehicles.* ***(A-B)*** *The average unexplained concentration of each compound and the percentage of unexplained mass out of total observations. Compounds that are well-correlated (r≥0.75) with the petroleum gas source are shown with shaded bars. A few compounds have negative residuals.* ***(C-D)*** *Examples of exceedances of observed over-predicted values are shown with a 1:1 line.*

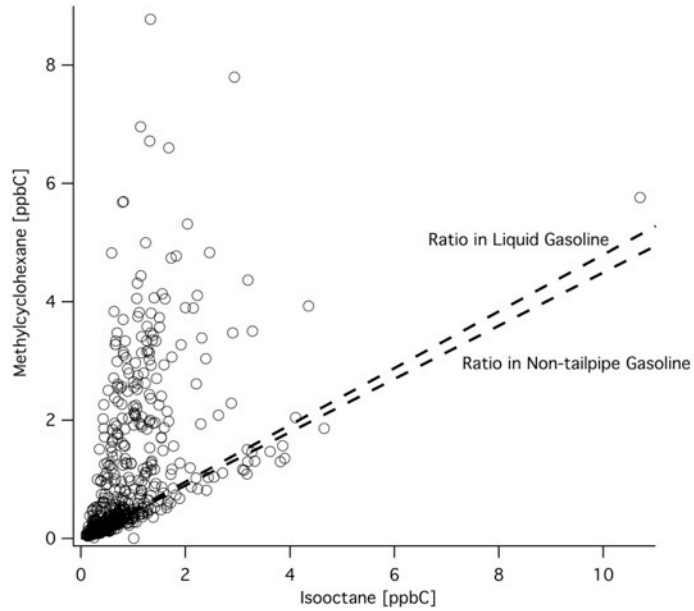

Figure 3.4.7. *Comparison of methylcyclohexane and isooctane at the Bakersfield ground site. Isooctane is a prevalent tracer for gasoline emissions and its ratios to methylcyclohexane are roughly equivalent for exhaust and non-tailpipe emissions. Many points agree with these ratios, but numerous points have considerably more methylcyclohexane than expected. This result is similar for many other compounds whose observed values are episodically greater than predicted from gasoline and diesel sources.*

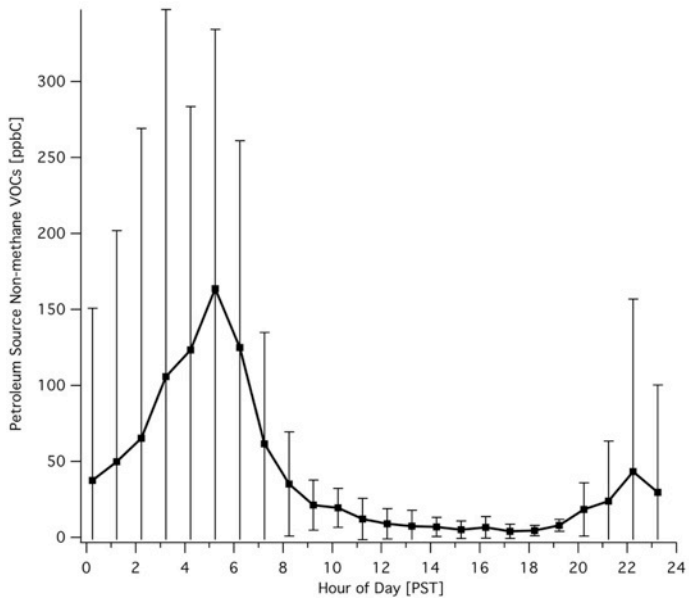

Figure 3.4.5. *Average diurnal pattern for the petroleum gas source contribution (before "unexplained" mass is added.*

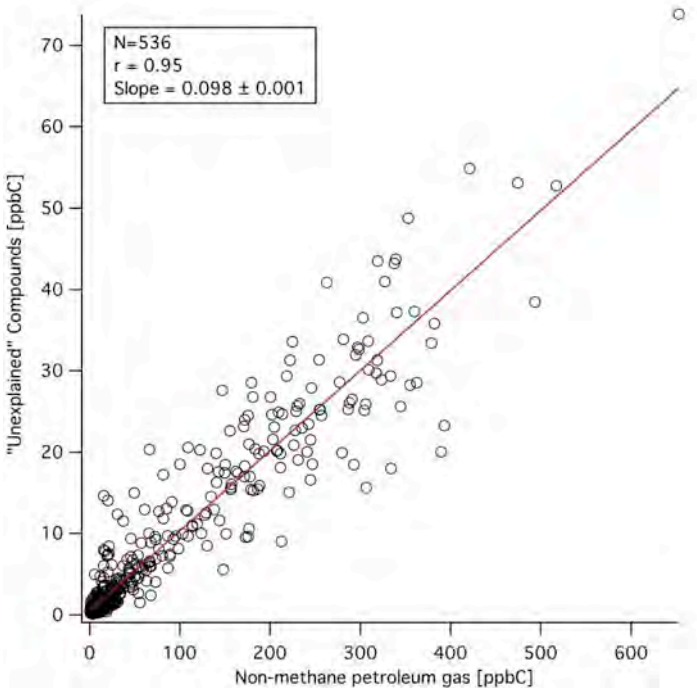

Figure 3.4.6. *The sum of unexplained compounds that were correlated with the petroleum gas source is very well correlated with a slope of 0.098 increasing emissions by 10% from the original profile.*

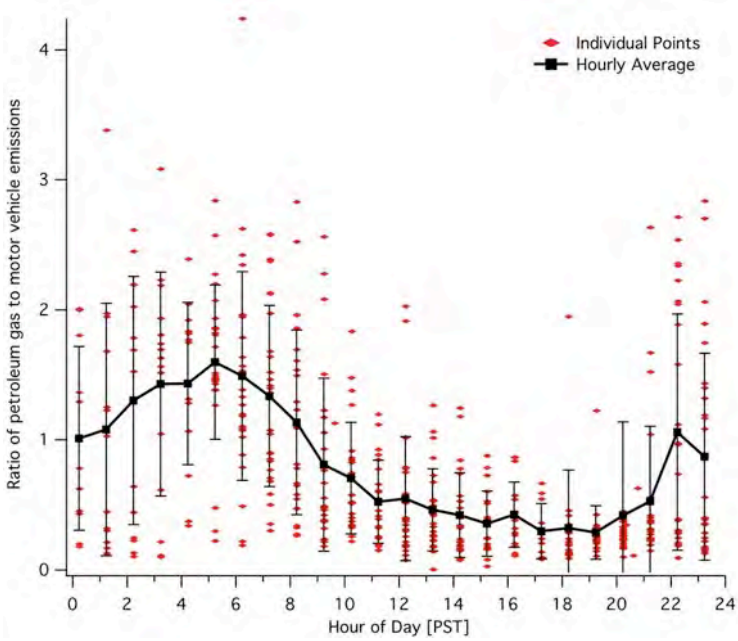

Figure 3.4.7. *The diurnal average of the ratio of petroleum gas (including "unexplained" mass) to the sum of motor vehicle emissions.*

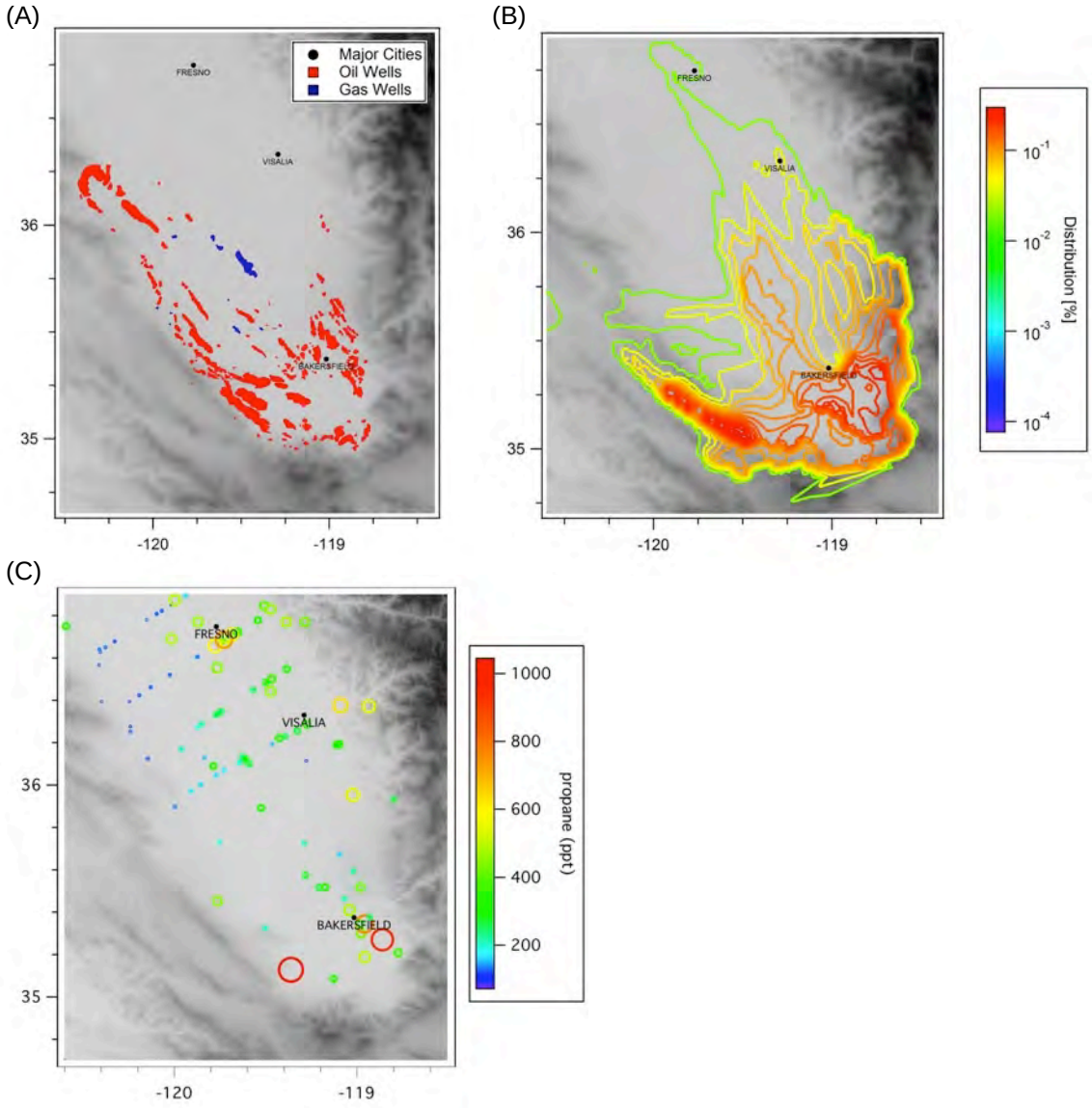

Figure 3.4.8. *Maps of southern part of the San Joaquin Valley with* ***(A)*** *the location of oil and gas wells,* ***(B)*** *the spatial distribution of petroleum gas emissions determined using statistical footprint analysis, and* ***(C)*** *aircraft canister measurements of propane, sized and colored by concentration. Together the maps show a similar distribution of wells and emissions in the region.*

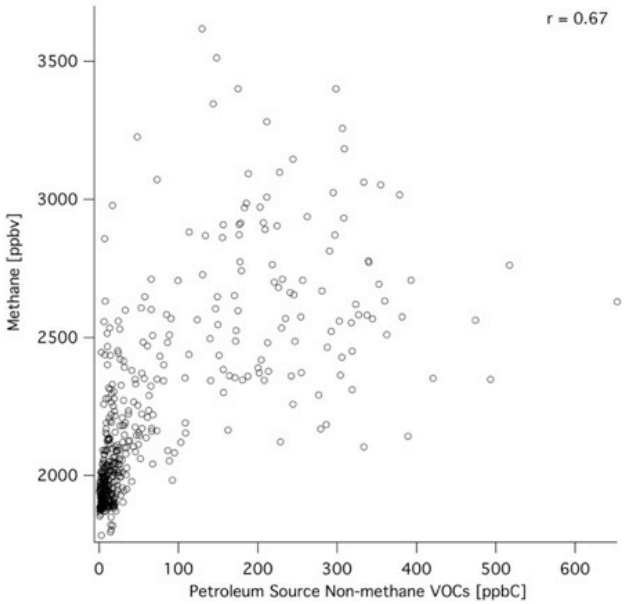

Figure 3.4.9. *Observations of methane are not well correlated with the petroleum gas source and much of the observed correlation can be attributed to simultaneous dilution or concentration due to boundary layer effects.*

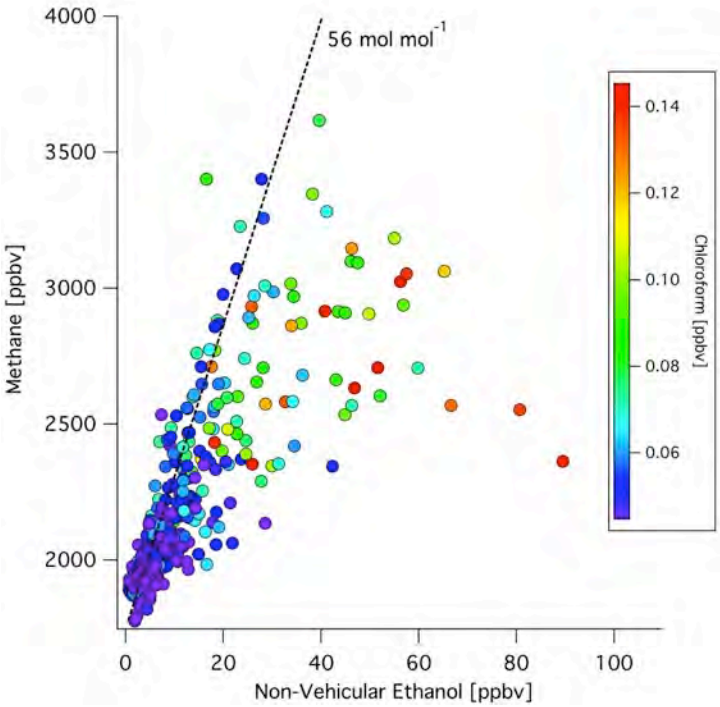

Figure 3.4.10. *Observations of methane vs. non-vehicular ethanol are correlated. Enhancements of ethanol from another source than the dominant source of methane and ethanol are shown by enhancements in chloroform. No major enhancements of methane are observed beyond the inferred slope with non-vehicular ethanol. This, with Figure 3.4.9, suggests a minimal impact of petroleum gas emissions on methane concentrations in the region.*

4. Anticipated Analytical Research after this Contract

4.1. The Coupling of VOC reactivity, temperature, nitrogen oxides, and O_3 production

Analysis to be lead by Ronald Cohen (UCB) with all CalNex-SJV collaborators.

CalNex study topics addressed: *sources of NO_x and VOC, HO_x photochemistry, production and removal timescales of oxidation products, role of VOCs, SJVAB vs. SCAB - response to controls.*

In Section 3.1 (*On the observed response of ozone to NO_x and VOC reactivity reductions in San Joaquin Valley California 1995–present*), we use the historical record of the routine ground-based monitoring network to describe how the frequency of high ozone concentrations has changed over the past decade in response to changes in NO_x and the reactivity of organic molecules (VOCR) across the San Joaquin Valley. We also showed that in Bakersfield and the Southern SJVAB, reductions in VOCR have contributed to a decrease in the frequency of high ozone at moderate temperatures but have had essentially no impact under hot temperature conditions (when exceedances of the state 8-hour O_3 standard are most probable). This suggests two distinct categories of reactivity: the first from sources that have decreased inter-annually and dominate at moderate temperatures and the second from sources that dominate at high temperatures and have not changed over the last 10 years. A manuscript is in preparation by *Pusede et al.* that uses the extensive suite of radical, trace gas, and reactivity observations collected during CalNex to investigate the temperature dependence of the total and speciated reactivity and to assess the impacts of observed relationships on the chemistry of ozone production (PO_3). In combination with trends in select organics monitored with the PAMS network, we make an estimate of the change in total organic reactivity over the last decade. In this analysis, we plan to show that: **(1)** the organic reactivity in the Bakersfield region has a large temperature dependent component that is dominated by small aldehydes and alcohols, **(2)** there is evidence for an unknown source of organic reactivity that is strongly temperature dependent, that forms alkyl nitrates in very low yields (~2%), and that is on average 3 s^{-1} when temperatures are hottest, **(3)** O_3 chemistry in the Bakersfield region is NO_x-limited when temperatures are high (daily max T 34–45°C), near peak PO_3 when temperatures are moderate (28–33°C), and NO_x-saturated when temperatures are low (22–27°C), **(4)** over the last decade the total organic reactivity is estimated to have decreased by 18% at high temperatures, 25% at moderate temperatures, and by 35% at low temperatures, and **(5)** *sustained NO_x controls are the most effective strategy for reducing O_3 exceedances in Bakersfield at all temperatures*.

Temperature and organic reactivity. During CalNex we observe VOC reactivity contributions that are either ***temperature independent*** or ***temperature dependent***. In Figure 4.1.1 (left) the T-independent reactivity includes CO and the anthropogenic emissions: aromatics, alkenes, carbonyls, and some alkanes—these are likely tailpipe emissions. The T-dependent VOCR (driven by concentration increases with T and not effects on the OH rate constant) include small aldehydes, small alcohols, biogenic VOCs, a portion of the measured alkanes, and organic acids. The largest temperature dependent VOCR sources are small oxygenates. In Figure 4.1.1 (right) we show the measured temperature dependent VOCR with the reactivity calculated from measured VOC species separated into the temperature dependent and independent components. The difference between the measured and calculated T-dependent VOCR is the unaccounted for,

or *missing*, reactivity. We see this unknown source is near zero at low temperatures but becomes important as T increases.

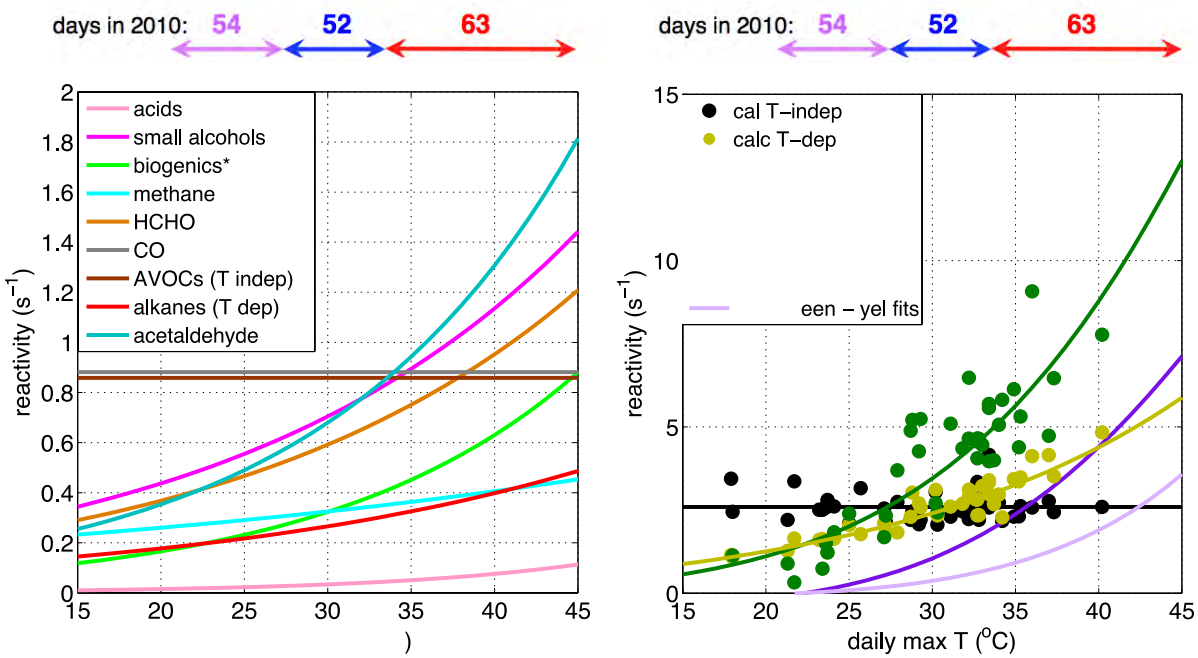

Figure 4.1.1. Top left: *Fits to the daily average (10 am–2 pm) speciated reactivity calculated from measured VOCs vs. the max 1-h average temperature. Acetaldehyde was not measured and was approximated from steady-state relationships with propanal, PPN, and PAN. Anthropogenic VOCs (AVOCs) include aromatics, alkenes, and non-biogenic aldehydes and ketones. Above both the right and left figures are shown the number of days in 2010 with a daily maximum temperature in this range: 54 days (22–27°C), 52 days (28–33°C), and 63 days (34–45°C).* ***Top right:*** *Daily average VOCR: the measured T-dependent VOCR is equal to the measured OH reactivity minus both the inorganic N and the summed T-independent VOCR* ***(green)*** *with fit* ***(green line)****; summed T-dependent VOCR* ***(yellow)*** *with fit* ***(yellow line)****; summed T-independent VOCR includes CO, AVOCs, 0.15 s^{-1} from alkanes, and 0.3 s^{-1} from HCHO* ***(black)*** *with the mean* ***(black line)****; missing VOCR is the green – yellow fit* ***(purple line)****; lower bound missing VOCR is 0.75*green – yellow fit* ***(violet line)****.*

Temperature and ozone chemistry. Daily average PO_3 for the CalNex data are shown for the three temperature regimes along with curves generated with an analytical model representing the free radical chemistry (Murphy et al., 2006). The inputs for VOCR, the instantaneous HO_x production rate (PHO_x), and the NO/NO_x were taken from the T-dependent fits to the CalNex data using the 2010 average temperatures in Bakersfield. The data exhibit expected relationships with both temperature and VOCR. From Figure 4.1.2 (left), we see that when temperatures are hottest O_3 chemistry is NO_x-limited (left of the peak in PO_3). Under moderate-T conditions O_3 chemistry is near the peak with numerous data points still NO_x-saturated. Chemistry is NO_x-saturated in the low-temperature regime. In Figure 4.1.2 (right) the fractional HO_x radical loss to reactions with NO and NO_2 is shown by weekday and weekend. The tan line marks the ratio at which the derivative of PO_3 is zero and where the NO_x-saturated to NO_x-limited transition occurs (Thornton et al., 2002; Kleinman et al., 2005). In Fgure 4.1.2 (right), we see that as temperature increases the amount of HO_x-HO_x loss increases suggesting an increase in both RO_2 from VOC reactions with OH and in the HO_2 production rate from HCHO photolysis. Secondly, according to Figure 4.2.2 (left) the chemistry has indeed become NO_x-limited when temperatures are

hottest, particularly at the low weekend NO_x abundances. NO_x-controls will be very effective at reducing O_3 concentrations in this T regime.

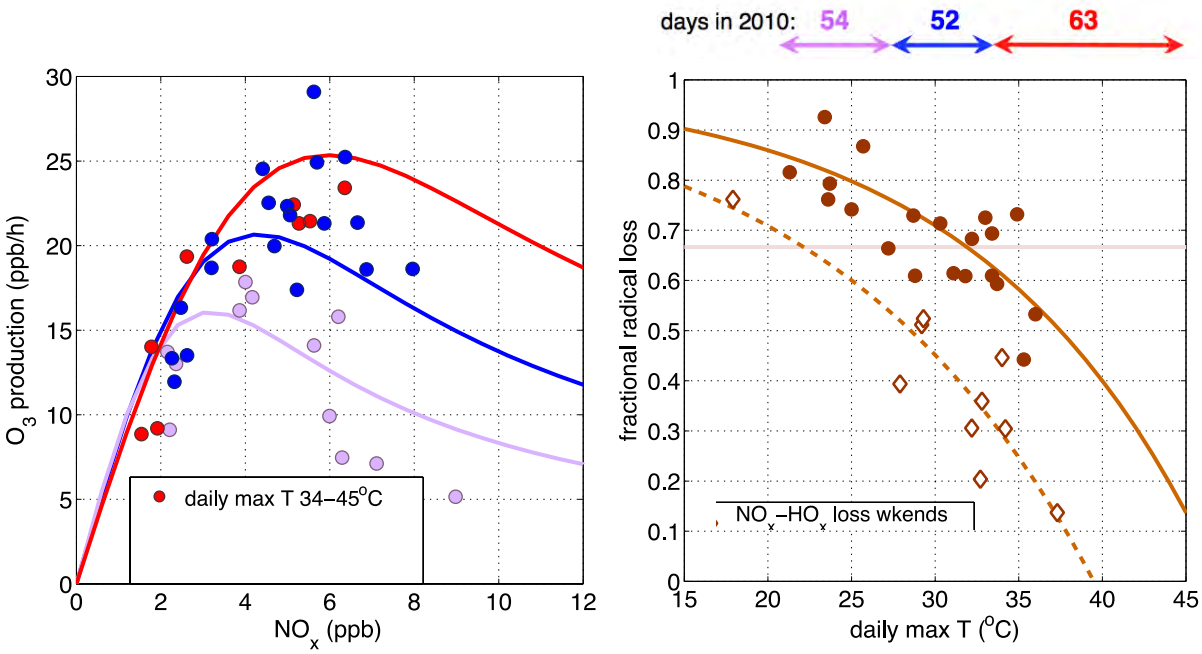

Figure 4.1.2. Left: *Daily average PO_3* ***(red, blue, violet)*** *calculated by radical balance and shown by temperature. The fits are the computed PO_3 with average conditions for 2010 (not just CalNex) where these inputs were generated with the 2010 temperature record and T fits for the observed VOCR, PHO_x, and NO/NO_x with an alkyl nitrate branching ratio (α) = 2%.* ***Right:*** *The fraction of HO_x chain termination due to reactions between HO_x (OH, HO_2, RO_2) and NO_x* ***(brown)*** *of the total loss (HO_x-NO_x loss + HO_x-HO_x loss). The lines are fits to the data. The dashed line is for weekend days* ***(open diamonds)*** *and the solid line is for weekdays* ***(closed circles)****. Only the NO_x-HO_x points are shown for clarity, as the HO_x-HO_x loss points are the inverse The radical loss fractions are computed with daily average (10 am–2 pm) concentrations of OH, HO_2, NO, and NO_2. RO_2 is set equal to HO_2.*

Unknown VOC reactivity source(s). The mean missing VOCR in Bakersfield in the high-T regime is 3 s^{-1} (considering 2010 temperature data) (Figure 4.1.1, right). In Figure 4.1.3 we visualize the required mixing ratio of this source. We include a curve for 1.5 s^{-1} as an estimate of the possible uncertainty in the observed OH reactivity and give examples of the required abundances for 3 s^{-1} reactivity for five temperature dependent classes/compounds: mid-sized alkanes (oil/gas extraction), C4 alcohols, acetaldehyde, a small amine (animals and agriculture), and a very reactive BVOC.

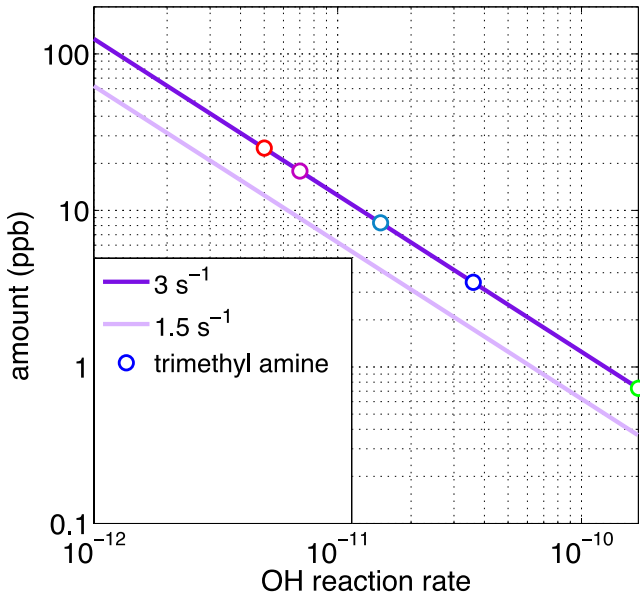

Figure 4.1.3. *Mixing ratio (ppb) vs. OH reaction rate for 3 s^{-1}* ***(purple)*** *and 1.5 s^{-1}* ***(violet)*** *reactivity from Figure 4.1.1 (right).*

Alkyl nitrates serve as an additional constraint on the missing VOCR. Alkyl nitrates (ANs) are formed through the minor channel of the reaction sequence producing O_3. The AN/O_3 branching ratio (α) is controlled by the local VOC mixture and can be inferred from the correlation of oxidant (O_x) vs. ANs (Day et al., 2002; Rosen et al., 2006). In this way CalNex TD-LIF observations of ΣANs offer an additional insight into the identity of the unknown VOCR when compared to the ratio of calculated O_x and ANs production rates (Figure 4.1.4).

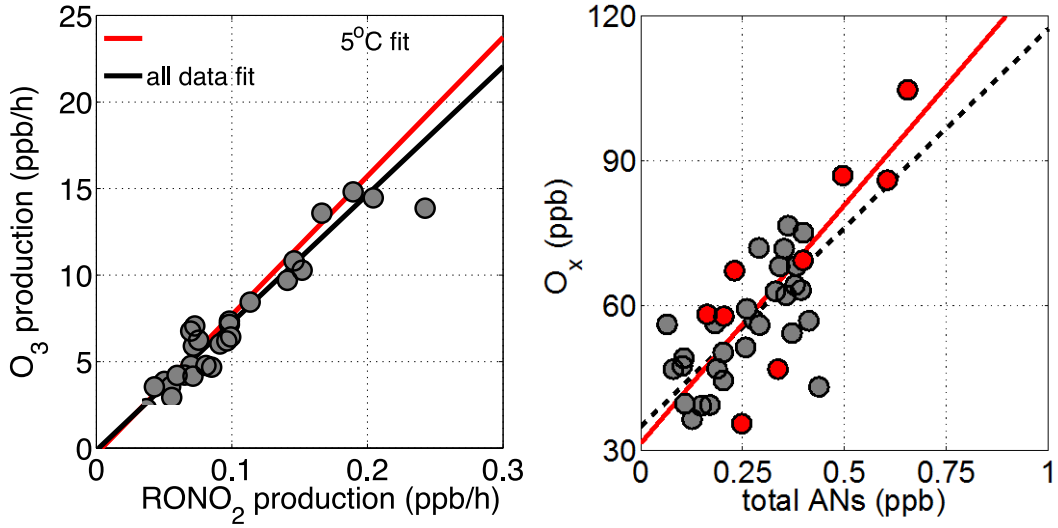

Figure 4.1.4. Left: *Daily average calculated PO_3 vs. $PRONO_2$ using the same set of VOC measurements and approximations as in Figure 4.1.1. The red circles are days with T_{max}>34°C with fits* ***(red line)*** *($y = 80\pm13\ x + 0\pm2$, $R^2 = 0.88$). All data* ***(gray circles)*** *are also fit* ***(gray line)*** *($y = 74\pm4\ x + 0\pm1$, $R^2 = 0.92$).* ***Right:*** *O_x vs. ΣANs. The slope of the relationship is approximately the ratio of the instantaneous O_3 and AN production rates, and assuming*

two O_3 molecules are formed during each VOC oxidation, gives the simple expression 2/α. The colors are the same as on the right (y = 99±25 x + 31±10, R^2 = 0.63; y = 82±12 x + 35±4, R^2 = 0.56).

In Bakersfield we observed α, both calculated and inferred, to be extremely small. The low propensity to form ANs, especially at high T, suggests that a very reactive BVOC or alkanes from nearby oil/gas operations (also well characterized with measurements) are not the missing VOCR source (Figure 4.1.5), as inclusion of this hypothetical reactivity source in the bottom-up estimate shifts the slope far from the observed slope of O_x/ANs. Moreover, amines and/or >C3 alcohols have low α but are not likely present in the amounts required. However, the exponential T dependence and low α do point to functionalized molecules, perhaps oxidation products. It is not apparent from the measured VOCs which these might be (an estimate for isoprene's oxidation products is included in Figure 4.1.1). In the future we will include the effects of temperature on α. Lab studies indicate AN yields decrease at higher temperatures and so not only the unique SJVAB VOC mixture but also the extremely high temperatures are working in concert to suppress AN formation. Inclusion of temperature into our calculation of the production rates will increase the likelihood of and/or possible contribution strength from a highly reactive BVOC source to the missing reactivity.

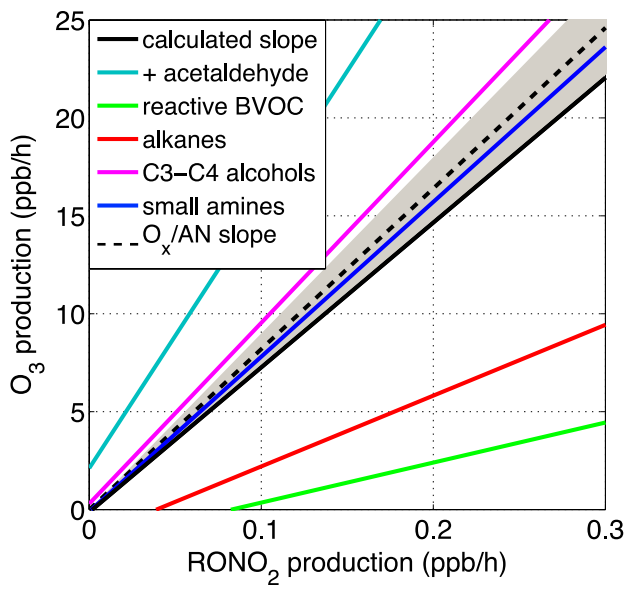

Figure 4.1.5. *PO_3 vs. $PRONO_2$ recalculated including the species shown in Figure 4.1.3* ***(colors in key)****, the CalNex PO_3 vs. $PRONO_2$ slope* ***(solid black line)****, and the inferred slope from O_x vs. ΣANs* ***(dashed black line)*** *with the uncertainty in the observed slope shown* ***(gray)****.*

In a related analysis, we are focusing how the formation of alkyl nitrates interplays with ozone production. During CalNex-SJV, we found the ΣAN production rates in Bakersfield (~2%) to be the lowest urban α ever observed and having the direct consequence that the ozone production per unit VOCR is higher here than in other cities - a typical urban α is ~7%, as in Los Angeles and Mexico City (Farmer et al., 2010; Perring et al., 2010). Figure 4.1.6 compares modeled Bakersfield PO_3 with α = 2% to that modeled with α = 7% and shows the large enhancement in ozone production from suppressed ΣAN formation. This increase is most pronounced at peak PO_3, where it is upwards of 20%.

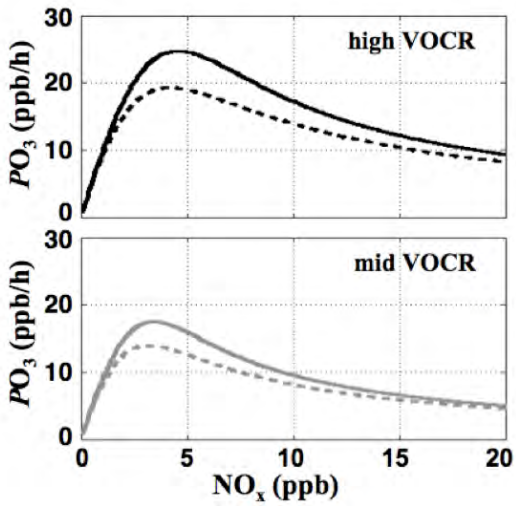

Figure 4.1.6. *Modeled PO_3 with α = 2%* ***(solid line)*** *and α = 7%* ***(dashed line)*** *for observed high* ***(top)*** *and mid VOCR* ***(bottom)*** *conditions during CalNex-SJV.*

We plan to investigate the reasons behind the unique ΣAN chemistry observed at CalNex-SJV. To do this, we will compare the UC-Berkeley TD-LIF ΣAN data to the speciated alkyl and multifunctional nitrate chemical ionization mass spectrometry data collected by the Caltech group (P. Wennberg) and to calculations based on measured VOCs to learn how the VOC mixture in Bakersfield suppresses ΣAN formation. It is of note that a low α is consistent with VOCR dominated by small-oxidized organics, such as those widely emitted by common SJV silage practices (Howard et al., 2010). If these emissions are indeed important to local VOCR, and thus ozone production, they have gone largely unregulated. As stated above, the effects of temperature on α will also be investigated and are expected to be important.

Inter-annual VOC reactivity and O_3 trends. In Pusede and Cohen (2012) we show that over the past decade decreases in VOCR dramatically reduced exceedances of the 8-hr O_3 standard in the Central (~Fresno) and Northern (~Stockton) SJV, but that these decreases had a smaller impact in the Southern SJV region when temperatures were hottest (34–45°C). We suggested that there are two distinct categories of reactivity in the Bakersfield region: one source that has decreased inter-annually and is more important at moderate temperatures and a second source that dominates at high T and has not changed. Indeed the data presented in Figure 4.1.1 support this conclusion as the temperature independent source is much larger at low and moderate T than at high temperatures. *We hypothesize that Figure 4.1.1 (right) quantifies the current value of VOCR in 2010 that is the end point of the long-term decrease (2.5 s^{-1}) and the amount that has not: 9.5 s^{-1} (34–45°C), 6.4 s^{-1} (28–33°C), and 4.3 s^{-1} (22–27°C).*

PAMS long-term data record. According to the daytime average PAMS data, the rates of decrease from 2001–2009 of sampled alkanes, aromatics, and ethene in the Central SJV (Fresno) range from ~3–10%. In Bakersfield, we find the rates of decrease of these same molecules to always be significantly slower. For some species, the change over the last decade was even positive due to recent increases. During CalNex, concentrations of all alkanes smaller than C10 were observed to increase with increasing T (Figure 4.1.1). We speculate that T-dependent emissions from nearby, upwind oil and gas extraction are masking local decreases in the alkane reactivity from vehicle emissions controls.

We combine the rate of VOCR decreases due to motor vehicles from the Fresno PAMS data, estimated at ~7%/year and similar to observed trends in Los Angeles (Warneke et al., 2012), with Figure 4.1.1 (right). *If we assume, reasonably we believe, that the fraction of VOCR exhibiting exponential temperature dependence has gone uncontrolled, we find the change in the total VOCR over the last decade to be 18% (34–45°C), 25% (28–33°C), and 35% (22–27°C).*

In the future:

NO_x emissions controls. High temperature PO_3 is NO_x-limited on weekends and beginning to transition to NO_x-limited chemistry on weekdays (Figure 4.1.2). NO_x emission reductions are thus poised to be highly effective at decreasing O_3 in this T regime. Moderate and low temperature PO_3 is NO_x-saturated on weekdays but nearing peak production on weekends. Of the 66 8-h O_3 exceedances in 2010, 44 occurred on high-T days, 18 exceedances occurred on moderate-T days, and 0 occurred on low-T days. *NO_x controls are thus most effective when high ozone days are most frequent.*

VOCR emissions controls. (1) VOCR reductions will continue to be effective until local photochemistry is fully NO_x-limited. **(2)** Impacts to O_3 will be largest if T-dependent agricultural emissions, including alcohols and acetaldehyde, can be targeted (also acetaldehyde produces three O_3 molecules per OH reaction). **(3)** Alcohols and aldehydes have low or zero α and reductions will have the combined effect of increasing the net α, further suppressing PO_3 (i.e. because these zero-α molecules are a large portion of the VOCR, the net α of the VOC mix will be accordingly reduced). **(4)** There remains an important T-dependent VOCR source that is not identified—*an emphasis on NO_x controls may thus be the most expedient strategy.*

Trends with temperature. As the Southern SJV shifts to NO_x-limited chemistry, the O_3 temperature dependence will diminish. Likewise, we expect a reduction in the variability in PO_3 during ozone season and therefore in the observed O_3.

4.2. Comparing the VOC sources in the San Joaquin and South Coast Air Basins

Analysis to be lead by Allen Goldstein (UCB) with CalNex collaborators from both the Bakersfield and Pasadena sites.

***CalNex study topics* addressed:** *sources of NO_x and VOC, role of VOCs, SJVAB vs. SoCAB: response to controls, SJVAB vs. SoCAB - biogenics.*

The goals of the CalNex project included an intercomparison of emissions and chemistry in the South Coast and San Joaquin Valley Air Basins. While this collaborative effort among researchers and NOAA is still in progress, Figures 4.2.1 and 4.2.2 compare the compounds that were measured at both the CalNex-LA and CalNex-SJV sites. Figure 4.2.1 shows that gasoline-related emission factors determined at the two sites are similar, which can be expected given that they are both using California reformulated gasoline.

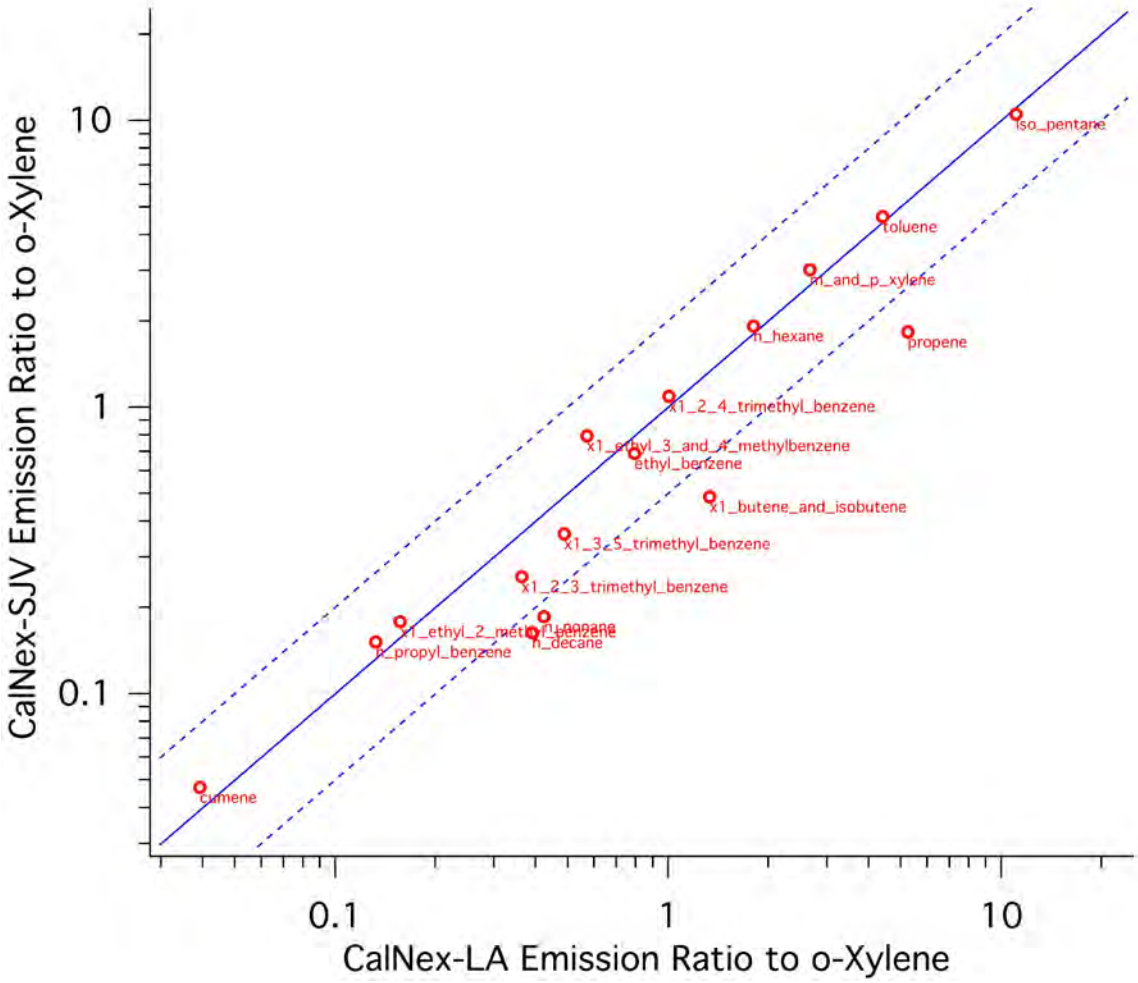

Figure 4.2.1. *Comparison of emissions ratios for prominent gasoline-related VOCs* ***(1:1, 2:1 & 1:2 lines shown in blue)****.*

For many of the VOCs, the abundances are lower in Bakersfield compared to the measurements in Los Angeles, as shown by Figure 4.2.1. Exceptions come from the unrefined natural gas source in the San Joaquin Valley and also the very high prevalence of light alcohols. Interquartile ranges of methanol and ethanol in Bakersfield were 9.5–26 ppbv and 4.1–15 ppbv, respectively, with only 87% of the ethanol being explained by gasoline-related emissions (determined by source receptor model for gasoline). Current work is focused on apportioning these alcohols and other oxygenated VOCs to sources in the San Joaquin Valley. Relative to Pasadena, Bakersfield is very close to sources with little evidence of aging; Pasadena measurements are more aged and thus the prevalence of more reactive VOCs are lower than they would be in downtown Los Angeles. Additionally, the biogenic VOCs are present in relatively similar quantities in these two urban areas, but are much greater in more vegetated areas of the SJV (e.g., agricultural regions or the foothills of the Sierra Nevada mountain range).

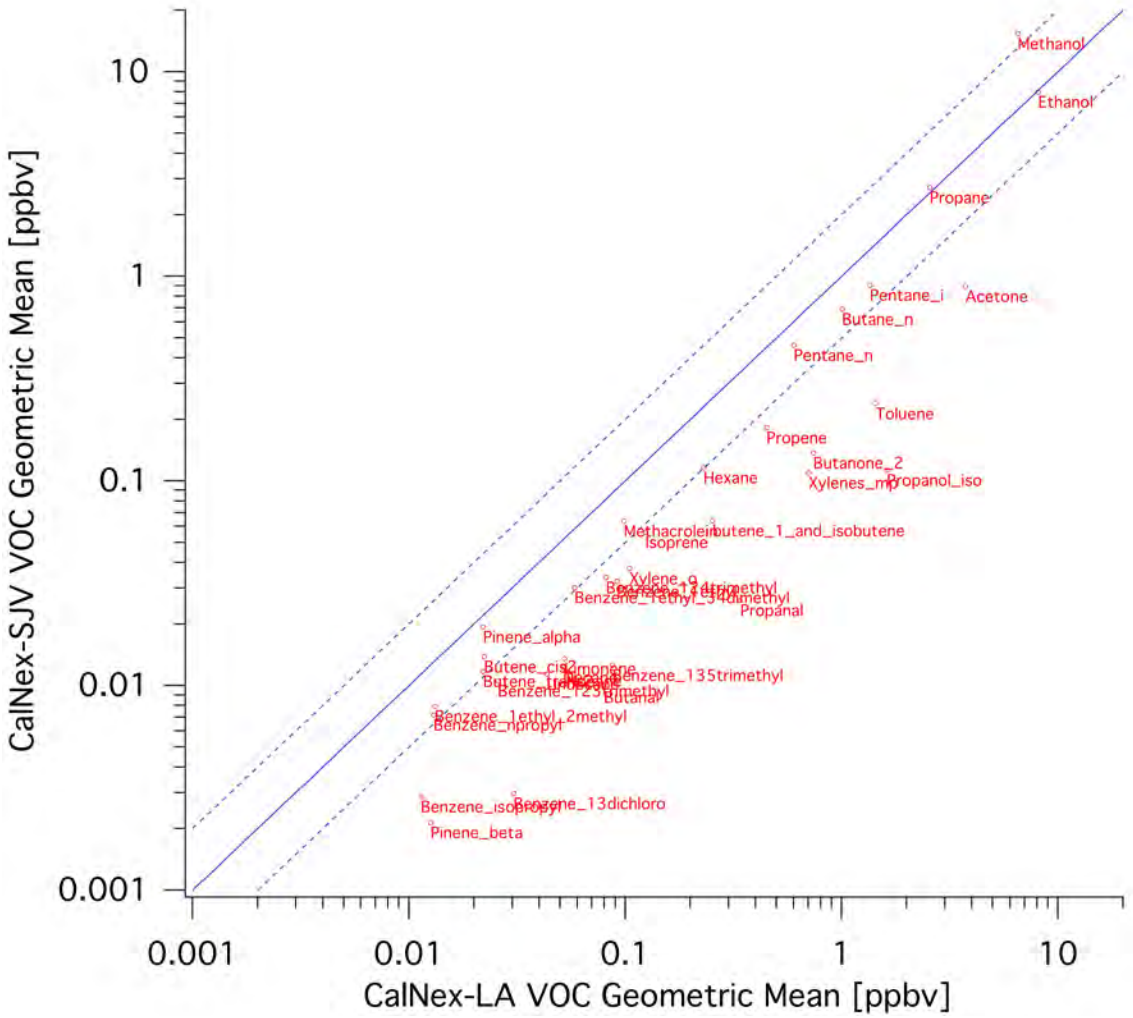

Figure 4.2.2. *Comparison of VOC abundances, expressed as geometric means, at both CalNex supersites* ***(1:1, 2:1 & 1:2 lines shown in blue)****.*

Work is also ongoing to assess the relative importance of biogenic vs. anthropogenic gas-phase organic carbon in the southern San Joaquin Valley. Figure 4.2.3 demonstrates the dominance of anthropogenic contributions from vehicular sources relative to the sum of biogenic compounds observed (i.e., terpenes & isoprene) in terms of concentration. The anthropogenic value shown here is a lower limit as other non-vehicular sources will increase the total concentration. Also, oxidation products from transported biogenic precursors may be relevant for atmospheric reactivity and as precursors to SOA/ozone, but due to instrument limitations they were not measured.

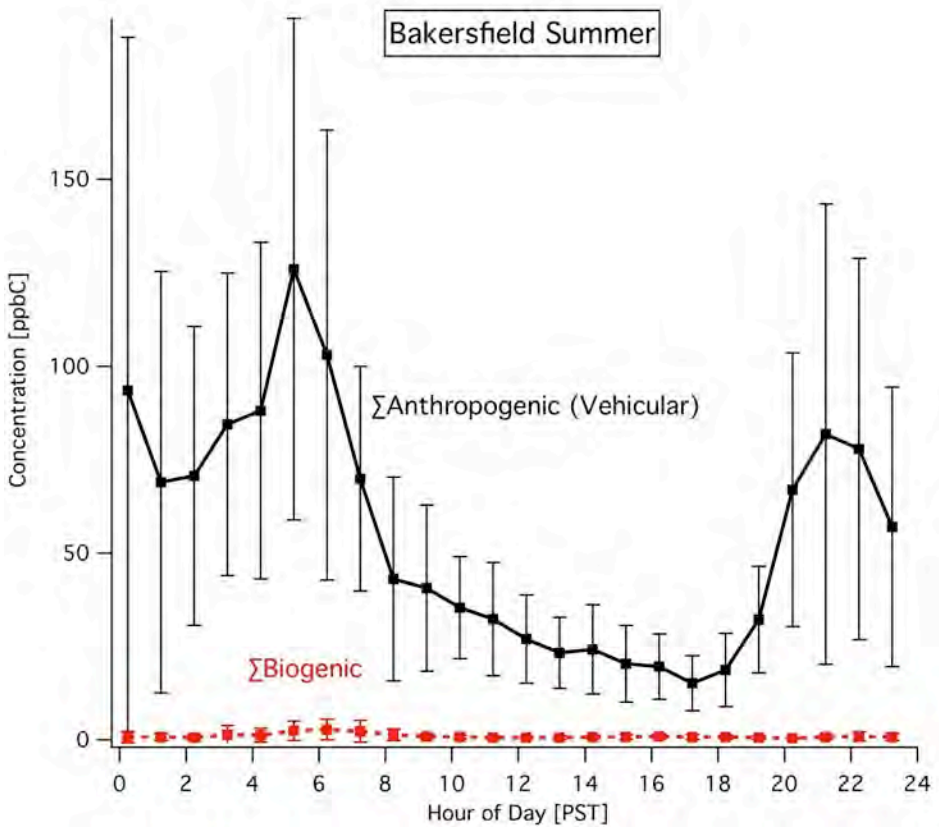

Figure 4.2.3. *Diurnal cycles of anthropogenic contributions to gas-phase organic carbon (from motor vehicles) with the sum of biogenic compounds observed. Both are shown with standard deviations.*

The extensive VOC and related data collected at Bakersfield presents many opportunities to address CalNex science questions. Much of the VOC-related analyses are currently focused on better understanding VOC sources in the San Joaquin Valley. Examples of on-going work include source apportionment of halocarbons, and examining the origins of the elevated levels of alcohols and oxygenated VOCs. Analysis of the work presented here is ongoing and subject to change. Results of this work have been presented at numerous conferences including the AGU Fall Meeting in 2010 and 2011, and the CalNex data workshop in spring 2011.

4.3. Understanding HO_x mechanisms

Analysis lead by William Brune (PSU) with collaborators.

***CalNex study topics* addressed:** *HO_x photochemistry, role of VOCs.*

The CalNex dataset will be modelled with the RACM mechanism as well as several other mechanisms. This comparison will provide a useful test of our understanding of HO_x chemistry in general and as it pertains specificly to the SJVAB.

4.4. Small-oxygenated VOCs, VOC sources, O_3, and aerosol formation

Analysis to be lead by Frank Keutsch (University of Wisconsin-Madison) with collaborators at the Bakersfield and Pasadena ground sites and the aircraft (P3) measurement suite

***CalNex study topics* addressed:** *sources of NO_x and VOC, HO_x photochemistry, production and removal timescales of oxidation products, role of VOCs, SJVAB vs. SCAB - O_3 precursors, SJVAB vs. SCAB - biogenic emissions, SJVAB vs. SCAB - particulate formation rate.*

The on-going (future) efforts of the Madison group will focus on observation-based analysis aimed at analyzing concentrations of oxygenated VOCs with respect to correlated sources of NO_x and VOC precursors. We are completing an analysis centered on using glyoxal and formaldehyde as tracers of VOC oxidation. Our analysis includes a method to determine factors for formaldehyde associated with **(1)** direct emissions from combustion, **(2)** fast photochemically generated formaldehyde, and **(3)** more slowly generated formaldehyde (background). Our analysis utilizes glyoxal, for which we found only extremely weak signatures of direct emission. We are also completing a study that utilizes glyoxal measurements as a proxy for the instantaneous ozone production rate: We have determined that glyoxal concentrations are highly correlated with RO_2 (organic peroxy radical) production rates. In contrast, formaldehyde is poorly correlated due to the variability of formaldehyde sources. Due to the coupling of RO_2 with ozone production, glyoxal could be a useful proxy for the ozone production rate.

Secondly, our future analysis will focus on observations of different VOC precursors and oxygenated VOCs will be analyzed for possible deconvolution of contributions from biogenic and anthropogenic precursors. We are conducting a study aimed at using the ratio of formaldehyde to glyoxal to identify the contribution of biogenic vs. anthropogenic VOCs to the reactive VOC mixture. We are conducting a study that combines glyoxal measurements from Pasadena, Bakersfield and airborne measurements during CalNex. CalNex represents the first time such a comprehensive suite of glyoxal measurements has been obtained. The goal is to evaluate how the scientific studies outlined above vary regionally.

Thirdly, we plan to analyze the contribution of small-oxygenated VOCs to secondary organic aerosol formation via direct uptake, sulfate-ester, imidazole or oligomer formation will be evaluated based on previous field and laboratory studies. We investigated small organosulfates with respect to their quantitative contribution to ambient PM2.5 during CalNex-2010 and with the goal of improving our understanding the processes that form these organosulfates. We developed a simple method for the synthesis of quantitative analytical standards for hydroxycarboxylic acid derived organosulfates and investigated the stability of hydroxycarboxylic acid-derived in commonly used solvents for filter extraction. By using our synthesized standards, quantitative hydroxycarboxylic acid organosulfate concentrations in ambient PM2.5 collected in Bakersfield during CalNex were determined. Together with other work we showed that glycolic acid sulfate (GAS) is a ubiquitous organosulfate in the troposphere. The importance of this finding is twofold. First GAS is abundant, contributes to PM2.5 mass, and is one of the few two-carbon compounds quantified in aerosol. This is relevant as two-carbon compounds correspond to non-traditional secondary organic aerosol species. This highlights the second important finding. Based on the previous statement and the fact that we

observed GAS during photochemical uptake experiments on wet aerosol, we propose that it could be a much sought after tracer for aqueous processing, although its formation mechanism remains unclear. Our initial effort has been published in Environmental Science and Technology (Olson et al., 2011) and we plan to continue investigating the formation mechanism(s).

We are currently conducting analyses to quantify the contribution of imidazoles and other species to PM2.5 from filter samples collected at Bakersfield during CalNex. The goal of this study is to investigate the potential of using these compounds as tracers of SOA formation via glyoxal, as glyoxal forms imidazoles in aerosol in the presence of ammonium. We have quantified the kinetics for this reaction, which has strong pH dependence. The results of this study will provide insight into the contribution of α-dicarbonyls to PM2.5 and will complement our gas-phase studies of α-dicarbonyls.

4.5. Peroxy nitrate chemistry in the SJVAB

Analysis to be lead by Joel Thornton (University of Washington).

***CalNex study topics* addressed:** *sources of NO_x and VOC, HO_x photochemistry, production and removal timescales of oxidation products, role of VOCs.*

There are three intriguing aspects of the PAN and peroxypropionyl nitrate (PPN) data at the CalNex-SJV site: **(1)** the broad similarity in terms of abundances to Blodgett Forest in the Sierra Nevada foothills, **(2)** the ability of detailed oxidation mechanisms to reproduce PAN and PPN precursors at an urban site, and **(3)** the identification of peroxy nitrates other than PAN and PPN.

Towards the first point, it is not entirely obvious why PAN and PPN abundances at an urban site in the San Joaquin Valley and at a rural site in the forested Sierra Nevada foothills that are hundreds of kilometers apart should be as similar as our data suggest. Moreover, the mix of VOCs at the two sites is apparently significantly different. For example, at Blodgett Forest during June, methyl vinyl ketone (MVK) and methacrolein (MACR), two important PAN precursors were together often 3 ppbv or more. In contrast, while MVK was not reported for the CalNex-SJV site, MACR rarely exceeded 0.5 ppbv and based on the MACR/MVK ratio at Blodgett Forest, it likely rarely exceeded 1 ppbv at the CalNex-SJV site. Because PAN levels were actually higher at the CalNex-SJV site on average, this suggests a greater role for non-isoprene derived precursors such as acetaldehyde (not measured at the Bakersfield site) and anthropogenic VOC generally. We plan to investigate whether the measured suite of VOCs can explain the PPN/PAN ratio and thus the balance between anthropogenic and biogenic VOC as radical sources.

In this regard, the only known precursor of propionyl peroxy nitrate (PPN) is via oxidation of propanal. At Blodgett Forest, we were able to reconcile our observations of PPN with measured propanal to within a factor of two, with most of the error likely from OH measurements. A similar analysis of the CalNex-SJV data suggested that the measured propanal concentrations are too low, perhaps by a factor of five, to explain our PPN measurements. In fact, the propanal measured at Blodgett Forest in 2009 is about 5x higher during midday than at the Bakersfield

site. We plan to explore this failure to replicate the PPN in Bakersfield using a more detailed oxidation mechanism in the Master Chemical Mechanism to determine whether the oxidation of larger alkanes can lead to PPN precursors in an urban environment.

That the mix of VOC could be substantially different between Blodgett Forest and CalNex-SJV is consistent with the possibility of generating a significant fraction of peroxy nitrates besides PAN and PPN. Thus, the difference between the UC Berkeley total PNs measurement and the UW PAN and PPN data provides a means to examine the abundance and diel patterns of other PNs. Here again, the Master Chemical Mechanism provides a means to examine the production of more exotic peroxy nitrates and their contribution to the total reactive nitrogen budget.

4.6. Impacts of organic and nitric acids

Analysis to be lead by Paul Wennberg (Caltech) with collaborators at the Bakersfield site.

***CalNex study topics* addressed:** *sources of NO_x and VOC, production and removal timescales of oxidation products, role of VOCs, SJVAB vs. SCAB - biogenics.*

In collaboration with the broader CalNex science team, the Caltech group intends to continue our investigation of the sources of formic and acetic acid in the San Joaquin Valley. Our initial analysis suggests that these acids are associated with the large feedlots located to the south of the site and that their concentrations are strongly temperature dependent.

Secondly, the HNO_3/NH_3 system provides an important constraint on the formation of nitrate aerosol via emissions of ammonia and photochemical production of nitric acid. We also intend to collaborate with Prof. Jennifer Murphy's group (U. of Toronto) to analyze this HNO_3/NH_3 system.

5. Publications and Presentations by Investigators Receiving Funding

Beaver, M. R. (2011) CIMS measurements of gas-phase acids during CalNex-SJV, Poster presented at the California Air Resources Board CalNex Planning Meeting, Sacramento, CA, 16–19 May.

Gentner, D. R., Goldstein, A. H. (2010) Ambient concentrations and emissions of a comprehensive suite of volatile organic compounds at the CalNex-Bakersfield supersite, Abstract A22B-02 presented at the 2010 Fall Meeting, AGU, San Francisco, Calif., 13–17 December.

Gentner, D. R. (2011) In-situ measurements of a broad range of volatile organic compounds at the CalNex-Bakersfield supersite, Poster presented at the California Air Resources Board CalNex Planning Meeting, Sacramento, CA, 16–19 May.

Gentner, D. R., Harley, R. A., Weber, R., Karlik, J. F., Goldstein, A. H. (2011) Investigating sources and emissions of volatile organic compounds in California's San Joaquin Valley, Abstract A34B-06 presented at the 2011 Fall Meeting, AGU, San Francisco, Calif., 5–9 December.

Goldstein, A. H., Gentner, D. R., Isaacman, G. A., Worton, D. R., Zhao, Y., Weber, R., Kreisberg, N. M., Hering, S. V., Williams, B. J., Hohaus, T., Jayne, J., Lambe, A., Williams, L. R., Jimenez, J. L., CalNex Bakersfield Science Team, CalNex Pasadena Science Team (2010) In-Situ observations of speciated organics in gas and particle phases: CalNex2010 Bakersfield and Los Angeles, Abstract A12A-06 presented at the 2010 Fall Meeting, AGU, San Francisco, Calif., 13–17 December.

Guha, A., Gentner, D. R., Goldstein, A., Provencal, R. A., Gardner, A., the CALNEX Bakersfield Science Team (2010) Measurement of greenhouse gases (GHGs) and source apportionment in Bakersfield, CA during CALNEX 2010, Abstract A21C-0090 presented at the 2010 Fall Meeting, AGU, San Francisco, Calif., 13–17 December.

Guha, A. (2011) Measurement of greenhouse gases (GHGs) and source apportionment in Bakersfield, CA during CALNEX 2010, Poster presented at the California Air Resources Board CalNex Planning Meeting, Sacramento, CA, 16–19 May.

Guha, A., Gentner, D. R., Weber, R., Gardner, A., Provencal, R. A., Goldstein, A., (2011) Measurement of greenhouse gases (GHGs) and source apportionment in Bakersfield, CA during CalNex 2010, Abstract A34B-05 presented at the 2011 Fall Meeting, AGU, San Francisco, Calif., 5–9 December.

Henry, S. B., DiGangi, J. P., Boyle, E., Keutsch, F. N., CalNex Science Team (2010) Concentrations of Glyoxal and Formaldehyde During CALNEX 2010, Abstract A21C-0087 presented at the 2010 Fall Meeting, AGU, San Francisco, Calif., 13–17 December.

Keutsch, F. N. (2011) Glyoxal and formaldehyde measurements in the Southern San Joaquin Valley: comparison with CMAQ model results and analysis of formaldehyde sources, Talk

presented at the California Air Resources Board CalNex Planning Meeting, Sacramento, CA, 16–19 May.

Olson, C. N., Galloway, M. M., Yu, G., Hedman, C. J., Lockett, M. R., Yoon, T., Stone, E. A., Smith, L. M., and Keutsch, F. N.: Hydroxycarboxylic acid-derived organosulfates: synthesis, stability, and quantification in ambient aerosol, Environ. Sci. Technol., 45(15), 6468–6474, 2011.

Pusede, S. E., Wooldridge, P. J., Browne, E. C., Rollins, A. W., Min, K., Cohen, R. C., Baier, B. C., Beaver, M. R., Boyle, E., Brune, W. H., DiGangi, J. P., Gentner, D. R., Goldstein, A. H., Keutsch, F., Ren, X., Sanders, J., St Clair, J. M., Thomas, J., Weber, R., Wennberg, P. O., Zhang, L. (2010) Ozone production in the Southern San Joaquin Valley: a NO_x perspective, Abstract A21C-0088 presented at the 2010 Fall Meeting, AGU, San Francisco, Calif., 13–17 December.

Pusede, S. E., Wooldridge, P. J., Browne, E. C., Rollins, A. W., Min, K., Cohen, R. C., Baier, B. C., Beaver, M. R., Boyle, E., Brune, W. H., DiGangi, J. P., Gentner, D. R., Goldstein, A. H., Keutsch, F., Ren, X., Sanders, J., St Clair, J. M., Thomas, J., Weber, R., Wennberg, P. O., Zhang, L. (2010) Ozone production in the Southern San Joaquin Valley: a NO_x perspective, Presented at the 2010 Atmospheric Chemical Mechanism Conference, ACM, Davis, Calif., 4–7 December.

Pusede, S. E., Wooldridge, P. J., Browne, E. C., Rollins, A. W., Min, K., Thomas, J., Zhang, L., Brune, W. H., Gentner, D. R., Goldstein, A. H., DiGangi, J. P., Keutsch, F., Ren, X., Sanders, J., Weber, R., Cohen, R. C., (2011) Southern San Joaquin Valley ozone production: Relationships with NO_x abundance, alkyl nitrate formation, VOC reactivity, and rates of primary HO_x production, Poster presented at the California Air Resources Board CalNex Planning Meeting, Sacramento, CA, 16–19 May.

Pusede, S. E., Wooldridge, P. J., Browne, E. C., Rollins, A. W., Min, K., Thomas, J., Zhang, L., Brune, W. H., Gentner, D. R., Goldstein, A. H., DiGangi, J. P., Keutsch, F., Ren, X., Sanders, J., Weber, R., Cohen, R. C., (2011) Extracting photochemical mechanisms from field observations by turning isoprene off: measurements from Nashville, TN and Bakersfield, CA. Poster presented at the American Chemical Society Meeting, Denver, CO, 28–31 August 2011.

Pusede, S. E., Wooldridge, P. J., Browne, E. C., Russell, A. R., Rollins, A. W., Min, K.-M., Thomas, J., Zhang, L., Brune, W. H., Henry, S. B., DiGangi, J. P., Keutsch, F. N., Sanders, J. E., Ren, X., Weber, R., Goldstein, A. H., Cohen, R. C. (2011) Observational constraints on projections of the ozone response to NO_x controls in the Southern San Joaquin Valley, Abstract A23B-0141 presented at the 2011 Fall Meeting, AGU, San Francisco, Calif., 5–9 December.

Pusede, S. E. and Cohen, R. C.: On the observed response of ozone to NO_x and VOC reactivity reductions in San Joaquin Valley California 1995–present, *Atmos. Chem. Phys.*, 12, 8328–8339, 2012.

Pusede, S. E. and Cohen, R. C.: On the observed response of ozone to NO_x and VOC reactivity reductions in San Joaquin Valley California 1995–present. Presented at the International Global Atmospheric Chemistry Conference, Beijing, China, September 2012, Poster.

Pusede, S. E., Gentner, D. W., Wooldridge, P. J., Browne, E. C., Guha, A., Goldstein, A. H., Thomas, J., Brune, W. H., DiGangi, J. P., Henry, S. B., Keutsch, F. N., Beaver, M. R., St Clair, J. M., Wennberg, P. O., and Cohen, R. C.: On the temperature dependence and decadal trends of ozone in the San Joaquin Valley: Constraints from measurements at the CalNex-Bakersfield supersite. Presented at the American Geophysical Union Fall Meeting, San Francisco, CA, December 2012, Poster.

Rollins, A. W., Min, K., Pusede, S. E., Wooldridge, P. J., Day, D. A., Liu, S., Russell, L. M., Gentner, D. R., Goldstein, A. H., Weber, R., Cohen, R. C. (2011) Gas/Particle partitioning of total alkyl nitrates measured in Bakersfield during CALNEX, Abstract A22C-07 presented at the 2011 Fall Meeting, AGU, San Francisco, Calif., 5–9 December.

Sellon, R. (2011) Molecular-level analysis of size resolved secondary organic aerosol (SOA) samples from CALNEX Bakersfield using high-resolution mass spectrometry, Poster presented at the California Air Resources Board CalNex Planning Meeting, Sacramento, CA, 16–19 May.

Thomas, J. L., Brune, W. H., Zhang, L., van Duin, D., Ren, X., Pusede, S. E., Cohen, R. C., Goldstein, A. H. (2010) OH, HO_2, and OH reactivity behavior in the Southern San Joaquin Valley during CalNex 2010, Abstract A21C-0089 presented at the 2010 Fall Meeting, AGU, San Francisco, Calif., 13–17 December.

Thomas, J., Brune, W. H., Cohen, R. C., Goldstein, A. H., Pusede, S. E., Ren, X., Van Duin, D., Zhang, L. (2011) Oxidation photochemistry in the Southern San Joaquin Valley during CalNex-2010, Abstract A23B-0148 presented at the 2011 Fall Meeting, AGU, San Francisco, Calif., 5–9 December.

Zhao, Y., Kreisberg, N. M., Worton, D. R., Isaacman, G. A., Weber, R., Hering, S. V., Goldstein, A. (2010) In situ gas-particle partitioning measurements of SVOCs: implications for SOA formation mechanisms, Abstract A11F-0129 presented at the 2010 Fall Meeting, AGU, San Francisco, Calif., 13–17 December.

Zhao, Y. (2011) Major components of summertime atmospheric organic aerosols in Bakersfield, CA during CalNex, Poster presented at the California Air Resources Board CalNex Planning Meeting, Sacramento, CA, 16–19 May.

Zhao, Y., Kreisberg, N. M., Worton, D. R., Isaacman, G. A., Weber, R., Liu, S., Day, D. A., Markovic, M. Z., VandenBoer, T. C., Russell, L. M., Murphy, J. G., Hering, S. V., Goldstein, A. H. (2011) In situ measurements of gas- and particle-phase organic compounds: insights for SOA formation mechanisms and contributions of SOA to organic aerosol, Abstract A13C-0321 presented at the 2011 Fall Meeting, AGU, San Francisco, Calif., 5–9 December.

Publications and Presentations by our Collaborators at the CalNex-SJV Site

Ahlm, L., Liu, S., Day, D. A., Russell, L. M., Weber, R., Gentner, D. R., Goldstein, A. H., DiGangi, J. P., Henry, S. B., Keutsch, F. N., VandenBoer, T. C., Markovic, M. Z., Murphy, J. G., Beaver, M. R., and Scheller S. (2011) Formation and growth of ultrafine particles from secondary sources in Bakersfield, California, *J. Geophys. Res.*, 117, D00V08, doi:10.1029/2011JD017144.

Ahlm, L., Russell, L. M., Liu, S., Day, D. A. Weber, R., Gentner, D. R., Goldstein, A. H., Keutsch, F. N., VandenBoer, T. C., Markovic, M. Z., Murphy, J. G. (2011) Formation and growth of ultrafine particles from secondary anthropogenic sources in Bakersfield, Abstract A31G-02 presented at the 2011 Fall Meeting, AGU, San Francisco, Calif., 5–9 December.

Kleindienst, T. E. (2011) Secondary organic aerosol contributions during CALNEX, Bakersfield, Talk presented at the California Air Resources Board CalNex Planning Meeting, Sacramento, CA, 16–19 May.

Liu, S., Russell, L. M., Day, D. A., Zhao, Y., Goldstein, A. H., Weber, R. (2011) Formation of anthropogenic and biogenic secondary organic aerosol at Bakersfield, CA, Abstract A13C-0319 presented at the 2011 Fall Meeting, AGU, San Francisco, Calif., 5–9 December.

Markovic, M. Z., VandenBoer, T. C., Murphy, J. G. (2010) Measurements of $PM_{2.5}$ NH_4^+- SO_4^{2-}-NO_3^- and associated precursor gases in Bakersfield, CA during CalNex 2010, Abstract A21C-0084 presented at the 2010 Fall Meeting, AGU, San Francisco, Calif., 13–17 December.

Miller, D. J., Sun, K., Khan, M. A., Tao, L., Zondlo, M. A. (2011) Ammonia dynamics and emissions sources: a case study during CALNEX 2010, Abstract A23B-0138 presented at the 2011 Fall Meeting, AGU, San Francisco, Calif., 5–9 December.

Murphy, J. G. (2011) A tale of two extremes: contrasting NH_3 at the Bakersfield and Pasadena supersites, Talk presented at the California Air Resources Board CalNex Planning Meeting, Sacramento, CA, 16–19 May.

Murphy, J. G. (2011) Measurements of soluble composition of fine atmospheric particulate matter (PM2.5) and associated precursor gases in Bakersfield, CA during CalNex 2010, Poster presented at the California Air Resources Board CalNex Planning Meeting, Sacramento, CA, 16–19 May.

Murphy, J. G., Ellis, R., Markovic, M. Z., VandenBoer, T. C., Hayes, P. L., Cubison, M., Ortega, A. M., Jimenez, J. L., Liu, J., Weber, R., Veres, P. R., Cochran, A. K., Roberts, J. M. (2011) Ammonia as an observational constraint on aerosol pH in rural and urban environments, Abstract A32A-01 presented at the 2011 Fall Meeting, AGU, San Francisco, Calif., 5–9 December.

O'Brien, R. E., Laskin, A., Laskin, J., Weber, R., Goldstein, A. H. (2011) Molecular-level analysis of size resolved secondary organic aerosol (SOA) samples from CALNEX Bakersfield using high resolution mass spectrometry, Abstract A13C-0303 presented at the 2011 Fall Meeting, AGU, San Francisco, Calif., 5–9 December.

Rubitschun, C. L. (2011) Isoprene- and monoterpene-derived organosulfates in PM2.5 during the CALNEX campaign in Bakersfield, CA, Poster presented at the California Air Resources Board CalNex Planning Meeting, Sacramento, CA, 16–19 May.

Russell, L. M. (2011) Regional Assessment of Organic PM during CalNex, CalMex, and CARES, Talk presented at the California Air Resources Board CalNex Planning Meeting, Sacramento, CA, 16–19 May.

Shang, L. (2011) Source signatures of organic compounds and particle growth in Bakersfield, CA, Talk presented at the California Air Resources Board CalNex Planning Meeting, Sacramento, CA, 16–19 May.

VandenBoer, T. C., Markovic, M. Z., Sanders, J. Ren, X., Murphy, J. G. (2010) Observations of the partitioning of trace acids during CalNex, Bakersfield: HONO, HCl and Oxalic Acid in an NH_3-rich environment, Abstract A21C-0083 presented at the 2010 Fall Meeting, AGU, San Francisco, Calif., 13–17 December.

VandenBoer, T. C. (2011) Los Angeles and Bakersfield HCl during CalNex: acid displacement, reactive Cl reservoir and partitioning, Poster presented at the California Air Resources Board CalNex Planning Meeting, Sacramento, CA, 16–19 May.

6. Conclusions and Recommendations

In conclusion, the extensive observations at the Bakersfield supersite provide a unique and exciting data set with which to assess current understanding of processes and mechanisms of emissions, chemistry, phase transformation and deposition that together are responsible for the composition of air in the region and beyond.

In addition to the research objectives outlined above, we list the following conclusions and recommendations for future work in this area of research:

1) Understanding the VOC reactivity in the SJV now, in the past, and projecting into the future, is essential to understanding the patterns of ozone violations. Indications presented here, confirm that the relationship between VOC reactivity and individual molecules is well understood at low temperatures but poorly understood under the conditions conducive to episodes of high ozone.

2) The data set collected at the SJV supersite has numerous internal consistency checks. For example, the measurements of OH should be consistent with various ratios of parent to daughter molecules, the measurements of total HNO_3 and the sum of separate gas and aerosol HNO_3 should be consistent and the measurements of PAN and its analogs should be consistent with aldehyde precursors. These internal consistency checks should be further enumerated and used to characterize the quality of the observations.

3) Aerosol chemistry in the region may have some unique features because of the exceptionally high NH_3. Understanding the role of NH_3 chemistry and whether it only has an effect on the inorganic chemistry or whether it also affects the organic chemistry will be a continuing challenge.

4) Long term records of a wide range of trace gases in the region offer a unique perspective on the changing chemistry. Modeling and observational analyses should take full advantage of these records as they seek a consistent chemical/meteorological explanation for trends on O_3 and/or aerosol.

5) Finally, we note that there remain unexplored opportunities for comparison of the SJV chemistry to that of the LA basin with respect to both O_3 and aerosol and their precursors.

7. References

Alanis, P., Ashkan, S., Krauter, C., Campbell, S., and Hasson, A.: Emissions of volatile fatty acids from feed at dairy facilities, Atmos. Environ., 44(39), 5084–5092, 2010.

Blanchard, C. L. and Fairley, D.: Spatial mapping of VOC and NOx-limitation of ozone formation in Central California, Atmos. Environ., 35, 3861–3873, 2001.

Beaver, M. R., St. Clair, J. M., Paulot, F., Spencer, K. M., Crounse, J. D., LaFranchi, B. W., Min, K. E., Pusede, S. E., Wooldridge, P. J., Schade, G. W., Park, C., Cohen, R. C. and Wennberg P. O.: Importance of biogenic precursors to the budget of organic nitrates: observations of multifunctional organic nitrates by CIMS and TD-LIF during BEARPEX 2009, Atmos. Chem. Phys., 12, 5773–5785, 2012.

Cai, C. and the Calnex Teams, CalNex-2010 photochemical air quality modeling: comparison of CARB and U.S. EPA results, EOS Transactions, AGU Fall Meeting 2011.

Cardelino, C. A. and Chameides, W. L.: Natural hydrocarbons, urbanization, and urban ozone, J. Geophys. Res., 95, 13 971–13 979, 1990.

Crounse, J. D., McKinney, K. A., Kwan, A. J., and Wennberg, P. O.: Measurement of gas-phase hydroperoxides by chemical ionization mass spectrometry, Anal. Chem., 78, 6726–6732, 2006.

Crounse, J. D., DeCarlo, P. F., Blake, D. R., Emmons, L. K., Campos, T. L., Apel, E. C., Clarke, A. D., Weinheimer, A. J., McCabe, D. C., Yokelson, R. J., Jimenez, J. L., and Wennberg, P. O.: Biomass burning and urban air pollution over the Central Mexican Plateau, Atmos. Chem. Phys., 9(14), 4929–4944, 2009.

Day, D. A., Wooldridge, P. J., Dillon, M., Thornton, J. A., and Cohen, R. C.: A thermal dissociation-laser induced fluorescence instrument for in-situ detection of NO_2, peroxy (acyl) nitrates, alkyl nitrates, and HNO_3, J. Geophys. Res., 107, D6, 10.1029/2001JD000779, 2002.

Day, D. A., Dillon, M. B., Wooldridge, P. J., Thornton, J. A., Rosen, R. S., Wood, E. C., and Cohen, R. C.: On Alkyl nitrates, ozone and the 'Missing NO_y', J. Geophys. Res., 108, D16, doi:10.1029/2003JD003685, 2003.

Faloona, I. C., Tan, D., Lesher, R. L., Hazen, N. L., Frame, C. L., Simpas, J. B., Harder, H., Martinez, M., Di Carlo, P., Ren, X. R., and Brune, W. H.: A laser-induced fluorescence instrument for detecting tropospheric OH and HO_2: characteristics and calibration, J. Atmos. Chem., 47, 139–167, 2004.

Farmer, D. K., Perring, A. E., Wooldridge, P. J., Blake, D. R., Baker, A., Meinardi, S., Huey, L. G., Tanner, D., Vargas, O., and Cohen, R. C.: Impact of organic nitrates on urban ozone production, Atmos. Chem. Phys., 10, 23423–23448, 2010.

Fraas, A. and Lutter, R.: Do some NO_x emissions have negative environmental damages: evidence and implications, Environ. Sci. Technol., 45, 7613–7614, 2011.

Gentner, D. R., Harley, R. A., Miller, A. M., and Goldstein, A. H.: Diurnal and seasonal variability of gasoline-related volatile organic compound emissions in Riverside, California, Envron. Sci. Technol., 43, 4247–4252, 2009.

Han, Z., Ueda, H., and Matsuda, K.: Model study of the impact of biogenic emission on regional ozone and the effectiveness of emission reduction scenarios over eastern China, Tellus, 57B, 12–27, 2005.

Heald, C. L., Goldstein, A. H., Allan, J. D., Aiken, A. C., Apel, E., Atlas, E. L., Baker, A. K., Bates, T. S., Beyersdorf, A. J., Blake, D. R., Campos, T., Coe, H., Crounse, J. D., DeCarlo, P. F., de Gouw, J. A., Dunlea, E. J., Flocke, F. M., Fried, A., Goldan, P., Griffin, R. J., Herndon, S. C., Holloway, J. S., Holzinger, R., Jimenez, J. L., Junkermann, W., Kuster, W. C., Lewis, A. C., Meinardi, S., Millet, D. B., Onasch, T., Polidori, A., Quinn, P. K., Riemer, D. D., Roberts, J. M., Salcedo, D., Sive, B., Swanson, A. L., Talbot, R., Warneke, C., Weber, R. J., Weibring, P., Wennberg, P. O., Worsnop, D. R., Wittig, A. E., Zhang, R., Zheng, J., and Zheng, W.: Total observed organic carbon (TOOC) in the atmosphere: a synthesis of North American observations, Atmos. Chem. Phys., 8, 2007–2025, 2008.

Hottle, J. R., Huisman, A. J., Digangi, J. P., Coens, K. L., Galloway, M.G., and Keutsch, F. N.: A laser induced fluorescence based instrument for in-situ measurements of atmospheric formaldehyde, Environ. Sci. Technol., 43, 790–795, 2009.

Howard, C. J., Kumar, A., Malkina, I., Mitloehner, F., Green, P. C., Flocchini, R. G., and Kleeman, M. J.: Reactive organic gas emissions from livestock feed contribute significantly to ozone production in Central California, Environ. Sci. Technol., 44, 2309–2314, 2010.

Huisman, A. J., Hottle, J. R., Coens, K. L., Digangi, J. P., Galloway, M. G., Kammrath, A., and Keutsch, F. N.: Laser-induced phosphorescence for the in situ detection of glyoxal at part per trillion mixing ratios, Anal. Chem., 80, 5884–5891, 2008.

Kang, E., Root, M. J., Toohey, D. W., and Brune, W. H.: Introducing the concept of Potential Aerosol Mass (PAM), Atmos. Chem. Phys., 7, 5727–5744, 2007.

Kleinman, L. I., Daum, P. H., Lee, Y.-N., Nunnermacker, L. J., Springston, S. R., Weinstein-Lloyd, J., and Rudolph, J.: A comparative study of ozone production in five U.S. metropolitan areas, J. Geophys. Res., 110, doi:10.1029/2004JD005096, 2005.

Kovacs, T., and Brune, W.: Total OH loss rate measurement. J. Atmos. Chem., 39, 105–122, 2001.

Kovacs, T. A., Brune, W. H., Harder, H., Martinez, M., Simpas, J. B., Frost, G. J., Williams, E., Jobson, T., Stroud, C., Young, V., Fried, A., and Wert, B.: Direct measurements of urban OH reactivity during Nashville SOS in summer 1999, J. Environ. Monitor., 5(1), 68–74, 2003.

LaFranchi, B. W., Goldstein, A. H., and Cohen, R. C.: Observations of the temperature dependent response of ozone to NO_x reductions in the Sacramento, CA urban plume, Atmos. Chem. Phys., 11, 6945–6960, doi:10.5194/acp-11-6945-2011, 2011.

Marr, L. C. and Harley, R. A.: Modeling the effect of weekday/weekend differences in motor vehicle emissions on photochemical air pollution in Central California, Environ. Sci. Technol., 26, 4099–4106, 2002.

Martien, P. T. and Harley, R. A.: Adjoint sensitivity analysis for a three-dimensional photochemical model: application to Southern California, Environ. Sci. Technol., 40, 4200–4210, 2006.

Martinez, M., Harder, H., Ren, X., Lesher, R. L., and Brune, W. H.: Measuring atmospheric naphthalene with laser-induced fluorescence, Atmos. Chem. Phys., 4, 563–569, 2004.

Martinez, M., Harder, H., Kovacs, T. A., Simpas, J. B., Bassis, J., Lesher, R., Brune, W. H., Frost, G. J., Williams, E. J., Stroud, C. A., Jobson, B. T., Roberts, J. M., Hall, S. R., Shetter, R. E., Wert, B., Fried, A., Alicke, B., Stutz, J., Young, V. L., White, A. B., and Zamora, R. J.: OH and HO_2 concentrations, sources, and loss rates during the Southern Oxidants Study in Nashville, Tennessee, summer 1999, J. Geophys. Res., 108(D19), D4617, 2003.

Milford, J. B., Russell, A. G., and McRae, G. J.: A new approach to photochemical pollution control: implications of spatial patterns in pollutant responses to reductions in nitrogen oxides and reactive organic gas emissions, Environ. Sci. Technol., 23, 1290–1301, 1989.

Millet, D. B., Donahue, N. M., Pandis, S. N., Polidori, A., Stanier, C. O., Turpin, B. J., and Goldstein, A. H.: Atmospheric VOC measurements during the Pittsburgh Air Quality Study: results, interpretation, and quantification of primary and secondary contributions, J. Geophys. Res., 110, D07S07, doi:10.1029/2004JD004601, 2005.

Min1, K.-E., Pusede, S. E., Browne, E. C., LaFranchi, B. W., Wooldridge, P. J., Cohen, R. C.: Eddy covariance fluxes and vertical concentration gradient measurements of NO and NO_2 over a ponderosa pine ecosystem: observational evidence for canopy removal of NO_x, *submitted to Atmos. Chem. Phys. Discuss*., 2013.

Murphy, J. G., Day, D. A., Cleary, P. A., Wooldridge, P. J., Millet, D. B., Goldstein, A. H., and Cohen, R. C.: The weekend effect within and downwind of Sacramento: part 1. Observations of ozone, nitrogen oxides, and VOC reactivity, Atmos. Chem. Phys., 7, 5327–5339, 2007.

Murphy, J. G., Day, D. A., Cleary, P. A., Wooldridge, P. J., Millet, D. B., Goldstein, A. H., and Cohen, R. C.: The weekend effect within and downwind of Sacramento: part 2. Observational evidence for chemical and dynamical contributions, Atmos. Chem. Phys. Discuss., 6, 11 971–12 019, 2006.

Newman, S., Jeong, S., Fischer, M. L., Xu, X., Haman, C. L., Lefer, B., Alvarez, S., Rappenglueck, B., Kort, E. A., Andrews, A. E., Peischl, J., Gurney, K. R., Miller, C. E., and

Yung, Y. L.: Diurnal tracking of anthropogenic CO emissions in the Los Angeles basin megacity during spring, 2010, Atmos. Chem. Phys. Discuss., 12, 5771-5801, doi:10.5194/acpd-12-5771-2012, 2012.

National Research Council: Rethinking the ozone problem in urban and regional air pollution, The National Academy Press, Washington, D.C., 1991.

Ngwabie, N. M., Schade, G. W., Custer, T. G., Linke, S., and Hinz, T: Abundances and flux estimates of volatile organic compounds from a dairy cowshed in Germany, J. Environ. Qual., 37(2), 565–573, 2008.

Olson, C. N., Galloway, M. M., Yu, G., Hedman, C. J., Lockett, M. R., Yoon, T., Stone, E. A., Smith, L. M., and Keutsch, F. N.: Hydroxycarboxylic acid-derived organosulfates: synthesis, stability, and quantification in ambient aerosol. Environ. Sci. Technol., 45(15), 6468–6474, 2011.

Perring, A. E., Bertram, T. H., Farmer, D. K., Wooldridge, P. J., Blake, D. R., Blake, N. J., Heikes, B., Avery, M. A., Sachse, G., Diskin, G., Fuelberg, H., Brune, W. H., Crawford, J., Singh, H. B., and Cohen, R. C.: Alkyl nitrate production and persistence in the Mexico City plume, Atmos. Chem. Phys., 10, 7215–7229, 2010.

Pusede, S. E. and Cohen, R. C.: On the observed response of ozone to NO_x and VOC reactivity reductions in San Joaquin Valley California 1995–present, Atmos. Chem. Phys., 12, 8328–8339, 2012.

Pusede, S. E., Gentner, D. W., Wooldridge, P. J., Browne, E. C., Guha, A., Goldstein, A. H., Thomas, J., Brune, W. H., DiGangi, J. P., Henry, S. B., Keutsch, F. N., Beaver, M. R., St Clair, J. M., Wennberg, P. O., and Cohen, R. C.: On the temperature dependence and decadal trends of ozone in the San Joaquin Valley: Constraints from measurements at the CalNex-Bakersfield supersite, manuscript in preparation.

Ren, X. R., Edwards, G. D., Cantrell, C. A., Lesher, R. L., Metcalf, A. R., Shirley, T., and Brune, W. H.: Intercomparison of peroxy radical measurements at a rural site using laser-induced fluorescence and Peroxy Radical Chemical Ionization Mass Spectrometer (PerCIMS) techniques, J. Geophys. Res., 108(D19), D4605, 2003a.

Ren, X. R., Harder, H., Martinez, M., Lesher, R. L., Oliger, A., Shirley, T., Adams, J., Simpas, J. B., and Brune, W. H.: HO_x concentrations and OH reactivity observations in New York City during PMTACS-NY2001, Atmos. Environ., 37, (26), 3627–3637, 2003b.

Ren, X. R., Harder, H., Martinez, M., Lesher, R. L., Oliger, A., Simpas, J. B., Brune, W. H., Schwab, J. J., Demerjian, K. L., He, Y., Zhou, X. L., and Gao, H.G.: OH and HO_2 chemistry in the urban atmosphere of New York City, Atmos. Environ., 37 (26), 3639–3651, 2003c.

Ren, X. R., Harder, H., Martinez, M., Faloona, I. C., Tan, D., Lesher, R. L., Di Carlo, P., Simpas, J. B., and Brune, W. H.: Interference testing for atmospheric HO_x measurements by laser-induced fluorescence, J. Atmos. Chem., 47, 169–190, 2004.

Ren X. R., Brune, W. H., Mao, J. Q., Mitchell, M. J., Lesher, R. L., Simpas, J. B., Metcalf, A. R., Schwab, J. J., Cai, C. X., Li, Y. Q., Demerjian, K. L., Felton, H. D., Boynton, G., Adams, A., Perry, J., He, Y., Zhou, X. L., and Hou, J.: Behavior of OH and HO_2 in the winter atmosphere in New York City, Atmos. Environ., 40(2), S252–S263, 2006.

Rollins, A. W., Smith, J. D., Wilson, K. R., and Cohen, R. C.: Real time in situ detection of organic nitrates in atmospheric aerosols, Environ. Sci. Technol. 44, 5540–5545, 2010.

Rosen, R. S., Wood, E. C., Wooldridge, P. J., Thornton, J. A., Day, D. A., Kuster, W., Williams, E. J., Jobson, B. T., and Cohen, R. C.: Observations of total alkyl nitrates during Texas Air Quality Study 2000: Implications for O_3 and alkyl nitrate photochemistry, J. Geophys. Res., 109, doi: 10.1029/2003 JD004227, 2004.

Rubin, J. I., Kean, A. J., Harley, R. A., Millet, D. B., and Goldstein, A. H.: Temperature dependence of volatile organic compound evaporative emissions from motor vehicles, J. Geophys. Res., 111(D3), D03305, doi:10.1029/2005JD006458, 2006.

Shirley, T. R., Brune, W. H., Ren, X., Mao, J., Lesher, R., Cardenas, B., Volkamer, R., Molina, L. T., Molina, M. J., Lamb, B., Velasco, E., Jobson, T., and Alexander, M.: Atmospheric oxidation in the Mexico City Metropolitan Area (MCMA) during April 2003, Atmos. Chem. Phys., 6, 2753–2765, 2006.

Scheirer, A. H., Ed., 2007, Petroleum systems and geologic assessment of oil and gas in the San Joaquin Basin Province, California: U.S. Geological Survey Professional Paper 1713, http://pubs.usgs.gov/pp/pp1713/, accessed 2007.

Sillman, S., Logan, J. A., and Wofsy, S. C.: The sensitivity of ozone to nitrogen oxides and hydrocarbons in regional ozone episodes, J. Geophys. Res., 95, 1837–1851, 1990.

Sillman, S., He, D., Cardelino, C., and Imhoff, R. E., The use of photochemical indicators to evaluate ozone–NO_x–hydrocarbon sensitivity: case studies from Atlanta, New York, and Los Angeles. J. Air Waste Manage. Assoc., 47, 1030–1040, 1997.

Steiner, A.L., R.C. Cohen, R.A. Harley, S. Tonse, D.B. Millet, G.W. Schade and A.H. Goldstein, VOC reactivity in central California: comparing an air quality model to ground-based observations, Atmos. Chem. Phys., 8, 351-368, 2008.

Thornton, J. A., Wooldridge, P. J., and Cohen, R. C.: Atmospheric NO_2: in situ laser-induced fluorescence detection at parts per trillion mixing ratios, Anal. Chem., 27, 528–539, 2000.

Thornton, J. A., Wooldridge, P. J., Cohen, R. C., Martinez, M., Harder, H., Brune, W. H., Williams, E. J., Roberts, J. M., Fehsenfeld, F. C., Hall, S. R., Shetter, R. E., Wert, B. P., and

Fried, A.: Ozone production rates as a function of NO_x abundances and HO_x production rates in the Nashville urban plume, J. Geophys. Res., 107, doi:10.1029/2001JD000932, 2002.

Trainer, M., Williams, E. T., Parrish, D. D., Buhr, M. P., Allwine, E. J., Westberg, H. H., Fehsenfeld, F. C., and Liu, S. C.: Models and observations of the impact of natural hydrocarbons on rural ozone, Nature, 329, 705–707, 1987.

Warneke, C., de Gouw, J. A., Holloway, J. S., Peischl, J., Ryerson, T. B., Atlas, E., Blake, D., Trainer, M., and Parrish, D. D.: Multi-year trends in volatile organic compounds in Los Angeles, California: Five decades of decreasing emissions, J. Geophys. Res., 117, doi:10.1029/2012JD017899, 2012.

Yokelson R. J., Urbanski, S. P., Atlas, E. L., Toohey, D. W., Alvarado, E. C., Crounse, J. D., Wennberg, P. O., Fisher, M. E., Wold, C. E., Campos, T. L., Adachi, K., Buseck, P. R., and Hao, W. M.: Emissions from forest fires near Mexico City, Atmos. Chem. Phys. 7, 5569, 2007.

8. Glossary of Terms, Abbreviations, and Symbols

AGU	American Geophysical Union
AMS	Aerosol Mass Spectrometer
amu	atomic mass unit
APN	Acyl Peroxy Nitrates
ARB	Air Resources Board
AVOC	Anthropogenic Volatile Organic Compound
BEARPEX	Biosphere Effects on AeRosols and Photochemistry EXperiment
BVOC	Biogenic Volatile Organic Compound
CA	California
CalNex-LA	CalNex super monitoring site in the Los Angeles basin (Pasadena)
CalNex-SJV	CalNex super monitoring site in the San Joaquin Valley (Bakersfield)
CARB	California Air Resources Board
CBL	Convective Boundary Layer
CH_2O	formaldehyde
CHOCHO	glyoxal
CIMS	Chemical Ionization Mass Spectrometer
CIT	California Institute of Technology
CMAQ	Community Multi-scale Air Quality model
CO	carbon monoxide
CO_2	carbon dioxide
CST	California standard time
EC	elemental carbon
GAS	Glycolic Acid Sulfate
GC/MS-FID	Gas Chromatography/Mass Spectrometry-Flame Ionization Detector
H_2O	water vapor
H_2O_2	hydrogen peroxide
HCl	hydrochloric acid
HCN	hydrogen cyanide
HNO_3	nitric acid
HO_2	hydroperoxy radical
HO_x	$OH + HO_2$
HONO	nitrous acid
IC	Ion Chromatography
IR	infra-red
IVOC	Intermediate-Volatility Organic Carbon
LGR	Los Gatos Research
MIR	Maximum Incremental Reactivity
MODIS	Moderate Resolution Imaging Spectroradiometer
MPAN	methyl peroxy acetyl nitrate
MSD	mass selective detector
N_2O	nitrous oxide
NO	nitric oxide
NO_2	nitrogen dioxide
NO_3	nitrate radical
NO_3^-	nitrate ion

NOAA	National Oceanic and Atmospheric Administration
NO_x	$NO + NO_2$
O_3	ozone
OC	organic carbon
OH	hydroxyl radical
OMI	Ozone Monitoring Instrument
PAN	peroxy acetyl nitrate
PFA	Perfluoroalkoxy
PHO_x	HO_x Production Rate
PM1	particulate matter less than 1 micron aerodynamic diameter
PM2.5	particulate matter less than 2.5 microns aerodynamic diameter
PMT	photo-multiplier tube
PO_3	Ozone Production Rate
PPN	peroxy propionyl nitrate
PSU	Pennsylvania State University
RACM2	Regional Atmospheric Chemistry Mechanism Version 2
REA	Relaxed Eddy Accumulation
RO_2NO_2	peroxyalkyl nitrate
$RONO_2$	alkyl nitrate
SJV(AB)	San Joaquin Valley (Air Basin)
SO_2	sulfur dioxide
SOA	Secondary Organic Aerosol
SoCAB	South Coast Air Basin
TD-CIMS	Thermal Dissociation Chemical Ionization Mass Spectrometer
TD-LIF	Thermal Dissociation Laser Induced Fluorescence
Tmax	maximum daily temperature
UC(B)	University of California, Berkeley
UCSD	University of California, San Diego
UNC	University of North Carolina
UV	ultraviolet
UW	University of Washington
UW-Madison	University of Wisconsin, Madison
VOC	Volatile Organic Compound
VOCR	Volatile Organic Compound Reactivity with OH